SPECTRUM MEASUREMENT WITH THE TELESCOPE ARRAY LOW ENERGY EXTENSION (TALE) FLUORESCENCE DETECTOR

by

Zachary James Zundel

A dissertation submitted to the faculty of
The University of Utah
in partial fulfillment of the requirements for the degree of

Doctor of Philosophy

in

Physics

Department of Physics and Astronomy

The University of Utah

August 2016

The University of Utah Graduate School

STATEMENT OF DISSERTATION APPROVAL

The dissertation of **Zachary James Zundel**

has been approved by the following supervisory committee members:

Charles Jui	, Chair	**3/1/2016** Date Approved
Paolo Gondolo	, Member	**3/3/2016** Date Approved
Stephan LeBohec	, Member	**3/1/2016** Date Approved
Andrey Rogachev	, Member	**3/3/2016** Date Approved
Sonia Salari	, Member	**3/1/2016** Date Approved

and by **Carleton DeTar** , Chair/Dean of

the Department/College/School of **Physics and Astronomy**

and by David B. Kieda, Dean of The Graduate School.

ABSTRACT

The Telescope Array (TA) experiment is the largest Ultra High Energy cosmic ray observatory in the northern hemisphere and is designed to be sensitive to cosmic ray air showers above 10^{18}eV. Despite the substantial measurements made by TA and AUGER (the largest cosmic ray observatory in the southern hemisphere), there remains uncertainty about whether the highest energy cosmic rays are galactic or extragalactic in origin.

Locating features in the cosmic ray energy spectrum below 10^{18}eV that indicate a transition from galactic to extragalactic sources would clarify the interpretation of measurements made at the highest energies. The Telescope Array Low Energy Extension (TALE) is designed to extend the energy threshold of the TA observatory down to $10^{16.5}$eV in order to make such measurements.

This dissertation details the construction, calibration, and operation of the TALE fluorescence detector. A measurement of the flux of cosmic rays in the energy range of $10^{16.5} - 10^{18.5}$eV is made using the monocular data set taken between September 2013 and January 2014. The TALE fluorescence detector observes evidence for a softening of the cosmic spectrum at $10^{17.25\pm0.5}$eV. The evidence of a change in the spectrum motivates continued study of $10^{16.5} - 10^{18.5}$eV cosmic rays.

For Zan

CONTENTS

LIST OF FIGURES

LIST OF TABLES

ACKNOWLEDGMENTS

I would like to thank my advisor, Professor Charlie Jui, for his constant guidance, support, and instruction. He taught me to doggedly attack problems from different directions until they are resolved and instilled in me a broad set of skills outside of the standard physics coursework. I would also like to thank Jeremy Smith, who was a partner in every phase of the TALE FD development and deployment. Dr. Tareq AbuZiad's work and dedication to understanding the TALE detector reconstruction software substantially sped up the analysis of this dissertation. Stan Thomas was fundamental in understanding the photometric scale of the TALE detector. Finally, special thanks to Dr. John Matthews for his constant support with both the TALE detector operations and the review of this dissertation.

CHAPTER 1

HADRON INDUCED EXTENSIVE AIR SHOWERS

The first indication that hadronic cosmic rays (protons and atomic nuclei) are accelerated to energies above 10^{15} eV was first discovered by Bruno Rossi in 1934 [19] and was later rediscovered by Pierre Auger in 1937 [20]. Pierre Auger recorded two Geiger counters regularly discharging at nearly the same time, despite the fact that distances of many meters separated them. After increasing the separation to over 160 meters, coincident discharges at a rate of a few events per hour continued [20]. These coincident detections of ionizing particles led Auger to hypothesize that cosmic rays with at least 10^{15} eV in primary energy were initiating showers of secondary particles when they interacted with the atmosphere [20]. This cascading process results in an expanding layer of particles, spread over many kilometers in extent, traveling down the atmosphere at essentially the speed of light [9]. This phenomenon is referred to as an Extensive Air Shower (EAS).

1.1 EAS Physics

When a cosmic ray (CR) enters the atmosphere, it eventually interacts with an atomic nucleus in the atmosphere. Due to the nonuniform density of the atmosphere, it is convenient to express the cross section for cosmic ray-nuclei interactions in terms of the interaction mean free path,

$$\lambda\rho = \frac{A}{N_A\sigma_{inel}}[g/cm^2], \tag{1.1}$$

in which λ is the mean free path of the cosmic ray moving through the atmosphere, ρ is the density of the atmosphere, A is the mass number of the nucleus, N_A is Avogadro's number, and σ is the inelastic cross section of the interaction. Up to TeV energies, collider experiments have measured the cross sections of such interactions and have parameterized them according to,

$$\sigma = \pi R^2(A_1^{1/3} + A_2^{1/3} - \delta)^2[mb], \tag{1.2}$$

where $\pi R^2 = 66.63$ mb, A_1 is the atomic number of the incident cosmic ray, A_2 is the atomic number of the target nuclei, and $\delta = 1.12$ [1]. Figure 1.1 displays the relationship between the mean free path for high energy cosmic rays in the atmosphere as a function of the cosmic ray mass number. Clearly, heavier primaries will interact higher in the atmosphere than lighter cosmic rays, and the root mean square (RMS) deviation of the depth of first interaction will be smaller for heavy nuclei. Importantly, the mean free path for any cosmic ray nuclei is much smaller than the 800 g/cm^2 vertical depth of the atmosphere [9].

Once a cosmic ray collides with an air nucleus, the details of the first interaction depend greatly on the atomic number of the cosmic ray. Understanding the differences between air showers induced by different cosmic ray primary types is important for the TALE experiment described in this dissertation. Cosmic rays arriving in the energy region to which the TALE detector is sensitive are expected to be of a mixed and transitioning composition [21].

At the energies in which we are interested, the initial interaction is well described by gluon-gluon interactions between the incident cosmic ray and the target nucleus. At the first interaction, both the primary cosmic ray and the target nucleus disintegrate, resulting in a spray of secondary relativistic hadrons [1]. This process is illustrated in Figure 1.2. While the total number of particles produced increases with the mass of the primary, the secondaries are composed of approximately 20% $\pi+$, 20% $\pi-$, 20% π^0, 15% Kaons, 10% protons and neutrons, and 15% heavier hadrons [7]. For proton primaries, the target air nucleus is left in an unstable state and fragments. The fragmentation products are left behind without much forward momentum [1].

The elasticity of an interaction is the ratio of the energy of the most energetic secondary product particle to the energy of the initial cosmic ray [1] and is given by,

$$\eta = \frac{E_{out}}{E_{total}} < 0.5 \tag{1.3}$$

for proton-nuclei interactions. The elasticity takes on typical values of $\eta = 0.3 \pm 0.1$ [1]. The remainder of the energy is invested in creating secondary particles and providing them with momentum. The number of charged hadrons produced in proton-proton interactions has been measured in collider experiments and follows,

$$< n_{ch} >= a + b \ln s + c(\ln s)^2, \tag{1.4}$$

where n_{ch} is the number of charged particles produced, $\sqrt{s}$ is the center of mass energy (in GeV), a=1.97 , b=0.21 , and c=0.148 in the energy range of $10 < \sqrt{s} < 540$ GeV [22]. However, it has been noted that simple $\ln s$ scaling is expected to be violated for air showers with energies greater than 10^{16} eV [23]. Since pions dominate the secondary particle

production, it is important to note that the cross section of the charged pions follow that of protons according to,

$$\sigma_{\pi-air} \approx (2/3)\sigma_{p-air} \tag{1.5}$$

and due to the relativistic extension of their lifetime, charged pions are more likely to interact with another air nucleus rather than decay [1]. Charged pions interacting with nuclei also have smaller elasticities and larger multiplicities than nucleons interacting with the nuclei [1].

The multiplicity of proton-nucleus secondary products increases as the mass number of the target increases. The scaling factor for the multiplicity of secondaries as compared to p-p collisions is given by,

$$R = c + dA^{1/3} \tag{1.6}$$

where R is the ratio of the p-A to p-p multiplicities, c=0.74, and d=0.31 for collision energies of 3 TeV [24], and A is the atomic number of the target. Figure 1.3 displays the charged particle multiplicity as a function of energy for p-p and p-air collisions. This plot shows that after the first interaction, there are hundreds of charged secondary particles.

In contrast to the detailed studies of collisions involving protons, the details of nucleus-nucleus interactions are still under investigation at accelerator facilities. Figure 1.4 schematically illustrates how the products of a nucleus - nucleus interaction include relativistic spallation products [9].

Studies of the relativistic fragmentation products of Fe in emulsion have not yet reached the level of determining the fragmentation multiplicity [2]. The determination of the charge multiplicity in nuclei-nuclei studies is complicated by the fact that the impact parameter of the two atoms greatly affects the resulting multiplicity [25]. For central collisions between nuclei, the charged multiplicity scales with the atomic number of the primary [2], leading to the result that proton-air multiplicities act as a lower bound for the multiplicities of heavier elements with air [25]. The ejected fragmented remains of the target nucleus (spallation products) are considered leading particles and carry away substantial fractions of the momentum of the system. It is important to note that the relativistic fragments have shorter interaction lengths than other secondary products due to their relatively large cross sections. Additionally, the number of distinct hadronic cores in an air shower increases with the atomic number of the cosmic ray [1]. Further investigation at RHIC will be valuable in understanding the fragmentation process of heavy nuclei.

Regardless of the cosmic ray's mass number, a relativistic cascade of secondary hadrons is produced during interactions with the atmosphere. Most of the secondary particles will

retain enough energy to initiate their own cascades. A schematic of the air shower process is shown in Figure 1.5 and demonstrates the interaction and decay processes for hadronic shower products. The process of secondary hadrons initiating additional cascades continues until the average hadron energy falls below the threshold of approximately 2GeV [9].

During the development of the hadronic cascade, neutral pions account for approximately 20% of all secondary products in each collision. They decay electromagnetically according to

$$\pi^0 \rightarrow \gamma + \gamma, \tag{1.7}$$

with a branching ratio of 0.998 and a mean lifetime of 10^{-17} s [21]. The photons resulting from the decay of a π^0 will pair produce electrons in the presence of a nucleus. These electrons will, in turn, bremsstrahlung additional high-energy photons. Energy deposition from bremsstrahlung follows the relationship,

$$-\frac{dE}{dx} \approx 4\alpha \cdot N_A \cdot \frac{Z^2}{A} \cdot z^2 \left(\frac{1}{4\pi\epsilon_0} \cdot \frac{e^2}{mc^2}\right)^2 \cdot E \ln \frac{183}{z^{1/3}}, \tag{1.8}$$

where α is the fine structure constant, N_A is Avogadro's Number, ϵ_0 is the permittivity of free space, Z is the atomic number of the medium, A is the atomic weight of the medium, z is the charge number of the radiating particle, m is the mass of the particle, and E is the energy of the particle [10]. It is convenient to define a radiation length from this equation according to the form,

$$-\frac{dE}{dx} = \frac{E}{X_0}, \tag{1.9}$$

where the radiation length of electrons in air is measured to be $X_0 = 37 g/cm^2$ [10].

The process of bremsstrahlung and pair production continues, exponentially increasing the number of particles in the electromagnetic shower. The electromagnetic cascade continues to develop until the average electron energy falls to a level where the ionization energy loss per interaction length becomes larger than the bremsstrahlung energy loss per interaction length at a value known as the critical energy E_c. When the average hadron energy is too small to undergo deep inelastic scattering with air nucleons and the average energy of electrons falls below the critical energy, the shower has reached a maximum number of particles (X_{MAX}). After this point, the shower ceases to grow in particle number and begins to "range out" through additional ionization losses.

The energy loss of electrons as is transits matter due to ionization and excitation follows the Bethe Bloch form,

$$-\frac{dE}{dX} = 4\pi N_A r_e^2 m_e c^2 z^2 \frac{Z}{A} \frac{1}{\beta^2} \left(\ln \frac{2m_e c^2 \gamma^2 \beta^2}{I} - \beta^2 - \frac{\delta}{2}\right) \tag{1.10}$$

where z is the number of units of elementary charge of the electron, Z is the atomic number of the target, A is the atomic weight of the target, m_e is the electron mass, r_e is the electron radius , N_A is Avogadro's number, I is the mean excitation energy of the target, γ is the Lorentz factor, β is v/c, and δ accounts for the screening effect of the target material's electrons [10].

The parameterization of the electron critical energy dependence versus the target gas atomic number is given by,

$$E_c = 710MeV/(Z + 0.92), \tag{1.11}$$

where Z is the atomic number of the medium [21] and is plotted in Figure 1.6.

The hadronic core of the shower continually generates electromagnetic cascades. The electromagnetic component dominates an EAS when X_{MAX} is reached [9].

In addition to hadronic and electromagnetic cascades, very high-energy muons and neutrinos are also generated in an EAS. They predominately come from charged pions with small Lorentz factors produced in the upper atmosphere that have a chance to decay before interacting with another nucleus in the air. The decay of charged pions follow,

$$\pi^{\pm} \rightarrow \mu^{\pm} + \nu, \tag{1.12}$$

with a branching ratio of 0.999 and a mean lifetime of 2.6^{-8}s [21].

1.2 Light Generation in an EAS

When an EAS moves through the atmosphere, it generates two additional forms of light aside from normal radiative processes. The first kind of light is known as Cerenkov light, and is generated when charged particles move through a medium in excess of the speed of light in that medium. The propagation of a particle faster than the response time of the media creates a coherent electromagnetic wavefront in analogy to a sonic boom. Although the generation of Cerenkov light is not a significant form of energy loss for relativistic electrons, it can be a useful tool in particle physics for particle identification [21]. Cerenkov light is emitted on the condition,

$$v > \frac{c}{n(h,\nu)}, \tag{1.13}$$

where v is the velocity of the charged particle, c is the speed of light, and $n(h,\nu)$ is the frequency (ν) and elevation (h) dependent index of refraction of light in the medium [26]. The Cherenkov light is beamed forward along the direction of the charged particles. An

illustration of this is shown in Figure 1.7. Cerenkov light is emitted at an angle θ from the path of the charged particle according to

$$\theta = \cos^{-1}\left(\frac{c}{n(h,\nu)\cdot v}\right). \tag{1.14}$$

Cerenkov light is emitted in a continuum described by,

$$\frac{d^2N}{dxd\lambda} = \frac{2\pi\alpha z^2}{\lambda^2}\left(1 - \frac{1}{\beta^2 n^2(\lambda)}\right) \tag{1.15}$$

where N is the number of photons, λ is the wavelength, x is the transit depth, n is the wavelength dependent index of refraction, α is the fine structure constant, and z is the charge of the particle [21]. Due to the $1/\lambda^2$ dependence of this radiation, the majority of the produced Cherenkov light is in the UV.

In addition to Cherenkov light, fluorescence light is also generated in the atmosphere during the passage of an EAS. Charged particles in an EAS shower excite molecular nitrogen, which in turn relaxes and emits predominantly UV photons [27]. Technically, when an atom is excited by another charged particle and emits light, it is known as scintillation or luminescence. The term fluorescence refers to the emission of a secondary photon following absorption of an initial photon of shorter wavelength by an atom or molecule [7]. However, because of the analogy to fluorescent lights, the term "fluorescence" is use in the field of particle astrophysics. The remainder of this dissertation will follow this convention. For molecular nitrogen, emission is dominated by the First Positive and Second Negative band structures [27][4][28] as shown in Figure 1.8. The Second Positive System of molecular nitrogen dominates the UV emission. Emission of light from this system is generated by the electron transition from the various vibrational $B^2\Pi_g$ electron configuration state to the $C^3\Pi_u$ state. The second most luminescent system is First Negative System and is generated by transitions between the singularly ionized $B^2\Sigma_g^+$ and $X^2\Sigma_g^+$ states. Fluorescence light is generated between the wavelengths of 300nm and 420nm with the main peaks being at 337.1nm and 357.7nm.

A number of experiments have measured the spectral emission lines of nitrogen including Kakimoto [29], FLASH [30], Nagano [31], and AirFly [4]. The goal of these experiments was to quantify the fluorescence emission generated by an electron moving through air. Figure 1.9 shows the results of several measurements. The data points, including error bars, indicate the fluorescence yields, in number of photons per electron per meter. The dE/dx estimates, including volume correction, are shown by the curves. The relative scales of these are obtained by fitting the dashed curve to the data points. For the studies described

in this dissertation, we used the parameterization of Kakimoto *et al* [29] to calculate the yield as a function of energy, temperature, and pressure according to

$$Y = \frac{(\frac{dE}{dx})}{(\frac{dE}{dx})_{1.4MeV}} \rho \left(\frac{a_1}{1 + \rho b_1 \sqrt{T}} + \frac{a_2}{1 + \rho b_2 \sqrt{T}} \right), \tag{1.16}$$

where $\frac{dE}{dx}$ is the electron energy deposition as shown in Figure 1.9, T is the atmospheric temperature, and ρ is the atmospheric density. The remaining parameters $a_1 a_2 b_1 b_2$ are constants that fit the Kakimoto yield pressure dependency result [29] [32].

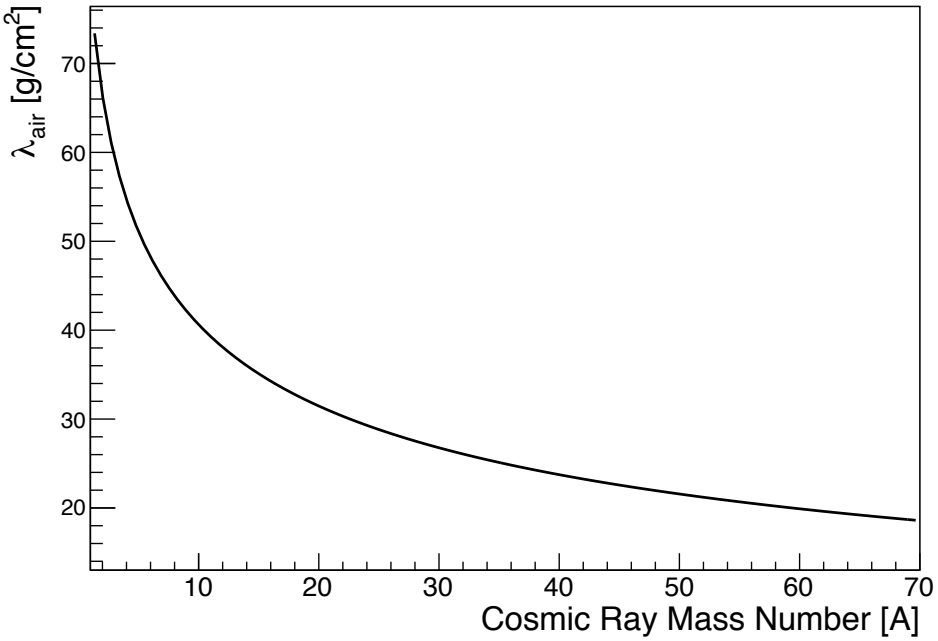

Figure 1.1: The Mean Free Path of a Cosmic Ray in the Atmosphere as a Function of Its Mass Number. This curve reflects a parameterization of data taken in TeV collisions at accelerators [1] and is described by Equation 1.2 . This parameterization from laboratory data has been verified by studying emulsion tracks [1] [2] of various primaries from balloon-born experiments. A review of the emulsion-based cross section can be found in a review by Saitio [3].

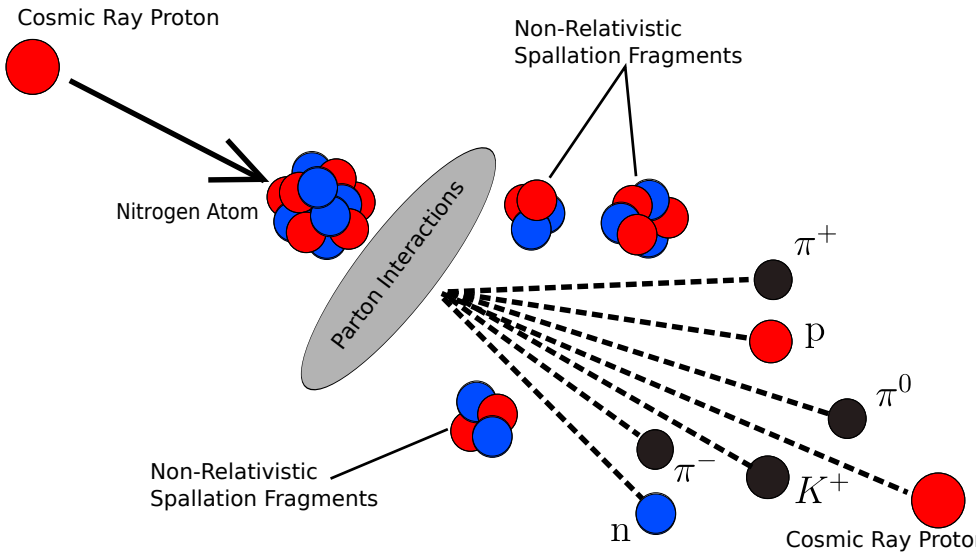

Figure 1.2: Illustration of the Collision of a Cosmic Ray Proton with a Nucleus of Nitrogen in the Atmosphere. Approximately 50% of the initial energy of the proton is carried away by the leading particle in the interaction [1]. The remainder of the energy generates new hadrons and imbues them with momentum. The nucleus initially impacted by the high energy proton is left in an unstable state and fragments. The remaining nucleus fragments are typically nonrelativistic.

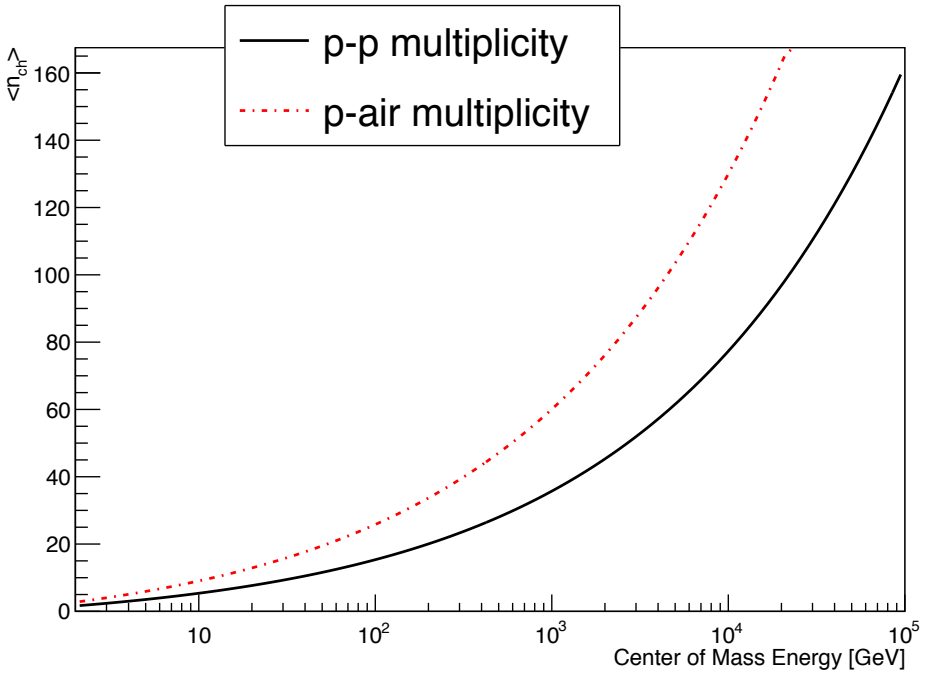

Figure 1.3: Secondary Particle Multiplicity vs. Center-of-mass Energy. Additionally, by folding together Equation 1.4 and Equation 1.6, the multiplicity for p-air collisions is estimated.

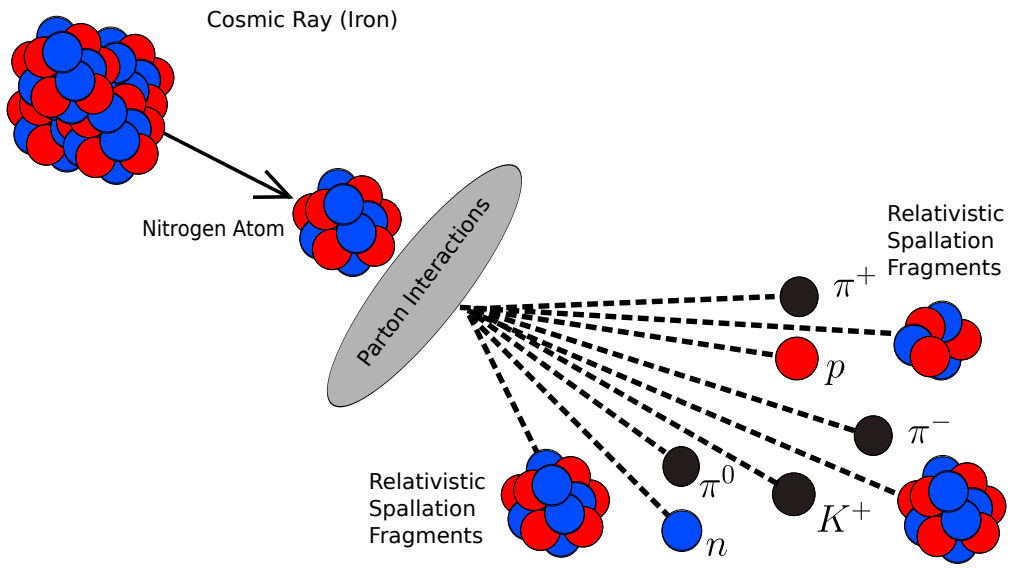

Figure 1.4: Schematic Drawing Showing an Iron Nucleus Cosmic Ray Interacting with a Nucleus of Nitrogen in the Atmosphere. The cosmic ray nuclei will interact with many of the nitrogen nuclei and produce hadronic showers. Spallation of the cosmic ray and nitrogen atom occurs. The spallation fragments of the energetic nucleus and jet products have large momentum in the forward direction. The elasticity of the Fe - Air collision is reported as $\eta < 0.15$ [1].

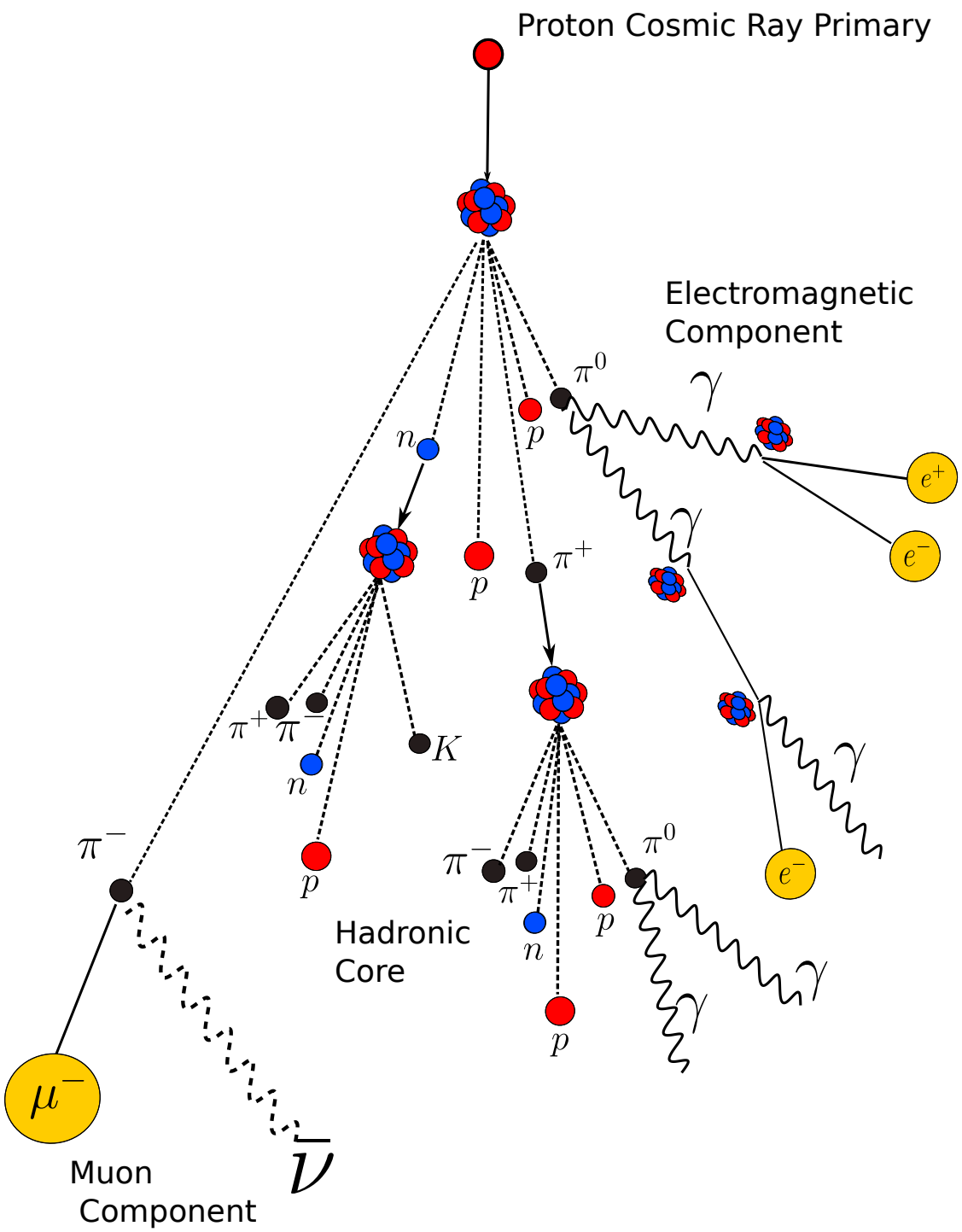

Figure 1.5: Schematic Diagram Showing the Shower Components of a Proton Induced Extensive Air Shower (EAS). An EAS is composed of a core hadronic cascade. The decay of $\pi^0 \rightarrow \gamma + \gamma$ initiates electromagnetic cascades. The decay of $\pi^{\pm} \rightarrow \mu^{\pm} + \nu$ generates the muon component of an EAS.

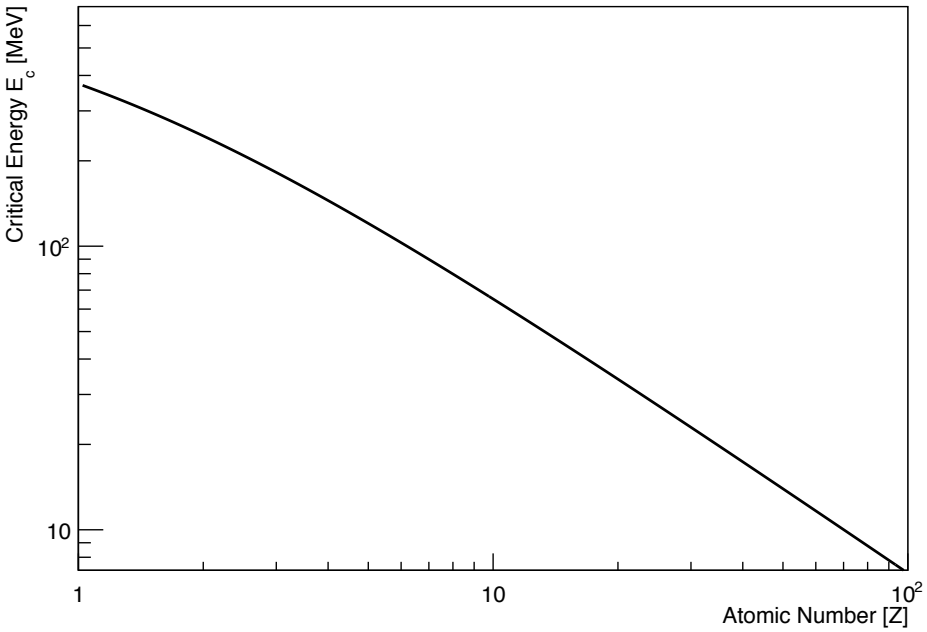

Figure 1.6: Critical Energy Curve for Electrons as a Function of the Atomic Number of the Gases. The critical Energy (Ec) is defined as the point where the ionization energy loss per interaction length becomes larger than the bremsstrahlung energy loss per interaction length.

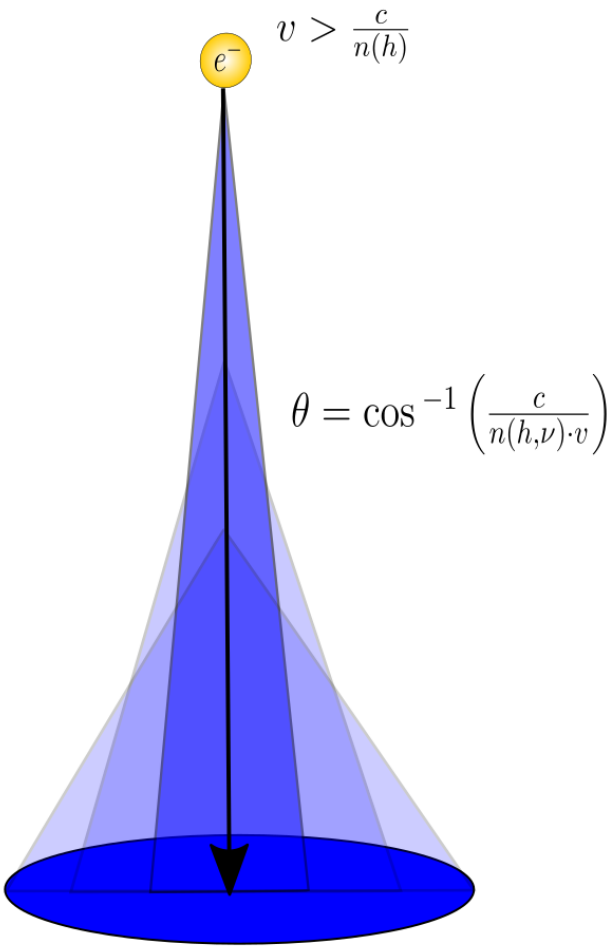

Figure 1.7: Illustration of the Emission of Cerenkov Light by an Electron Moving Down through the Atmosphere. The Cherenkov light is beamed forward in a cone around the direction of the particle. The increased density of the air at lower altitude increases the emission angle of light. The lateral distribution of the Cherenkov light is the convolution of the emission angle of the Cherenkov light at a given altitude and the number of charged particles above the Cherenkov emission threshold at that altitude. This results in the lateral distribution of Cherenkov light being indirectly related to longitudinal development of the shower.

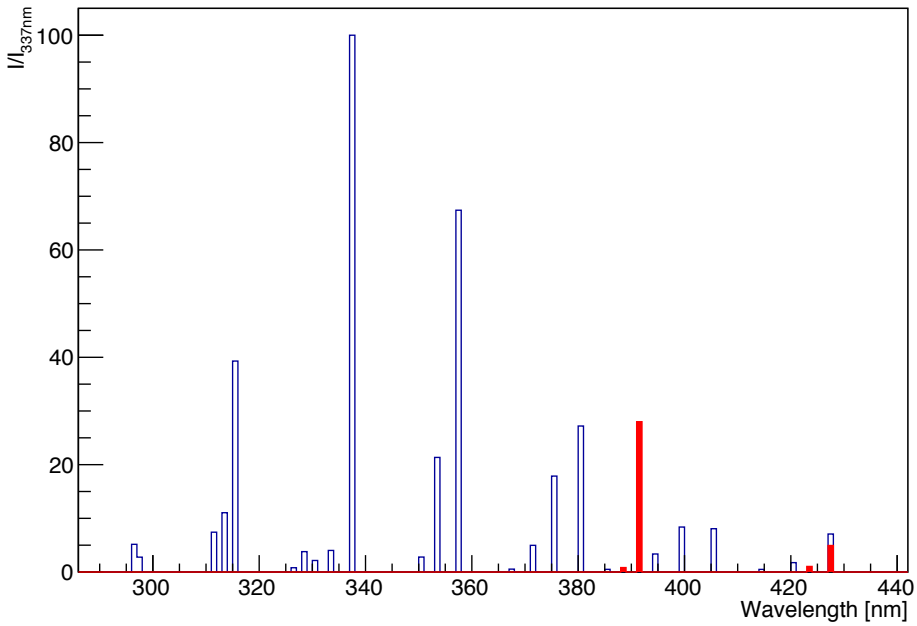

Figure 1.8: The Emission Lines for Nitrogen Excited by Electrons Reported by the AirFly Experiment [4]. The Second Positive System of molecular nitrogen dominates the UV emission. Emission of light from this system is generated by the electron transition from the various vibrational $B^2\Pi_g$ electron configuration state to the $C^3\Pi_u$ state. The second most luminescent system is First Negative System and is generated by transitions between the singly ionized $B^2\Sigma_g^+$ and $X^2\Sigma_g^+$ states. The relative intensity from each of the spectral lines is graphed as a function of wavelength. Open bars indicate the Second Positive System, filled bars indicate the First Negative System.

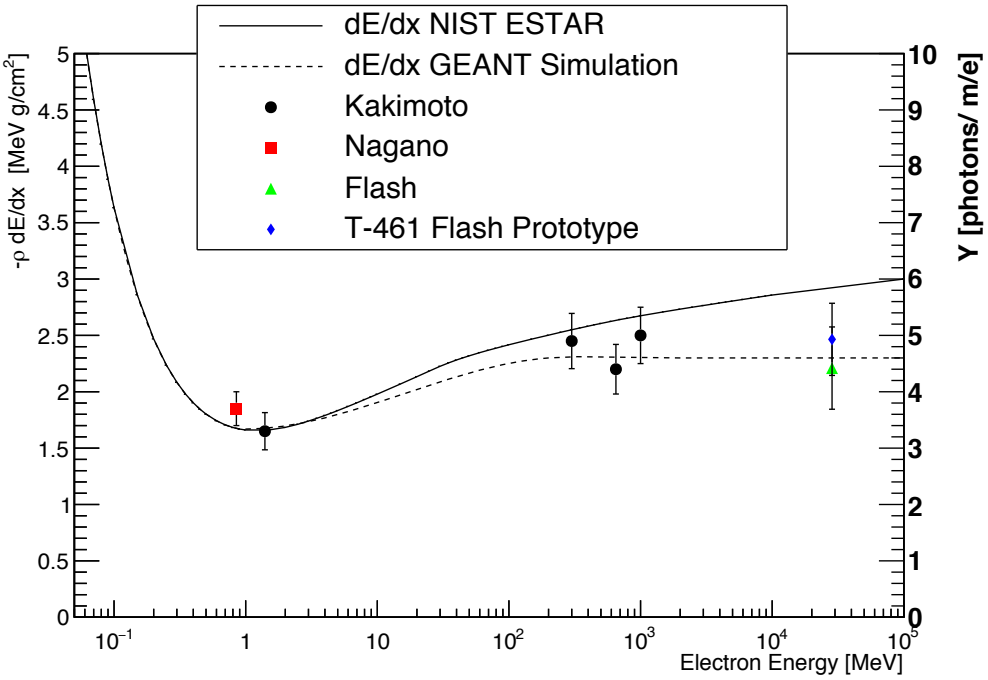

Figure 1.9: The Reported Fluorescence Yield of Kakimoto, Nagano, and FLASH. These experimental results are shown against the dE/dx curve available from NIST [5] that follows semi-empirical correction to the Bethe-Bloch equation and models an infinite volume limit [6]. Additionally, the results from a GEANT simulation are also shown and include the finite volume effect [7].

CHAPTER 2

DETECTION OF ULTRA HIGH ENERGY COSMIC RAYS AND THE TELESCOPE ARRAY EXPERIMENT

The flux of cosmic rays arriving at Earth with energies greater than 10^{15} eV is sufficiently small ($< 1 particle/m^2/year$) [33] that direct observation using balloon-based or satellite-based detectors is impractical. The large observation area required to make statistically useful measurements requires the utilization of indirect detection techniques, which observe EASs in order to infer information about the parent cosmic ray. Types of detectors used to observe an Extensive Air Shower (EAS) include water and scintillator ground arrays, fluorescence detectors, and Cherenkov detectors.

The Telescope Array (TA) Experiment is the largest Ultra High Energy Cosmic Ray (UHECR) observatory in the northern hemisphere. The TA observatory includes a ground array of scintillator detectors (SDs) overlooked by three fluorescence detector (FD) stations [7]. The TA surface array consists of 507 SDs spaced onto a 1.2 km square grid as shown in Figure 2.1 and is designed to be fully efficient at detecting air showers above 10^{19} eV [16]. An important aspect of any SD array is choosing the spacing between detectors. If the spacing is large, then the lateral distribution of charged particles at the ground is not adequately sampled. If the spacing is small, then the cost of the array becomes prohibitively expensive. An SD array needs to be large enough to sample the small flux of Ultra High Energy Cosmic Rays (UHECRs) while maintaining a detector spacing whose trigger efficiency and angular resolution are sufficient to make the recorded data useful. The size and spacing of the TA surface detectors were chosen from Monte Carlo simulation studies [34].

The three FD stations are called Black Rock (BR), Long Ridge (LR), and Middle Drum (MD) and observe the florescence signals from EASs on clear moonless nights. These FD stations are efficient at detecting EAS with energies down to 10^{18}eV at a distance of 10km.

The purpose of the experiment described in this dissertation is to extend the sensitivity of the TA experiment down to $10^{16.5}$ eV through the construction of an additional FD station, known as the Telescope Array Low Energy Extension FD (TALE-FD). The TALE-FD overlaps with sensitivity of the other TA FD stations and can use coincident events in order to ensure that the energy scale between detectors is properly understood. Due to the orientation of the TALE-FD, it observes events with large fractions of the signal being from Cherenkov light since the TALE cameras look higher in the sky and see showers from angles other than side-on. This means that the TALE-FD operated in a similar fashion to both a FD and a Cherenkov detector. Ultimately, the new complete TALE detector will include an infill SD array, the TALE-FD station, and the original MD FD station.

2.1 Surface Detector Arrays

Surface detector arrays sample the lateral distribution of charged particles deposited by air showers at the ground in order to determine the energy and arrival direction of cosmic rays. The main advantage of the SD technique over other methods lies in the ability to operate with nearly 100% duty cycle. The disadvantage of the SD technique is that the overall EAS energy estimation depends significantly on Monte Carlo predictions of particle distributions [35]. A diagram of a surface array is shown in Figure 2.2. An array of surface detectors can use one of two methods to sample the distribution of charged particles produced by an EAS. The first is by using a scintillator to convert energy deposited by charged particles into an optical signal for readout. The second is to use the Cherenkov light produced by highly relativistic particles as the optical signal.

The first method of instrumenting an EAS surface array is depicted in Figure 2.3, which demonstrates how the passage of charged particles through a plastic scintillator creates photons that are gathered by wavelength shifting fibers and read out by a photomultiplier tube (PMT). This is the type of SD that is used by the TA experiment and is equally sensitive to both the hard muon component of an EAS and the soft electromagnetic component [36]. A photograph of a SD counter used by the Telescope Array (TA) Collaboration is shown in Figure 2.4.

While wavelength-shifting fibers are typically used to match the emission spectrum of a scintillator with the sensitive region of a PMT, this is not the main motivation for using wavelength shifting fibers with the TA SDs. The primary purpose of using the fibers here is to ensure that a uniform signal is read out by the PMT regardless of the location in the plastic scintillator through which the charged EAS particles pass. The emission peak of

the polyvinyl toluene plastic scintillators used in the TA SDs occur near 420nm [10]. The scintillation photons are gathered by Y-11 Kurray wavelength shifting fibers [35] which have emission and absorption spectra shown in Figure 2.5. The absorption peak of the fibers matches the emission peak of the plastic scintillator. The wavelength shifting fibers direct the collected light to an Electron Tube (ET Enterprises 9124SA PMT [37]). The typical spectral response curve for the 9124SA PMT is shown in Figure 2.6 which shows that the PMT operates in the range of 350-450nm with greater than 25% Quantum Efficiency. The SD PMT sensitivity shown in Figure 2.6 is responsive to the full range of wavelength shifting fiber absorption and emission spectra shown in Figure 2.5.

In contrast to the scintillation surface detectors used by the TA experiment, the AUGER experiment utilizes water tanks and measures the Cherenkov signal generated by superluminal particles. A schematic of an AUGER water tank is shown in Figure 2.7.

Cherenkov water tanks are more sensitive to the hard muon components of the EAS than the soft electrons and gammas at the termination of the electromagnetic cascades [36]. This is due to the fact that superluminal electrons deposit nearly all of their energy in the water tank while muons do not [36]. This results in Cherenkov tanks and plastic scintillator detectors effectively measuring different parts of the EAS at the ground.

The angular arrival direction and curvature of an EAS shower front is first determined by a timing fit [35]. For this reason, accurate and reliable timing is an essential part of any SD array. For both TA and Auger, GPS units mounted on each SD unit provide absolute timing accuracy to 10ns [35]. After the arrival direction is determined, the Lateral Distribution Function (LDF) of the shower is estimated. TA uses the AGASA LDF [35, 38],

$$\rho = A\left(\frac{s}{91.6m}\right)^{-1.2}\left(1+\frac{s}{91.6m}\right)^{-(\eta(\theta)-1.2)}\left(1+\left(\frac{s}{1000m}\right)^{2}\right)^{-0.6} \tag{2.1}$$

where,

$$\eta(\theta) = 3.97 - 1.79[\sec\theta - 1], \tag{2.2}$$

and A is a scaling constant and s is the distance from the shower axis. To fit Equation 2.1, the core locations and A are varied until the χ^2/DOF between the data and the fit function is minimized. The energy of the shower is then determined by comparing the LDF at a fixed distance from the shower core to the results of Monte Carlo simulation. The fixed distance used by the TA experiment is 800 meters. An example of an SD event recorded by the TA collaboration is shown in Figure 2.8 along with the associated fit to the LDF in Figure 2.9.

2.2 Fluorescence Detectors

Another method for measuring cosmic ray air showers is the fluorescence technique. Fluorescence Detectors (FDs) utilize the fact that the charged particles created in an EAS excite the nitrogen gas in the atmosphere. When the nitrogen molecules relax, they emit photons with frequencies predominantly in the ultraviolet [27] as detailed in Section 1.2. Fluorescence photons are emitted isotropically from the shower, which allows a large volume of atmosphere to be observed using a single telescope. A diagram of an FD telescope is shown in Figure 2.10.

The FD method of detecting cosmic rays was pioneered by Greisen and Suga [39], but was only successfully demonstrated by the University of Utah cosmic ray group in 1976 [34]. The successful demonstration of the FD technique led to the instrumentation and operation of the Fly's Eye experiment which collected data between 1981-1993 [34]. The Telescope Array is an example of a third-generation FD, a picture of which is shown in Figure 2.11.

All FDs consist of a light collector that focuses the light from EAS tracks onto a camera of PMTs. Early optics included Fresnel lenses, but the TA and AUGER experiments utilize mirrors. The primary disadvantage of an FD is that because the fluorescence light is dim, these detectors can only be operated on clear moonless nights [7]. An example of the number of hours available to a FD detector is displayed in Figure 2.12. This gives a duty cycle of about 10%.

Light generated by an EAS is attenuated while traveling to an FD. The scintillation light may undergo molecular or aerosol scattering in addition to being absorbed by ozone. The effects of light propagation must all be taken into account when estimating the number of scintillation photons generated by an EAS.

However, FDs are able to make a direct calorimetric measurement of an air shower by measuring the shower's longitudinal development [40]. Accordingly, FDs provide better determination of the energy of an airshower than the surface detector method. The development of a shower can be fit to the Gaisser-Hillas parameterizations according to,

$$N_e(X) = N_{max}(\frac{X - X_0}{X_{max} - X_0})^{\frac{(X_{max}-X_0)}{\lambda}} \exp(\frac{X_{max} - X}{\lambda}), \tag{2.3}$$

where the number of electrons in a shower available to produce scintillation light is given as a function of three parameters X_{max}, X_0, and λ [32]. Here X_{max} is the depth of shower maximum, x_0 is the depth of initial interaction for the shower, and λ is a scale factor. The geometry of the showers is determined by the timing of PMTs that observe the shower. An example of the event display of a FD event is shown in Figure 2.13 and the associated reconstructed profile is shown in Figure 2.14.

Since the FD measures the longitudinal development of the shower, the total energy of and EAS can be determined by integrating the Gaisser-Hillas profile fit according to

$$E_{em} = 2.18MeV \int N_e(x)dx, \tag{2.4}$$

where the 2.18 MeV is determined from the fluorescence yield measurements; see Figure 1.9.

2.3 Hybrid Observatories

Due to the limited duty cycles of FDs, the two largest cosmic ray observatories to date, Auger and Telescope Array, couple a large surface array to the FDs as illustrated in Figure 2.1. This allows the experiments to benefit from the high efficiency of the SD array while simultaneously having the superior EAS energy measurements of FDs. In fact, without the use of FD detectors to properly calibrate an SD array, the reconstructed energy of UHECR showers reported by an array using current particle interaction models to reconstruct the event would systematically overestimate the energy. For example, with the detector configuration of TA for $E > 10^{19}$ eV, the energy estimation of the SD array is systematically 27% higher than the FD [16] measurement. The EAS information from the SD can be combined with the FD information to further constrain the geometry of FD events in order to improve geometrical resolutions [40]. The example SD event shown in Figure 2.8 was also observed by the MD FD and was shown in Figure 2.13. An example of the benefit of hybrid detection can be seen in the combined timing fit between the two detectors as illustrated in Figure 2.15.

Additionally, the hybrid detection technique provides a smaller uncertainty in the determination of X_{max} than using an FD alone. This makes hybrid data sets ideal for performing composition studies of cosmic rays [40].

2.4 Cherenkov Detectors

The Cherenkov light generated in the atmosphere by EAS particles can also be used to measure the direction and energy of an EAS. Detectors of this type fall into two categories: non-imaging and imaging detectors.

Non-imaging Cherenkov detectors consist of an array of individual Cherenkov light detectors distributed on the ground as demonstrated in Figure 2.16. The counters sample the intensity of Cherenkov light and can determine the lateral distribution of the light in a method similar to that used by SDs. Due to the majority of Cherenkov light falling within a few hundred meters of the core of a shower, arrays of this type become impractical for the investigation of EAS with energies much greater than $10^{15}eV$ [41]. The BLANCA

experiment utilized counters composed of a single PMT mounted to a Winston cone in order to increase the sensitivity by increasing the collection area [41]. Non-imaging Cherenkov detectors are able to infer the longitudinal development of a shower from the lateral distribution of light since light from lower elevations fills the center of the light pool and light from higher elevations fills the outer rings of the light pool. This is the technique proposed for the NICHE infill array that is designed to compliment and enhance the TALE detector [42].

Imaging Cherenkov telescopes are effectively FD telescopes pointed at sources. Also known as Air Cherenkov Telescopes, these instruments are used to perform $\gamma - ray$ astronomy and are far more common than cosmic ray detectors. Air Cherenkov Telescopes measure the Cherenkov light production as a function of atmospheric depth. This is the method utilized by the DICE [43] experiment for studying PeV cosmic rays. The TALE detector is sensitive to events that are dominated by either Cherenkov or scintillation signal. A display of a Cherenkov event seen by the TALE-FD is shown in Figure 2.17. The ellipsoid shape of imaged events is used by $\gamma - ray$ experiments to determine the geometry of the shower.

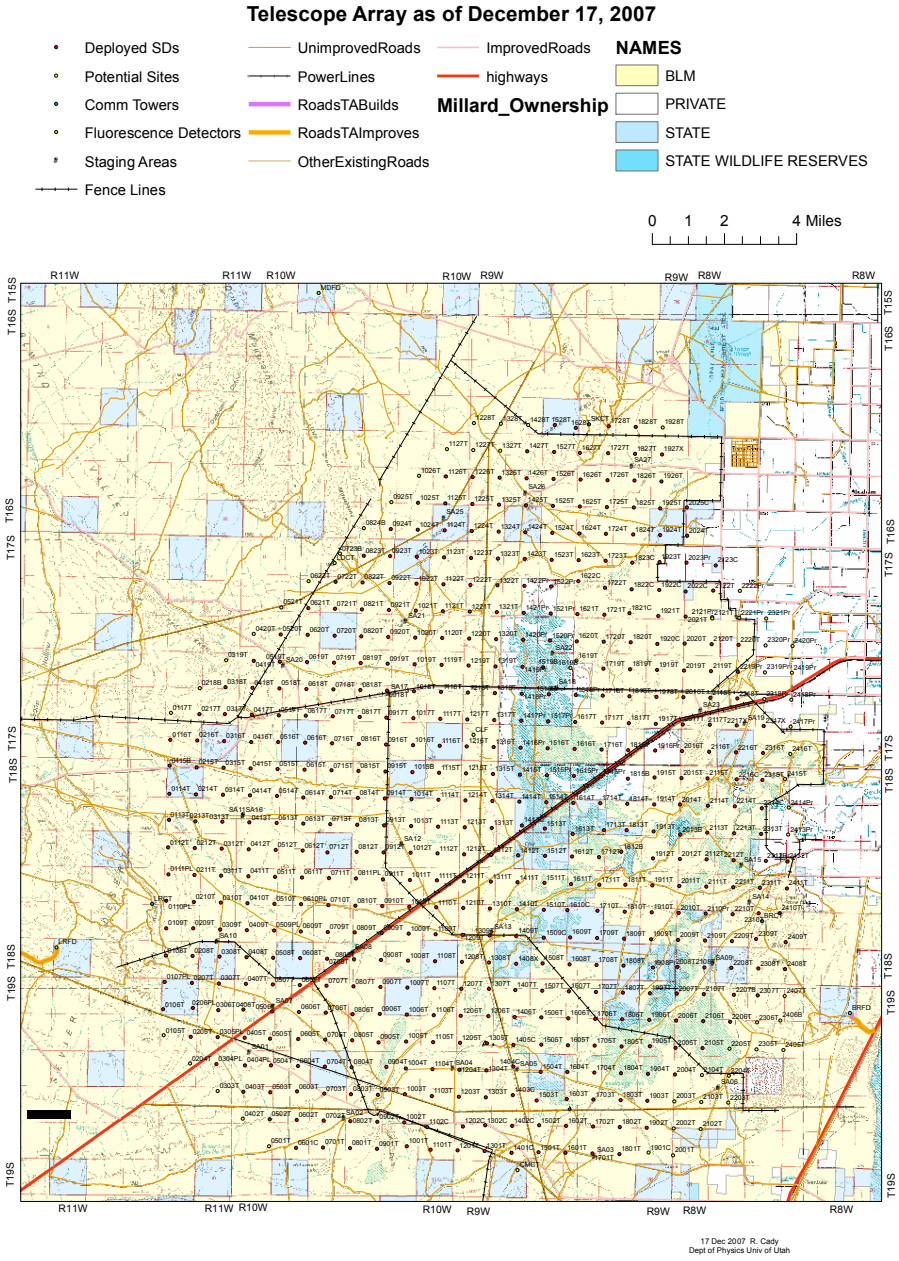

Figure 2.1: Layout of the TA Detectors. The surface detectors are laid out on a 1.2 km square grid spacing, which gives it a threshold of about 10^{19} eV for full efficiency. This array of surface detectors is overlooked by three fluorescence detector stations located at Black Rock Mesa (BR), Long Ridge (LR), and Middle Drum (MD) which view the air space over the SD array [8].

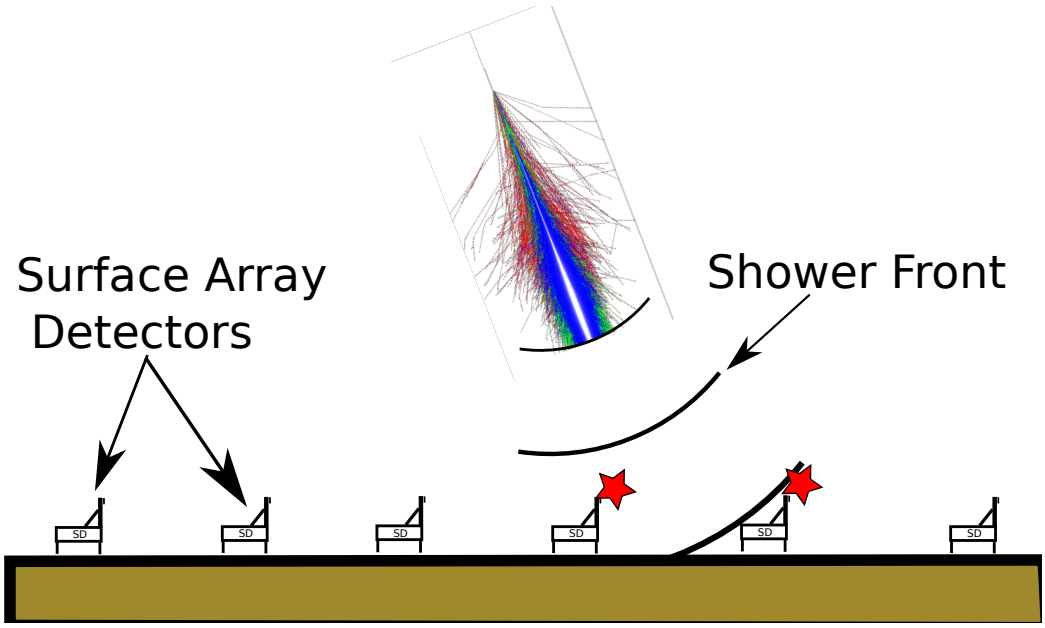

Figure 2.2: Diagram of a Surface Detector Array Used for Measuring Cosmic Ray Air Showers. During an EAS, the cascading process results in an expanding layer of particles traveling down through the atmosphere at approximately the speed of light. This "pancake" of particles can spread over many kilometers in extent [9]. The density of charge particles is sampled using a diffuse array of counters. Timing is used to determine the geometry of the shower, whereas signal size from the detectors is used to determine the energy of the air shower. SDs that trigger from the shower front are indicated with stars.

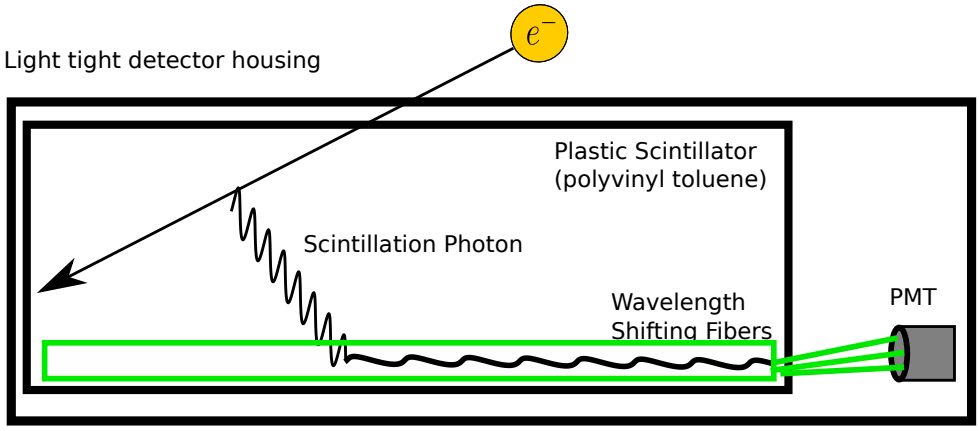

Figure 2.3: Schematic Diagram of a Surface Detector Utilizing Plastic Scintillator to Measure the Distribution of Charged Particles on the Ground. The device consists of a light tight housing that contains the sensitive components. The bulk of the detector is composed of two layers of 0.5 inch plastic scintillator (polyvinyl toluene) which converts deposited energy from passing charged particles into UV photons. The scintillator is extruded with grooves in it. Wavelength shifting optical fibers are placed in the grooves. They gather the light and take it to the PMTs. Polyvinyl toluene scintillators have an emission peak near 420nm [10]. The emitted UV light is gathered by wavelength shifting fibers and are channeled to a PMT. The PMT converts the optical signal into an electronic signal which is then digitized for later analysis.

Figure 2.4: Photograph of One of the Telescope Array Surface Detectors. The scintillators are contained in a stainless steel box. The solar panel is used to charge the detectors battery, which supplies power at night. Additionally the communications antenna can be seen on the top of the pole extending from the detector. The scintillating plastic is located on the "bed" of the detector while the control/readout electronics are housed in a box behind the solar panel[11].

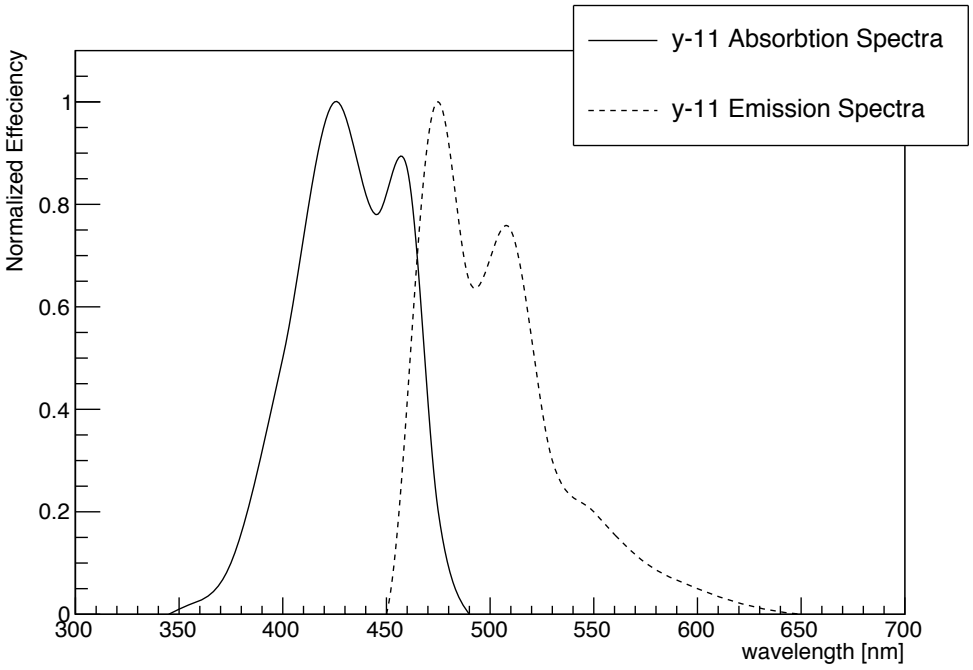

Figure 2.5: Emission and Absorption Spectra of the Y-11 Kurray Wavelength Shifting Fibers [12]. Notice that the peak of the absorption spectra occurs near the 420nm peak of the plastic scintillator emission spectra. The emission spectra has a significantly longer wavelength and transmits with a green color.

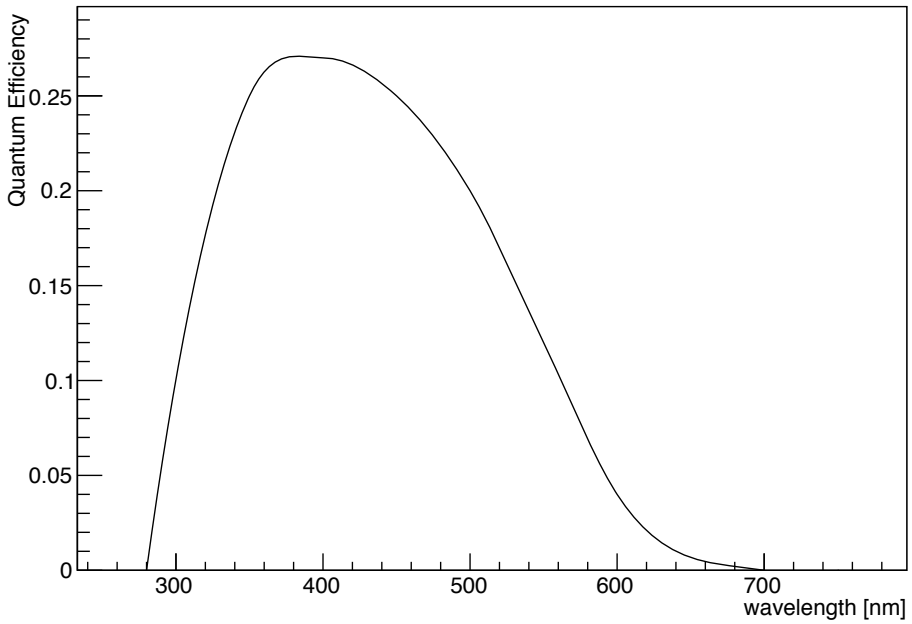

Figure 2.6: The Spectral Response Curve for the ET Enterprises 9124SA PMT [13]. The Quantum Efficiency (QE) of the tube is graphed against the wavelength of incident light. The QE of a tube is defined as the rate at which photons incident to the photocathode are converted into photoelectrons.

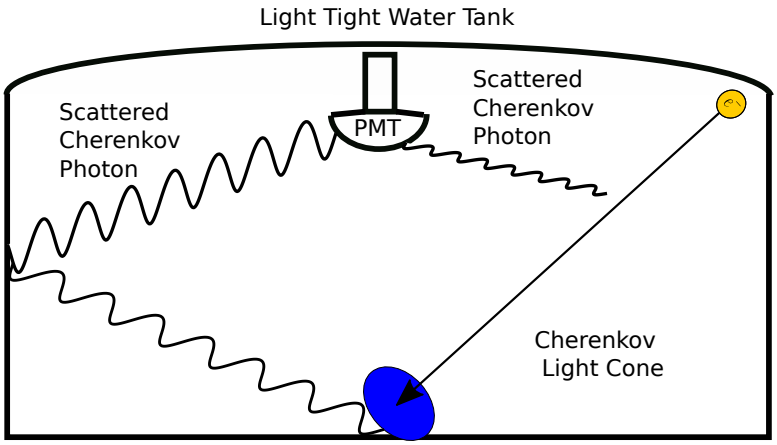

Figure 2.7: Diagram of a Cherenkov SD Water Tank Utilized by the AUGER Experiment. The tanks consists of $10m^2$ surface area and a water depth of 1.5 m. The water is contained with a Tyvek reflective liner and the Cherenkov signal is observed by three 9" diameter hemispherical PMTs [14].

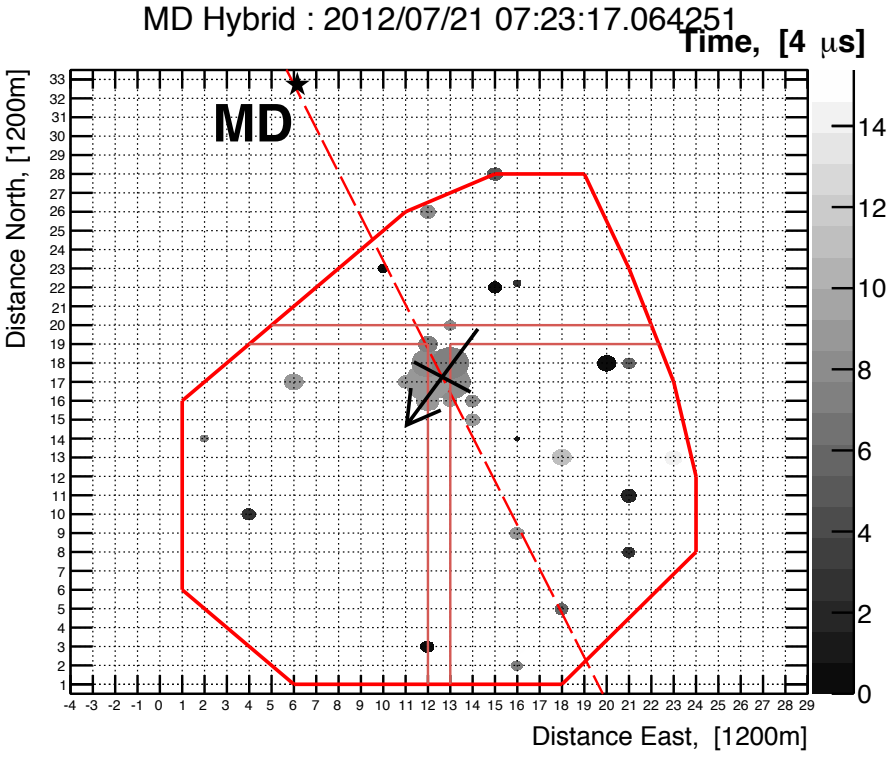

Figure 2.8: Event Display of a Typical SD Event. Timing is given by the shade of the circle and the size of the circle is proportional to the signal. Subarray boundaries are indicated along with the location of the MD detector. The MDFD shower detector plane is shown by the dashed line and the cross indicates the reconstructed core of the shower. The dots far away from the main events were SDs that triggered on noise in coincidence with the air shower.

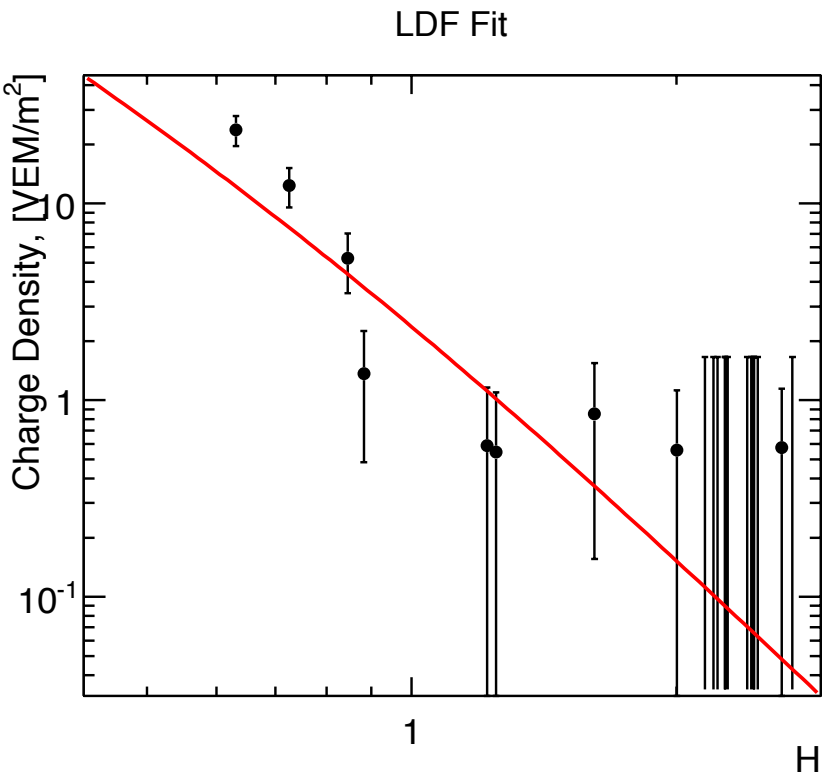

Figure 2.9: LDF Fit. The fit LDF to the event in Figure 2.8 is shown. This is a plot of the charge density in VEM/m^2 vs. the distance from the shower core (H) in units of 1200m.

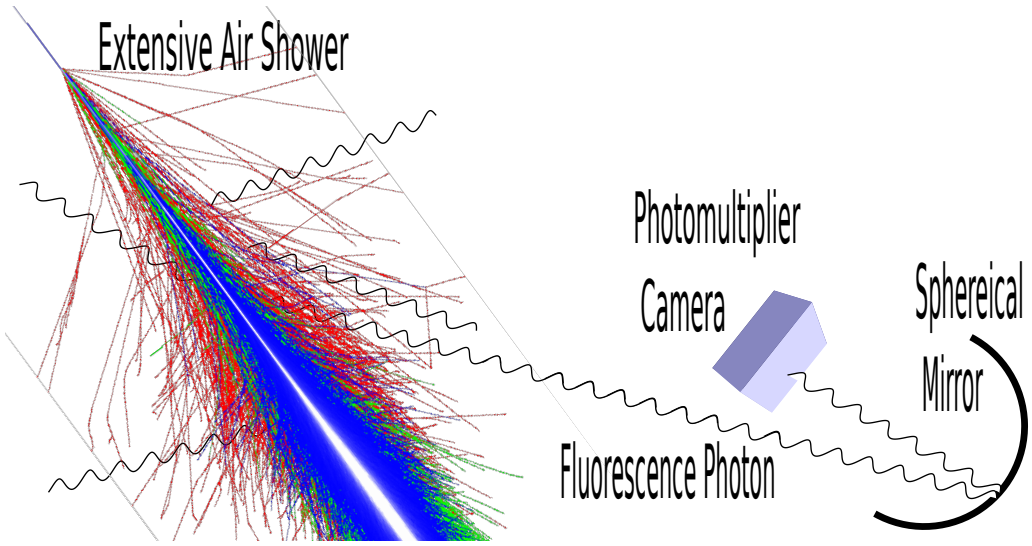

Figure 2.10: Schematic Diagram of a Fluorescence Detector. An EAS excited molecular nitrogen, which de-excites and emits fluorescent photons isotropically. The fluorescent photons are gathered with the use of optical instruments (in the case of this diagram, a spherical mirror is used) to gather the photons and focus them on a camera of photomultiplier tubes (PMTs) located at the focal plane of the optical system. The signal of the PMTs is then recorded by readout electronics.

Figure 2.11: Photograph of Telescopes at the MD Station. A telescope consists of a clover leaf spherical mirror which is used to gather fluorescence light generated by EASs and focus it onto a camera consisting of a cluster of PMTs. The cluster of PMTs can be seen to the right of the mirror although a UV filter placed in front of the PMTs prevents seeing the honeycomb pattern the PMTs are arranged in. Behind the mirror is the electronics crate responsible for triggering on and reading out the PMT signals.

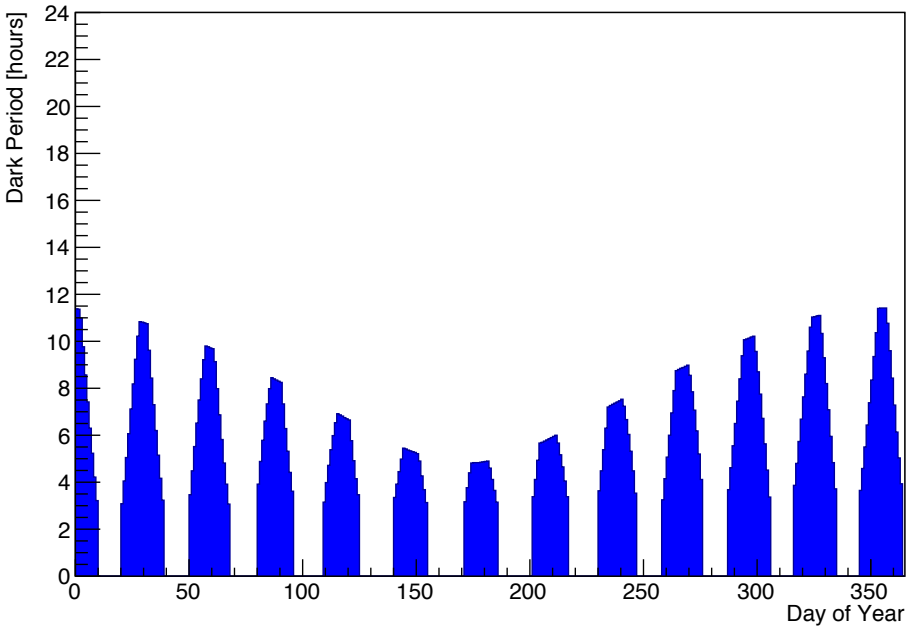

Figure 2.12: Dark Period Graph. Graphs number of available dark hours for TA FD detectors during the 2014-2015 observation period. The time shown here is only the duration where both the sun and moon were set. The detectors are not operated when less than 3 hours are available for data collection. This limits the duty cycle of FD detectors to 14% under ideal circumstances. Weather conditions further reduce the available ontime to about 10% duty cycle.

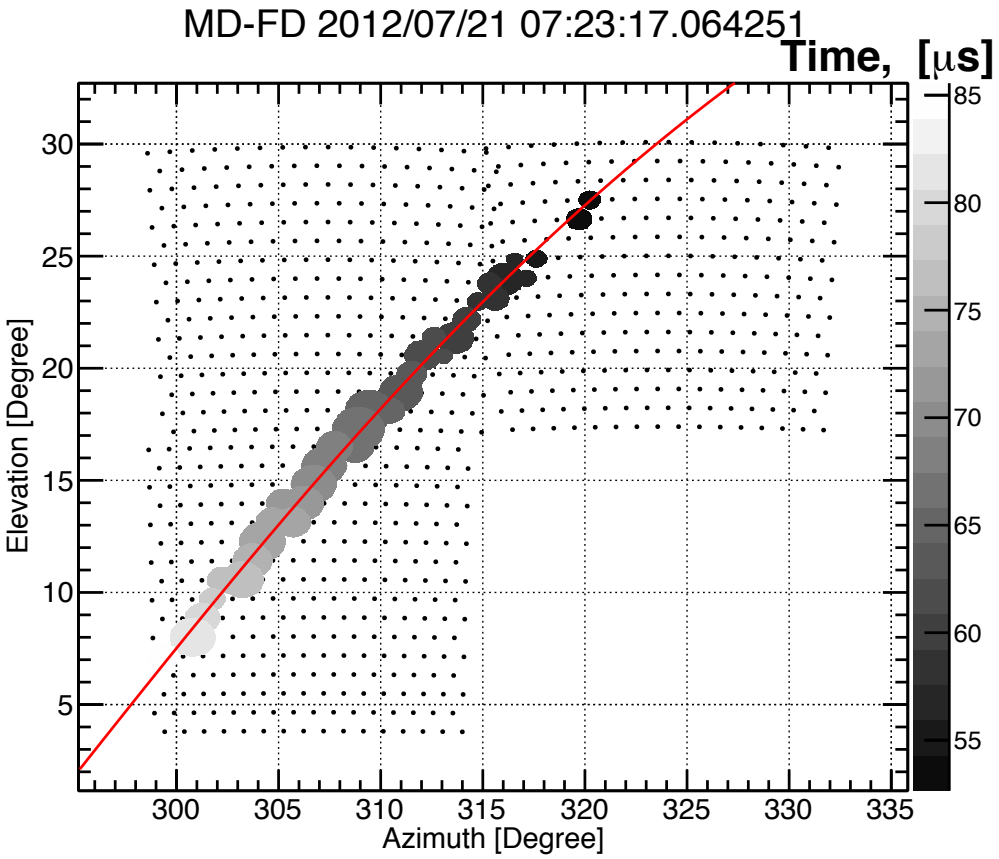

Figure 2.13: Event Display of a Typical FD Event. Timing is given by the shade of the circle and the size of the circle is proportional to the signal measured by that PMT. The uniform unshaded circles represent the positions of PMTs, which did not participate in the event.

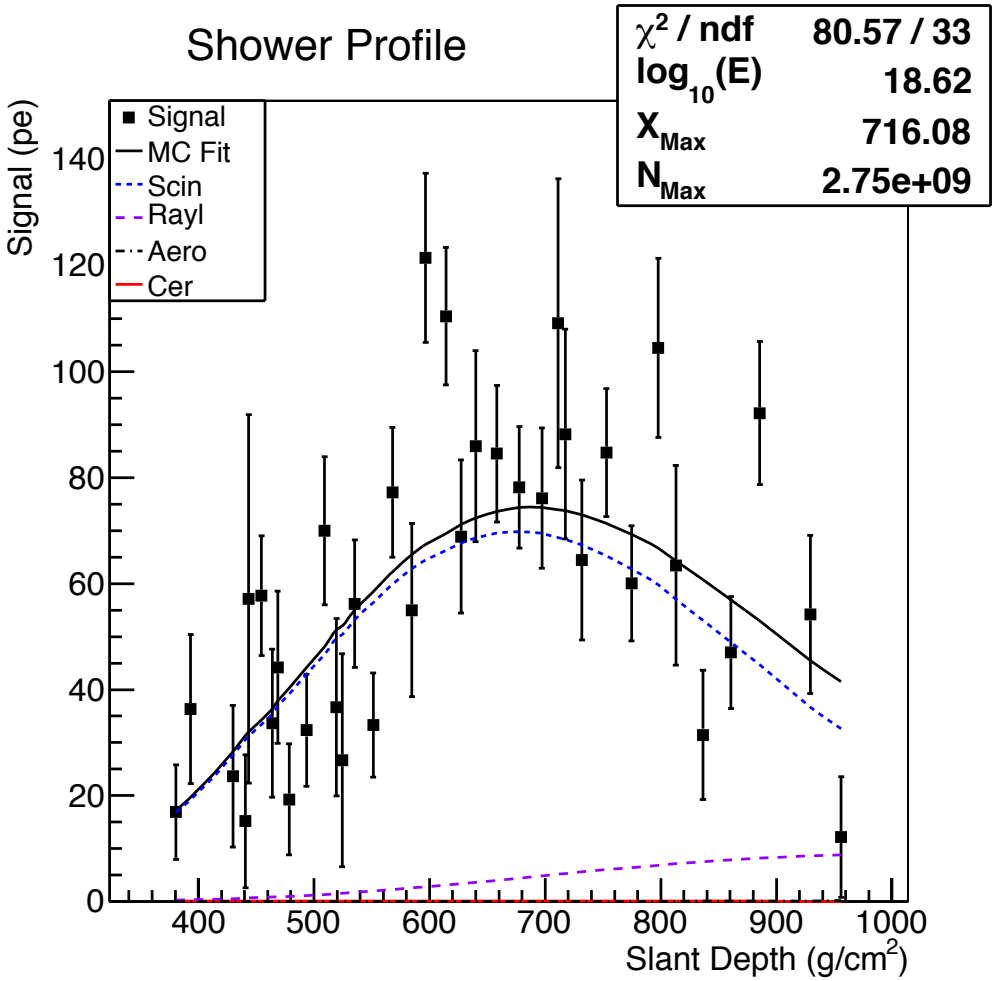

Figure 2.14: An FD Profile Fit. The Gaisser-Hillas fit to the event shown in Figure 2.8 is displayed. This plot shows the signal vs. the slant depth of the shower in the atmosphere.

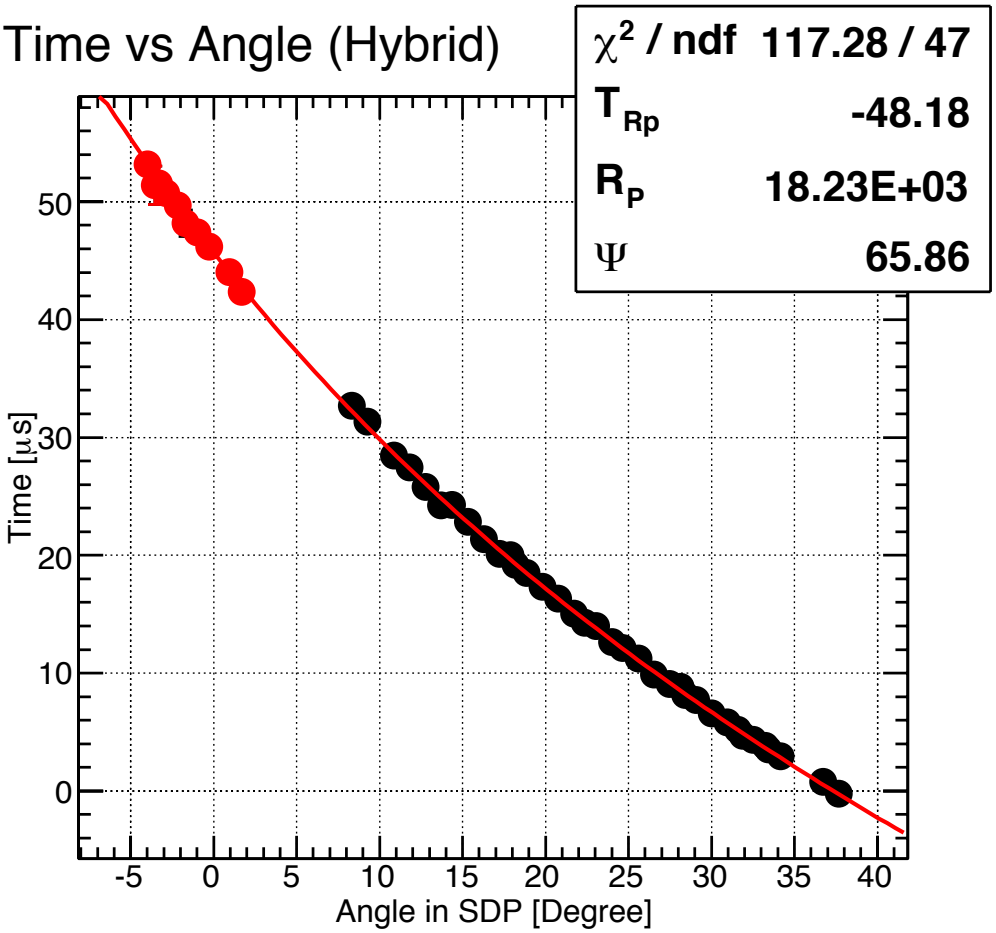

Figure 2.15: Hybrid Geometry Timing Fit. The combined time vs. angle fit the event shown in Figure 2.8 and Figure 2.13 is displayed. The darker points represent observations from the FD while lighter points are those from the SD. By extending the time vs. angle plot, the resulting fit is more tightly constrained and results in a better geometrical fit.

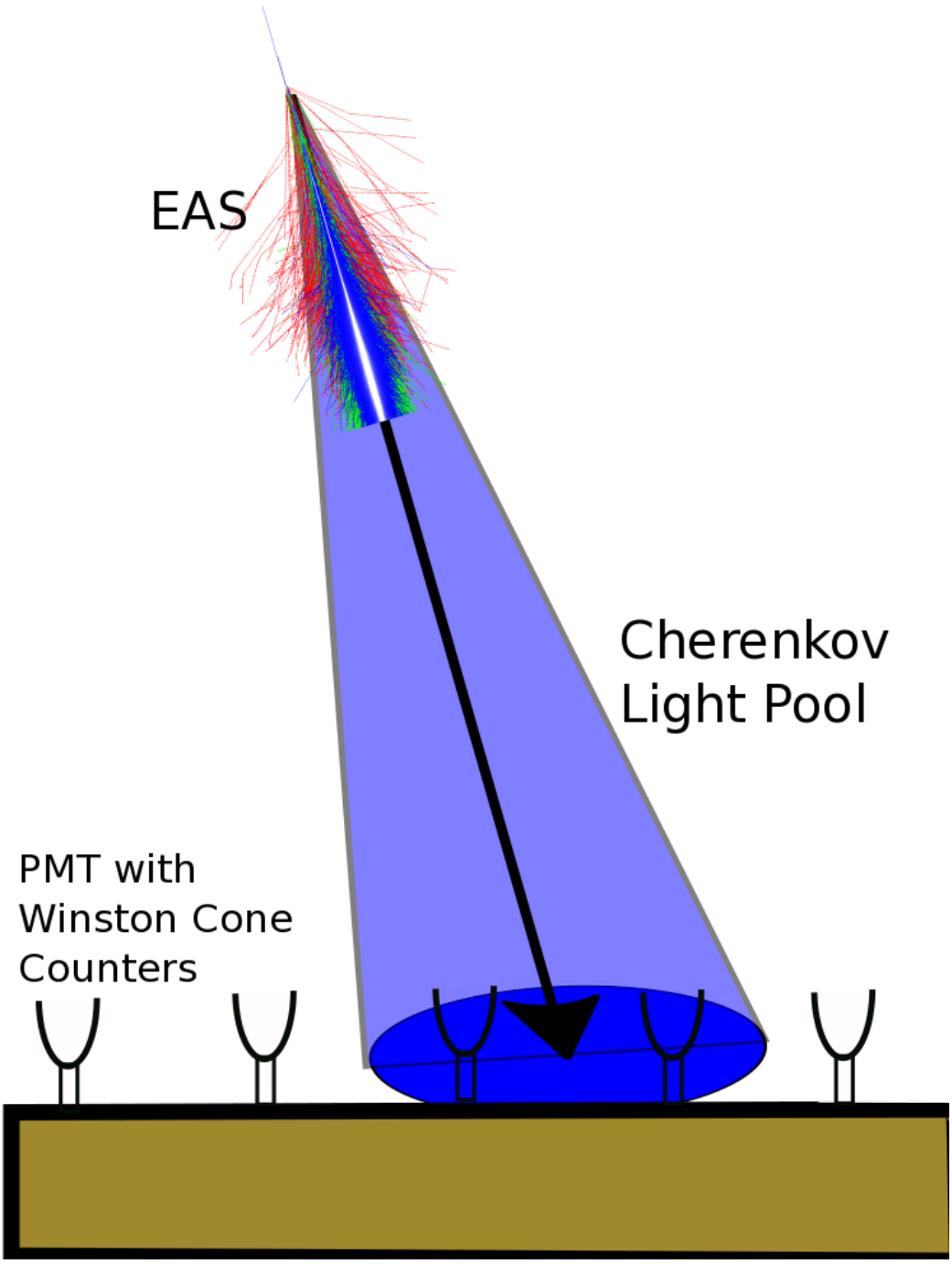

Figure 2.16: Non-imaging Cherenkov Array Diagram. The array samples the pool of Cherenkov light in the ground. The majority of the Cherenkov light is emitted within a few degrees of the core of the EAS requiring that array spacing of this type be no larger than approximately 100m.

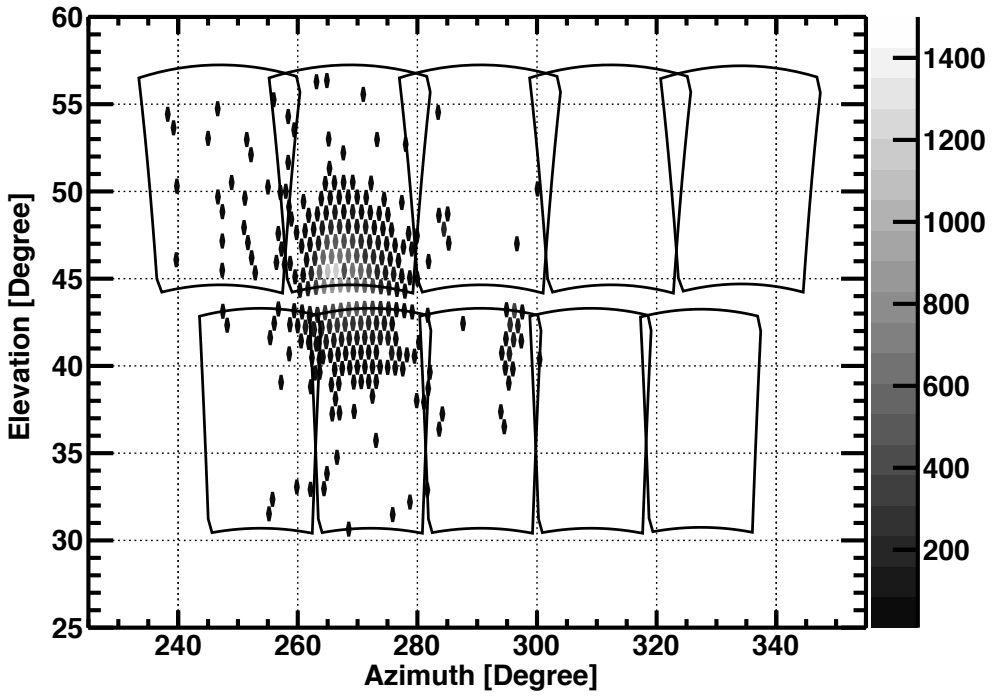

Figure 2.17: Typical Imaging Cherenkov Event Seen by the TALE Detector. The shade of the tubes indicates the signal size. The circular shape of the event indicated that the camera was looking along the shower axis. The shape becomes more ellipsoid for showers that are not pointed directly at a camera.

CHAPTER 3

A SURVEY OF CURRENT COSMIC RAY RESULTS

Cosmic rays have been of interest to nuclear and particle physicists since they were first discovered by Victor Hess in 1912 [9]. Since that time, there has been substantial effort to measure the energy, particle type, and arrival direction of cosmic rays. Experiments are performed with the hope that accurate measurement of the energy and particle type will reveal fundamental information about how cosmic rays are accelerated. Similarly, studies of the cosmic ray arrival directions are expected to reveal the location of cosmic ray sources. This chapter contains a survey of cosmic ray studies for particles over 10^{15} eV in energy. This survey is important in order to orient the reader to the state of the field but also to demonstrate how measurements of cosmic rays with energies between $10^{16.5} - 10^{18.5}$ eV have implications for the interpretation of experimental results at other energies.

3.1 Summary of the Cosmic Ray Spectrum

Cosmic rays are accelerated to energies higher than either the Tevatron or LHC are capable [21]. This makes the study of cosmic rays the only currently available tool to investigate particle interactions with center-of-mass energies greater than 14 TeV[21].

A compilation of the world data of the energy dependence of the cosmic ray flux is shown in Figure 3.1 [15]. The energy dependence of the flux is known as the cosmic ray spectrum. Figure 3.1 shows a power law dependence of the cosmic ray flux. In the energy region of $10^{10} - 10^{15}$ eV, the flux of cosmic rays is accurately expressed by $F(E) \propto E^{-2.7}$ [9]. At 10^{15}eV, the slope of the power law steepens to -3.1 [9]; this is a feature known as the "knee". The index returns to a value of approximately -2.69 between the energies of $10^{18.5}$eV to $10^{19.5}$eV [44]. This "hardening" of the spectral index from -3.1 to -2.7 is known as the ankle [9]. For energies above 4×10^{19}eV there is an observed suppression of the cosmic ray flux with an index steeper than -4.2 [44].

Additionally, Figure 3.1 indicates that above 10^{15} eV, the flux of cosmic rays is less than $1 particle/m^2/year$. The low flux of cosmic rays is what makes the indirect detection techniques described in Chapter 2 necessary.

Hillas first parameterized the possible sources of cosmic rays acceleration, where the particle is assumed to be confined for a time by a magnetic field and accelerated to a maximum energy given by

$$E_{max} \propto ZBcL, \tag{3.1}$$

where Z is the atomic number of the particle, B is the strength of the confining magnetic field, c is the speed of light, and L is the radius of the accelerator [7]. Figure 3.2 graphs the magnetic field strength vs. the size of various galactic and extragalactic accelerator candidates. The lines indicate the threshold for an object to be capable of accelerating protons and iron nuclei to the indicated energies. The Hillas Criterion suggests that nearly all of the sources capable of accelerating protons up to approximately 10^{20} eV are of extragalactic origin. In contrast, many galactic and extragalactic CR source candidates are capable of accelerating both protons and heavier nuclei to energies up to approximately 10^{16} eV.

3.2 The Ultra High Energy Cosmic Ray Limit

At the highest end of the cosmic ray spectrum, a suppression has been observed at energies above 6×10^{19} eV [16]. This feature was first observed by the High Resolution Fly's Eye (HiRes) experiment [45] in contradiction to measurements made by the AGASA experiment as illustrated in Figure 3.3. These contradictory results of the HiRes and AGASA experiments resulted in the collaboration of the two experimental groups to form the Telescope Array experiment. The failure of AGASA to observe the suppression has been studied and used to inform subsequent experiments about ground array detection of cosmic rays.

Due to computation limitations, the AGASA experiment had modeled their detector response by taking vertically simulated showers and rotating them. Later analysis of this procedure by Capdevielle [46] indicates that the AGASA parameterization of these rotated showers led to the overestimation of shower energies in their data. Even when showers are properly simulated, it is now understood that, at the highest energies, the reconstructed energies of air showers by ground arrays are on the order of 30% too high [16]. Additionally, AGASA utilized logarithmic amplifiers, which read out the pulse height and the time over

threshold of scintillator signals [47]. The number of particles in the detector was then measured using the relation

$$\ln N = \frac{t_d - t_1}{\tau}, \tag{3.2}$$

where N is the number of particles, t_d is the pulse width, t_1 is the single particle pulse width, and τ is the $10\mu s$ decay constant [47]. This choice of readout allows neutrons arriving later than $4\mu s$ after the shower front to extend the pulse width of the readout and artificially increase the estimation of the number of particles in the shower front [47]. It is currently believed that these three factors combined to give a systematic overestimation of shower energies and resulted in the obscuration of the GZK suppression in the AGASA spectrum [9].

The suppression has since been confirmed by the Auger Collaboration [48] and the TA experiment [16]. Figure 3.3 shows the measurements of the cosmic ray spectrum for energies above 10^{18} eV but multiplies the flux by the cube of the energy (E^3) in order to elucidate the details of the spectrum. The low point in the E^3J plot near $10^{18.7}$ eV is the feature known as the ankle. The suppression can be seen in Figure 3.3 as the dramatic reduction of the flux above 6×10^{19} eV. The systematic uncertainty of the flux measurements for these experiments is on the order of 10% [21].

There are at least two competing models that explain the suppression of the cosmic ray flux above 6×10^{19} eV. The first is know as the Greisen, Zatsepin, and Kuzmin (GZK) effect, and the second is a model of transitioning flux components from galactic to extragalactic sources.

In the GZK model, protons with energies above approximately 6×10^{19} interact with the cosmic microwave background (CMB) and lose energy through the process of photo-pion production shown in Equation 3.3 and Equation 3.4 [44].

$$\gamma_{CMB} + p \rightarrow \Delta^+ \rightarrow p + \pi^0 \rightarrow p + \gamma + \gamma \tag{3.3}$$

$$\gamma_{CMB} + p \rightarrow \Delta^+ \rightarrow n + \pi^+ \rightarrow p + e^- + \bar{\nu_e} + \pi^+ \tag{3.4}$$

The original paper of Greissen predicted that the interaction length for this process to be about 4×10^{24}cm, which corresponds to 13×10^6 parsec [49]. This distance is known as the GZK horizon. A sharp drop off of the flux of cosmic rays above 6×10^{19} eV would be a strong indicator that the cosmic rays have traveled at least 13×10^6 parsec from the source [49]. It has also been noted that the threshold energy for spallation of heavier cosmic rays (such as iron nuclei) occurs at roughly the same energy as that of photo-pion production [21]. In either case, current estimates of the location of the cutoff due to cosmic ray interaction with the CMB are placed at $E_{1/2} = 5.8 \times 10^{19}$ eV for UHECR protons, where $E_{1/2}$ is the

energy at which a power law extrapolation of the integral spectrum exceeds twice the flux calculated by accounting for CMB energy losses [50]. The HiRes experiment measured the location of $E_{1/2}$ to be 5.75×10^{19} eV [33].

Aside from the actual location of the suppression, there are additional features in the cosmic ray spectrum that give evidence for the particle type of UHECRs. Modeling of the UHECR interaction with the CMB performed by Berezinsky *et al* indicates that dip features of the spectrum before the suppression as seen in Figure 3.3 are well modeled if the source of cosmic rays with energies above 10^{18} eV were extragalactic protons and not heavier nuclei [17]. The feature known as the "ankle" is then predicted at approximately 8×10^{18} eV and is explained by accounting for energy losses due to the expansion of the universe (adiabatic losses) in addition to proton anti-proton production resulting from UHECR interactions with the CMB

$$\gamma_{CMB} + p \rightarrow p + e^{+} + e^{-}. \tag{3.5}$$

Figure 3.4 displays the contributions to the UHECR spectrum divided into bands of red shift and accounting for all losses due to CMB interactions. The dip feature is then predicted to be centered at an energy of approximately 8×10^{18} eV, and would be present regardless of the distribution of sources and the intervening magnetic fields [17]. It is important to note that heavier elements will not produce a dip feature and would be incompatible with the HiRes data in the Berenzinsky model [17].

An alternative hypothesis that can explain the suppression effect is an acceleration cutoff. This model would suggest that the acceleration mechanism for UHECRs expires at the location of the suppression and that the ankle is generated by a galactic to extragalactic transition [9].

While the transition model can be tuned to occur at the location of the suppression, it fails to (1) predict the location of the ankle feature of the cosmic ray spectrum and (2) predict the location of the suppression [17]. HiRes has the interpretation that the galactic to extragalactic transition occurs before the ankle region and the highest energies CR's are of extra-galactic origin. The results of the HiRes experiment match the location of the ankle and the suppression for protonic cosmic rays of extragalactic origin.

3.3 Composition at the Ultra High Energy Limit

The cosmic ray composition (or average particle mass) is inferred from measurements of the depth of shower maximum (X_{MAX}). As Chapter 1 details, cosmic rays with larger mass number have larger cross sections, larger multiplicities, and less energy per nucleon

than protons of the same energy. These factors lead to cosmic rays of higher mass number generating air showers that reach X_{MAX} at shallower depths. Studies of mass composition have been performed by AUGER, HiRes, and the TA experiments.

The composition measurement of the HiRes experiment is shown in Figure 3.5, which displays the $< X_{MAX} >$ for the HiRes Stereo data in addition to the HiRes Prototype+MIA data. The HiRes results at the highest energies indicate that above 10^{18} eV, cosmic rays are predominately protonic in nature [51, 33]. The measurement of the composition made by HiRes was performed using a stereo data set. Stereo events require that two different FD stations observe the air shower. Events seen in stereo are able to have their geometry determined to higher accuracy. Increasing the geometrical resolution reduces the uncertainty in the observed depth of shower maximum [33].

The TA experiment performed a measurement of the composition in the same energy regions using a different configuration of detectors. Instead of constraining the geometry by requiring events the be seen in stereo, the MD Hybrid analysis required that the Middle Drum FD see events in coincidence with the SD array. The geometrical constraint on the core of the shower provided by a ground array improves the geometrical resolution of measured air showers. The result of this measurement is shown in Figure 3.6 and indicates the composition at the highest energies is protonic in nature [18, 40].

In contrast to the measurements made by HiRes and TA experiments, the AUGER composition measurement indicates a protonic composition from $10^{18} - 7 \times 10^{18}$ eV. At energies higher than 7×10^{18} eV, the AUGER data suggest that the composition begin to trend toward heavier elements [52]. This is indicated both in the Auger reported values of the $< X_{MAX} >$ and the RMS of the XMAX distributions. [52].

The discrepancies in the measured composition at the highest energies motivate detailed measurements of cosmic ray spectrum and composition at lower energies in order to help clarify the interpretation of the data.

3.4 Anisotropy at the Ultra High Energy Limit

Anisotropy studies can also be used to study the location where cosmic rays are accelerated. Locating the sources of UHECRs would immediately resolve the interpretation of the measured suppression by determining if the sources are local in origin or extragalactic in nature. However, locating the point sources of cosmic rays is complicated by the fact that the intervening galactic and extragalactic fields deflect charged particles with a Larmor radius of

$$R \approx \frac{1}{Z}\frac{E}{B}, \tag{3.6}$$

here R is the radius of curvature in kpc, Z is the atomic number of the particle, E is the energy in EeV, and B is the magnetic field in μG [7]. This means that for iron cosmic rays above 10^{21}eV in a $5\mu G$ field, the Larmor radius is on the order of the size of the galaxy [9]. Thus if the highest energy cosmic rays were iron, they would appear to be arriving isotropically even if they were produced within our own galaxy. Protons are not expected to be accelerated to the highest energies by galactic sources, but if they were, an anisotropy would be expected to be observed. If charged particles are extragalactic in origin, and using conservative estimated for the intervening magnetic fields, protons at the highest energies would be deflected by at least 5° [9].

The HiRes experiment reported a loose correlation of UHECR events with BL-LACs, although the statistical significance never reached the level of discovery [53]. Similarly, the AUGER experiment has reported a correlation of their data with active galactic nuclei (AGN) [54] on the order of 3σ significance.

The TA experiment has reported a hot spot in their sky map of the northern hemisphere with a significance of 3.4σ [55]. If this excess achieves 5σ significance, it would support the spectrum and composition indication of previous TA and HiRes measurements that the highest energy cosmic rays are extragalactic and protonic in nature.

3.5 Spectrum and Composition Measurements below $10^{18}eV$

The interpretation of the UHECR suppression remains unresolved with the current spectrum, composition, and anisotropy measurements made by HiRes, TA, and AUGER. Looking at the cosmic ray composition and spectrum at lower energies may help illuminate this picture should the signatures of a galactic to extragalactic transition be located at energies lower than the GZK threshold. If a transition from galactic sources is observed below 10^{20}eV, then the interpretation that the measured suppression above 10^{20}eV is caused by the GZK effect becomes more likely.

An indication that a transition in composition from heavy to light came from measurements performed by the HiRes prototype + MIA detectors. The HiRes prototype was a fluorescence detector station arranged in a tower configuration that covered elevation angles from $3^\circ - 70^\circ$ [56] and overlooked a muon infill array (MIA) [57]. The result of the measured composition of this experiment can be seen in Figure 3.5. The HiRes prototype + MIA composition measurement indicates that below 10^{17} eV, cosmic rays are predominantly iron and transition to primarily protons above 10^{18} eV.

The HiRes prototype + MIA detector configuration also measured the cosmic rays spectrum as shown in Figure 3.7. Many experiments have measured this energy region and, in aggregate, hint at a break in the spectral index in the mid $10^{17} - 10^{18}$ decade known as the "second knee". The correspondence in a change in composition at the same place as a measured change in the spectrum suggests a change in the acceleration sources of cosmic rays.

Although the HiRes prototype + MIA hints at a galactic to extragalactic transition, the experiment had a number of limitations. The HiRes prototype detector overlapped at the high end of the energy sensitivity of the MIA experiment and recorded coincident events at the low rate of 1 per hour [56]. This mismatch of FD and SD sensitivity reduced the statistical power of the HiRes prototype + MIA dataset. Additionally, the HiRes prototype + MIA experiment overlapped with the HiRes stereo measurements by only 1/4 decade in energy which reduced the HiRes experiments ability to determine the absolute separation between the second knee and the ankle. The purpose of the TALE detector is to overcome the deficits of the HiRes prototype + MIA experiment by deploying a FD detector and SD array that are both designed to be sensitive in the region of the second knee in order to provide a high statistic measurement of the spectrum and composition in that region. Additionally, the TALE detector will overlap the TA measurements of the UHECR spectrum by a decade in energy. This will provide a continuous measurement of the cosmic ray energy spectrum and composition from $10^{16.5} - 10^{20+}$ eV.

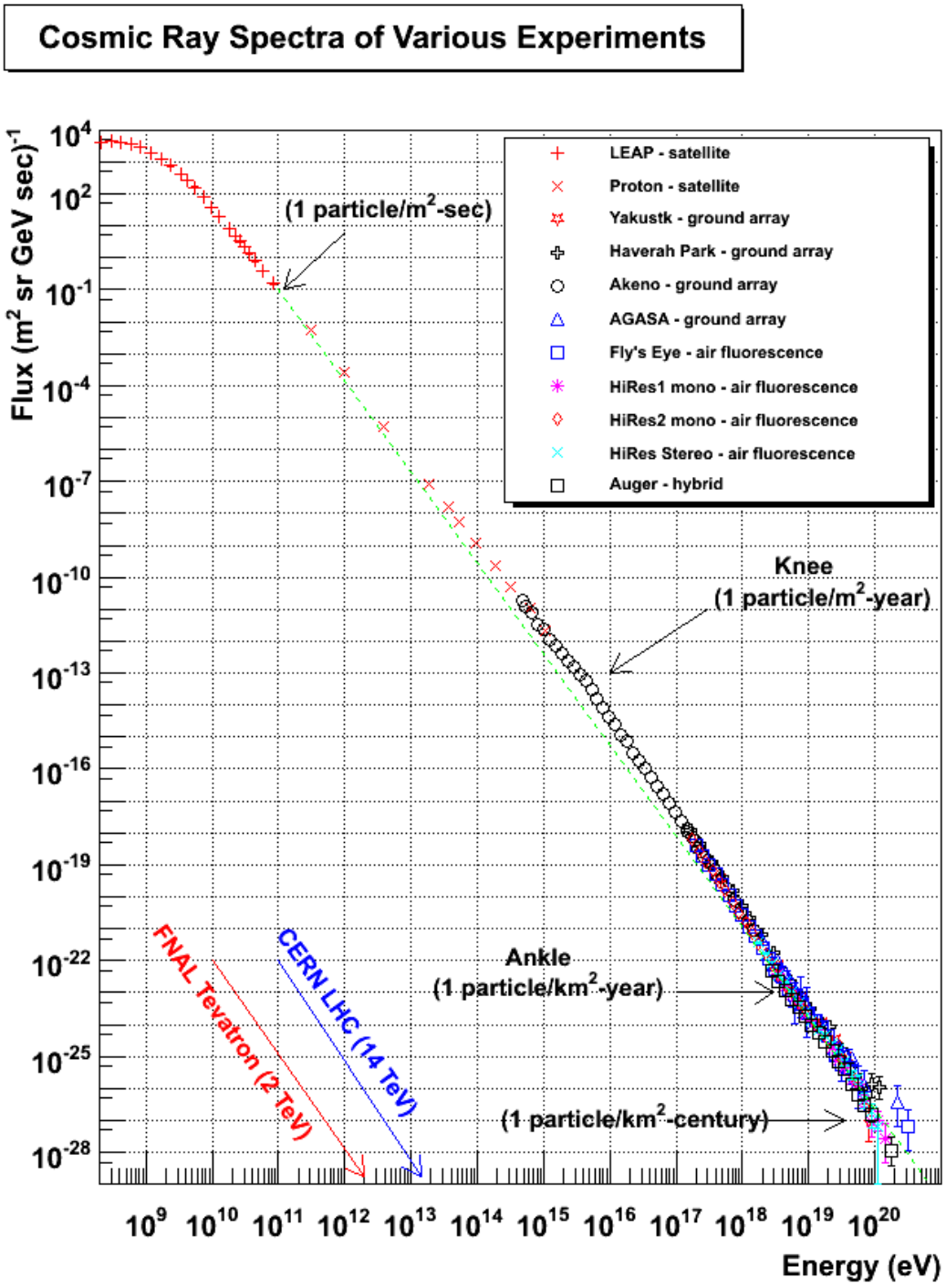

Figure 3.1: Compilation of the World Data of the Cosmic Ray Flux versus Energy (i.e., spectrum). The experiments used to take these measurements employ both direct and indirect detection techniques, with direct balloon and satellite experiments being feasible for cosmic rays with energies less than 10^{15} eV. Additionally, the equivalent primary proton energies corresponding to the world's largest accelerators are indicated. Reprinted with permission from W. Hanlon [15].

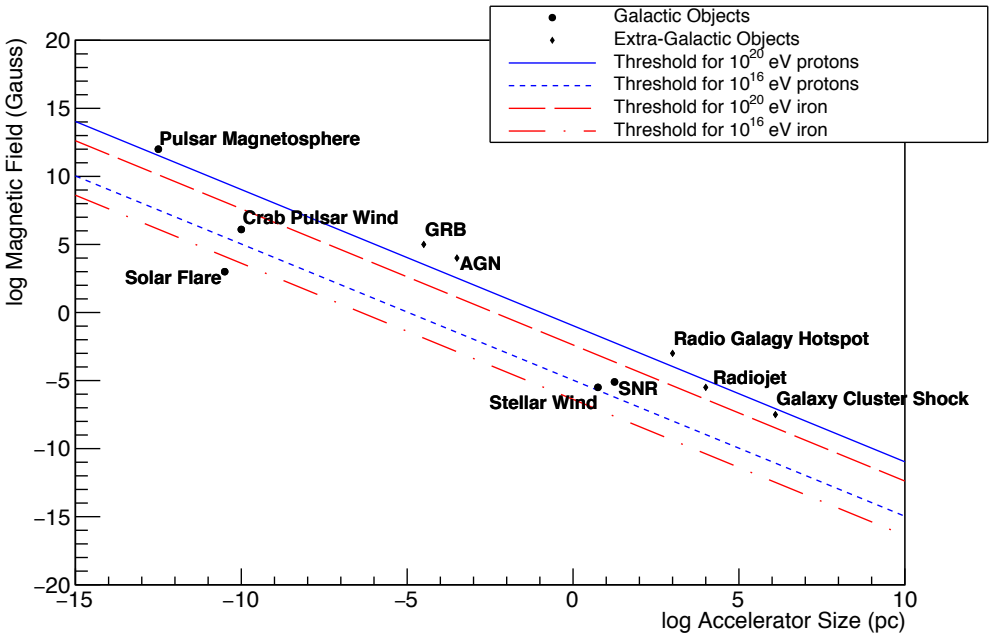

Figure 3.2: Hillas Plot of Candidate CR Sources. Circles indicate galactic sources and diamonds indicates extragalactic sources. The lines indicate the energy thresholds for various CR types and energies. Objects above the line are capable of accelerating the given CR to the indicated energy. Objects below the line are not capable of accelerating the specified CR type to the given energy [9].

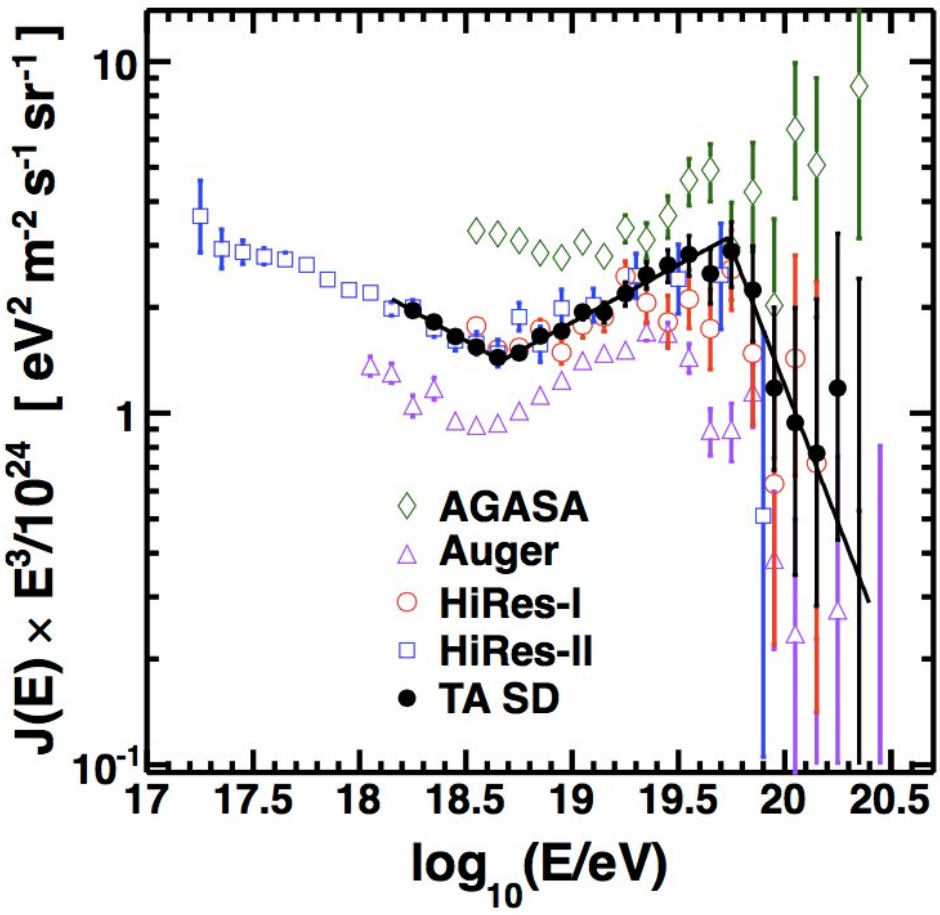

Figure 3.3: Measured Flux of Cosmic Rays at Energies above 10^{18} eV as Reported by Several Experiments. The measured flux has been multiplied by the cube of the energy (E^3) in order to remove the overall power law dependence of the flux which makes it easier to see features of the spectrum. Additionally, a broken power law has been fit to the TA SD data. Reprinted with permission from D. Ivanov [16].

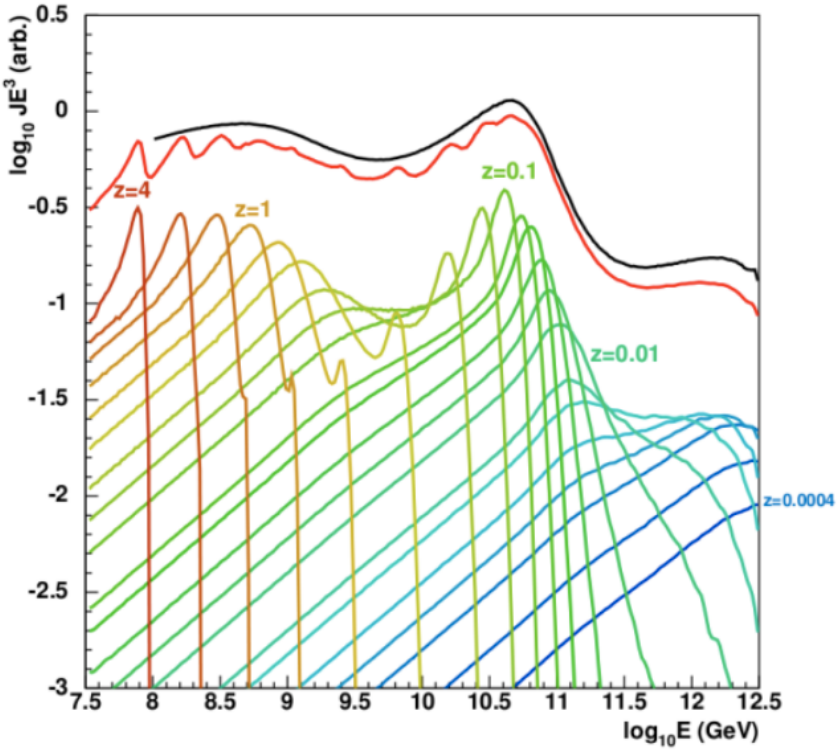

Figure 3.4: UHECR Source's Contribution to CR Flux Divided into Bands of Red Shift. This model takes into accounts the proton-antiproton production interactions and the adiabatic losses described in [17] in order to show how the ankle feature of the UHECR spectrum is "naturally" created by an extragalactic source of protons. Reprinted with permission from D. Bergmann.

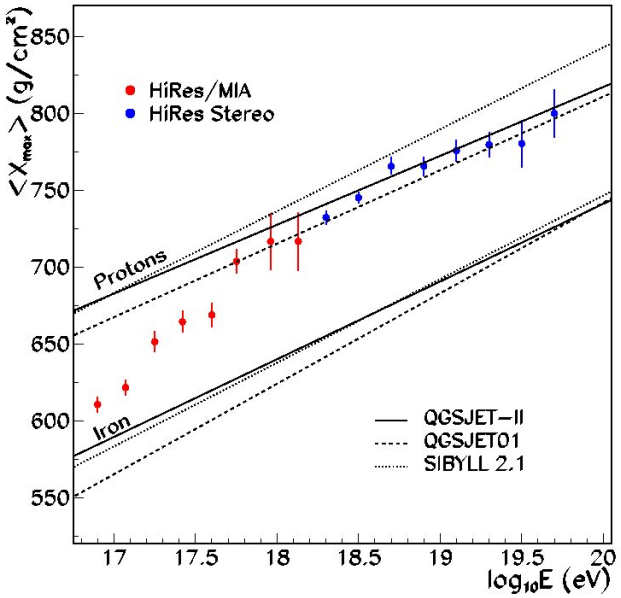

Figure 3.5: HiRes Composition Measurement. Graph shows the depth of shower maximum vs. the log of the energy. This graph contains the measurements of two different experiments, the HiRes stereo experiment and the HiRes prototype+MIA experiment. The top and bottom set of rails indicate the Monte Carlo expectations for proton and iron, respectively. Reprinted with permission from C. Jui.

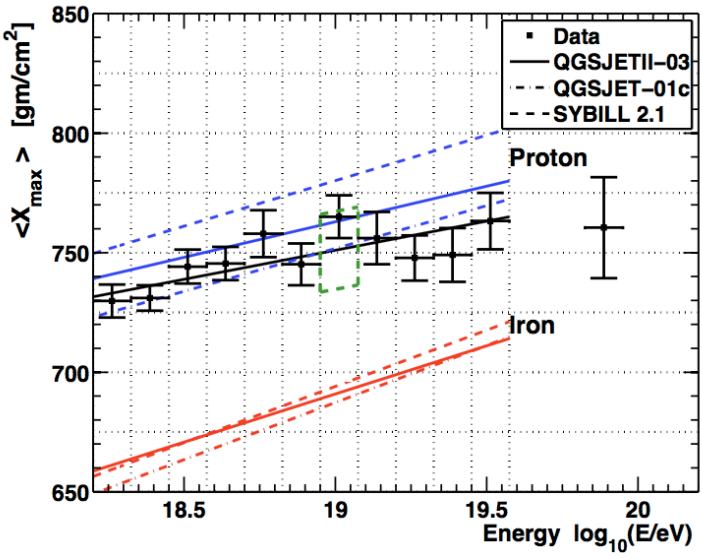

Figure 3.6: MD Composition Measurement. This graph shows the depth of shower maximum vs. the log of the energy. The rails for different Monte Carlo expectations are indicated. The MD hybrid measurement indicates that cosmic rays of the highest energies are protonic in nature. Reprinted with permission from J. Lundquist [18].

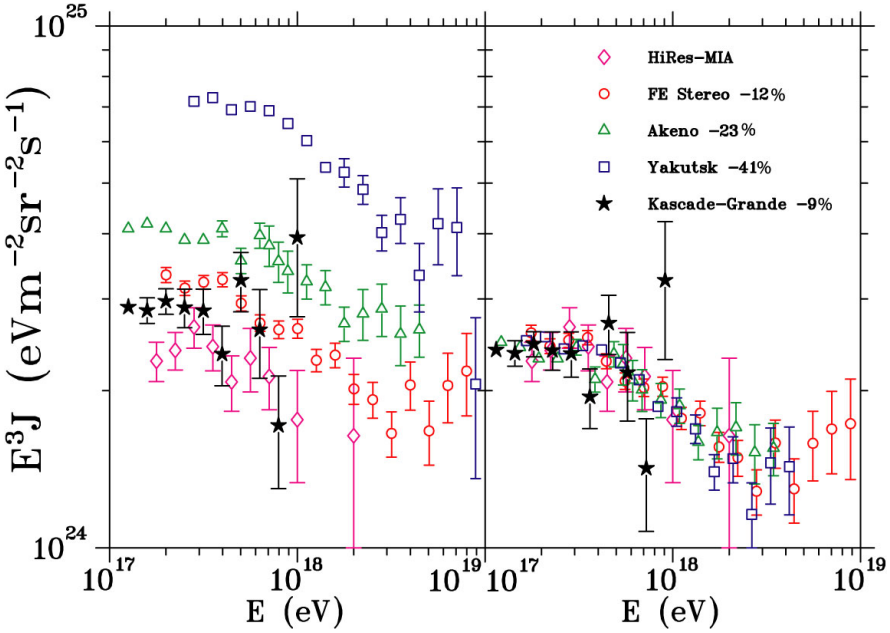

Figure 3.7: HiRes Spectrum Measurement. The left panel shows the HiRes measurement of the spectrum along with the experimental results of a number of other experiments. The right panel shows the same measurement with their energy scales normalized to that of the HiRes experiment. The evidence for the second knee is completely based in shifting the spectra of many experiments. Reprinted with permission form C. Jui.

CHAPTER 4

TALE FLUORESCENCE DETECTOR

The instrumentation and deployment of the TALE fluorescence detector (TALE FD) was a major part of the effort documented in this dissertation. The TALE FD is composed of repurposed and refurbished telescopes and electronics from the HiRes-II detector [58] in addition to new electronic components designed to handle the higher data rate required for measuring lower energy showers.

The TALE FD consists of 10 independent telescopes, as shown in Figure 4.1. Five of the cameras are pointed to observe between 30° and 45° in elevation and the remaining five between 45° and 60°. The telescopes that observe lower elevation angles are designated Ring 3 telescopes while the telescopes that observe higher in elevation are called Ring 4, whereas the telescopes of the MD FD comprise Rings 1 and 2. Figure 4.2 illustrates the field of view of each telescope. Ring 1 through 4 all observe approximately the same azimuthal range.

The TALE FD is collocated with the Middle Drum FD and observes the sky directly above the region covered by the MD telescopes. Due to the configuration of these two detectors, future analysis will continuously observe the atmosphere between 3° and 60°. The analysis of air showers using MD and TALE in cooperation will require accounting for the parallax between the two detectors. This is beyond the scope of the analysis of this dissertation, but will be done for the TALE hybrid analysis after the full instrumentation of the TALE infill SD array.

An individual TALE telescope consists of three major components: a mirror for light collection, a PMT camera, and readout electronics. A photo of a TALE telescope is shown in Figure 4.3. The instrument racks and cameras used for the TALE detector are related to the HiRes-II crates according to Table 4.1. Keeping track of the cameras is important because the individual PMT characteristics were measured in detail and cataloged during their installation into the original HiRes cameras. This archival information is provided for the benefit of future collaborators. The rack mapping is of less importance as (1) the internal

electronics of the crate have both been greatly modified and (2) the internal electronics are interchangeable between racks.

The TALE detector converts detected air shower photons into an electrical signal that can be digitized, triggered on, and eventually stored to disk. An overview of the data stream for a single channel in the TALE detector is shown in Figure 4.4. This chapter details the major components of the TALE detector, including mirrors, cameras, readout electronics, Link Modules, power supply, and detector operation.

4.1 TALE Mirrors

The mirrors used for the TALE detector collect light from cosmic ray air showers onto PMT cameras. The pointing directions of the mirrors also determine the field of view of the TALE detector. Accurate measurements of the mirror reflectivity are necessary in order to properly model photon propagation to the detector.

The TALE mirrors have a $5m^2$ collection area each, are formed from four clover leaf segments, and they focus light onto a camera composed of 256 PMTs. The four lobes of a telescope mirror can be clearly seen in Figure 4.5. The surveyed pointing directions for each mirror are listed in Table 4.2 along with the measured radius of curvature and reflectivity for each mirror.

Mirror reflectivity is measured annually before and after the mirrors are washed. The measurement is performed by illuminating four points on each of the mirror segments with light. The wavelength of light is varied between 360nm and 740nm in 10nm steps. The raw data reported in the mirror washing logs for each segment are normalized to reference calibrations made before and after the reflectivity measurements. The values reported in Table 4.2 can be separated into mirrors that have reflectivities near 89% and another group with a lower reflectivity near 85%. The difference in reflectivity is due to the fact that some of the mirrors were taken from the older HiRes-I detector, which have slightly lower reflectivity than the mirrors that where used at Hires-II.

4.2 TALE Camera

The purpose of the TALE camera is to convert photons into electrical signals that can be measured. A TALE camera consists of an ultraviolet filter, 256 PMT assemblies, and a custom backplane. A picture of a camera with the filter lowered is shown in Figure 4.6, showing the honeycomb pattern the PMTs. The hexagonal tube shape was chosen in order to minimize the amount of dead space between PMTs.

Photons reflected from a mirror are focused onto a camera. The front face of the camera includes a UV filter that blocks light outside the wavelength range of 300nm-420nm from reaching the PMT as shown by the transmissivity curve in Figure 4.7.

4.2.1 PMT Assemblies

The PMT cameras used in the TALE detector were previously deployed at the HiRes II site. Specifically, the PMTs that make up the pixels are Philips (later known as photonis) XP3062/FL photomultiplier tubes which were developed specifically for the HiRes experiment. These are 8 stage linear focused PMTs using a bi-alkali photocathode and borosilicate window that are designed to be sensitive to the range of 300nm-420nm with a single photon time width of less than 2ns [58]. The PMT wavelength sensitivity is shown in the quantum efficiency curve in Figure 4.8. The phototubes are positively biased at about 1050 V while the photocathodes are held at ground. A full PMT package contains not only the photo-multiplier tube but also a HV divider chain, a pre-amplifier, and an aluminum housing shown in Figure 4.9.

The schematic diagram of the HV divider chain is shown in Figure 4.10 and illustrates two important features of the TALE PMTs. First, the largest voltage differential is between the focusing electrode and the first dynode. This is intentionally done in order to maximize the collection efficiency of photoelectrons produced at the photocathode onto the first dynode. Second, the voltage differential between subsequent dynodes is equal, ensuring a linear amplification of incident light into an output signal.

A pre-amplifier is integrated into the PMT assembly for two reasons. First, the pre-amplifier converts that current collected at the anode into a voltage. Second, the pre-amplifier ensures that signals from the PMT can be driven across the 10m signal cable to the TALE readout electronics. Placing the pre-amplifier before the transmission cables improves the signal to noise ratio for the TALE detector.

During normal operation, the TALE PMTs have a nominal gains just below 10^5. A photon that successfully ejects a photoelectron at the photocathode produces an avalanche of secondary electrons that are gathered at the anode. The electron cascade results in a voltage signal that can be measured by the readout electronics of the TALE detector. The differential analog signal from each PMT is transmitted to the TALE readout electronics by signal cables following the cable trays seen in Figure 4.5. Signals are transmitted differentially in order to ensure that any noise picked up while traversing the cable will be cancelled at the FADC amplifiers.

4.2.2 HV Noise

High voltage is supplied to the TALE PMTs using off-the-shelf Bertan supplies. The stability of the HV supplies over large timescale is documented in Appendix B and is found to provide an uncertainty in the PMT gains on the order of 1%.

Additionally, Nevis Labs performed a study of the level of HV ripple for the Bertan supplies. HV ripple can be a concern because a 0.1mV fluctuation at the anode will be propagated through the pre-amplifier and FADC amplifiers, resulting in a 8 mV fluctuation at the ADC. For reference, 8mV corresponds to a single ADC count at the ADC. To limit the level of HV ripple, HV filters are included between the HV supplies and the cameras. The added filtering ensures that HV ripple is less than 1 part in 10^8 on the timescale of 100ns-5μs [58].

4.2.3 PMT Shot Noise

The Shot Noise from a PMT arises from the discrete nature of the electric charges that are being measured and amplified. One source of the inherent noise of PMTs comes from thermionic emission. Electrons in the photocathode will have energies that vary according to Boltzmann statistics. Accordingly, some electrons will have enough energy to overcome the work function of their material and become liberated. These electrons can be subsequently accelerated toward a dynode and amplified. The current produced due to thermionic emission follows Richardson's Law

$$J = AT^2 \exp -W_{th}/kT, \tag{4.1}$$

where J is the current density, A is a constant, T is the temperature (in Kelvin), k is the Boltzmann constant, and W_{th} is the work function of the photocathode [59]. Thermionic emission, along with current leakage, is the major sources of what is known as dark current for a PMT.

In addition to sources of noise that occur due to the production of anonymous electrons, the signal from a PMT can vary substantially when measuring photon fluxes due to the statistical nature of light production and amplification. Every electron that is incident upon a dynode will cause the emission of secondary electrons according to a statistical process that is well modeled by a Poisson distribution. The fluctuation in the number of secondary electrons created, especially for the first few dynodes, introduces noise in the final signal. This process is modeled in detail in Appendix G and results in an shot by shot Signal to Noise Ratio (SNR) on the order of 3 for the PMT configuration used in the TALE detector.

4.3 Readout Electronics

The readout electronics are responsible for continuously digitizing the PMT waveforms, deciding on trigger conditions, and sending up event data for permanent storage. A schematic overview of the readout electronics for a single TALE camera is shown in Figure 4.11. The readout electronics for each camera are composed of 16 FADC cards and a single TRIGGER-HOST board. The FADC boards continuously digitize the PMT signals and store triggered waveforms in memory long enough to be read out. The FADC also sums the voltage across each row and column of PMTs and sends the resulting digitized waveforms to the HOST/Trigger Board. The primary role of the HOST/Trigger Board is to monitor the horizontal and vertical signal sums for patterns and issue a STORE to the FADC boards to ensure the waveforms from the triggered region are properly saved to memory.

4.3.1 FADC Boards

The differential voltage signal from a PMT is sent to an FADC board for digitization. A photograph of an FADC board is shown in Figure 4.12 and a more detailed diagram of an FADC card is shown in Figure 4.13. An FADC board is divided into an analog front-end and a digital back-end. The front-end amplifies, digitizes, and stores the PMT signal waveforms. The back-end performs pulse finding scans and reports the result of those scans to the HOST/Trigger Board.

One of the additional roles of the FADC board is to apply an appropriate gain to each of the PMT channels in order to account for differences in PMT HV gains and set the desired gain for modeling in Monte Carlo simulations. All of the PMT channels are set to the same gain. The difference in HV PMT gain is compensated for by adjusting the individual channel DACs (Analog Devices AD8522 [60]) which control the gains of the input amplifiers. The details of solving the circuit diagrams for the channel gains are documented in Appendix C and reveal that the input signal has a controllable gain applied to it that varies from 0 to 23.59. The resulting signal is then digitized by an Analog Device AD775 8-bit ADC [61] and stored in the M1 ring buffer. The gains also need to be set so that the photometric calibration of the detector can be properly simulated in Monte Carlo.

In addition to the the waveforms for the individual tubes, each FADC records the analog sum for the column of PMTs that it digitizes along with the sum for one of the camera rows. The sum channels signals are digitized and recorded separately with high and low gain channels. In total, each FADC board has 20 channels comprised of 16 PMT signals, a

high gain vertical sum, a low gain vertical sum, a high gain horizontal sum, and a low gain horizontal sum.

The high gain horizontal and vertical sums are used to determining the trigger conditions for the TALE detector. If the digitized sum is in excess of 12 ADC counts above pedestal, the discriminated signal is set high. Discrimination is handled by an Amtel ATV750 PLD device [62] which is on the FADC boards. If threshold is not met, then the discriminated signal is set low. The discriminator output bits are sent to the Trigger Board over the custom backplane. Should the FADC boards not receive a STORE instruction from the Trigger Board within the $820\mu s$ length of the M1 memory buffer, then the waveforms are simply overwritten. However, if trigger conditions are satisfied, then the Trigger Board will send a STORE instruction to the FADC boards. The STORE trigger window is calculated as $2 \cdot t_{coincidence} + 10\mu s$ up to a maximum of $200\mu s$.

A STORE causes the waveform within the trigger window to be copied to the M2 memory buffer during the subsequent write cycle for the M1 buffer. Additional scans are then performed on the waveforms stored in M2 before being read out through the Trigger Board.

The M1 memory ring buffer is indexed by a 13-bit timing counter and is stored on Integrated Device Technology CMOS Static RAM (SRAM) IDT7164 [63]. As the memory index moves through M1, the previously recorded value in M1 is transferred into temporary memory R2. This previous value can either be discarded or transferred to a long-term buffer M2 memory for eventual readout if a STORE has been issued by the Trigger Board. In this way, data are stored from M1 into M2 as the M1 ring buffer is overwritten. M2 is a 32x8k deep SRAM (Integrated Device Technology CMOS Static RAM IDT71256SA) [64].

Importantly, the FADC boards communicate through their HOST ports over a custom backplane to the rack HOST/Trigger Board. All communication to and data from the FADC boards are transferred over the backplane and through the HOST/Trigger DSP. The backplane allows command and message packets to be exchanged between the FADC DSPs and the HOST DSPs. The backplane also ensures that the 10MHz system clock is distributed to all DSPs.

4.3.2 Trigger Board

The TALE Host/Trigger Board has three functions: (a) it acts as a HOST device for the 16 FADC boards in each crate, (b) is responsible for generating the primary trigger for the detector, and (c) determines if triggered events should be read out. A picture of the TALE Trigger Board is shown in Figure 4.14. The Trigger Board consists of four

primary device components: a Trigger DSP (Motorolla 56309) [65] , two coincidence PLDs (Altera EPF8425ALC84) [66], a trigger/timing PLD (Altera EPF8425ALC84) [66], and a communication PLD (Altera EPM7128ELC84) [67].

The Trigger DSP and the communication PLD handle the Host function of the Host/Trigger Board. The Trigger DSP communicates to the outside world over its built-in HOST port. Commands and messages are either handled locally or redirected to FADC boards using the communication PLD and a custom backplane. This makes the Host/Trigger responsible for booting, configuring, and routing the communication from all of the FADC boards. Accordingly, all data and communication from any of the FADC boards must be transmitted through the HOST/Trigger Board. The full details of the Host/Trigger to FADC operation are documented in Appendix D.

The primary trigger for the TALE detector is determined by calculating the 3-fold coincidence of camera rows or columns on the Horizontal or Vertical counter PLDs respectively. The trigger levels on the Trigger Board are documented in Table 4.3. This full process of 3-fold coincidence generation is diagramed in Figure 4.15. Determination of 3-fold coincidence begins with the counter PLDs analyzing threshold discriminated signals of the row and column signal sums from the FADC boards. The 16 discriminated row signals are inputs to the row coincidence PLD. Similarly, the 16 discriminated column signals are inputs into the column coincidence PLD. Both of the coincidence PLDs detect 3-fold overlaps in the sum signals via a two-step process. First, each signal has the logical AND performed between it and the logical OR of the next two sum channels. For example, the AND is performed between sum channel 0 and the result of channel 1 OR channel 2. This is done for each set of channels and form a 15-channel set of 2-fold coincidences. This process is repeated with the 2-fold coincidences in order to form a 14-channel set of 3-fold coincidences. An example of the 3-fold coincidence formed from signals only in channels 1, 2, and 4 is shown in Figure 4.16.

The 3-fold coincidence signals are then sent to the timing/trigger PLD, which forms a trigger code and interrupts the trigger DSP in the event that minimal trigger criteria are met. The trigger/timing PLD includes a 13-bit counter that increments synchronously with the external 10Mhz clock. When this counter rolls over, it generates an interrupt on the Trigger DSP and increments the two 24-bit timing rollover registers t0 and t1 on that device.

Additionally, the timing/trigger PLD watches the 3-fold coincidence output from the counter PLDs and creates a trigger code according to Table 4.4. The trigger code reflects

the number of horizontal and vertical 3-fold coincidences reported for the event. For any combination of 3-fold coincidence to generate a trigger, it must be followed by either 5μs without coincidence or the coincidence window must reach its maximum range of 200μs. When the trigger PLD has at least a single 3-fold coincidence (Level 0 Trigger), it will interrupt the trigger DSP. The trigger DSP will check the trigger code and either generate a STORE event (Level 1 Trigger) or pre-scale the event based on the code. Pre-scaling events means that events meeting minimal trigger conditions only issue a STORE for 1 out of every 64 such events.

After a STORE saves waveforms from M1 to M2, the Trigger Board sends instructions to the FADC boards in order to scan the stored waveforms for pulses. The pulse summary scan is performed by a filter that compares the filter value to a modifiable threshold. A summary of the pulse times and integrated ADC counts are sent to the Trigger Board to determine if the event passes readout criteria (Level 2 Trigger).

The TALE detector operates in two possible modes. The first is a traditional UHECR detection mode that requires that the triggered events be track-like and develop in both space and time. An alternate operation mode requires that only five tubes pass the high threshold scan summary filter. The latter operation mode allows for readout of air shower signals that are pointed at the TALE detector and become more oval and circular (Cherenkov blast) rather than track like. Events that pass the Level 2 trigger have the waveforms read out. Before readout, the waveforms are scanned again with a lower filter threshold than that required during the trigger summary scan. An example of a waveform created when a muon passes through a phototube is shown in Figure 4.17 and demonstrates how the anti-aliasing filter spreads impulsive signals over 3-4 digitization bins.

4.4 Link Module

The individual telescopes are integrated into the full TALE detector through a network of Link Modules, as shown in Figure 4.18. Each Link Module consists of a TS-7350 single board computer (SBC), which connects to a custom CPLD timing and HOST board via the on-board PC-104 interface. Together, the SBC and the CPLD board handle all communication and clock distribution to the FADC boards. The SBC has built-in 100Mb ethernet access, which is used for communication with the control PC for transfer of cosmic ray airshower data. An image of the TALE Link Module is shown in Figure 4.19, which shows both the Link Module and the power controller board on which the Link Modules are mounted. Since only one power board is needed for each crate of electronics, the convention was chosen to

mount odd numbered Link Modules on the power controller board while even numbered Link Modules are mounted onto blank boards.

Aside from managing reading and writing to the Trigger and FADC Boards through the Trigger Board's HOST port, the Link Module is also responsible for distribution of the system clock. The Link Module receives a 10MHz system clock and synchronous command over a RJ45 connector and custom interface. This 10MHz clock can be enabled or disabled via software commands. The system clock is translated to BTL logic levels for driving the Trigger Board over coaxial cable. This external system clock also drives a 64-bit system time counter (32 bits in CPLD and 32 bits software in the Linux driver).

The Link Module also includes a serial port that allows control of a UVLED flasher mounted at the center of each telescope mirror. This custom port includes UVLED communication, external trigger, and power. Data are transferred through the Link Modules and to the control PC where they are written to disk for later transfer to the University of Utah.

4.5 Rack Power

This section is largely for archival documentation and for the benefit of future collaborators. Every TALE electronics rack is supplied with 220 VAC power whose distribution to the rack breaker panel is controlled by the Mapway power controller shown in Figure 4.20. The 220 VAC power is distributed through a custom breaker panel shown in Figure 4.21 to the HV and LV supply modules for the racks. The breaker panel has three built-in relays that are controlled by the Power Control board. The relays in the breaker panel allow for power supply to the LV supplies, HV supplies, and heat exchanger to be independently controlled.

4.5.1 Power Control Board

Power to rack electronics is controlled by a power controller board designed specifically for the TALE detector. The power controller board is directly interfaced with using a 9600 baud port via a R.E. Smith [68] ethernet to serial communication module and is available whenever auxiliary power is enabled to the building. Additionally, the power controller board also communicates to the TALE Link Modules over a 38400 baud RS232 serial link. A full list of the responsibilities of the power controller board is summarized in Table 4.5

4.5.2 Low Voltage Supplies

Power is supplied to FADC cards and Trigger Boards with one of two different generations of Low Voltage (LV) supplies. Originally, the TALE detector was instrumented with repurposed custom HiRes II NEVIS LV supplies. HiRes II had a power supply failure rate ≈1.5 per month and the detector began operation with only 22 total supplies. The HiRes-II supplies had to be replaced with off-the-shelf TDK-Lambda supplies. This upgrade dramatically increased the reliability of all of the telescope crates and dramatically improved the detector on-time. After the first year of operation with the TDK-Lambda supplies, there have been no power supply failures.

All of the necessary voltages are now supplied by using TDK-Lambda SWS600-5 for +5V digital lines, the TDK-Lambda SWS300A-5 for the +6V analog line, and the DK-Lambda LS200-5 for the +/-5V analog supplies. The maximum current draw for each of these replacement supplies is 100A, 45A, and 40A, respectively. A picture of the new LV power supplies is shown in Figure 4.22. In order to substitute the new TDK supplies into the already operational TALE racks, a Power Supply Emulation Board was developed in order to simulate the control and read back interfaces of the Nevis supplies.

4.6 TALE Data Acquisition Software

Control programs running on the Control PC, the Link Modules, Trigger Boards, and FADC boards operate the TALE detector. A major part of the work of this dissertation was developing the software to handle control and communication of these devices. Nevis Labs had developed the assembly code to operate the Trigger and FADC boards [58] for the HiRes-II detector, and this contributed to the speed of the deployment of the TALE detector. However, Jeremy Smith (University of Utah) and I were responsible for reviewing the Trigger and FADC code and developing the appropriate software to communicate with and control the TALE readout electronics. The communication and control of the readout electronics is handled by the Control PC and the Link Modules, which were developed by Jeremy Smith and me in a joint effort. Many of the details in this section are documentation for the benefit of collaborators that will be working on the TALE detector in the future. A diagram indicating how the different pieces of software communicate is shown in Figure 4.23.

The TALE PC runs two major programs for the TALE Detector, which are designated “Skynet” [69] and “Talerun”. “Skynet” acts as a central server and handles communication between the individual telescope Link Modules and the control PC. “Skynet” is also connected to the Middle Drum control software named HAL, the TALE building rain sensor bus, and the Central Timing computer. The “Talerun” program has a Graphic User

Interface (GUI) written in python and is designed to allow semi-automated operation and control of the TALE detector. The "Talerun" program is the only interface to the TALE detector that most operators will experience. Console access to the "Skynet" server is also available by a stand-alone client named "Skyterm". "Skyterm" allows for advanced control and debugging of TALE detector in addition to offsite access to the detector. A screenshot from the control PC during normal operation is seen in Figure 4.24.

The Talerun program consists of a GUI checklist interface, automatic generation of operations logs, and a real-time event display.

4.7 TALE Run Procedure

During detector startup, operators are first required to visually inspect the TALE telescopes and verify that all UV filters have not been damaged, all garage doors had been properly closed the previous night, all telescope mirrors are clean, and that all electronics racks are closed. Should any of these initial checks fail, the issue is investigated before power is enabled to any of the electronics racks.

Next, Talerun will start the Skynet Central Server and connect to it via a TCP socket. Additionally, Talerun starts an independent thread that is dedicated to monitoring incoming data from Skynet and updating the detector status monitor accordingly.

Connections are established to the rack power boards and are in turn instructed to enable 220 VAC power to the racks by turning on a relay in the 220V Mapway products power controller shown in Figure 4.20. The 220 VAC power is distributed through a custom breaker panel shown in Figure 4.21 before being distributed to the HV and LV supply modules.

After enabling the LV supplies, the Power Control Board digitally controls the output from the LV supplies over a ribbon cable. The LV supplies provide the voltages documented in Section 4.5.2 to the FADC and Trigger Boards in each electronics crate. The majority of the communication, control, and trigger software for the rack electronics is run using DSP 56309 [65] on the Trigger Board and the DSP56166 [70] on the FADC boards. Details of communication to and operation of the DSPs are documented in Appendix D.

Once all Trigger and FADC DSPs are booted and configured a series of tests, known as FADC tests, are performed to verify the readout of all of the channels. The details of the FADC test are documented in Appendix H.

After the FADC tests conclude, the test routines in the FADC DSP program memory are overlaid with data collection routines (see Appendix D for details). Additionally, a configuration file generated every month during detector calibration using a Roving Xenon

Flasher (RXF) is read in order to set the gain and pedestal DACs to the appropriate values. Pedestal DACs are set to ensure that the PMT channels and high gain sum channels have a pedestal of 10 ADC counts while the low gain sum channels have a pedestal of 20 ADC counts.

The last step of detector startup is gradually ramping up the HV supplies to the cameras. Each camera is equipped with a fuse in order to protect the PMTs. The rate of blowing camera fuses increases if the HV is turned on too quickly.

After the TALE detector has successfully booted and initialized all telescope electronics, data collection can begin. UVLED calibration, dark noise, and night sky data are the three types of data collected during each operation of the TALE detector. UVLED and noise data are taken primarily for detector calibration.

Following the UVLED data collection, a check of the memory space of the TALE detector is performed known as the Trigger Test. During this operation, a test pattern is written to the M2 memory on the FADC boards. Readout for the detector is enabled and the output for each detector is monitored to ensure that the test pattern successfully passes all trigger requirements of the detector and that the correct pattern is read out. Should any region of M2 report a read error, it is flagged as needing to be replaced by the operator.

The second form of data collected by the TALE detector is known as noise data. During these data parts, the garage doors remain closed and the triggers are enabled. Noise data are used to measure the trigger rate from atmospheric muons passing through the PMT cluster and from triggers due to random fluctuations of PMT voltages. An example of a muon track seen by the TALE detector is displayed in Figure 4.25.

After the Noise data are collected, the garage doors are opened. The garage doors are controlled by a series of relays switched by a Weeder board [71]. The position of the doors is monitored by a potentiometer that is coupled to the drive shaft. The rack power board reads out the output voltage from the potentiometer in each bay. Once all doors are in the open position, a program is started designed to calculate which PMTs will have UV bright objects (documented in Appendix A) within 1.5° of their field of view and place them in a list of tubes to disable. Disabled tubes have the gain of the analog signal set to zero. This ensures that bright stars passing through the field of view do not cause the trigger rate to increase to the point where the detector crashes. An example of the tubes disabled while the constellation Orion was in the field of view of the detector is shown in Figure 4.26.

While night sky data are collected, snapshots of the night sky background are generated in order to measure both the pedestal of all channels that are read out but, more importantly, the fluctuations in the night sky background. Snapshots are read out once every 12 seconds

during normal operation. A snapshot summary consists of the running sum of the mean and variance for the previous 48 requested snapshot windows. A snapshot window is 256 ADC bins in length. The summaries are reported for all channels in the TALE detector.

Night sky data close a data part every 20 minutes and promptly open a new one. This serves the dual purpose of limiting file size and making it simple to locate specific portions of the night's data.

Operators are also required to regularly check the weather and cloud coverage and report it in the log. The TALE detector begins shutdown a half an hour before astronomical twilight to ensure there is time to appropriately cover the mirrors should any of the garage doors suffer mechanical issues and fail to close.

Once the doors are closed, an additional set of noise and UVLED is taken before ramping down the High Voltage and safely powering off the remainder of the TALE electronics. After each night of operation, the data are transported from the TALE detector to the city of Delta by the operators via USB. The data are uploaded to a computer in Delta and transferred to the University of Utah Telescope Array Data Server (TADSERV) for long-term storage.

Table 4.1: HiRes to TALE Electronics Mapping. Originally, HiRes-II camera 01 was installed in TALE telescope 15. However, the camera developed a short on the backplane and was replaced with HiRes-II camera 39.

TALE Camera Number	**HiRes Camera Number**	**TALE Crate Number**	**HiRes Crate Number**
15	39	15/16	25/26
16	02	15/16	25/26
17	03	17/18	01/02
18	04	17/18	01/02
19	05	19/20	03/04
20	06	19/20	03/04
21	07	21/22	05/06
22	08	21/22	05/06
23	09	23/24	07/08
24	10	23/24	07/08

Table 4.2: TALE Mirror Survey and Reflectivity Measurements. All of the results are reported in the CLF coordinate system. In this coordinate system, the origin is centered at the CLF and the azimuth angle is measured North of East. The reported azimuth and elevation angles are measured from the center of the camera. The Camera Rotation is the angle the camera is rotated about the axis formed by drawing a line from the center of the camera to the center of the mirror. The Mirror-Camera distance is the distance from the center of the mirror to the plane of the surface of the PMTs (not the UV filter). Average mirror reflectivity is summarized based on the measurements taken in May 2015. The reported reflectivity is the average for all measured wavelengths.

Mirror Number	**Azimuth [deg]**	**Elevation [deg]**	**Camera Rotation [deg]**	**Mirror-Camera Distance [m]**	**Radius of Curvature [m]**	**Reflectivity**
15	334.278	50.955	-0.432	2.278	4.781	0.863
16	327.418	37.166	0.038	2.277	4.777	0.833
17	312.342	50.135	0.721	2.308	4.838	0.899
18	308.954	37.041	0.192	2.288	4.769	0.908
19	290.462	37.002	-0.629	2.286	4.795	0.857
20	290.646	51.071	-0.441	2.284	4.772	0.848
21	272.089	37.133	0.496	2.281	4.776	0.893
22	268.785	51.045	0.316	2.283	4.770	0.893
23	253.541	37.076	-0.337	2.281	4.787	0.863
24	246.824	51.025	1.547	2.285	4.783	0.847

Table 4.3: TALE Trigger Levels. This table documents the trigger levels of the TALE front-end electronics.

Trigger Level	**Criteria**
Level 0	Trigger PLD registers at least a single 3-fold coincidence
Level 1	Trigger Board Issues a STORE
Level 2	Scan results pass Trigger Board readout criteria

Table 4.4: TALE Trigger Code Generation. This table explains the formation of the 3-fold coincidences used to determine the primary trigger of the TALE detector. The discriminated signal sums enter at the bottom of the figure where they go through the indicated logic. The top of the table indicates the 3-fold coincidence channels that are sent to the Trigger PLD.

TALE Trigger Code Bit	**Set Criteria**
00000	Single 3-fold Coincidence
00001	Two 3-fold, One View Only
00010	Two Views>0
00100	Two 3-fold, One View Only
01000	Two Views> 1
10000	Two Views >2

Table 4.5: Power Controller Board Activities. This table summarizes the responsibilities of the Power Controller Board. Aside from power control, there are a number of monitor lines.

Monitor rack Temperature and Humidity
Monitor garage door position
Monitor 220V current
Monitor HV Interlock
Enable/Disable 220VAC power controller
Enable/Disable 220VAC Heat Exchanger
Enable/Disable 220VAC power to low voltage supplies
Enable/Disable 220VAC power to HV supplies
Enable/Disable and monitor DC outputs of LV supplies
Enable/Disable, set voltage and current limits and monitor the HV supplies

Figure 4.1: TALE Detector Picture. This image shows the five bays of the TALE FD building along with the ten telescopes that compose the detector. Ten mirrors collect light from CR air showers and focus it onto their respective PMT cameras.

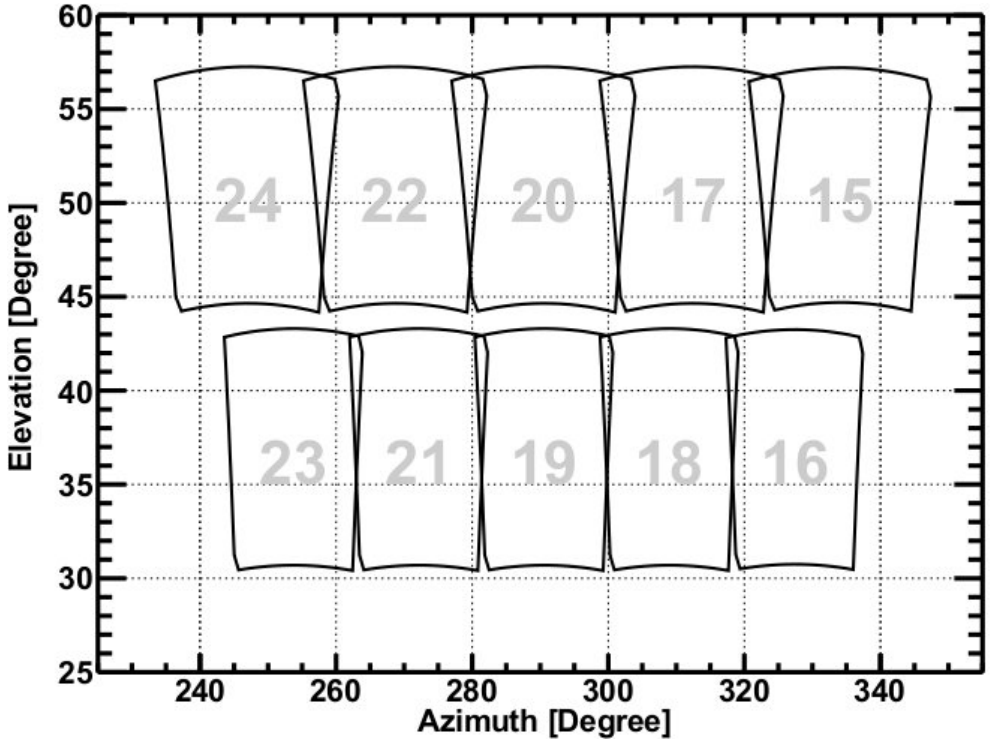

Figure 4.2: TALE Sky Coverage. This example of the TALE event display illustrates the portion of the sky observed by each of the ten TALE telescopes. The boundaries of each camera are drawn 1° inside the actual observation boundary in order to keep the display from looking cluttered.

Figure 4.3: Side View of TALE Telescope. The spherical mirror is in the center of the image and is used to focus light from CR air showers onto the PMT camera box mounted on the red stand to the right of the image. The readout electronics for a pair of cameras are housed in the black rack on the left of the image labeled 17,18.

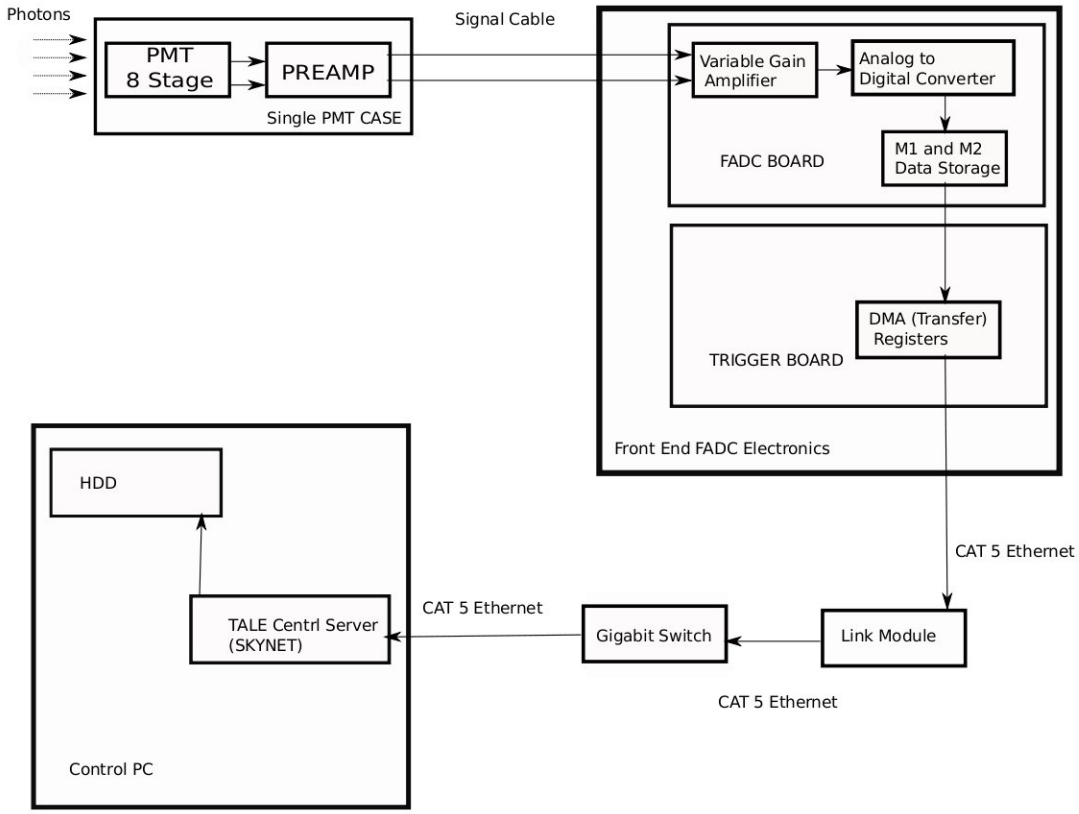

Figure 4.4: Tale Data Flow. This diagram details the data chain for the TALE detector. Light arriving at a photo-multiplier tube (PMT) is converted into an electrical signal by the PMT. The signal from the PMT is then passed through a pre-amplifier housed in the base of the PMT unit and transmitted over a signal cable to the readout electronics of the TALE detector. The readout electronics for a given channel consist of a variable, gain amplifier which enhances the signal before digitizing the waveform and storing it into memory. The waveform is then passed through a number of devices including the Trigger Board, Link Module, and local network before finally arriving at the control PC where it is written to disk.

Figure 4.5: Front View of TALE Telescopes. This is an image of a pair of TALE telescopes as seen when facing the mirrors. The four-segmented lobes of each mirror are clearly seen in this photograph. Additionally, the cable tray that connects the PMT camera to the readout electronics is also visible. As can be seen, the readout cables for each pair of cameras in a garage bay are bundled together.

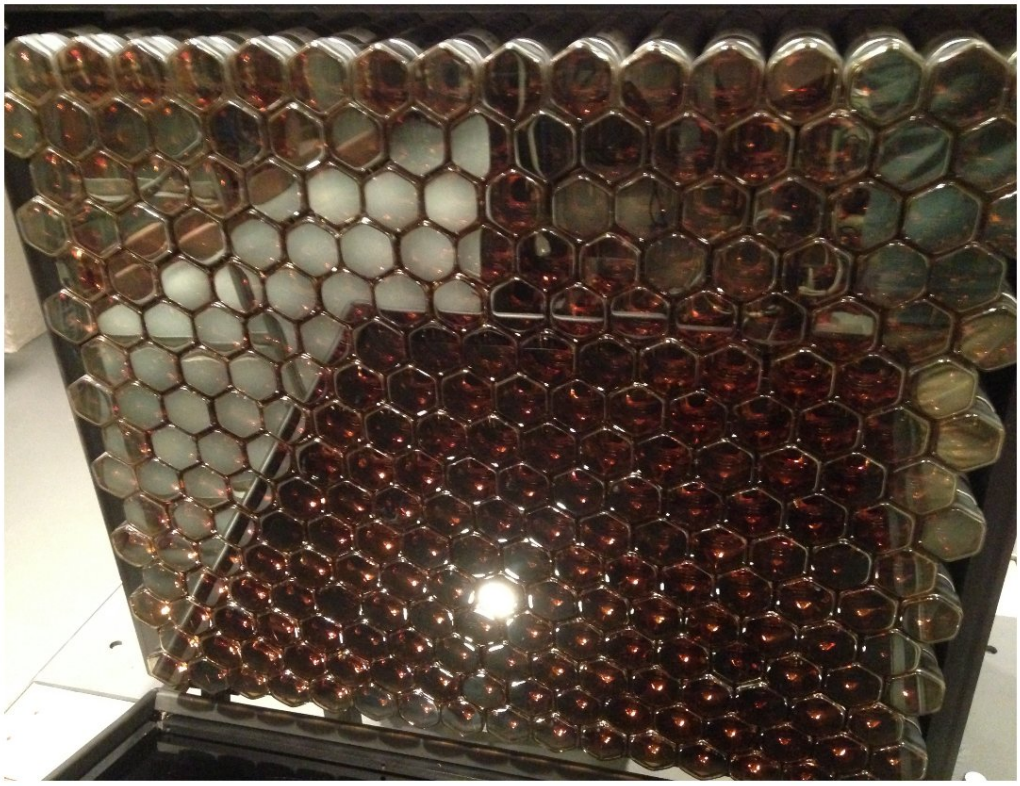

Figure 4.6: PMT Camera Face. This is an image of the face of the PMT camera with the UV filter lowered. The 256 PMTs are arranged in a 16x16 hexagonal close pack grid.

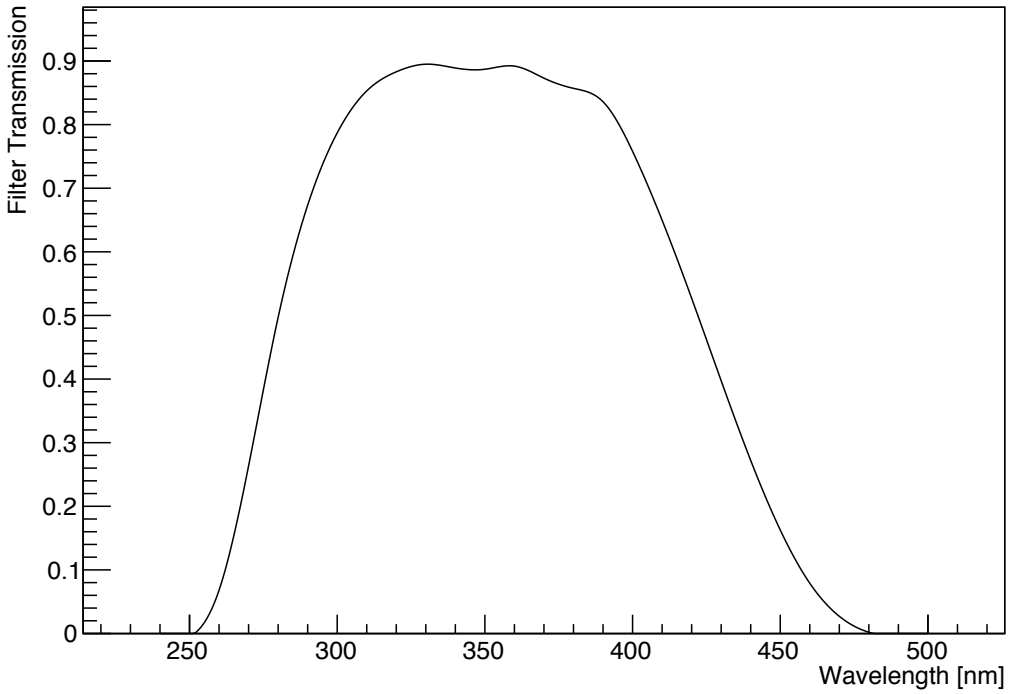

Figure 4.7: UV Filter Transmissivity. This figure shows the transmissivity of a UV filter as a function of wavelength as measured by the HiRes experiment. The majority of the light stimulated by the air shower particles is between 300 and 400nm. The filter passes this light while blocking most visible light from stars and man-made sources.

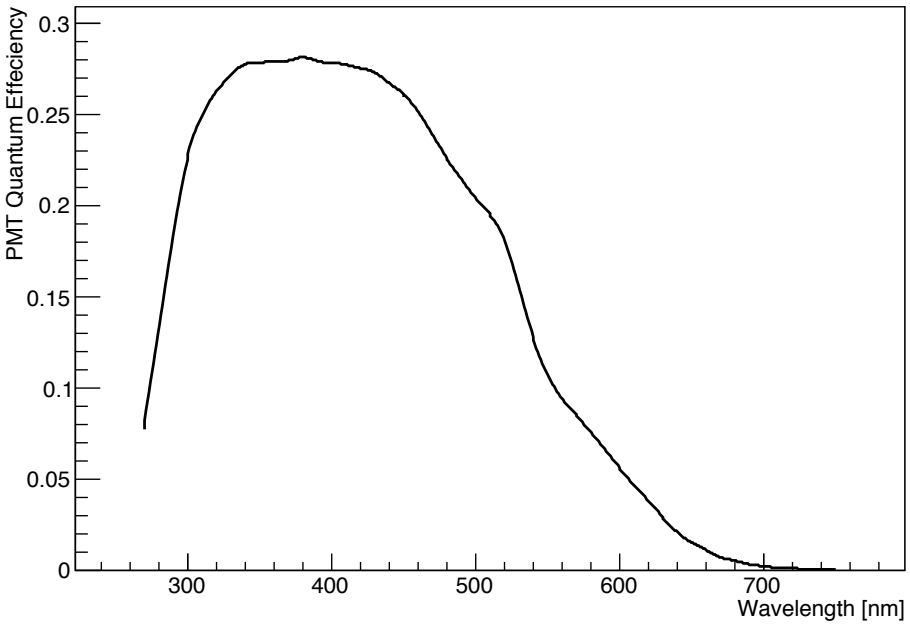

Figure 4.8: PMT QE Wavelength Dependence. This plot show shows the Philips XP3062/FL PMT Quantum Efficiency dependence on wavelength.

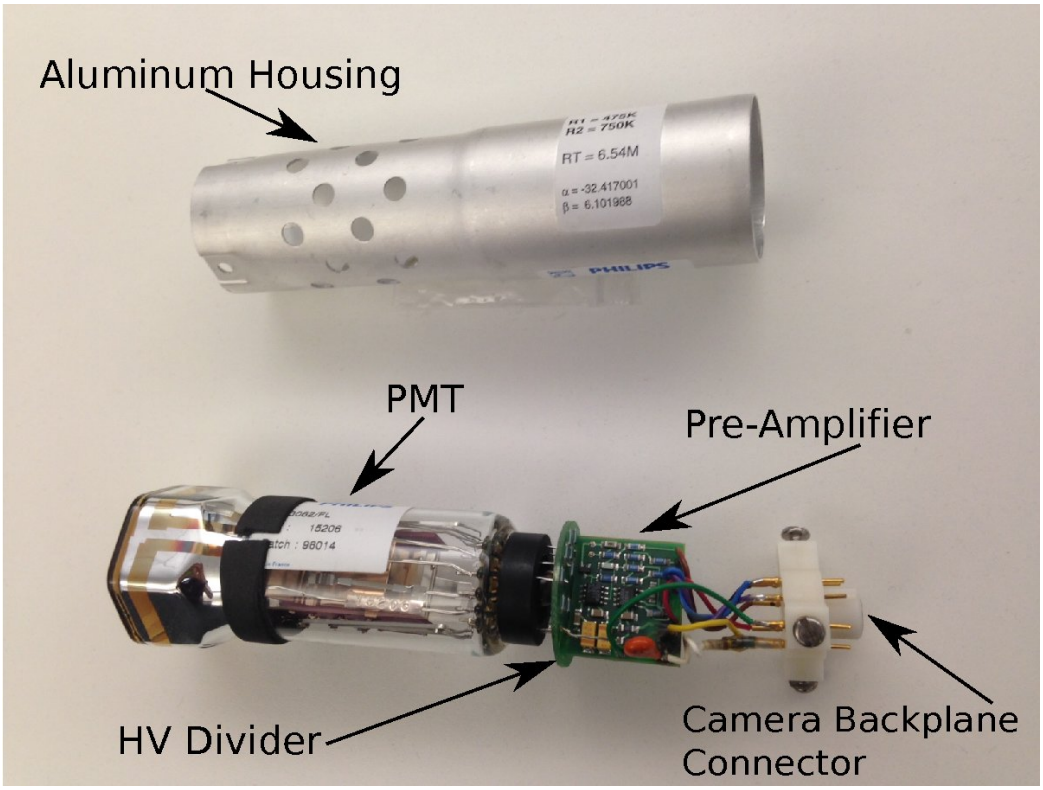

Figure 4.9: Philips XP3062/FL PMT Assembly Picture. This picture details the constituent parts of a PMT assembly. In addition to the actual PMT, the PMT assembly includes a HV divider chain and a pre-amplifier. The HV divider chain is used to step down the voltage between dynodes while the preamplifier ensures that signals from the PMT can be driven across the signal cable to the readout electronics. The entire assembly is housed within an aluminum shield.

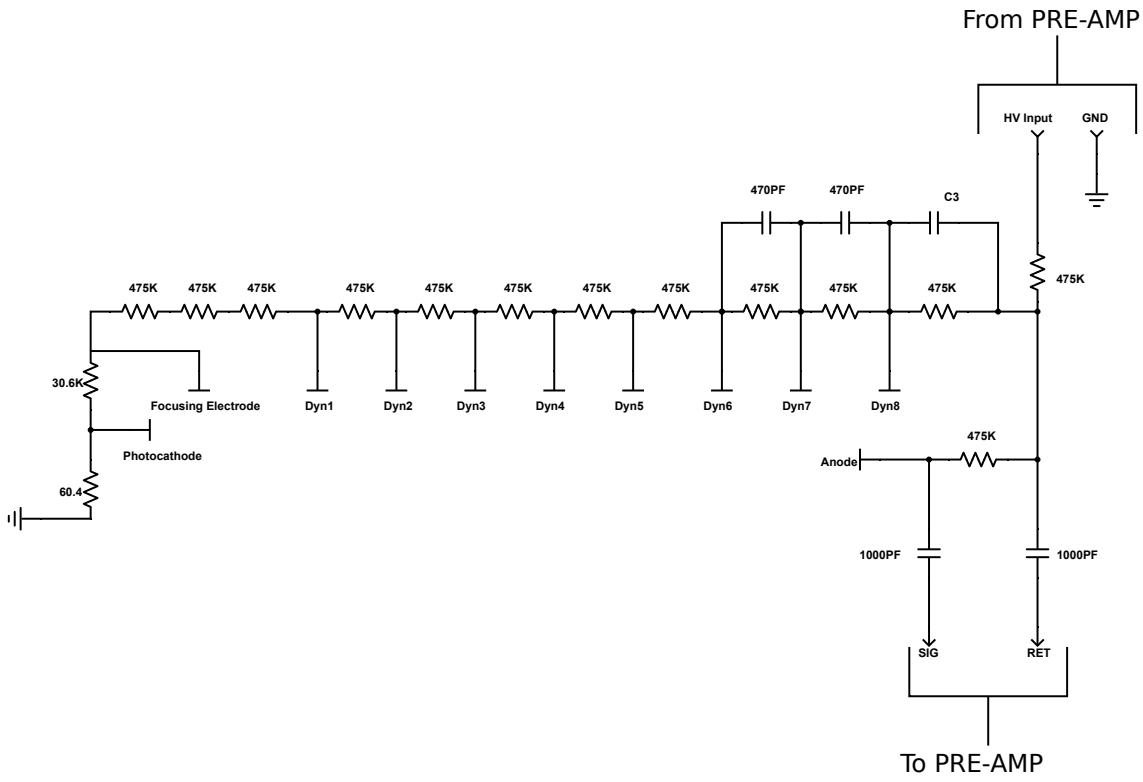

Figure 4.10: HV Divider Chain. This is the schematic diagram for the TALE PMT HV divider chain.

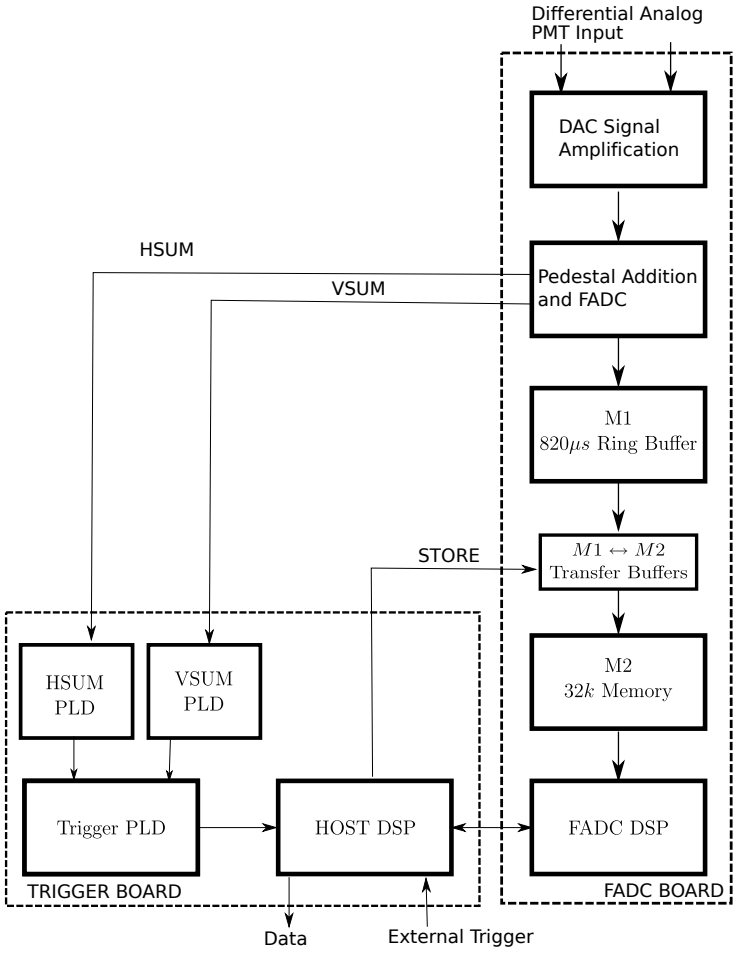

Figure 4.11: Single Camera Readout Overview. This is a schematic overview of the the readout electronics for a single camera. This diagram traces the path a single PMT signal channel takes as it navigates the FADC and trigger components of the readout electronics.

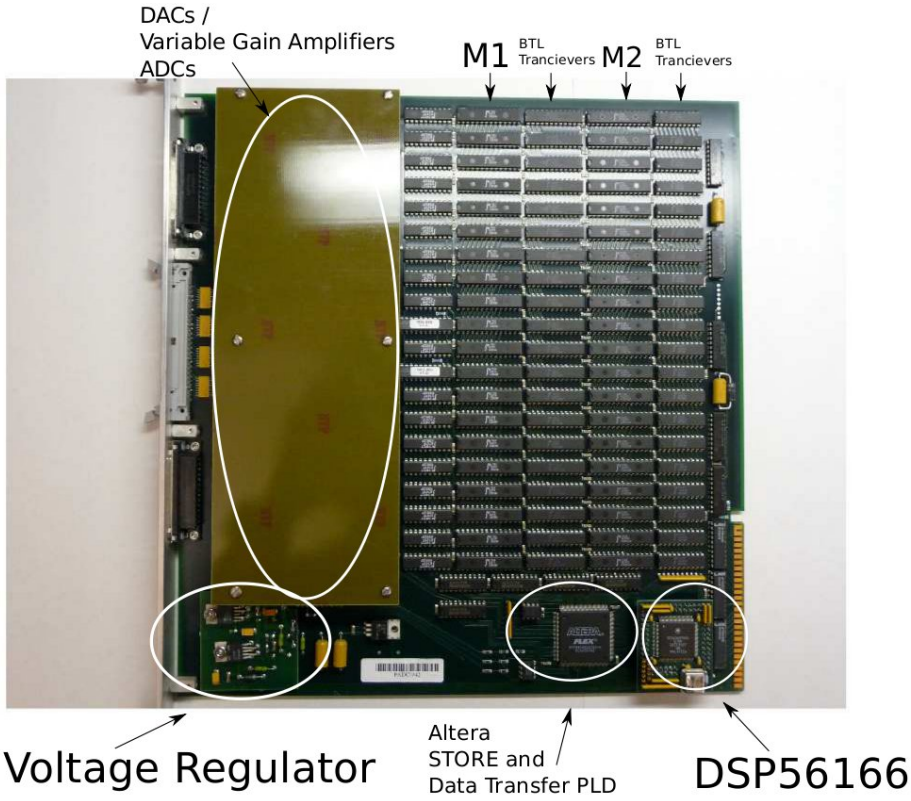

Figure 4.12: TALE FADC Board. This is a picture of a TALE FADC board. A copper shield protects the amplifier and digitization modules for each channel on the left of the board. The M1 and M2 chips are clearly seen on the right of the board.

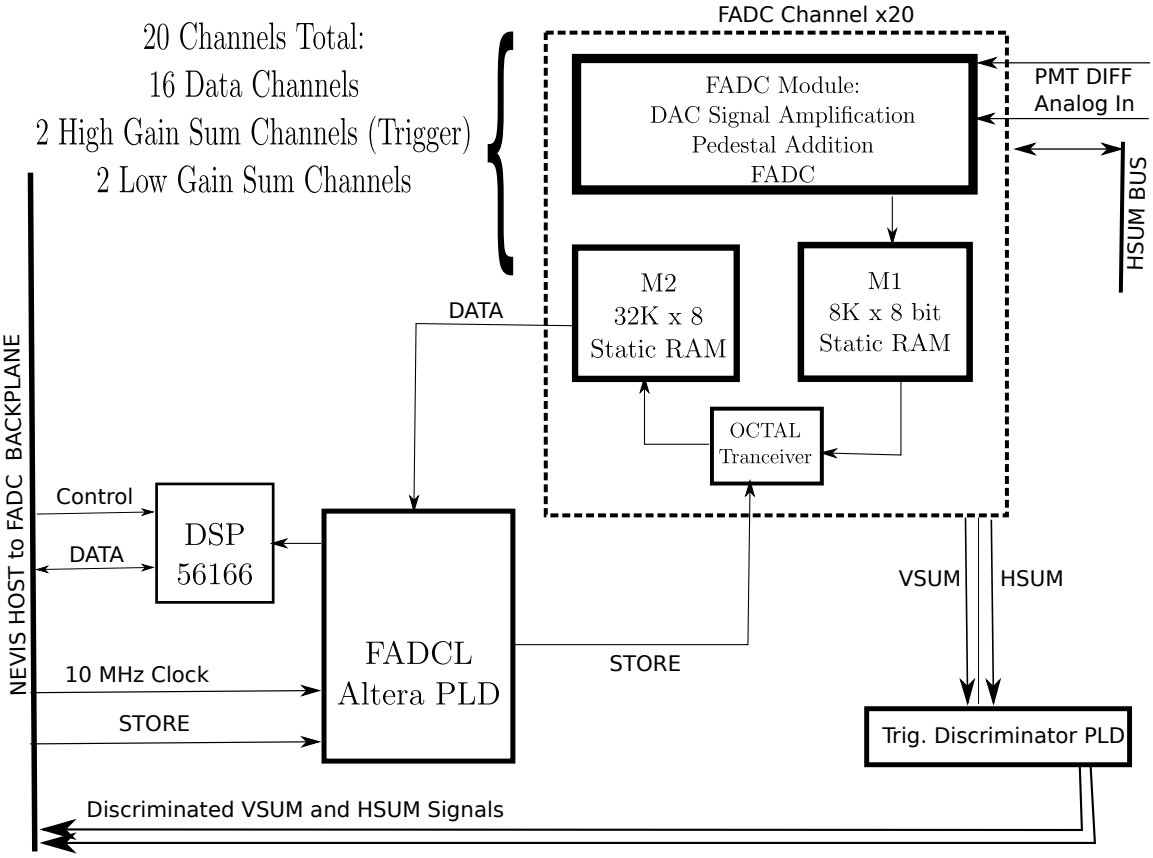

Figure 4.13: FADC Card Diagram. This is a schematic diagram for the TALE FADC cards.

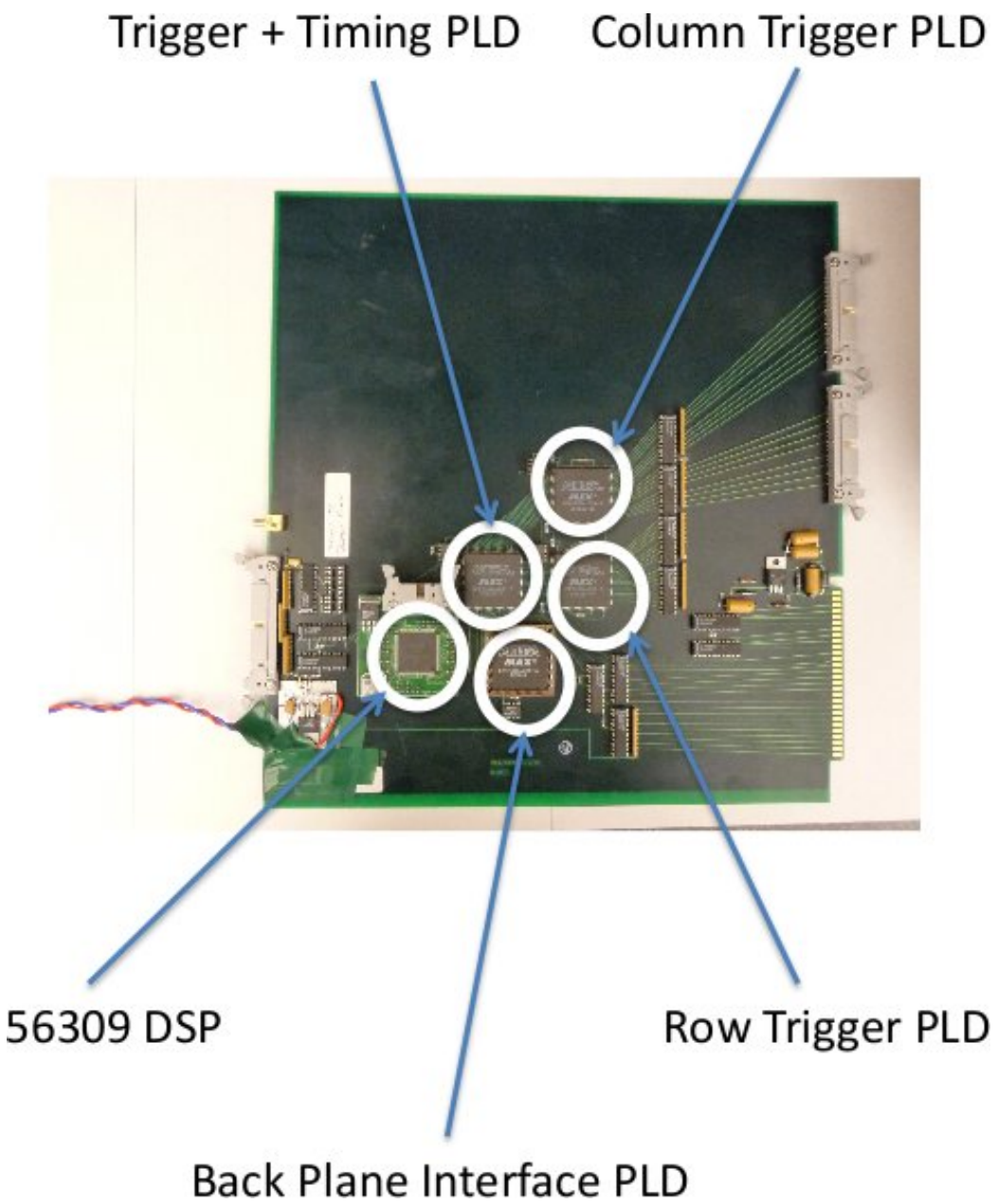

Figure 4.14: TALE Trigger Board. This is a picture of the TALE Trigger Board. The TALE Trigger Board consists of five primary components, the trigger/timing PLD, the row counter PLD, the column counter PLD, communication PLD, and the trigger DSP.

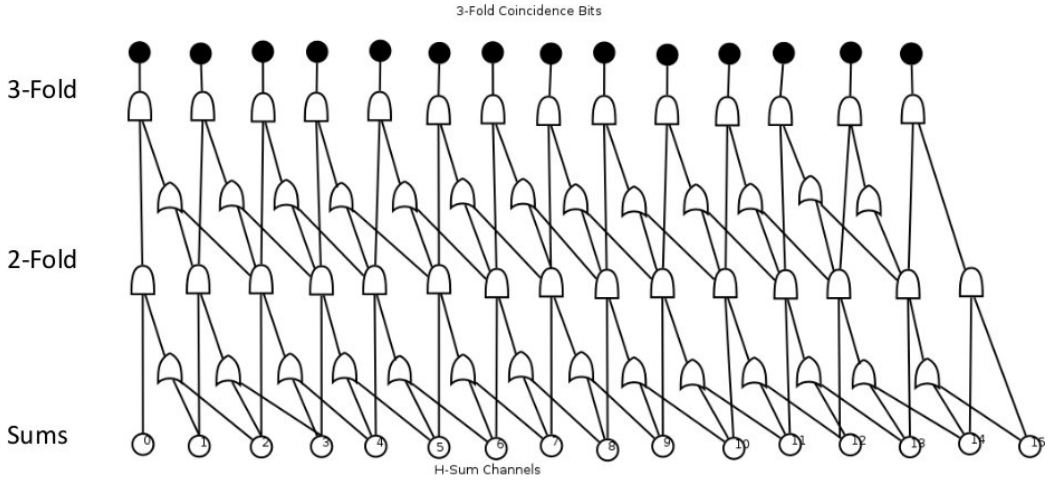

Figure 4.15: TALE 3-Fold Coincidence Formation. First, each signal has the logical AND is performed between it and the logical OR of the next two sum channels. For example, the AND is performed between sum channel 0 and the result of channel 1 OR channel 2. This is done for each set of channels and forms a 15-channel set of 2-fold coincidences. This process is repeated with the 2-fold coincidences in order to form a 14-channel set of 3-fold coincidences.

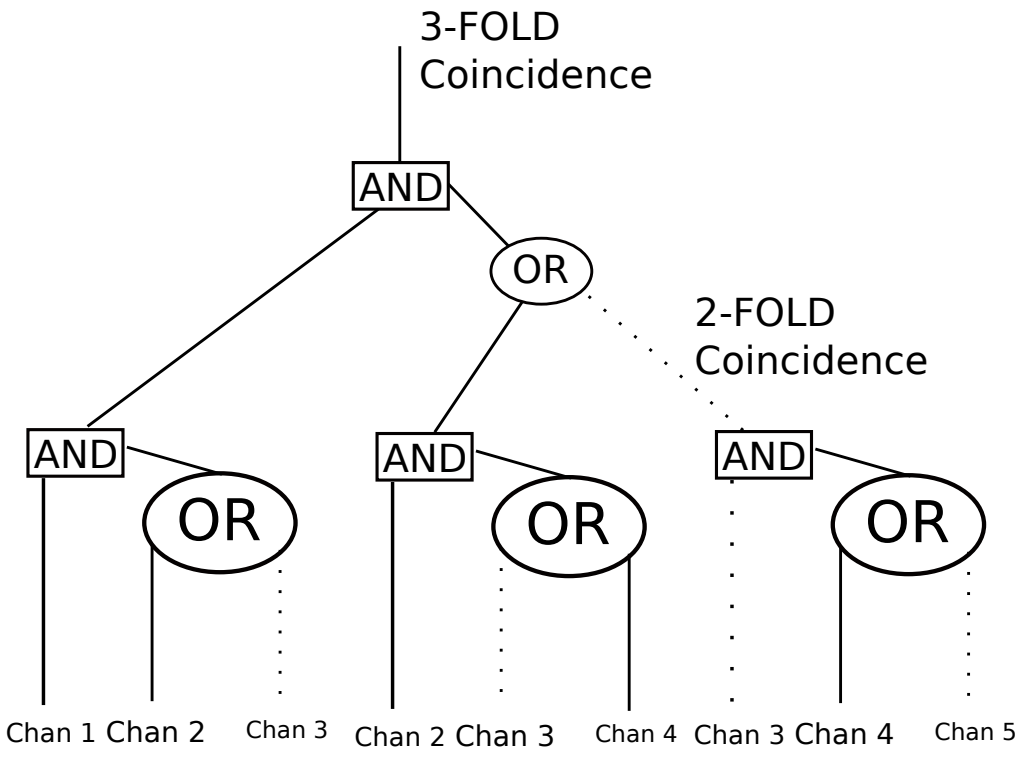

Figure 4.16: TALE 3-Fold Coincidence Example. In this example, the channels 1, 2, and 4 have discriminated signals indicated by solid line while all other channels do not have discriminated signals (indicated by dashed lines).

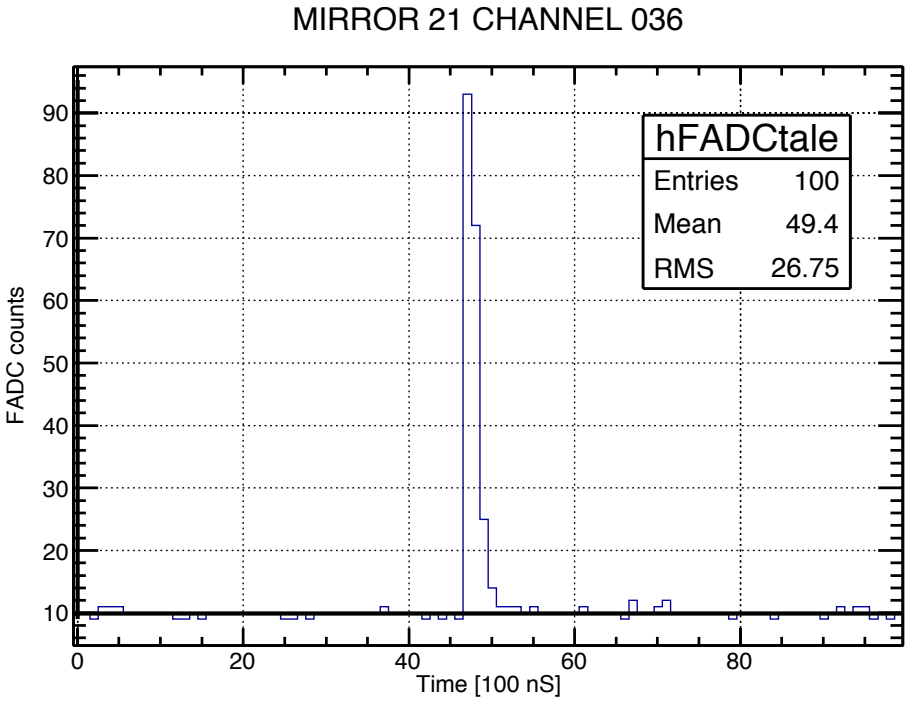

Figure 4.17: Muon Waveform. This histogram shows the digitized waveform generated by an atmospheric muon passing through one of the camera PMTs. The impulsive nature of the muon passing through the phototube demonstrates how the anti-aliasing filter spreads signals over a 3-4 digitization bins.

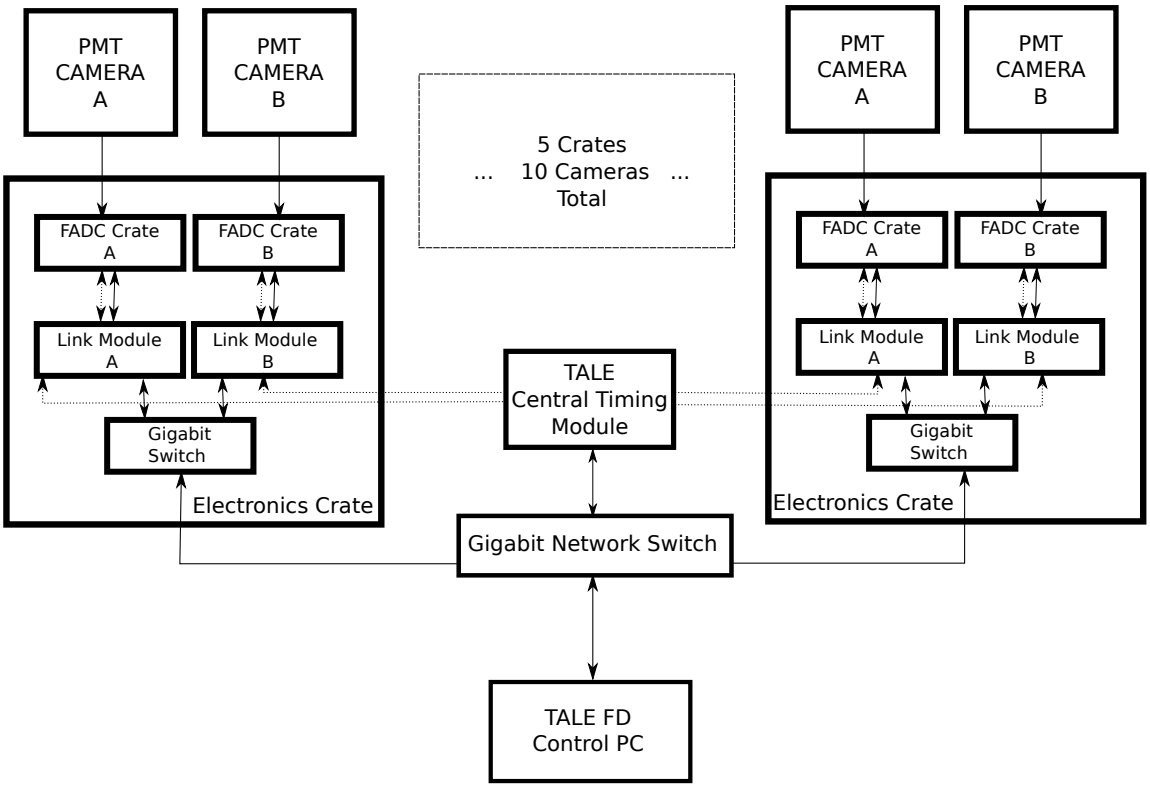

Figure 4.18: TALE Detector Communication Diagram. This diagram shows the communication overview of the TALE detector. This diagram shows how the Control PC communicates to the Central Timing system and each of the mirror Link Modules in a star network pattern.

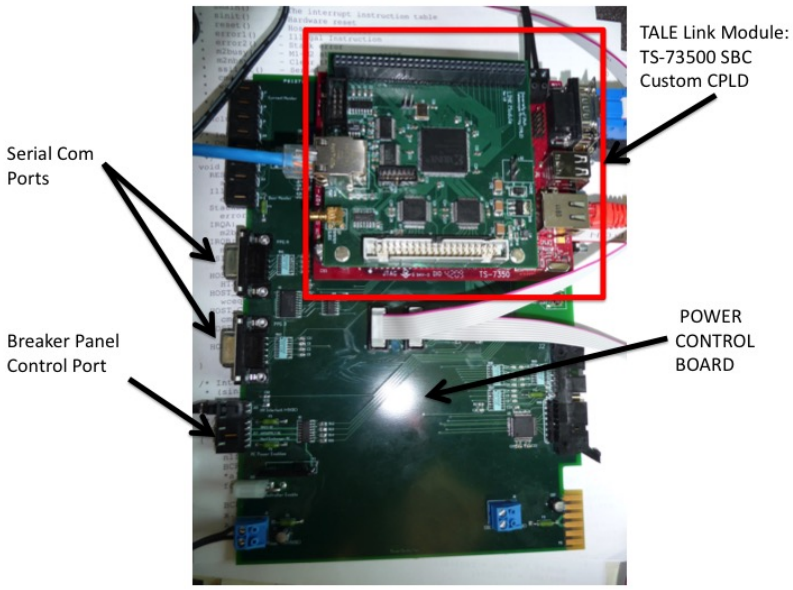

Figure 4.19: TALE Link Module. This image shows the TALE Link Module and the power controller board is is mounted on. Each Link Module consists of a TS-73500 single board computer and a custom CPLD daughter board.

Figure 4.20: 220 V Power Controller. This is a picture of a 220V Mapway power controller module. 220 V power is switched by external power board control lines connected to an internal relay on the control module.

Figure 4.21: TALE Breaker Panel. The HiRes-II panel was composed of GFCI breakers, which frequently tripped when HV power was enabled to the cameras. The new unit (pictured here) is composed of a series of standard over-current breakers and control relays. The internal relays in the breaker panel allow the power control board to determine when HV and LV supplies are provided power.

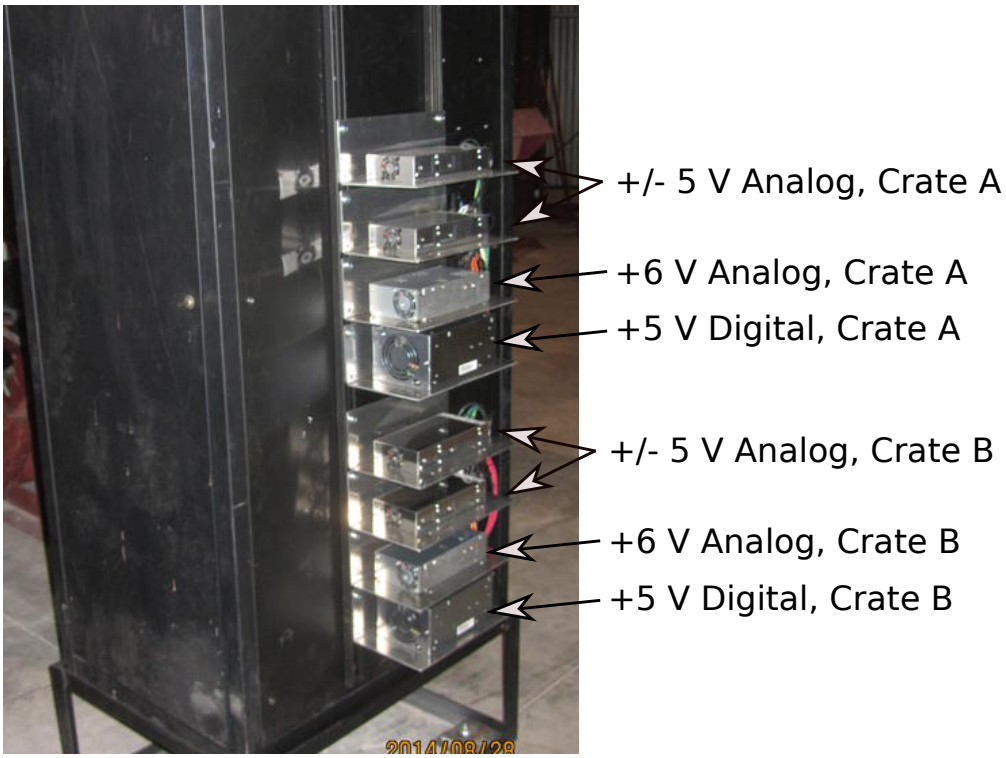

Figure 4.22: New TDK LV Supplies. This photograph shows the new LV supplies mounted to the side of a TALE electronics crate.

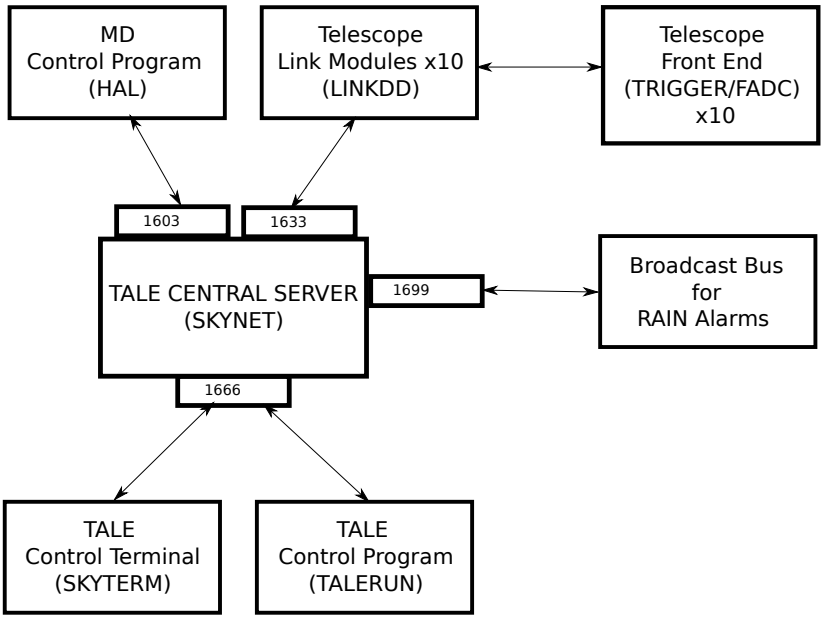

Figure 4.23: TALE Software Communication Overview. All front end electronics (FADC and Triggers boards) communicate through their respective Link Modules. The Link Modules run a driver called LINKDD, which is responsible for packet transmission to and from the front-end electronics. LINKDD also contains much of the code responsible for the initialization and control of the front end electronics. Nearly all communication of the TALE detector passes through the TALE Central Server (Skynet), which is hosted on the Control PC and allows other programs to attach to it as clients. The operator interface to the TALE detector is through the TALERUN GUI program running on the Control PC. Additionally, the MD control software and the rain bus are also able to connect to the Central Server.

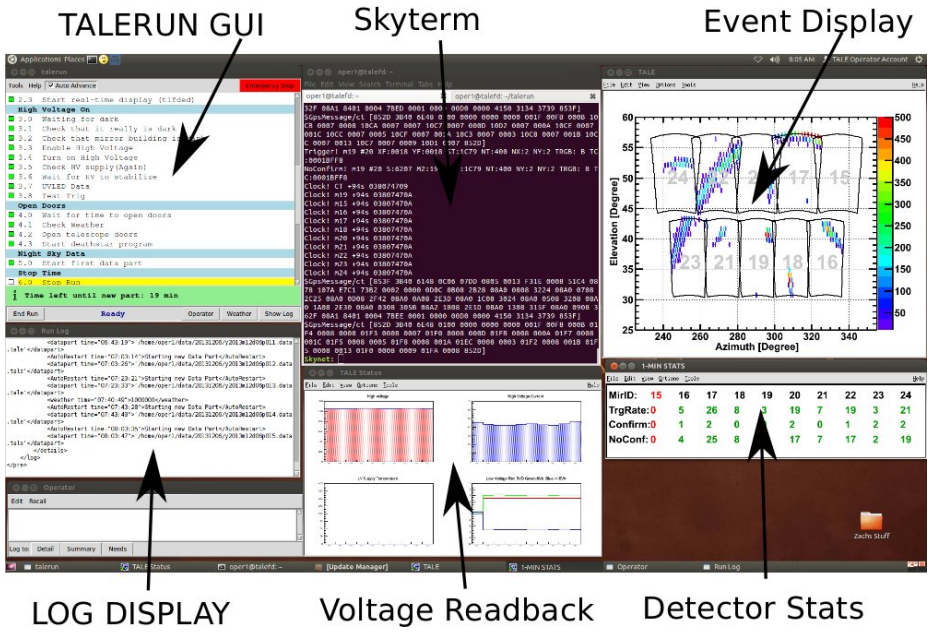

Figure 4.24: TALE Control Screen Shot. This image shows the Control PC interface to the TALE detector.

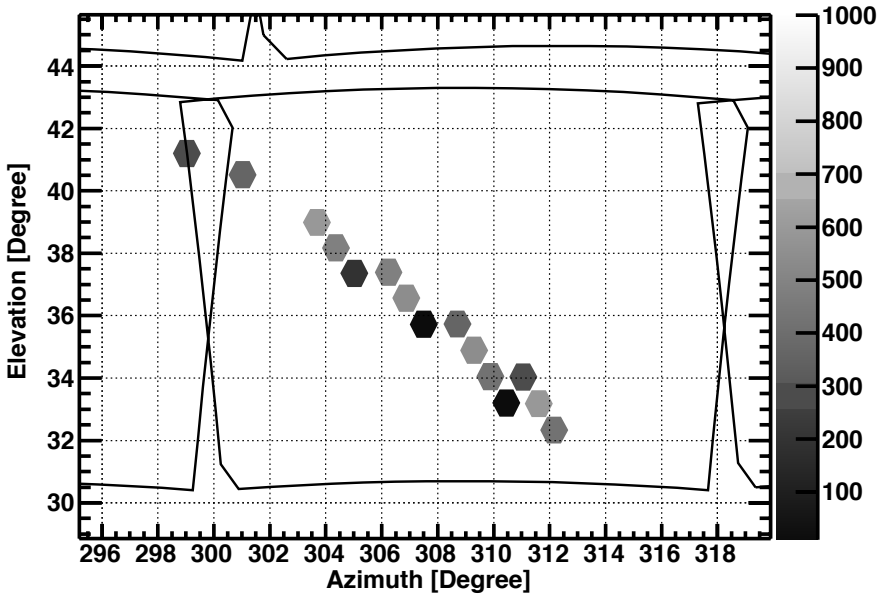

Figure 4.25: Muon Event Track. This is an example of a muon track generated when an atmospheric muon passes through a PMT camera and deposits energy directly into multiple PMTs.

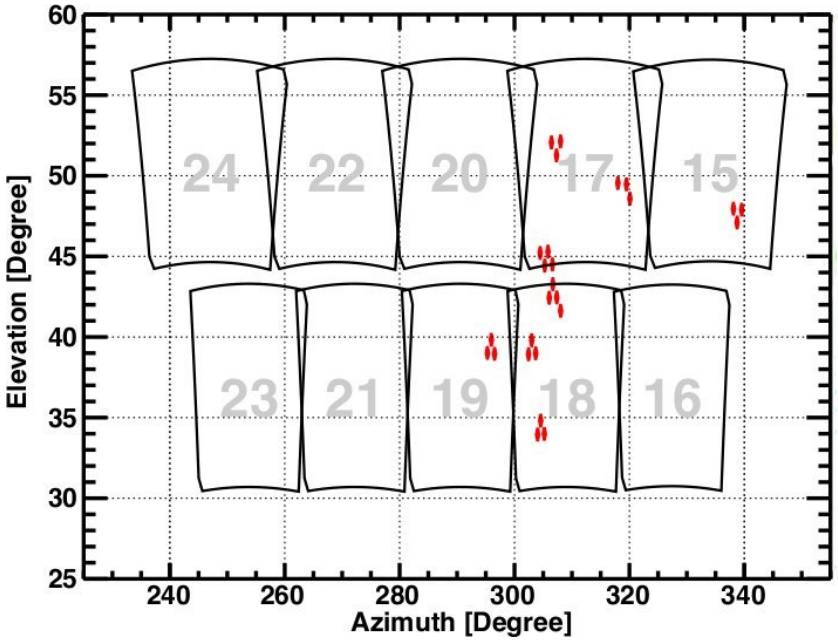

Figure 4.26: Orion in FOV. This is a display of the tubes that were disabled while the constellation Orion was in the FOV of the detector. As objects pass out of the FOV of a tube, the gain of the analog signal is returned to the operational value and new tubes are disabled.

CHAPTER 5

PHOTOMETRIC CALIBRATION

The photometric calibration of the TALE detector refers to the ratio of photoelectrons produced at the PMT photocathode to the number of Analog to Digital Converter (ADC) counts for the corresponding pulse read out by the detector. This calibration is important because it determines the energy scale of the detector measurements and in turn the aperture. The TALE detector is calibrated using two different types of light sources. The first light source is a Roving Xenon Flasher (RXF) and is instrumented with a FX 1101 short arc flash lamp whose emission spectrum is shown in Figure 5.1. The 0.5% nightly stability [72] of the RXF flasher at wavelengths over 350nm combined with the ability of the device to be moved from telescope to telescope makes it the primary calibration method for FDs in the TA experiment. The RXF has also been shown to have a stable light output on the order of a few percent over a period of months [72]. In addition to the RXF, each TALE telescope is equipped with a SETI UVTOP355 UVLED. The UVLED flashers are operated at the beginning and end of each nights telescope operation.

5.1 RXF Calibration

The TALE detector is calibrated using the RXF approximately once per run period. The geometric setup of the RXF is diagramed in Figure 5.2 and shows the relevant components of the calibration.

The RXF is mounted in the center of the mirror of each telescope facing the camera. The RXF flash lamp emits a broad spectrum of light. However, the RXF module is equipped with a narrow band filter centered at 355 nm and is shown in Figure 5.1. Additionally, the RXF module includes a teflon diffuser that insures the light is distributed isotropically.

Light is emitted from the RXF module and is attenuated through a neutral density filter (NDF). Photons that pass through the NDF travel to the UV filter, shown in Figure 5.3, at the PMT camera face. Most of the photons will travel through the UV filter and arrive at a PMT in the camera. This chapter details the calibration of the TALE detector to 1.0

NPE/ADC, which is the calibration of the TALE detector for all dates after January 2014. It is important to note for the analysis of the Epoch 1 data set, which preceded this, that the calibration was set to a lower level of 1.589 NPE/ADC. This was due to the lack of a secondary NDF available for calibration. Accordingly, the gain of PMTs was set to a lower value to avoid saturation of the ADCs by the RXF pulse. An example of the RXF pulse waveform is shown in Figure 5.4, which exhibits a sharp rise and a long tail.

RXF calibration is a two-step process and involves first iteratively balancing the programmable gains for the individual channels of each telescope so that the average integrated pulse of all of the tubes is the same. Programmable Digital to Analog Converters (DACs) are used to change the individual channel gains, and the details of their operation are covered in Appendix C. A display of the tube response of a uniformly illuminated cluster before balancing is shown in Figure 5.5a, whereas the tube response of the same cluster after adjusting the PMT signal gains is shown in Figure 5.5b. After the PMT gains are balanced, each camera is illuminated at least 500 times in order to allow adequate statistics for a determination of the number of photoelectrons per ADC count.

The RXF is too bright for calibrating the TALE cameras to a level of 1.0 ADC/NPE. Accordingly, a neutral density filter is placed in front of the RXF in order to reduce the effective brightness of the flasher. The nominal transmission coefficient of the NDF filter is specified at 0.55 but measured to be 0.576 by the TALE detector operating under a low gain setting. The latter is the value used in calculating the photon flux of the RXF.

Photons traveling toward the PMT camera first pass through a UV filter mounted at the front of the camera. A picture of the PMT camera with the filter lowered is shown in Figure 4.6. The transmissivity of the UV filter depends on the wavelength of light and is plotted in Figure 4.7. Some fraction of the photons is reflected at the surface of the UV filter but will be reflected back to the camera by the spherical mirror with a small loss. Illuminating a balanced camera with the RXF and then lowering the UV filter and illuminating the camera again performed a measurement of the UV filter transmissivity for each camera. The results of this measurement are shown in Table 5.1 and an example of the measured RXF output with the filter open and closed is shown in Figure 5.6.

The observed flux of photons at a PMT will also have a geometrical dependence due to the orientation of the RXF and the tube face as demonstrated by Figure 5.7. Photon flux falls off with a $1/R^2$ dependence where $R = D/\cos\theta$. Two more factors of $\cos\theta$ are expected to weigh the measured flux since both the teflon diffuser of the RXF and the surface of the PMT are better approximated as plates. This yields a final geometrical correction to the

flux which follows a $\cos^4\theta/D^2$ dependence.

Photons that transit the UV filter arrive at a PMT. An image of a PMT assembly is shown in Figure 4.9 and diagramed in Figure 5.8. Photons entering the phototube pass through the front window, which is made of borosilicate. They then interact with the photocathode to produce photoelectrons. Some important parameters of a PMT are (a) the effective area and uniformity of the tube and (b) the quantum efficiency (QE) of the photocathode.

The effective area of all of the TALE PMTs was measured by scanning the surface of every tube with a CO_2 laser at 321nm with a 1mm spot size. The resulting response profile for a tube is shown in Figure 5.9. The average response profile is used to calculate an effective area for all PMTs in the analysis and Monte Carlo simulations. The distribution of effective areas for the TALE PMTs is shown in Figure 5.10 and reports a mean effective area of 1197 $mm^2 \pm 2.4\%$.

Additionally, the manufacturer measured the QE of each PMT at 337nm. The resulting distribution of quantum efficiencies at 337nm for the PMTs in the TALE detector is shown in Figure 5.11 and shows three separate populations of PMT gains. Population A (composed of cameras 15, 18, 19, 20, 22, 23, and 24) has the mean centered at 0.263 as shown in Figure 5.12. Population B (composed of cameras 16 and 17) has the mean centered at 0.285 as shown in Figure 5.13. Population C (camera 21) has the mean centered at 0.269 but had a larger width than the other populations as shown in Figure 5.14. The QE of a PMT also depends on the wavelength of incident light and varies according to Figure 4.8.

Photoelectrons produced at the photocathode are accelerated and focused onto the first dynode. The collection efficiency of a PMT is the fraction of photoelectrons created at the photocathode that arrive at the first dynode and is reported by the manufacturer to be 0.9 [73]. A resistor chain incrementally steps up the voltage between dynodes (the PMTs have the cathodes held at ground). Secondary electrons are liberated from the surface of the dynode and are in turn accelerated to the next dynode. In this manner, the number of electrons at each dynode grows exponentially. The overall gain (number of electrons per initial photoelectron) is a function of the number of dynodes of the PMT, the secondary emission probability distribution, and the operational voltage. Individual tubes are characterized according to

$$G_{tube} = \exp\alpha \cdot V^{\beta}, \tag{5.1}$$

where $\exp\alpha$ is a normalization parameter, V is the bias voltage of the PMT, and β is

determined by the number of stages of the PMT and the secondary electron production rate. The measured distribution of values for α and β are shown in Figure 5.15a and Figure 5.15b, respectively.

When the PMTs are operated at the nominal value of 1050V, the resulting distribution of PMT gains is shown in Figure 5.16. The width of the PMT gain distribution explains the necessity for balancing the resulting PMT signal channels.

Using the 500 shot calibration RXF data sets, the number of photoelectrons can be determined through statistical means. Since the number of photons produced by the RXF follows a Poisson distribution, if the secondary emission of each dynode was a fixed number, then the number of photoelectrons is determined by

$$NPE \propto \frac{< S_{int} >^2}{RMS^2}, \tag{5.2}$$

where $< S >$ is the average integrated number of ADC counts a tube reports for an RXF flash, and RMS is the root mean square deviation of the integrated signals for a tube. However, secondary emission is a statistical process and the added fluctuation inflates the measured RMS and leads to an underestimate the number of photoelectrons. To this end, a term called the excess noise factor (ENF) is introduced which accounts for the statistical noise generated by the secondary emission process giving

$$NPE = \frac{< S_{int} >^2}{RMS^2} \cdot ENF, \tag{5.3}$$

where ENF is the excess noise factor.

An estimate of the ENF can be determined through simulation and is presented in Appendix G. A study of the Middle Drum telescopes, half of which are instrumented with similar phototubes as the TALE detectors, shows that the ENF for the TALE PMTs has an average value of 1.55. This value was confirmed by the phototube manufacturer [73]. The flux of photons from the RXF is calibrated against a NIST photodiode. The RXF flux is measured to emit $11.27 photons/mm^2$ at $6.1°C$ and a reference distance of 82.375 inches, a value which can be measured by the TALE detector cameras using the relation

$$\begin{aligned} Flux[photons/mm^2] = & \left(\frac{< S_{int} >^2}{RMS^2} \cdot ENF \right) \cdot \left(\frac{\left(CC_{dist} - RXF_{length}\right)^2}{R_{dist}^2} \cdot \cos^4 \theta \right) \\ & \cdot \left(\frac{1}{QE \cdot Eff_{col}} \right) \cdot \left(\frac{1}{UV_{trans} \cdot NDF_{trans}} \right) \cdot \frac{1}{Area_{effect}}, \end{aligned} \tag{5.4}$$

where the parameters of this equation are detailed in Table 5.2.

The RXF photon flux at the reference distance was calculated using average tube values for the ENF, QE, effective area, and collection efficiency. Actual camera UV filter transmission coefficients and separation distances were used. The resulting estimate of the photon flux as determined by the TALE detector is shown in Figure 5.17 and reports a measurement for the RXF flux of 11.25 $photons/mm^2$ compared to the 11.27$photons/mm^2$ determined by calibration of the RXF against the NIST photodiode. The width of the resulting distribution is also expected since the total uncertainty in a given PMT's estimate of the flux is given by,

$$\sigma^2_{TOT} = \sigma^2_{NPE} + \sigma^2_{ENF} + \sigma^2_{QE} + \sigma^2_{UV\,filter} + \sigma^2_{RXF} + \sigma^2_{NDF} + \sigma^2_{AREA}, \tag{5.5}$$

where the individual contributions are documented in Table 5.3. Combined, this gives a total expected fractional width to the estimated photon flux distribution of 0.126 with a measured width in Figure 5.17 of 0.128. This result shows that the photometric scale of TALE is consistent with the calibrated expectation of the RXF.

There are two major calibration epochs for the TALE detector. From the dates of Sept 2013 - Jan 2014, the nominal calibration was set to 0.59 ADC/NPE. This was done in order to ensure detector stability while issues related to background and star noise were resolved. In Jan 2014, the calibration was changed to 1ADC/NPE. A summary of the calibration epochs is shown in Figure 5.18.

5.2 UVLED

Every night that the TALE detector takes data, a UVLED run is performed before and after night sky data are collected. UVLED data are taken with the garage doors closed. During normal operation, a UVLED module is mounted in the center-post of each telescope mirror and is pointed at the PMT camera. An example of a UVLED module is shown in Figure 5.19.

During a UVLED run, the camera face is illuminated at a rate of 5 Hertz for 500 shots. This allows the photometric calibration of the detector to be calculated on a nightly basis and tracked between the monthly RXF calibrations. The UVLED data taken before Jan 2014 were discarded due to nonuniformity of quartz diffusers installed in the modules. In Jan 2014, the quartz diffusers were replaced with teflon diffusers which provide near uniform illumination of the camera face (see Appendix F). An example of the stability of the detector calibration after Jan 2014 can be seen in Figure 5.20 which shows the average tube gain

for the tale detector as calculated by the UVLED modules over the course of a week. The detector calibration can be seen to be stable within statistical error from night to night.

Table 5.1: TALE UV Filter Transmission Coefficients.

TALE Camera Number	**Filter Transmission** ± 0.03
15	0.86
16	0.88
17	0.90
18	0.91
19	0.89
20	0.89
21	0.89
22	0.91
23	0.89
24	0.88

Table 5.2: RXF Flux Calculation Parameter Summary.

Parameter	**Description**
$< S >$	Average integrated number of ADC counts a tube reports for an RXF flash
RMS	RMS of the integrated signals for a tube
CC_{dist}	The perpendicular distance between the mirror center-post and the face of the PMTs
RXF_{length}	The length of the RXF, R_{dist} is the reference distance of 82.375 inches
θ	Angular offset a particular PMT from the RXF to cluster axis
QE	Average quantum efficiency for the PMTs in the TALE clusters
Eff_{col}	Collection efficiency of a PMT to gather a photoelectron generated at the photocathode onto the first dynode
UV_{trans}	Transmission efficiency of the UV filter
NDF_{trans}	Transmission efficiency of the neutral density filter
$Area_{effect}$	Effective area of a PMT

Table 5.3: RXF Flux Calculation Parameter Summary.

Parameter	**Value**	**Description**
σ_{NPE}	0.045	Uncertainty in the estimated NPE
σ_{ENF}	0.087	Uncertainty in the excess noise factor
σ_{QE}	0.064	Uncertainty in PMT QE
$\sigma_{UVfilter}$	0.03	Uncertainty in the UV filter transmission coefficient
σ_{RXF}	0.01	The stability of the RXF
σ_{NDF}	0.008	Uncertainty in the transmission of the NDF
σ_{AREA}	0.03	Uncertainty in tube effective areas

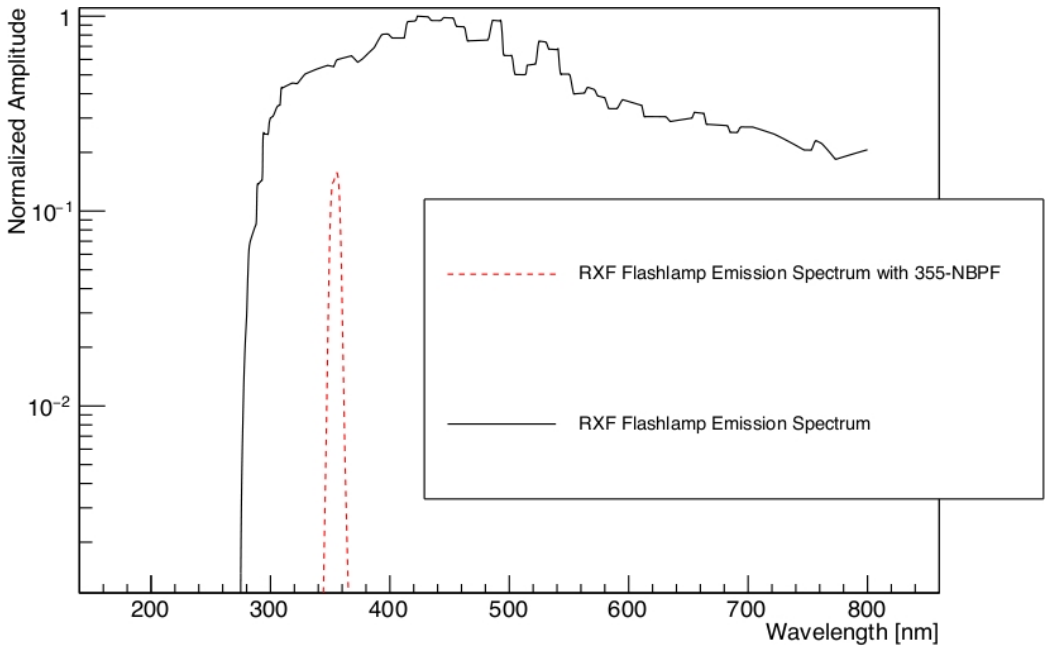

Figure 5.1: RXF Spectrum. The solid line shows the normalized emission spectrum of the RXF flash lamp. The RXF has a number of optical elements including a 355nm narrow band filter. Therefore, the light out is 355nm with 10nm FWHM. The dashed line shows the emission spectrum that leaves the RXF module.

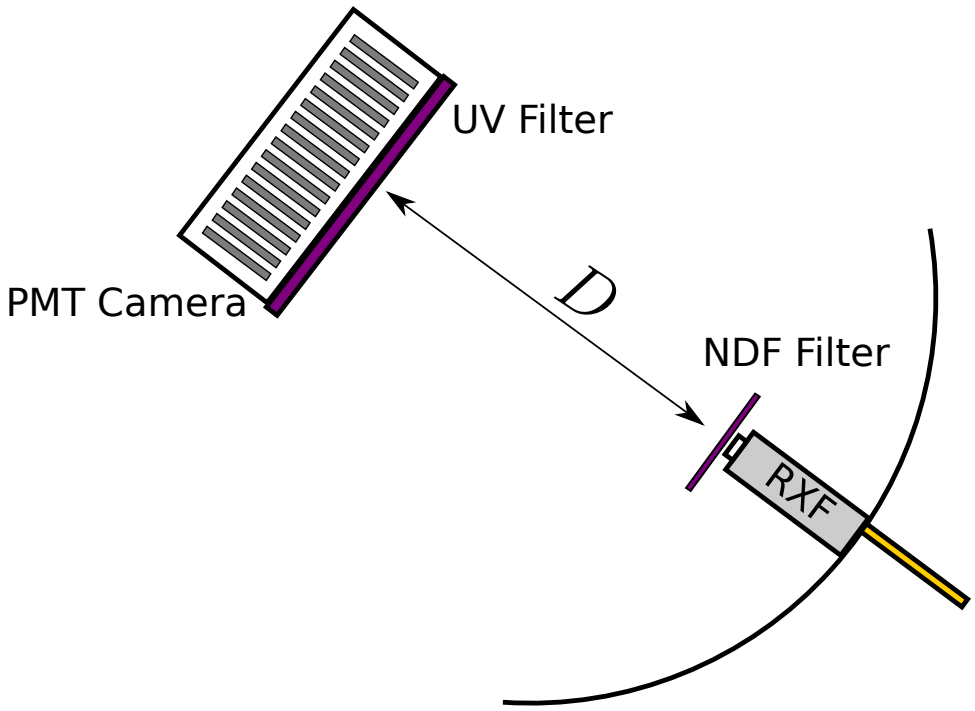

Figure 5.2: Schematic Diagram of RXF Calibration. This image indicates how the RXF flasher is mounted in the center of the mirrors facing the TALE cameras. The RXF discharges at approximately one Hertz and nearly uniformly illuminates the surface of the camera face. The distance D is the distance measured between the face of the RXF and the face of the PMTs. The light at the camera follows a $\cos^4\theta/D^2$ distribution.

Figure 5.3: PMT Camera Filter Picture. The PMT face of a camera is shown by lowering the UV filter, which is seen in the bottom of the frame. Phototubes are packed in a honeycomb pattern, minimizing the dead space between tubes.

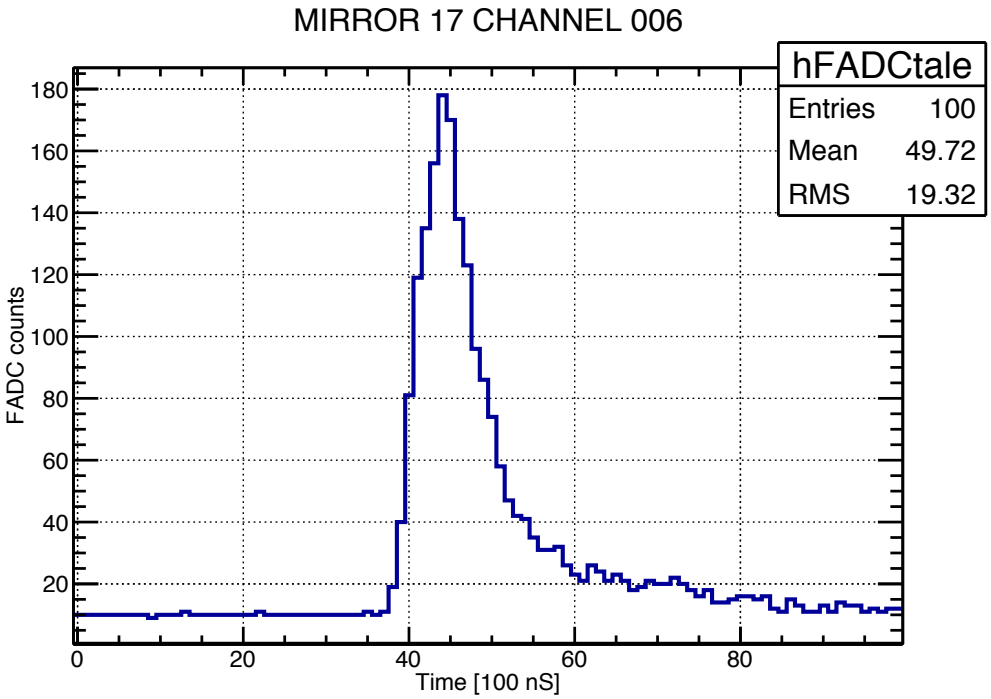

Figure 5.4: RXF Waveform. This is an example of a recorded waveform of the RXF flasher recorded by TALE camera and electronics.

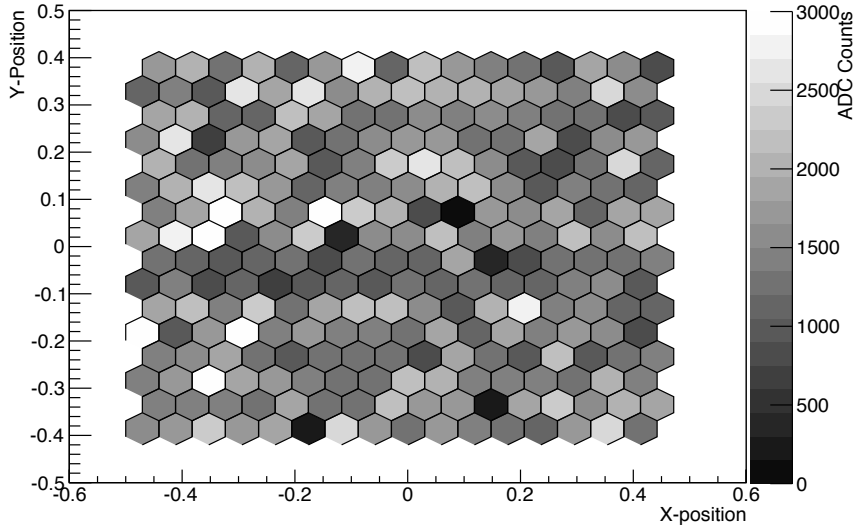

(a) Unbalanced Camera

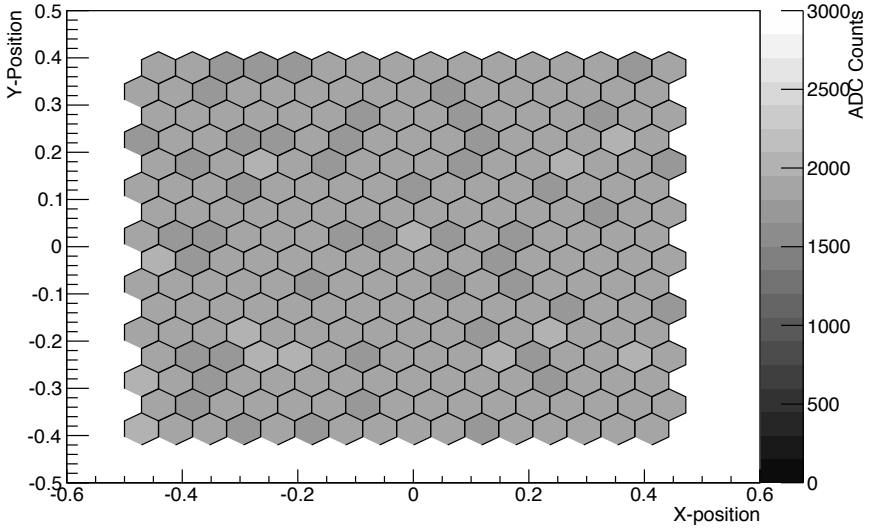

(b) Balanced Camera

Figure 5.5: TALE Camera Response to RXF. Shown is the camera response to the RXF as the input signal gains are balanced. The integrated signal in each tube of the camera is shown by the shade of the PMT area. The starting (unbalanced) point is shown in figure (a) and the final balanced point is shown below in figure (b).

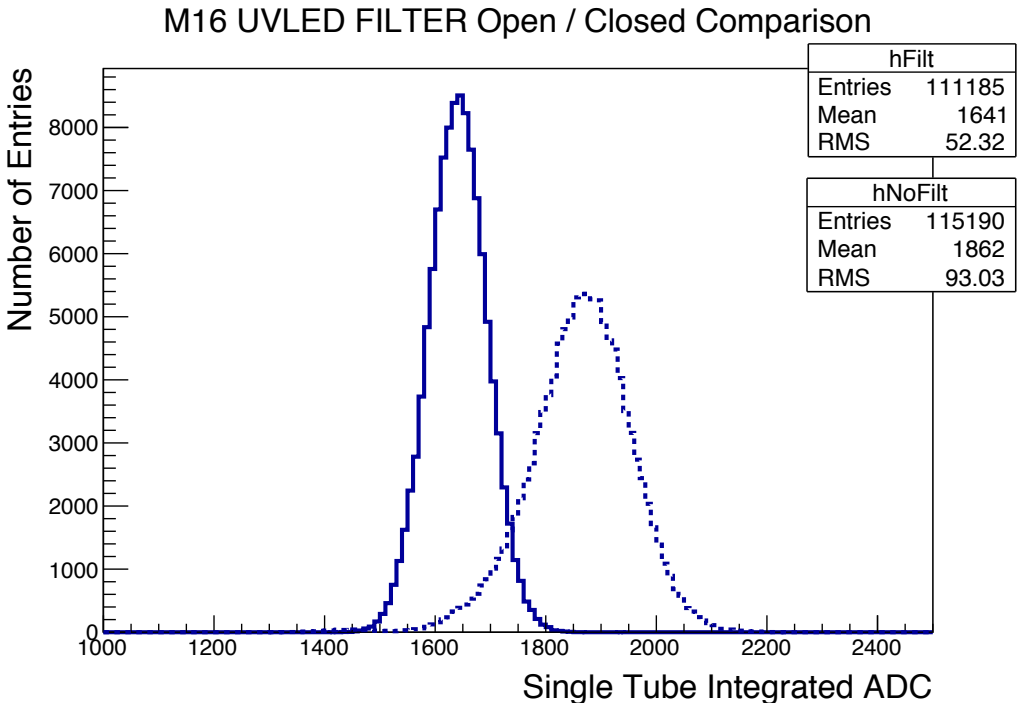

Figure 5.6: UV Filter Open and Closed Comparison. This figure shows the histogram for the integrated PMT response to the RXF with the UV filter in place (solid line) along with the same measurements taken after the filter was removed (dashed line). The data presented in this figure are from camera 16 and the ratio of the mean of the histograms results in the 0.88 transmissivity reported in Table 5.1. These data were taken on y2014m01d22.

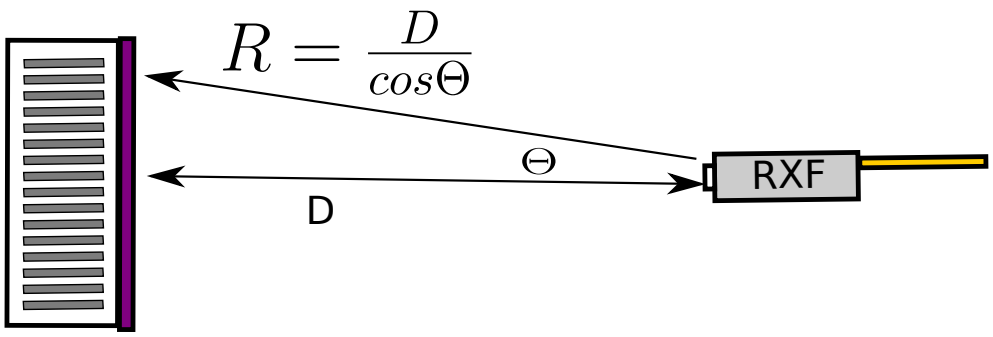

Figure 5.7: Schematic Diagram of RXF Calibration Geometry Dependence. The diagram shows part of the geometrical dependence of the measured photon flux by a PMT depending on the relative locations of the PMT and the RXF.

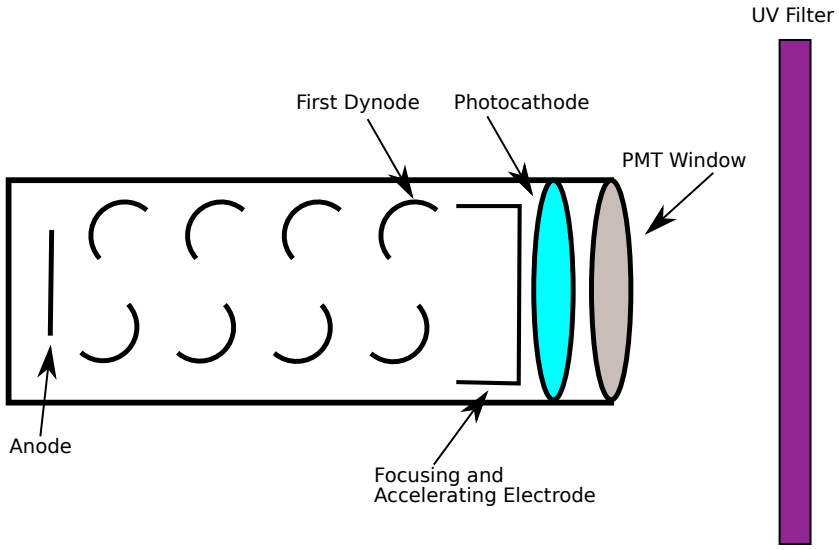

Figure 5.8: PMT Diagram. This is a diagram of the individual optic components of the TALE camera.

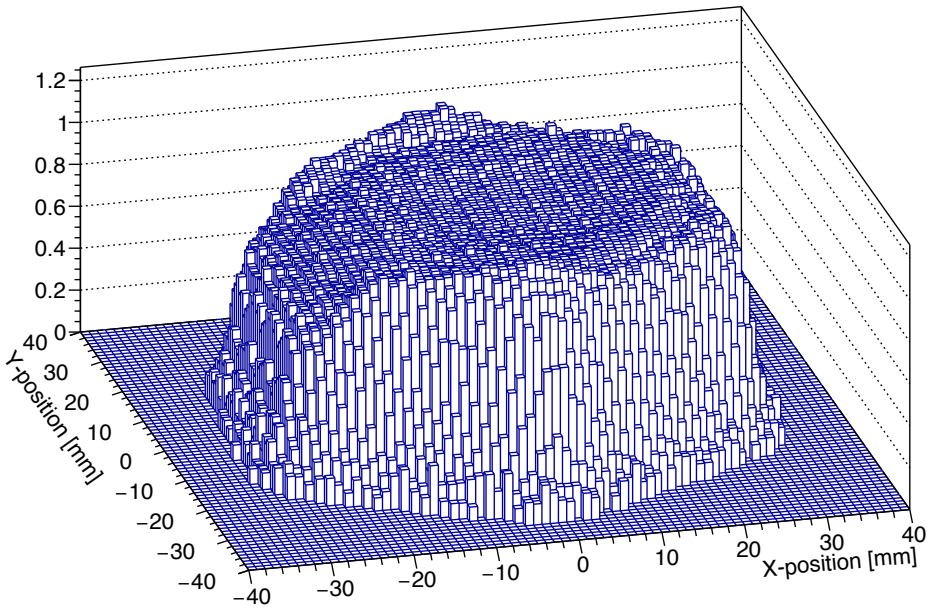

Figure 5.9: PMT Response Profile. The normalized response profile for a tube is shown. Scans of this type are used to determine the effective area of each of the PMTs in the TALE detector. The grid pattern indicates the step size as the laser scanned the surface of the PMT.

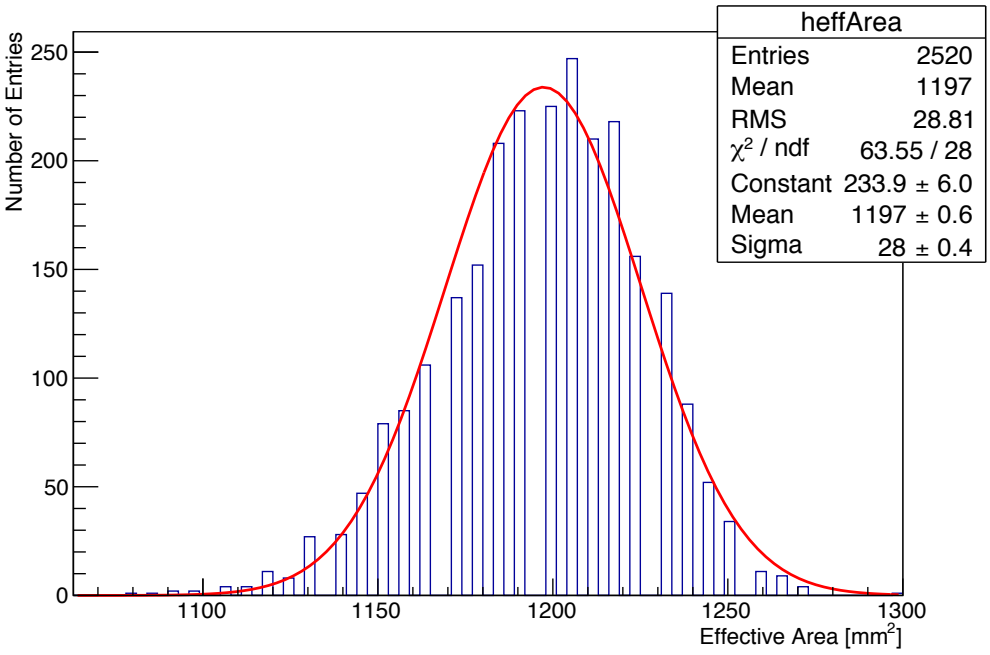

Figure 5.10: PMT Effective Area Distribution. The distribution of effective areas for TALE PMTs and provides a mean effective area of $1197 mm^2 \pm 2.4\%$.

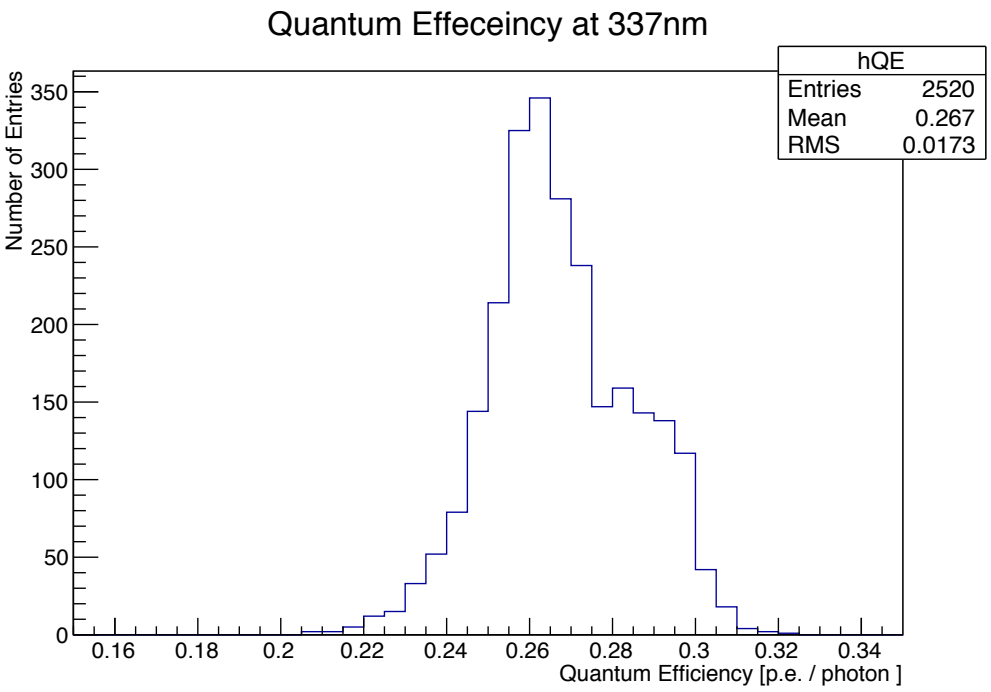

Figure 5.11: PMT QE Distribution. This plot show the distribution of QE at 337nm for tubes in the TALE detector.

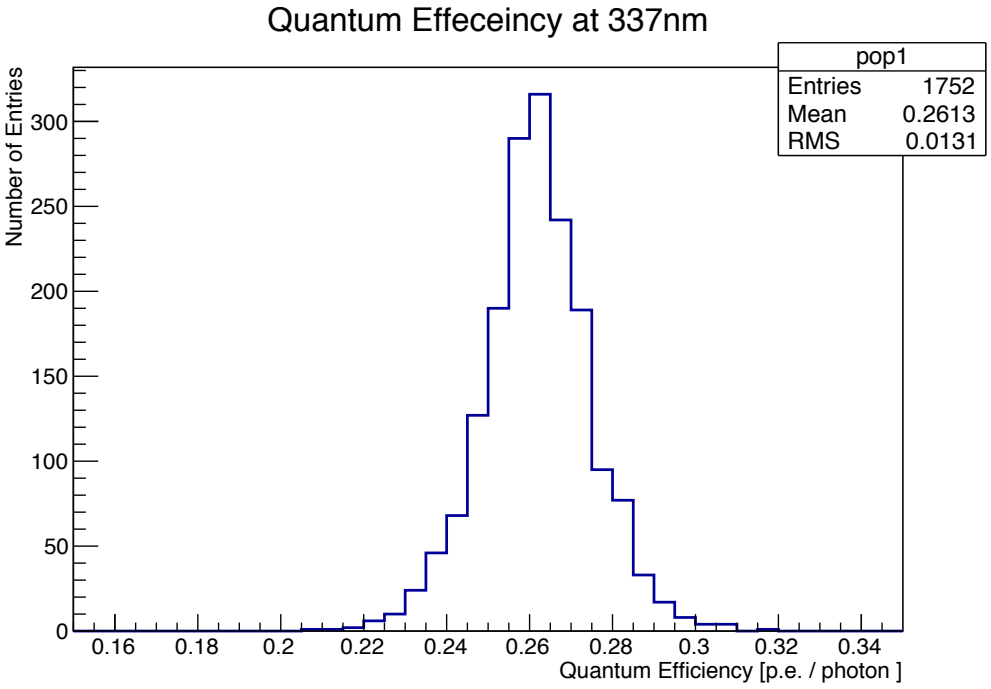

Figure 5.12: PMT QE Population A Distribution. This plot shows the distribution of QE for the tubes in cameras 15,18,19, 20, 22,23, and 24. This distribution has a mean of 0.261.

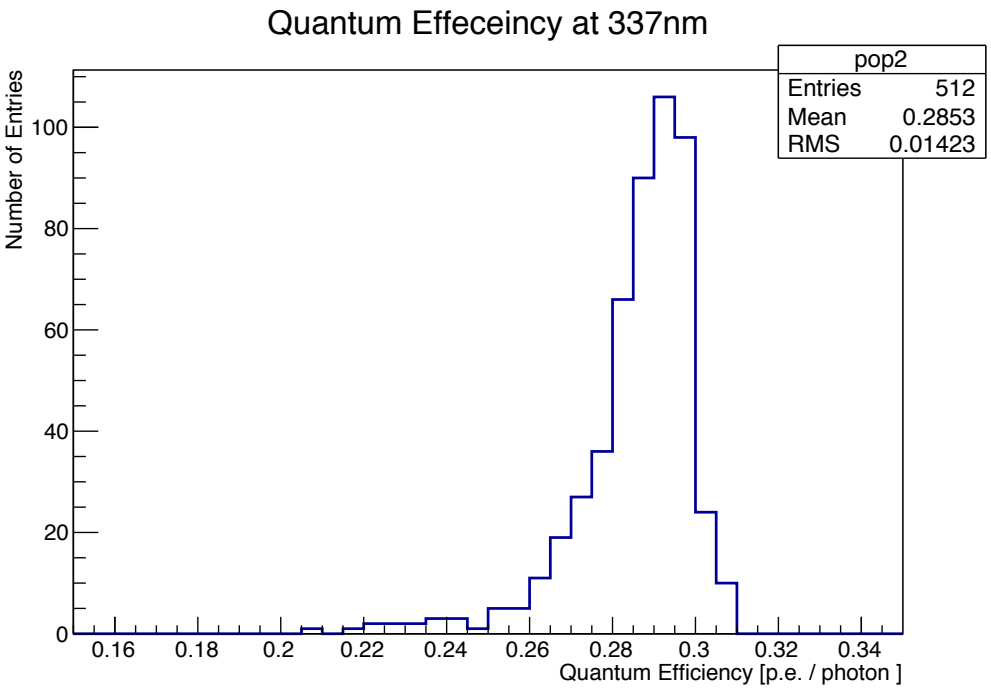

Figure 5.13: PMT QE Population B Distribution. This plot show the distribution of QE for tubes in cameras 16 and 17. This distribution has a mean of 0.285.

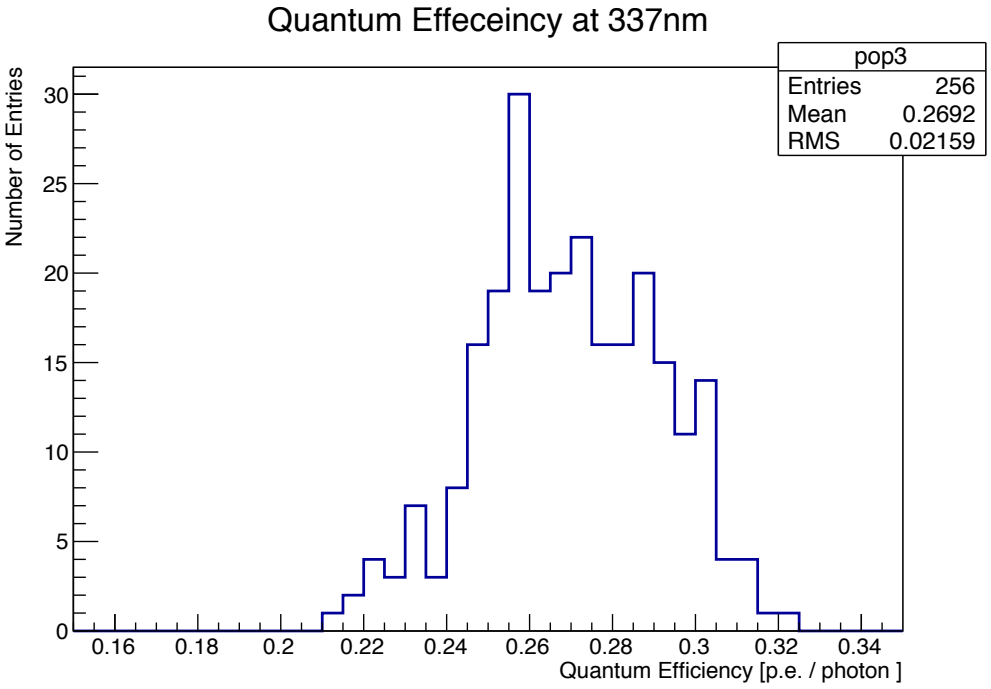

Figure 5.14: PMT QE Population C Distribution. This plot show the distribution of QE for tubes in cameras 21. This distribution has a mean of 0.269 but has a substantially larger spread than the other two camera QE populations.

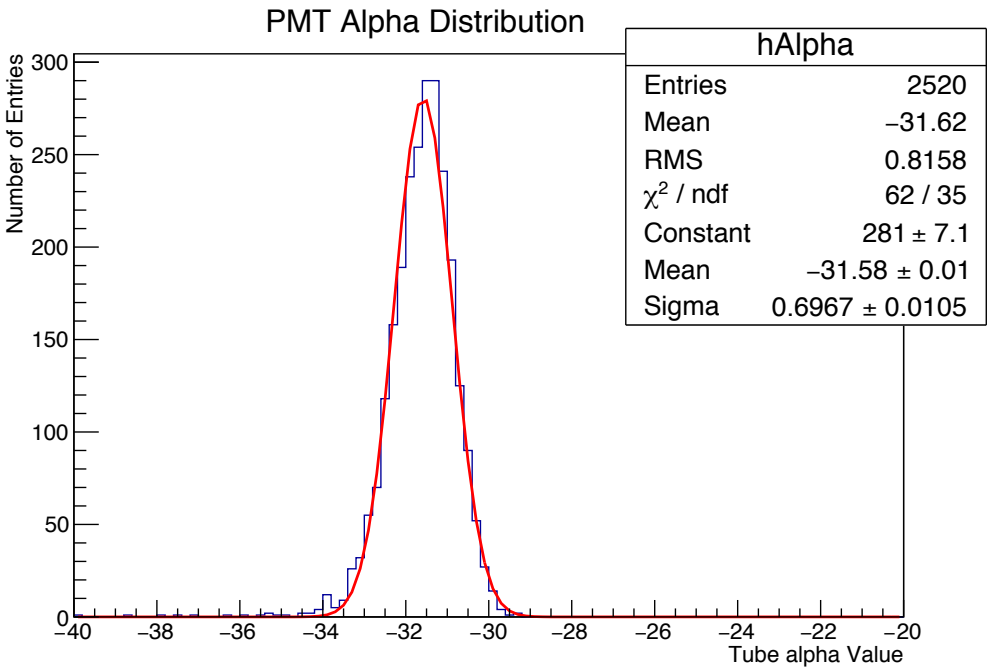

(a) Measured PMT ALPHA Values

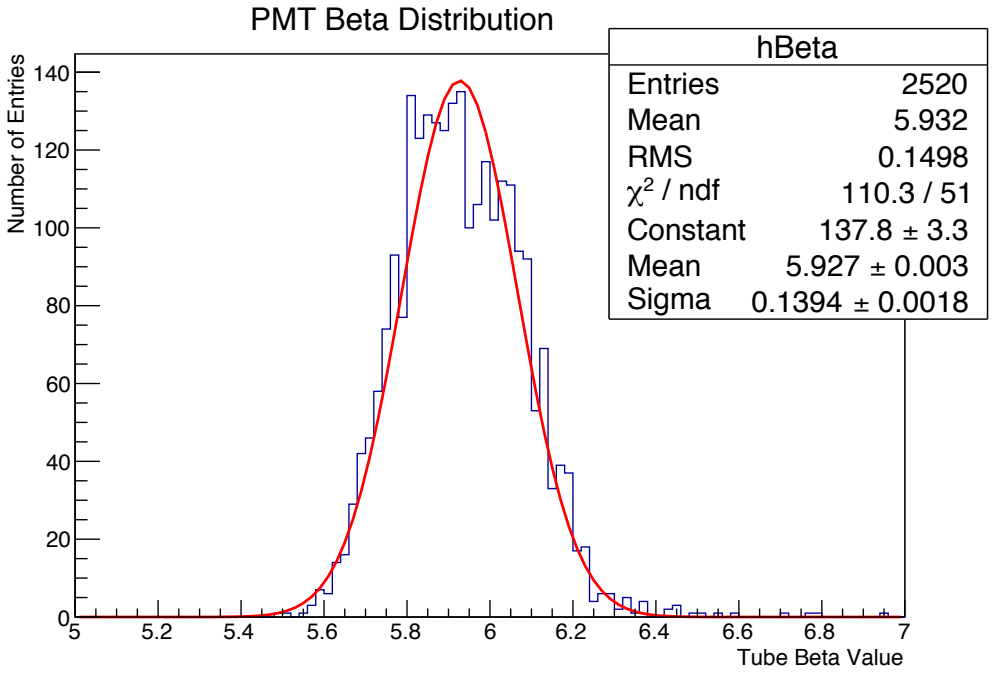

(b) Measured PMT BETA Values

Figure 5.15: TALE PMT α and β values. This is a distribution of all measured α and β values for the PMTs used in the TALE detector.

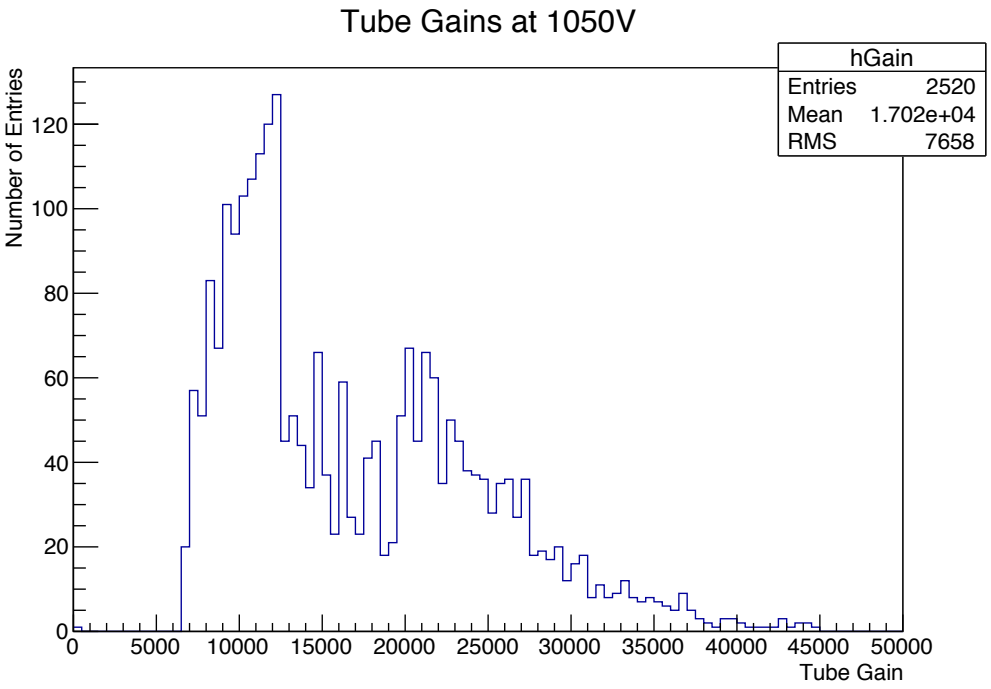

Figure 5.16: TALE PMT Gain. Unlike the QE_{337} measurements, the gains do not separate into distinct populations based on camera number.

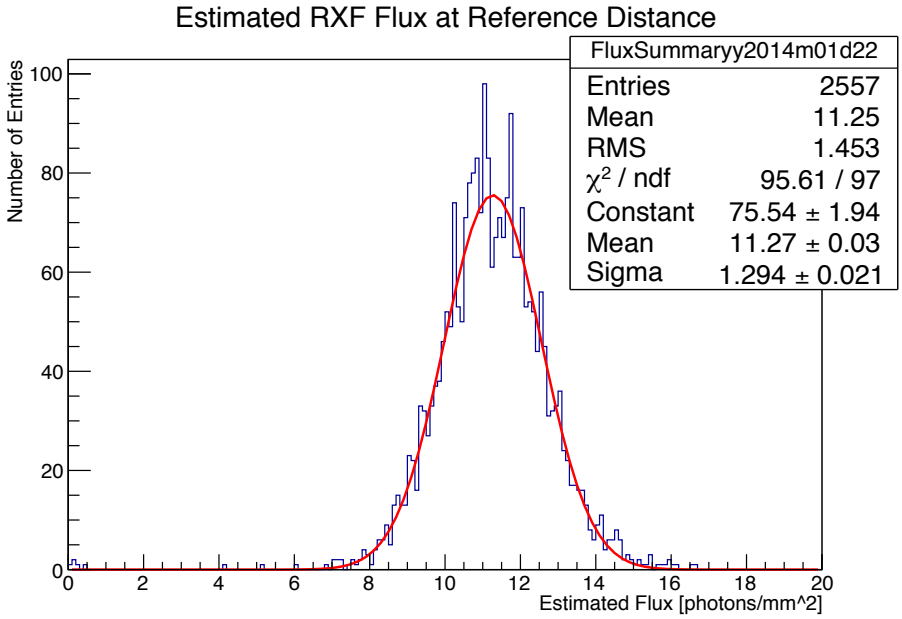

Figure 5.17: TALE Measurement of RXF Photon Flux. This plot show a histogram of the estimated photon flux determined by each PMT in the TALE detector during an RXF calibration run. The width of the distribution is due to the use of average values for tube gain, Effective Area, and Quantum Efficiency (corrected to 355nm). However, the measure of importance is the mean and the uncertainty of the mean (11.25 ± 0.03).

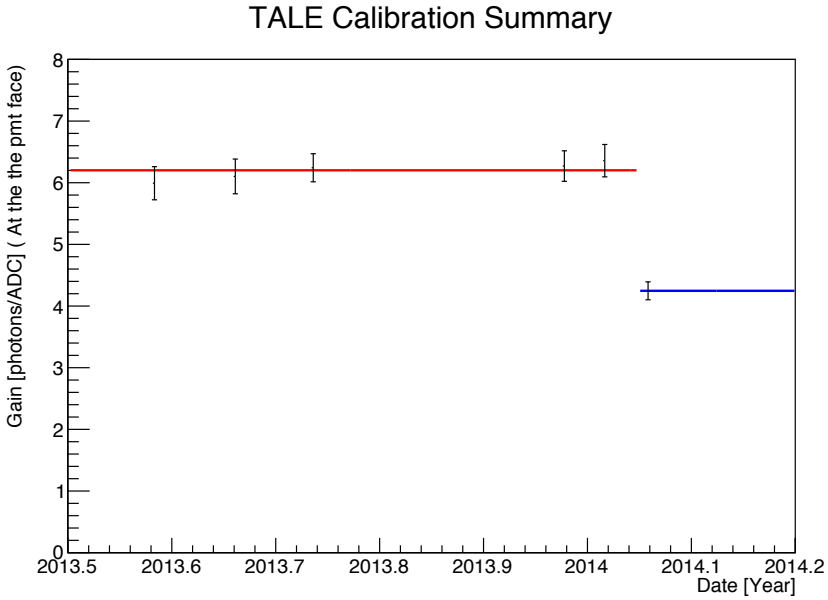

Figure 5.18: TALE Calibration Epochs. This plot illustrates the two different calibration epochs of TALE detector. Each data point represents the calculates gain in terms of Photons (not NPE) per ADC from an RXF calibration. After Jan 2014, the nominal gain was set to 1 ADC/NPE in order to increase detector sensitivity and timing resolution.

Figure 5.19: UVLED Module. This image shows an example of a UVLED module that is installed in the center-post of all TALE telescope mirrors. The module is inside a temperature-controlled housing.

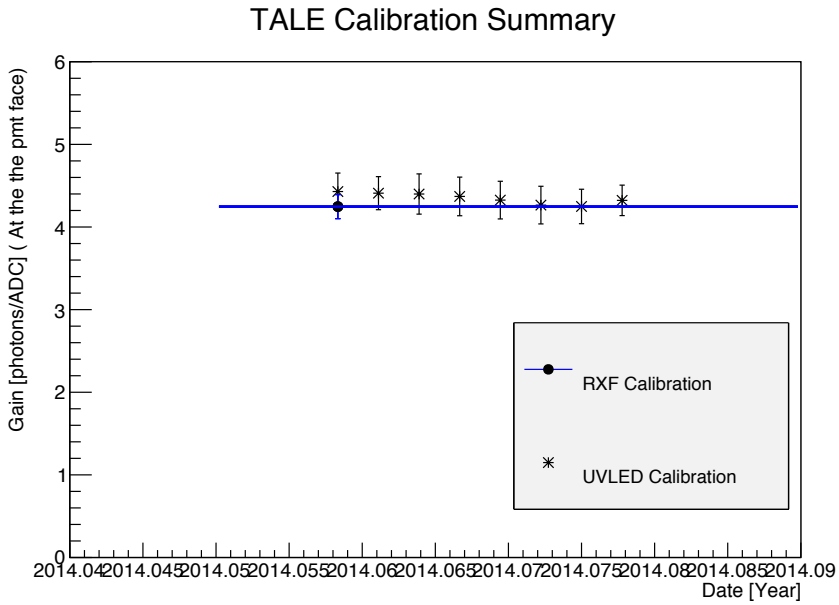

Figure 5.20: UVLED Calibration Results. This graph shows the calculated average detector gain in photons per ADC as calculated by the UVLED modules in a week following an RXF calibration. As can be seen, the calibration is stable within statistical errors over the course of the week and agrees with the calculated calibration of the RXF. The RXF calibration value is shown as a solid line and was taken on the same night as the first UVLED record.

CHAPTER 6

MONTE CARLO GENERATION

Understanding the acceptance and aperture of the TALE detector depends on both accurate simulation of air shows and reliable modeling of the TALE detector. The TALE Monte Carlo involves simulating cosmic ray air showers, modeling the light production from the showers, ray tracing the light to the detector, and simulating the detector response.

6.1 Air Shower Simulation

Air showers are simulated using the CORSIKA air shower generator and the QGSJET II-3 hadronic model simulator [74]. An example of an air shower generated using this model can be seen in Figure 6.1.

Ideally, every particle would be simulated and tracked by CORSIKA. However, the large number of particles produced in cosmic ray air showers makes such simulations impractical, both in terms of computation time and file size. Accordingly, a thinning method is used whereby the number of particles tracked is reduced. This is accomplished by taking all particles produces in an interaction step that fall below a fraction of the initial particle energy (know as the thinning threshold, ϵ_{th}) and only following one of them while discarding the rest. Energy is conserved by giving the surviving particle a weight according to

$$w_i = \frac{\sum_j E_j}{E_i}, \tag{6.1}$$

where w_i is the weight, E_i is the energy of the surviving particle, and E_j is the energy of the j-th particle that has fallen below ϵ_{th}.

The TALE Monte Carlo (MC) includes two libraries of CORSIKA air showers generated with a 10^{-5} thinning level. One library contains simulated proton air showers and the other simulated iron air showers. Each library contains approximately 18,000 simulated air showers at a variety of energies and zenith angles.

Monte Carlo events are generated using the program mc2k12_main in the UTAFD software package. When generating Monte Carlo simulations of events, events from the

shower library are sampled and "thrown" around the detector. This is accomplished by taking a shower from the CORSIKA libraries and supplying it with uniformly random values for azimuth, zenith, and distance from the detector according to Table 6.1. Light generated as the shower passes through the atmosphere is then simulated and propagated to the TALE Detector.

The TALE MC was generated according to an E^{-3} power law. Figures 6.2a and 6.2b show the number of thrown showers at each energy bin.

6.2 Simulated Light Generation

The types of light that can be observed from a cosmic ray air shower fall into two categories: produced light and scattered light. Scintillation and Cherenkov light are directly produced by the passage of charged air shower particles through the atmosphere. These produced light types can be scattered off of molecular gases (Rayleigh Scattering) or aerosols. The contribution of these four constituent light categories is determined when reconstructing the detector response to an air shower.

6.2.1 Scintillation Light Production

Scintillation light is produced by a cosmic ray air shower when the charged particles in the shower excite the molecular nitrogen in the atmosphere. The excited nitrogen atoms relax and emit UV photons through the first negative and second positive systems of diatomic nitrogen.

The scintillation light producing mechanism results in the emission of approximately 4 photons per meter per charged particle. It is this scintillation light that the fluorescence detectors are designed to measure.

This allows the amount of scintillation light emitted to be related to the number of charged particles to be normalized by a fluorescence yield at a given wavelength.

$$\frac{d^2N_\gamma}{dld\Omega} = \frac{YN_e}{4\pi}, \tag{6.2}$$

where N_γ is the number of photons, Y is the fluorescence yield, and N_e is the number of charged particles.

6.2.2 Cherenkov Light Production

In addition to the scintillation light produced by the charged particles moving through the atmosphere, Cherenkov light is also generated. Cherenkov light is generated when particles in the airshower move faster than the speed of light in the same medium. This

generates a coherent wavefront of light according to Equation 1.15, which is simulated in the mc2k12_main routines.

Cherenkov light has historically been considered a contamination to the scintillation signal from cosmic ray air showers and events with large Cherenkov contributions were previously discarded. We have since learned to reconstruct such events and they make a valuable contribution to our measurements. The high elevation angles observed by the TALE detector make accurately modeling of this light contribution important.

6.2.3 Scattered Light

Scattered light depends on the condition of the atmosphere at the time of observation. Rayleigh scattering is a fundamental condition of the atmosphere but varies with the atmospheric density profile. The aerosol scattering is typically limited to the bottom 10km of the atmosphere, but varies greatly night to night.

Rayleigh scattering is the phenomenon that gives rise to a blue sky. The mechanism for this is detailed in most graduate textbooks on Electromagnetism such as J.D. Jackson's Classical Electrodynamics [75]. For this case, it is assumed that the size of the scatter is much smaller than the wavelength of the light. In the detector simulation, the following relationship determines the number of photons scattered per unit length:

$$\frac{N_\gamma}{dl} = -\rho \frac{N_\gamma}{x_m} (\frac{400}{\lambda})^4. \tag{6.3}$$

In this case, ρ is the atmospheric density and x_m is the mean free path for scattering at 400nm. Additionally, λ is the wavelength of the light. For this analysis, $x_m = 2970 \frac{g}{cm^2}$ is assumed.

The angular dependence of this distribution varies according to:

$$\frac{d^2 N_\gamma}{dl d\Omega} = \frac{dN_\gamma}{dl} \frac{3}{16\pi} (1 + cos^2\theta), \tag{6.4}$$

where $\frac{dN_\gamma}{dl}$ is the number of scattered photons per unit length, Ω is the solid angle of scattered events, and θ is the scattering angle.

As is expected from parameterizing the Rayleigh scattering process as having a mean free path, the transmission of photons through a given atmospheric depth is given by

$$T_{ray} = \exp(-\frac{\Delta x}{x_m} (\frac{400}{\lambda})^4) \tag{6.5}$$

When the size of the scattering object is equivalent to or larger than the wavelength of light, the simple Rayleigh scattering solutions no longer apply. Scattering now depends on

the shape of the scatters and their distribution. This scattering is parameterized according to

$$\frac{d^2N_\gamma}{dld\Omega} = \frac{N_\gamma}{L_M(\lambda)}\rho_a(h) \times \phi(\theta), \tag{6.6}$$

where $L_M(\lambda)$ is the horizontal extinction length as a function of wavelength, $\rho_a(h)$ is the reduced aerosol density as a function of height, and $\phi(\theta)$ is the scattering phase function [32].

6.2.4 Night Sky Background

The night sky background is an important parameter in the generation of MC data. The simulated background noise alters the acceptance of the detector by increasing the likelihood that events which would normally not trigger the detector do trigger it. This effect is known as noise assisted triggering. Additionally, the χ^2/dof for reconstructed profiles is increased as the night sky background increases.

The TALE MC was generated assuming a Poission noise of 3 photo-electrons in each 100ns digitization. This value was confirmed by analyzing the detector snapshot data. An example of the tube variances reported by snapshots during a noise closed data file are shown in Figure 6.3. The door closed tube variance is a measure of the inherent noise of the tubes.

Alternatively, the results of the tube variance when the door are open and the detector is exposed to the night sky are shown in Figure 6.4. The difference in the mean of the distributions shown in Figures 6.3 and 6.4 is a measure of the night sky background light. The measured night sky background of 3.2 ADC/bin is in agreement with the Monte Carlo assumption of 3 PE/bin.

Table 6.1: TALE MC Parameters. This table details the parameters determining how MC events were thrown around the TALE detector.

MC Parameter	**Value**	**Notes**
γ	3	Power Law Index
minEnergy	1e16	Minimum Energy of Simulated Event
maxEnergy	1e19	Maximum Energy of Simulated Event
rpMin	100	Minimum Impact Parameter of Air Shower [meters]
rpMax	20000	Maximum Impact Parameter of Air Shower [meters]
thesh1	0	Minimum Zenith Angle of Air Shower [deg]
thesh2	70	Maximum Zenith Angle of Air Shower [deg]
phish1	-180	Minimum Azimuth Angle of Air Shower [deg]
phish2	180	Maximum Azimuth Angle of Air Shower [deg]

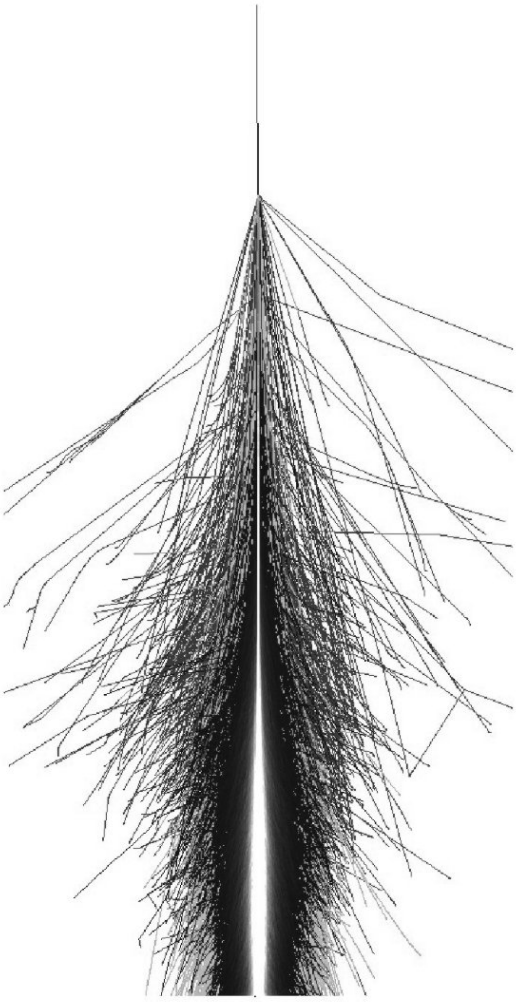

Figure 6.1: Example Iron MC shower. This simulated event is a $10^{15}eV$ iron shower generated using CORSIKA as the air shower simulator and QGSJET II-3 for the hadronic interaction model.

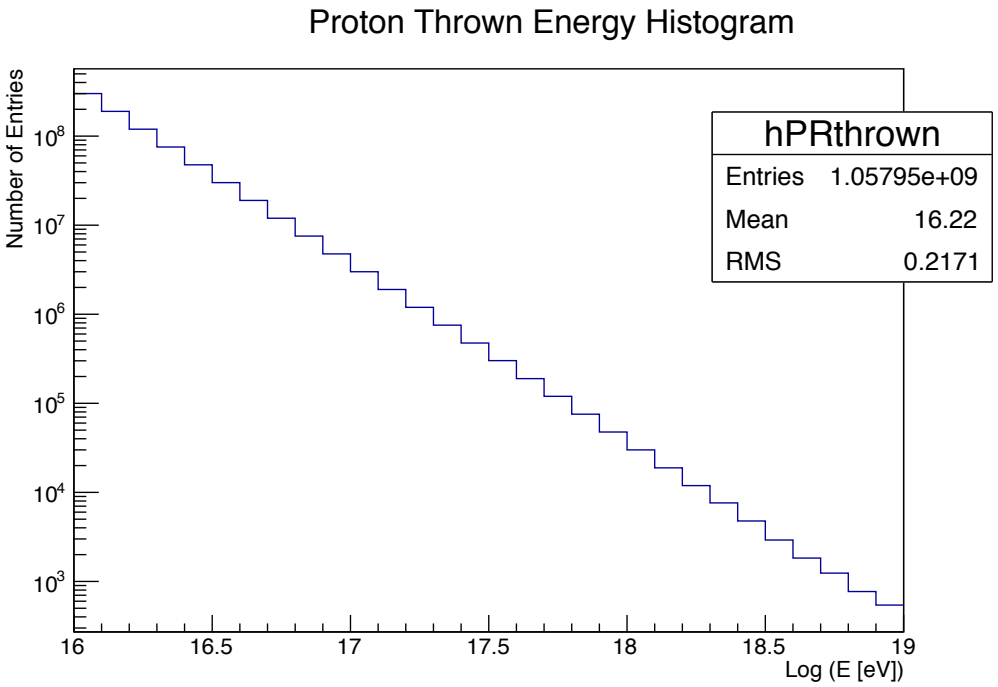

(a) Proton MC Thrown Energies

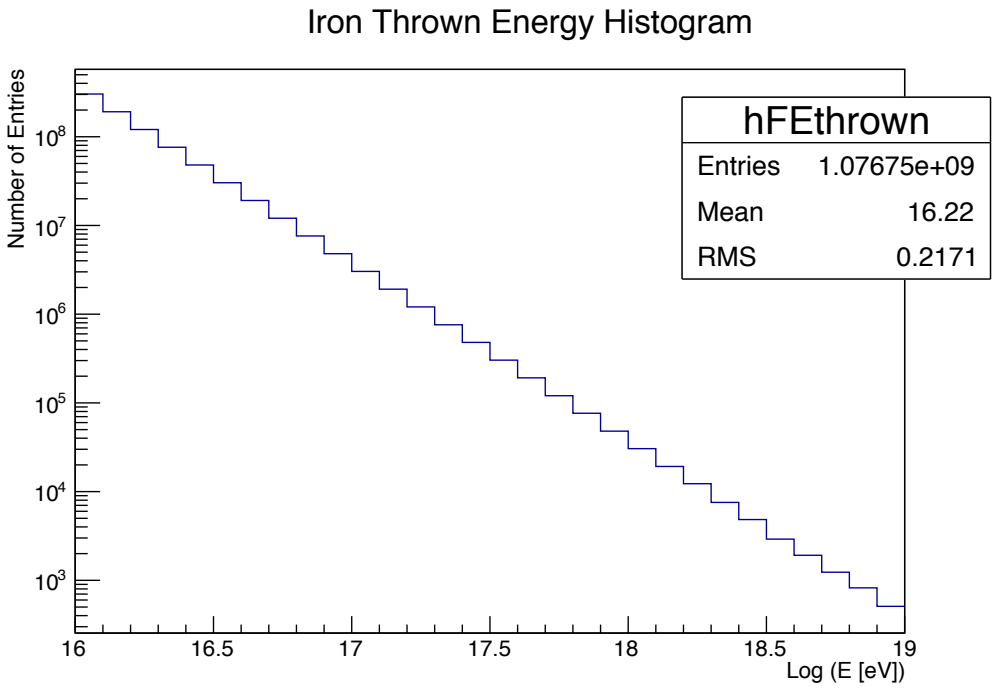

(b) Iron MC Thrown Energies

Figure 6.2: Thrown Energy Distributions. This plot shows the number of events thrown for each energy bin for the proton and iron Monte Carlo data sets.

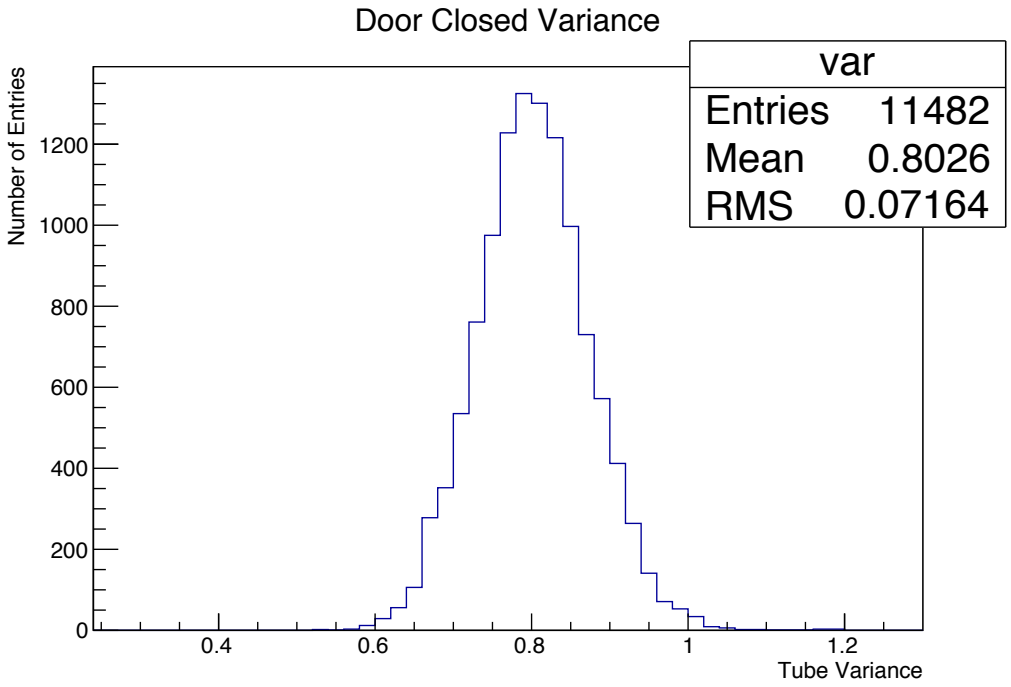

Figure 6.3: Tube Signal Variance. This histogram shows the TALE PMT channel variance, in ADC counts, reported from snapshots taken during the y2014m12d18 noise closed data part.

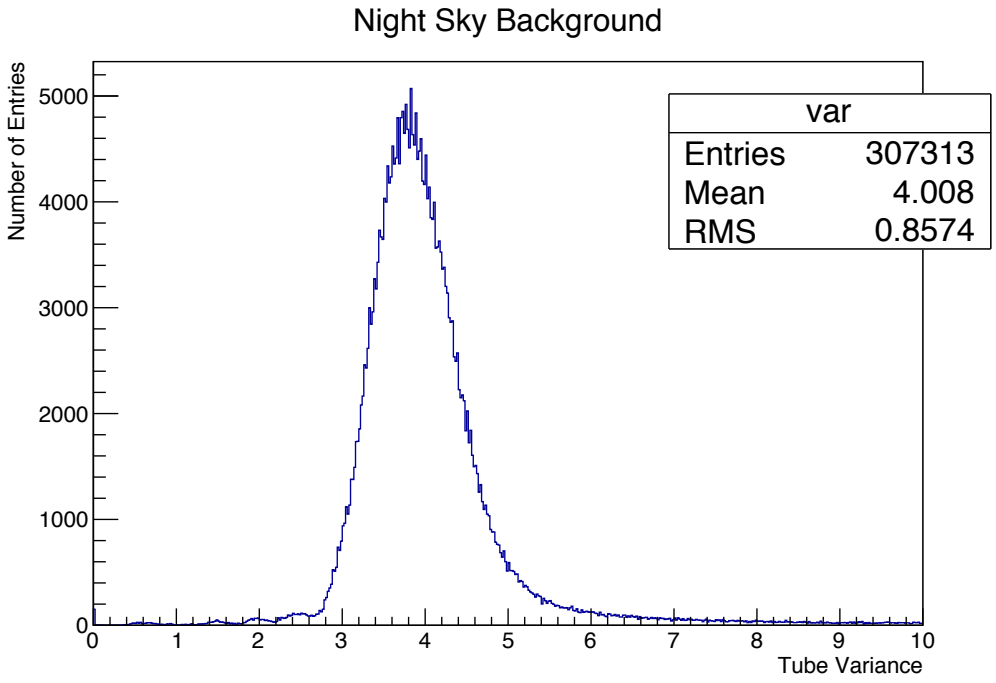

Figure 6.4: Night Sky Tube Signal Variance. This histogram shows the TALE PMT channel variance, in ADC counts, reported from snapshots taken during the y2015m09d20 night sky data part. The difference in the variance from the doors being opened and closed reflects the night sky background noise.

CHAPTER 7

TALE EVENT FORMATION

The raw TALE data are a stream of data packets from each camera that are parsed and formed into events. This chapter details the data files, packet format, and structures used to store event data. This chapter is written in part as documentation for the benefit of future collaborators.

7.1 Raw Data Files and Packets

There are seven different file types created during normal nightly operation of the TALE detector, which are detailed in Table 7.1. Five of the data types store the binary data of the telescopes, timing system, and Link Modules during different stages of the detector operation. The final two file types are a XML log file and a MDSUM file. The log file includes the opening and closing times of data parts, the weather during the night, the times doors are opened and closed, and any other details the detector operator logs. The MD5SSUM file is used to confirm files are not corrupted during transfer.

Every night sky data file contains about 20 minutes of night sky data. At 20 minutes after the start of the data part, the file for the part is closed and a new part is opened. This 20-minute duration limits the size of any individual data part. Night Sky data parts are taken with the doors open and are the files where data from cosmic ray air showers are stored.

When the TALE detectors boot, a series of DAC settings are made and the ADC readout is checked. One *testFADC* file is created for each camera with the results of this electronics test. They are used for checking proper operation of the gain DAC, pedestal DAC, and ADC for each of the channels. Channels that have a variance of greater than 0.8 ADC count are flagged as problem channels and automatically noted in the nightly log.

Additionally, UVLED files are created for each of the telescopes before the doors are opened and after the doors are closed. During these parts, a UVLED mounted in the center

of the mirror illuminates the camera. The flash-to-flash variation in the PMT response is used to determine the gain of the PMTs and track the detector response over time.

After the UVLED calibration is collected, the trigger is tested for all of the cameras. Following this trigger test, a data part is collected with the doors closed and all normal trigger conditions enabled. The dark noise trigger rate can be determined from these files. Additionally, the muon trigger rate can also be measured with these "noise" parts. Given the correct geometry, an atmospheric muon can pass through the dynodes of multiple PMTs in a camera and generate a track that will trigger the detector.

The raw data format is determined by the packet structure formed by the HOST and FEADC DSPs. Due to the 16-bit architecture of the DSP56166 used on the FEADC boards, the maximum size of an individual member (called a "word") of a data packet is 16-bits, despite the fact that the HOST DSP is a 32-bit device. Keeping the individual packet member size to a universal value simplifies the overall communication structure. Figure 7.1 shows a screenshot of the raw data stream written to disk during Night Sky data collection. Every packet's first word is called the header and is paired with a matching word at the end of the packet called the tail. The header and tail are offset by a number of words equal to the AND of the header with $0x3F$. An example of the header-tail offset for the first packet in Figure 7.1 is detailed in Figure 7.2. The header-tail packet convention allows the integrity of the data steam to be monitored during detector operation. All ten TALE telescopes transmit packets to the TALE PC simultaneously. The header-tail convention allows the central data acquisition (DAQ) system on the TALPC to ensure entire packets are written in a continuous block to disk and do not have their words interleaved with words of other packets from different telescopes. An example of the asynchronous nature of packets from different telescopes being stored onto the TALE PC hard disk is diagramed in Figure 7.3. The details of the packets depend on whether the packet is a *command packet*, *message packet*, or *data packet*.

7.1.1 Command Packets

Command packets are sent from the TALE Link Modules to the Host/Trigger DSPs or FADC DSPs in order to control the the detector. The headers of command packets contain both the number of words that will follow in the packet and the identity of the command that is to be executed. Bits 0-4 of the header contain the number of words that are to follow in the packet. Bits 8-13 of the header provide the command ID for the command that is being sent. Bits 5, 6, and 7 in the header are used to indicate that the DSPs should execute a nonstandard version of a given command. A summary of the various commands for the

HOST/Trigger DSPs and FADC DSPs are given in Tables 7.2 and 7.3.

Any command being sent to the Host/Trigger DSP must include a route count. This word tells the Host/Trigger whether the command packet is meant for the HOST or if it should be forwarded to the dsp56166 on the FADC boards. A route count of 0 indicates that the command is a Host/Trigger command. A route count of 1 indicates that the command is intended for the FADC modules. In the event that the command is for the FADCs, then the next word in the packet needs to be a select word to determine which of the FADC modules should handle the packet. Each bit in the select word represents a single FADC board. The remainder of the packet is specific to each type of command. An illustrative example of a command packet is described in Figure 7.4.

7.1.2 Message Packets

Message packets are sent up from either the Trigger/Host or the FADC boards in order to indicate the state of a particular component, or respond to command instructions. The type of message is determined by the message ID encoded by the second word of the message packet. A diagram of a message packet is shown in Figure 7.5. The IDs are defined in the assembly code files *message.inc* and *hmessage.inc*. The second word of the message packet includes the message ID in bits 8-13 and a mirror identifier in bits 0-5. The message packet details have been documented on the Telescope Array Wiki [76].

7.1.3 Data Packets

A cosmic ray event is constructed from a number of different types of "data" packets. The first of these is a trigger packet that stores the state of the 14 horizontal and 14 vertical trigger bits. Each bit encodes the state of a 3-fold coincidence of rows and columns. The trigger packet also contains the STORE start time and duration as well as a summary word (used in determining if an event is read out documented in Table 7.4), and the 10MHz system clock count of the trigger time. Trigger packets can be passed to nearest neighbors (in terms of sky pointing directions) in order to generate a STORE in that telescope.

After a trigger packet is broadcast, a *Confirm Packet* will follow it. This packet reflects if the event that generated the trigger satisfies a second level of criteria to be considered a valid event for readout. This second level of criteria is determined by *moments* and *clusters* routines of the HOST/Trigger DSP, which calculate the shape of the event and the time spread. The results of this event processing are reported in a *scan diagnostic* packet for events that pass cut criteria. The requirement of passing the *moments* and *clusters* routines was removed in January 2015 in order to allow readout of events that had a "circular" shape

characteristic of Cherenkov blasts. Previously, these events were eliminated since airplanes also tend to present circular events. The *scan diagnostic* packet includes an event summary with the spatial first and second moments, the number of tubes with reported hits, and the time spread.

Following the *scan diagnostic* packet for an event, there are a number of *scan hit* and *data* packets. For each of the sixteen FADC boards, there will be one *scan hit* packet followed by a *data* packet for each triggered channel. The *scan hit* packet contains information about the times and integrated signals for each channels found by the FEADC scan routines. Each of the following FEADC data packets contain the one hundred sample 10 μs waveforms for each channel that registered a HIT from the scan routine.

Finally, an *end event* packet is broadcast to indicate that the camera is done reading out information on a given event. Figure 7.1 shows the trigger, confirm, scan diagnostic, and initial waveform packets.

7.1.4 Clock Packets

The clock is maintained in the data steam with a series of *GPS packets* and *PPS packets*. The GPS packets are generated by the TALE Central Timing device and include information about the GPS location, time, and uncertainty in the GPS engine. The PPS packets are sent out once every GPS second by all of the Link Modules and include the GPS time from clock enable along with the Link 10MHz clock cycle count. These packets are entered into the data stream and are used to associate a given 10 MHz clock count to a specific GPS time. The 10 MHz clock completes approximately 9999995 cycles per second. The slow drift of the 10MHz clock (due to temperature) is accounted for during event formation by determining the second by second clock rate according to

$$T_{event} = GPS_{ppsPrior} + \frac{CC_{confirm} - CC_{ppsPrior}}{CC_{ppsAfter} - CC_{ppsPrior}}, \tag{7.1}$$

where T_{event} is the time of the event in GPS seconds, $GPS_{ppsPrior}$ is the GPS time from the prior PPS packet, $CC_{confirm}$ is the clock count of the confirm packet, $CC_{ppsPrior}$ is the clock count of the prior PPS packet, and $CC_{ppsAfter}$ is the clock count of the following PPS packet.

7.2 DST Data Structure

The Data Storage Template (DST) system utilized by the Telescope Array Experiment is a compact event storage system that uses a collection of *banks* in order to store event information and add the results of analysis to an event. DST banks are similar to a C

structure with methods to read and write to binary files. When processing TALE data, the following banks are used [32].

FRAW1 contains the raw data for an event. This includes the individual channel waveforms, event timing information, and mirror numbers.

FPHO1 contains the integrated pedestal subtracted signals for each channel and the calculated time for the signal.

FSCN1 contains information about the scan filter used to locate the pulses in a waveform. This information includes the pedestal, pedestal rms, amplitude, NPE, time, and duration for each of the scanned pulses in an event.

STPS2 stores the information about the Rayleigh vector used for the Rayleigh filter. This includes the probability that the event is randomly generated, the magnitude of the Rayleigh vector, the time spread of the event, and the direction of the Rayleigh vector.

STPLN contains the plane fit results for an event. This includes a designation for each tube determining if it is consistent in time and space with the rest of the event. It also gives the best fit Shower - Detector (SD) Plane for the event.

HCTIM contains the geometric fit results to the timing fit and the PRFC fits.

PRFC stores the reconstructed shower profile parameters and the total reconstructed energy of the event.

The FRAW1, FPHO1, and FSCN1 banks are all filled during the event formation stage of the analysis. The remainder of the banks are formed during subsequent analysis stages.

7.3 Pass 0: Event Formation and Time Matching

When the TALE data stream is written to disk, checks are performed to ensure that words from separate packets are not interleaved. However, there is no guarantee that packets from separate mirror events are not interleaved. This requires that data parts are to be scanned through and all of the event information before the FRAW1 bank is filled from the parsed stream during analysis. At the same time, the GPS clock time for each event is appropriately calculated and stored for each event. A program called *tlfdp0* handles this event formation.. This program is primarily authored and maintained by Dr. Dmitri Ivanov in consultation with Zachary Zundel and Jeremy Smith. As additional functionality is added to the TALE detector, *tlfdp0* is updated to include new data (such as snapshot data) to the event banks.

The *tlfdp0* program also combines individual camera events into multi-mirror events if they match in time. The default time matching window requires that the trigger times for

different cameras be within 100μs to be considered as part of the same event.

After events have the FRAW1 banks filled and are matched in time, the *tlfdp0* program calculates the information needed to fill the FPHO1 and FSCN1 banks based on the results of a software SCAN routine that simulates the SCAN routine that is on the FEADC boards.

Table 7.1: TALE Raw Data File Types. The raw data stream from the TALE detector is stored in binary data file labeled in the yYYYYmMMdDDpPPP.EXTENSION convention. In this convention, the yYYYYmMMdDD portion designates the day and the pPPP part of the title gives the part number.

File Type	**File Name Extension**	**Details**
MD5SUM File	.MD5SUM	The MD5SUM file for the nights files used to ensure no errors during data transfer
Log File	.log	The XML log file created by TALERUN and the detector operator
UVLED	pPPP.mMIRuvled.tale	A UVLED data file for the camera MIR
Test FADC	pPPP.mMIRtestFADC.tale	The File that contains the FADC test data performed to check the readout of all channels.
Noise Closed	pPPP.noiseclosed.tale	Triggers enabled and data taken with the doors closed.
Test FADC	pPPP.noiseclosed.tale	Triggers enabled and data taken with the doors closed.
Night Sky data	pPPP.data.tale	Triggers Enabled with garage doors opened.

Table 7.2: TALE Host Command Packets. This table documents the most commonly used commands that are issued to the HOST/Trigger DSPs.

Command Name	**Hex ID**	**Details**
fload	00	Send assembled program memory to the FADCs
config	01	Modify the X: or P: memory of the DSPs
strtinit	02	Clear all clocks and prepare for data collection
confirm	03	Confirmation of broadcast trigger
testtrig	05	Write test waveform into FADC memory and read it out
testsl	08	Used to run an FADC test
stopcmd	09	Disable triggers
enable	0A	Enable Triggers
storeoff	10	Generate a STORE
clkread	1C	Read out the DSP clock time
tstmode	1D	New Command implemented to toggle the readout conditions of the Host/Trigger boards

Table 7.3: TALE FADC Command Packets. This table documents the most commonly used commands that are issued to the FADC DSPs.

Command Name	**Hex ID**	**Details**
config	01	Modify the X: or P: memory of the DSPs
reset	02	Used to restart the FADC board
scan	03	Scan Memory for Waveforms
readm2	04	Que up waveform packets to be read out
initm1	05	Initializes the M1 memory
dacset	11	Load the DAC setting stored in X memory to the DACs
read_hit	12	Special readout where only Hit Summary information is read (NO Waveforms)
servo	13	Automatically adjust individual Row/Column trigger threshold to maintain constant rate (NOT USED CURRENTLY)

Table 7.4: Trigger Summary Word.

Word Bits	Detail
9-12	Number of set 3 fold COLUMN bits
5-8	Number of set 3 fold ROW bits
bit 4	$Nrow >= 3$ AND $Ncol >= 3$
bit 3	$Nrow >= 2$ AND $Ncol >= 2$
bit2	$Nrow >= 3$ AND $Ncol >= 3$
bit 1	$Nrow >= 1$ AND $Ncol >= 1$
bit 0	$Nrow >= 2$ AND $Ncol >= 2$

```
Trigger! [8609 1713 0780 003C 202E 01B8 089F 72C1 0000 8609]
$TrigScanDiag/m19 [850F 8F13 1713 0002 1312 0000 0057 008D 0
0A3 0056 05E9 0000 0000 0137 010D 850F]
Confirm! [C309 6247 1713 4493 202E 01B8 089F 72C1 0000 C309]
ReadM2+ [0405 1713 0130 4493 85C9 0405]
ReadM2+ [0439 1713 0100 4596 0064 1212 1112 1212 1111 1111 1
112 1111 1011 1112 1214 1415 1415 1415 1516 1718 1718 1819 1
919 191A 1A1B 1B1B 1B1B 1A1A 1919 1919 1819 1919 1818 1616 1
413 1212 1214 1617 1819 1818 1716 1414 1313 1313 1313 1313 1
212 1110 1010 0F0F 0F10 0F0F 0E0E 0F10 1011 181C 0013 0439]
ReadM2! [8439 1713 0120 4590 0064 1010 0F0F 0E0F 0E0E 0E0E 0
E0E 0D0E 0F10 1112 1214 1415 1414 1313 1212 1111 1112 1314 1
517 181A 1B1C 1B1B 1A1B 1B1B 1A1A 1919 1818 1716 1515 1514 1
414 1414 1312 1112 1212 1213 1315 1516 1718 1717 1616 1517 1
718 1717 1616 1515 1414 1212 1112 1314 1414 1803 0013 8439]
```

Figure 7.1: Raw Data Dump. This is a screenshot of the raw data packets recorded during operation of the TALE detector. This packet dump shows the TALE detector triggering an event followed by the results of the Scan Diagnostic and a Confirmation that the event passed the Host/Trigger board readout criteria. Waveforms for the event begin being read out for each channel that observed a signal with the ReadM2 packets.

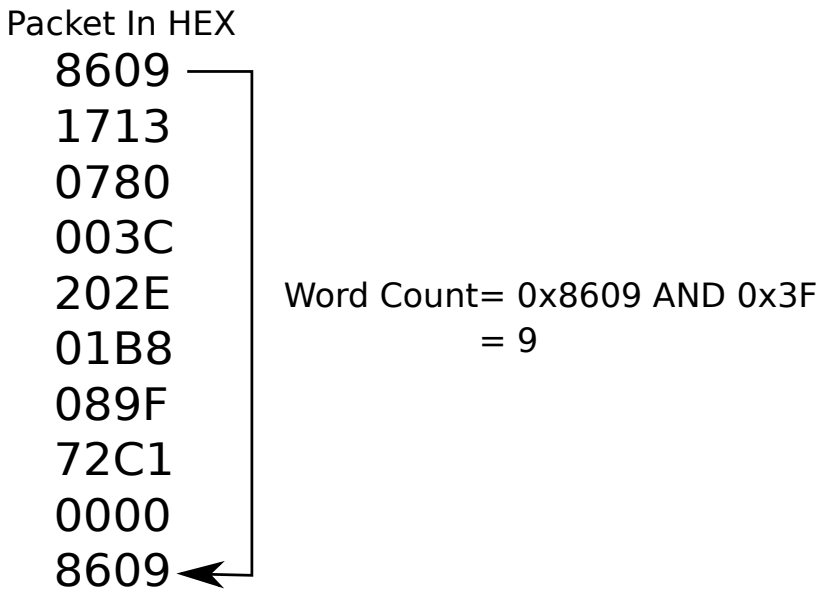

Figure 7.2: Packet Header Tail Offset. This is an example of the header-tail offset convention for packets.

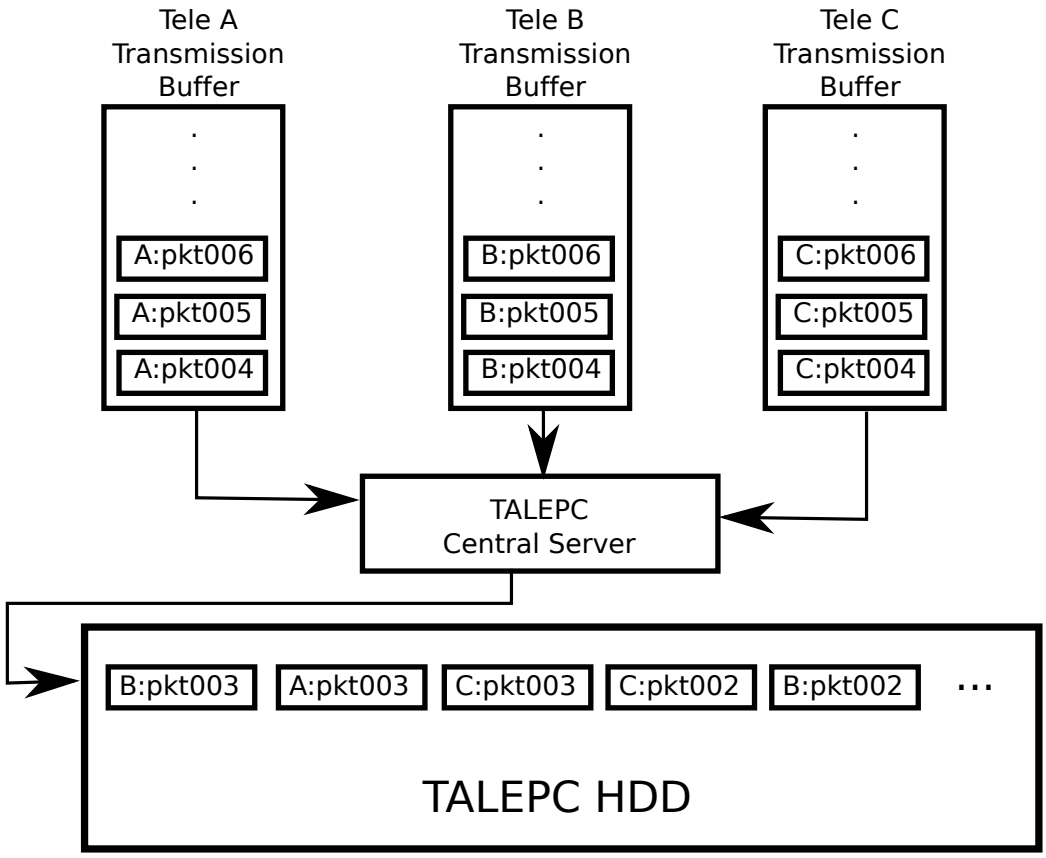

Figure 7.3: Packet Storage Diagram on TALECP. This is an example of how packet streams from different telescopes are stored onto the TALEPC disk in an asynchronous manner.

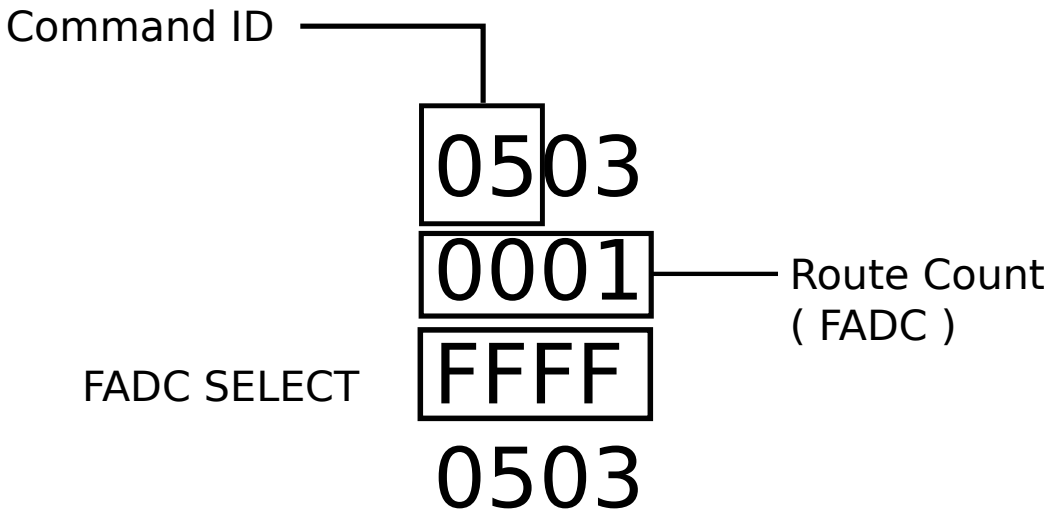

Figure 7.4: TALE Command Packet Example. This figure diagrams the init_m1 command. This command is one of the simplest commands formed but is illustrative of the structure of command packets.

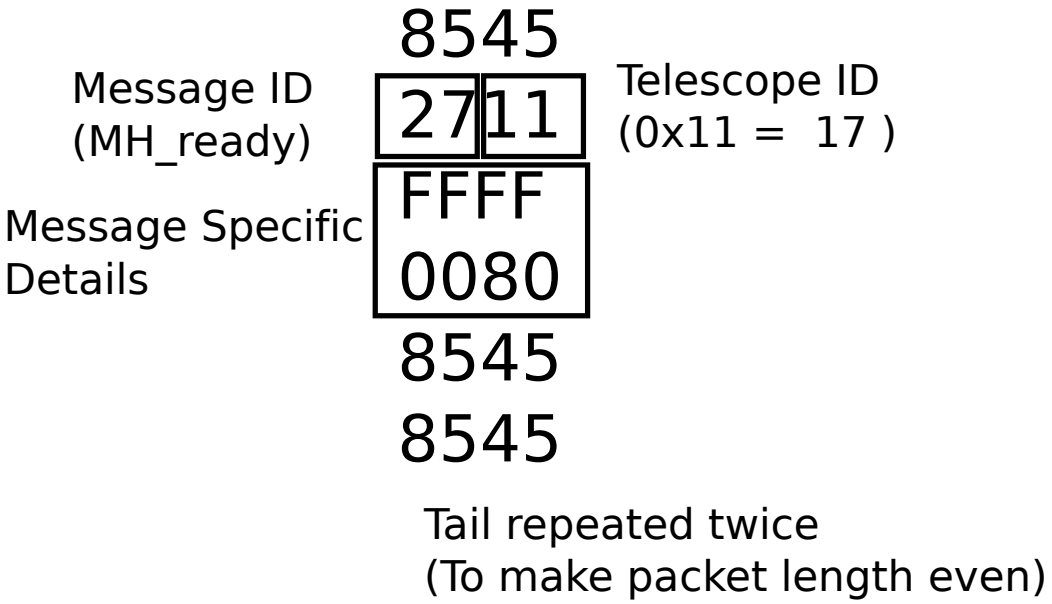

Figure 7.5: TALE Command Packet Example. This figure diagrams the Mirror Ready to Start message. This command is one of the simplest commands formed but is illustrative of the structure of command packets.

CHAPTER 8

TALE EVENT PROCESSING

Cosmic ray air showers are reconstructed using a set of software tools named UTAFD[32]. These tools have been primarily developed by Dr. Tareq Ziad AbuZayyad and have been demonstrated to provide reliable reconstruction of shower geometry, energy, and shower maximum [7] [32] [40](the specific software revision used in this analysis was rev. 828). Some additional adjustments to this revision were made in order to match the proper photometric calibration for this data epoch. The files

`UTAFD/src/mc2k12/src/generate_tale_fadc_waveform.cu`

and

`UTAFD/recon/src/rc_plug_in_fraw1_data.c`

were modified to give the tube gains the appropriate value. Specifically, the nominal RXF calibration of 1.0 ADC/NPE was scaled by a correction factor

`TMP_FIX_RXF_CALIB = 1.0 / 1.589,`

where the photometric calibration was determined by the analysis described in Section 5.1. The nominal calibration was scaled to match the actual state of the detector during the Epoch 1 data set.

Both data and Monte Carlo events are reconstructed using the exact same programs. The procedure for reconstruction is to: (1) determine the Shower Detector Plane (SDP) for the event, (2) filter out noise events using a Rayleigh filter, (3) remove laser events, (4) determine the shower geometry, (5) use inverse Monte Carlo to reconstruct the shower profile, (6) apply quality cuts to the data. The relative pass rates for each step of data processing are detailed in Table 8.1. The remainder of this chapter is dedicated to discussing the details of each of these reconstruction passes.

8.1 Plane Fit

The plane fitting is an iterative process that determines the Shower Detector Plane and also flags noise tubes. Noise tubes are tubes that are removed from the event in either space or time. A display of an event that has not undergone the plane fit process is shown in Figure 8.1a.

For every event, a shower detector plane is determined by minimizing the value of

$$\chi^2 = \sum_i \frac{(\hat{n} \cdot \hat{n_i})^2 \cdot w_i}{\sigma_i^2}. \tag{8.1}$$

In this equation $\hat{n}$ is the normal vector defined by the SDP, $\hat{n_i}$ are the individual tube pointing directions, w_i are the weights given to each tube based on their Number of Photo-Electrons (NPE), and σ_i is the uncertainty in a given tube pointing direction. In this case, the uncertainty in the tube pointing direction is set to 1°, which is the field of view of a PMT and hence the angular resolution. Once a SDP is determined, the tube event times are plotted against their angle in the SD plane as shown in Figure 8.1b.

Tubes that fired, but are not associated with a shower, are identified by fitting the Time vs. Angle in SDP distribution shown in Figure 8.1b to a simple quadratic and noting which tubes deviate more than 3σ from the curve. Outliers from the fit are removed one at a time. After a tube is removed, a new SD plane fit and quadratic fit is performed. This iterative process continues until all of the outliers are removed. This information is stored and referenced for later processing. The final result of this process is shown in Figure 8.2a where the bad tubes have been removed and the SD plane is drawn as a line.

A plane is determined if the fit passes all of the criteria detailed in Table 8.2. Events that have a defined plane are advanced to the next level of processing.

8.2 Rayleigh Filter

The Rayleigh filter is used to remove non-track-like events that trigger the detector such as fluctuations of the night sky background. The filter determines the probability that a given event is randomly generated. For each event, a Rayleigh vector is calculated by drawing a unit vector in the plane of the camera from every tube to all adjacent tubes with a later firing time and summing all of the vectors. The probability density function of the length of a random Rayleigh vector $\vec{r}$ being generated by noise is given by

$$p(r) = \frac{r}{\sigma^2} \exp(\frac{-r^2}{2\sigma^2}), \tag{8.2}$$

where r is the magnitude of the Rayleigh vector in units of PMT spacing, N is the number of random steps, and $\sigma^2 = \frac{N}{2}$. From this formula, we determine the probability that a Rayleigh vector of length R can be generated from a random walk of N steps, as given in

$$Prob(r > R) = \int_R^\infty p(r)dr = \exp(\frac{-R^2}{2\sigma^2}). \tag{8.3}$$

An example of an event that fails to pass the filter is shown in Figure 8.3a and can be compared to Figure 8.3b which has a long Rayleigh vector and passed the Rayleigh filter. The Rayleigh filter parameters returned for these two events are detailed in Table 8.3. Once the Rayleigh vector statistics are determined, an event passes the filter if it meets the criteria detailed in Table 8.4.

8.3 Laser Filter

During the data collection period of this analysis, the only laser that was fired in the field of view of the TALE detector was the Central Laser Facility (CLF). Although these laser events are at the edge of the detector trigger sensitivity, they are recorded by TALE and MD and they need to be removed from the cosmic ray air shower data set. An example of a CLF event seen in coincidence with both MD and TALE is shown in Figure 8.4.

Events are flagged as laser events if they satisfy the following criteria:

1. $plog > 1.0$: The event is not noise
2. $70^\circ < angle < 110^\circ$: The event is within ± 30 deg of vertical
3. The event occurred within $\pm 100ms$ of the CLF GPS firing time
4. The event occurred in TALE telescope 19.

It is understandable that the CLF is not visible at elevation angles greater than 45°. The CLF is a vertical laser located 20km away from the TALE FD. This means that above 45°, the laser is scattering at an altitude of 20km. At this altitude, the laser has already traversed the dense troposphere. Most scattered light seen by TALE is from the CLF and is scattering off of the stratosphere. It is important to note that data collected after January 2014 will also include inclined Xenon flasher events in the data set that will not be removed by this cut criterion. Further work will be needed in the analysis of later data sets in order to correctly identify and remove inclined laser events.

8.4 Geometry Fit

The geometry fit, STGEO, provides a reconstruction of the air shower axis using the PMT pointing direction and pulse arrival time. This procedure assumes that both the air shower and the photons generated by the shower travel at the speed of light, c. Accounting for the propagation of both the shower and the photons, then the arrival time of signal photons at the detector from a part of the shower at in-plane viewing angle, χ, is given by

$$t_i = t_0 + \frac{R_p}{c}\tan(\frac{\pi - \Psi - \chi_i}{2}), \tag{8.4}$$

where t_0 is the time when the shower passes the distance of closest approach, R_p is the distance of closes approach to the Shower Detector Plane (SDP), Ψ is the angle of the air shower in the SDP, and χ is the observation angle to a given track segment. The geometry is depicted in Figure 8.5.

The time vs. angle, χ, for an event is fit to Equation 8.4 in order to determine the shower geometry. This procedure works best for events with long track lengths, where the curvature of the time vs. χ data series is pronounced. An example of a time vs. χ fit for the air shower displayed in Figure 8.2 is shown in Figure 8.6.

8.5 Profile Constrained Geometry Fit

The air shower profile is reconstructed using the inverse Monte Carlo method. This method involves referencing a library of Monte Carlo air showers, calculating the detector response to these air showers, and then determining which Monte Carlo event best matched the actual observed air shower. Ideally, the shower geometry would be known well enough that the profile could be fit to the Gaisser-Hillas parameterization, Equation 8.5, explicitly.

$$N_e(x) = N_{max}(\frac{x - x_0}{x_{max} - x_0})^{\frac{(x_{max}-x_0)}{\lambda}}\exp(\frac{x_{max} - x}{\lambda}) \tag{8.5}$$

In the shower profile parameterization of Equation 8.5, x is the slant depth along the shower track. Of the remaining terms, λ is a scale constant and x_0 is the depth of first interaction. There parameters are held fixed at values of $\lambda = 70\frac{g}{cm^2}$ and $x_0 = 40\frac{g}{cm^2}$. A traditional reconstruction would use the shower geometry determined in Section 8.4 and solve for the best values of N_{max} and x_{max}. When performing a Profile Constrained Geometry Fit, the values of x_{max} are fixed to set of depths. For each of those depths, the angle in the SDP, Ψ, is allowed to vary in order to produce the best profile fit. In the case of this analysis, the fixed values of x_{max} tested were 500, 550, 600, 650,700, and 750 $\frac{g}{cm^2}$. After the best-fit value of Ψ is determined for each of these fits, the geometry is fixed to the best fit value and the profile is fit with N_{max} and x_{max} as free parameters.

In practice, many of the observed air showers have track lengths that are too small for an accurate reconstruction of the shower geometry when tube timing alone is used. The Profile Constrained Geometry Fit (PCDF) allows the shower energy for such an event to be determined. A comparison of the reconstructed energy resolution is shown with and without the PCGF in Figure 8.7. Plots for determining energy resolution report that a histogram of the natural log of the ratio of the reconstructed energy to the thrown energy can be interpreted as a fractional error on the reconstructed energy. The fractional uncertainty interpretation follows from,

$$\ln(1+\epsilon) = \epsilon - \frac{\epsilon^2}{2} + \frac{\epsilon^3}{3} + O(\epsilon^4) \approx \epsilon, \tag{8.6}$$

for small epsilon. The reconstructed profile of the example event in Section 8.4 is shown in Figure 8.8.

8.6 Postreconstruction Quality Cuts

Quality cuts are determined by examining the resulting reconstructed parameters for Monte Carlo Events and comparing them to the known thrown values. Cuts are determined in order to maximize statistics while achieving a 10% reconstructed energy resolution. The minimal static quality cuts are detailed in Table 8.5 and the effects these cuts have on the energy resolution are shown in Figure 8.9a and Figure 8.9b.

While the cuts documented in Table 8.5 can be applied to the TALE events regardless of the energy of the event, there are three cuts that change depending on shower energy. The energy dependent cuts are documented in Table 8.6. The first two are geometrical cuts on RP_{max} and Θ_{min} analogous to the static cuts in Table 8.5. The XH cut requires that the first observed depth (in g/cm^2) be lower than the cut value. This cut is implemented in order to minimize the uncertainty of the measured flux due to the uncertainly in primary chemical composition. Without the implementation of the XH cut, the proton aperture is as much as 35% greater than the iron aperture. The implementation of the XH cut equalizes the aperture of the TALE detector for different primary types. Figure 8.10 documents the ratio of the proton to iron aperture before and after the XH cut. The XH cut reduces the uncertainty in the aperture due to composition from 35% to the 5% level. More details on determining the energy dependent cuts are presented in Appendix J.

8.7 Event Examples

The TALE detectors observe three different classification of events: Cherenkov, scintillation, and mixed signal events. Cherenkov events have the majority of the measured signal come from Cherenkov light, whereas scintillation events have the majority of the measured signal come from scintillation light. Mixed events have a geometry where both Cherenkov and scintillation contribute significantly to the measured signal. An example of a scintillation event observed by TALE has already been presented in Figure 8.8 and Figure 8.1. Event displays and reconstructed profiles for a Cherenkov and mixed events are shown in Figure 8.11 and Figure 8.12

Table 8.1: TALE Processing Pass Rates. This table summarizes the number of events that survive each level of processing using the y2013m11d07 TALE data.

Processing Level	**Number of Events**	**Number Pass**	**Fraction Of Events that Pass**
Plane Fit (STPS2)	29875	4590	0.15
Rayleigh Filter (STPS2)	4590	3788	0.82
Geometry Fit (STGEO)	3748	3744	0.99
Profile Fit (STPFL)	3744	3295	0.88

Table 8.2: STPLN Cut Criteria.

Cut Criteria	**Details**
MAX Tube Time RMS	1.0 [μs]
MAX RMS of Plane Fit	0.05236 [radians]
MIN Tracklength	3.0 [deg]
MIN Inverse Angular Speed	0.005 [$\mu s/deg$]
MIN Photons per Good Tube	75.0 [photons / good tube]
MIN Good Tubes per Degree	0.75 [good tube / deg]
MAX Good Tubes per Degree	10.0 [good tube / deg]

Table 8.3: STPS2 Event Examples.

STPS2 Parameter	**Real Event**	**Noise Event**	**Details**
rvec	8.7	3.4	Rayleigh Vector
plog	3.29	0.72	$rvec^2/log10(npair)$ 1% probability equals plog of 2
rwalk	2.76	1.28	Rayleigh Vector for an equivalent random walk
ang	248.2	283.4	Angle between y-axis and Rayleigh Vector
aveTime	-2.57	-12.05	Mean of Trigger Times
sigmaTime	0.014	0.59	RMS of Trigger Times
avePhot	373.3	99.96	Mean photon count
sigmaPhot	39.1	9.8	RMS photon count
intimetubes	13	12	tubes within 3σ of the tube time distribution
lifetime	0.17	6.5	Difference in first and and last fired tube time
totalLifetime	9.3	24.1	Difference of first and last "intime" tube times

Table 8.4: TALE STPS2 Cut Pass Criteria.

Cut	**Value**
plog minimum	1.0
npair minimum	3
rvec minimum	3.5

Table 8.5: TALE Postreconstruction Static Quality Cuts. This table documents the quality cuts used in the TALE analysis that are not energy dependent. These cuts are designed to improve the energy resolution of the reconstructed events.

Post Recon Cut	**Pass Requirement**	**Notes**
χ^2_T/NDF	< 3.5	The χ^2 of the geometry fit
χ^2_P/NDF	< 5.0	The χ^2 of the profile fit
$XL - XH$	$> 150.0 g/cm^2$	The minimum track length in g/cm^2 observed
Tracklength	$> 5.0 degrees$	The minimum track length in *degrees* observed
Inverse Angular Speed	$> \mu s/degree$	The minimum inverse angular speed
Theta Max (Zenith Angle)	$< 65 degree$	The maximum zenith angle allowed.
RP (Distance of closest approach) Min	$> 500 meters$	The minimum RP allowed.
PEPGT6	> 35	The minimum number of average photons in the six highest signal tubes.
Bracket	$(XL + 100) < XMAX < (XH - 100)$	The reconstructed shower maximum must be within $100 g/cm^2$ of the observed track.

Table 8.6: TALE Postreconstruction Energy Dependent Quality Cuts. This table documents the quality cuts used in the TALE analysis that are energy dependent. The parameters that evolve with energy are RP_{max}, Θ_{min} (Zenith angle), and XH (the maximum first observed depth of the shower).

Energy log(E[eV])	RP_{max} **[km]**	Θ_{min} **[deg]**	XH $[g/cm^2]$
16.55	3.8	24	300
16.65	4.2	25	320
16.75	4.2	25	320
16.85	4.2	25	320
16.95	4.6	22	340
17.05	4.6	17	365
17.15	5.0	3	365
17.25	5.0	0	385
17.35	5.4	0	385
17.45	5.4	0	410
17.55	6.2	0	365
17.65	6.6	0	410
17.75	7.8	0	450
17.85	9.0	0	635
17.95	10.2	0	720
18.05	11.4	0	810
18.15	12.6	0	895
18.25	13.8	0	980
18.35	15.0	0	1065
18.45	16.2	0	1155

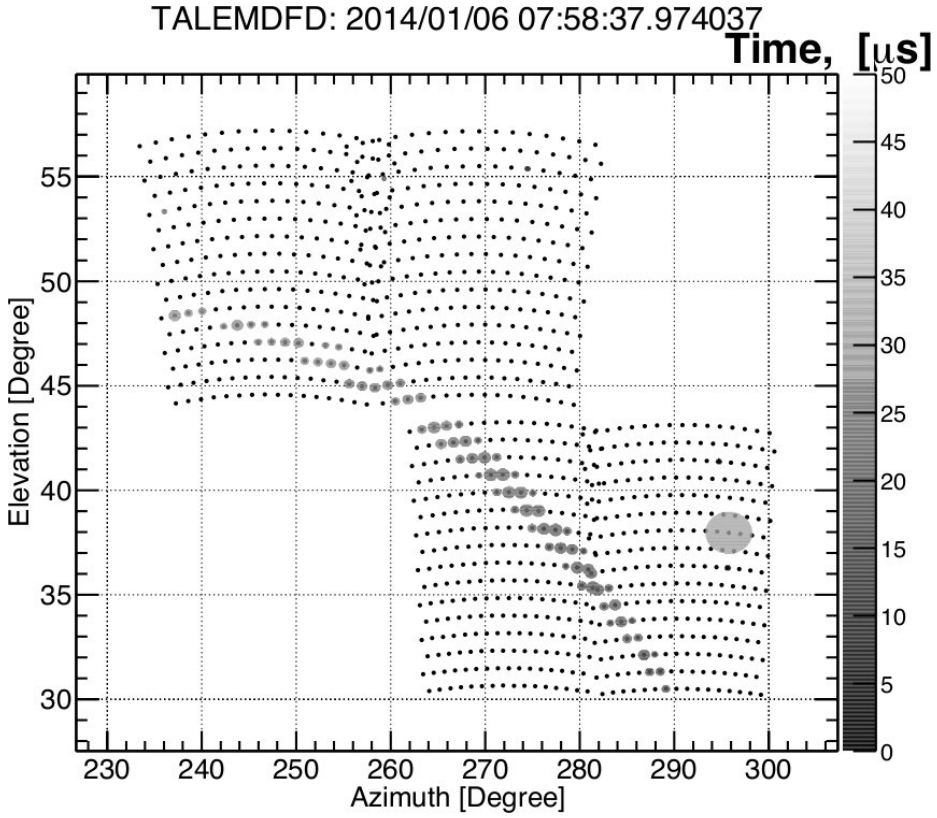

(a) TALE Raw Data Event Display.

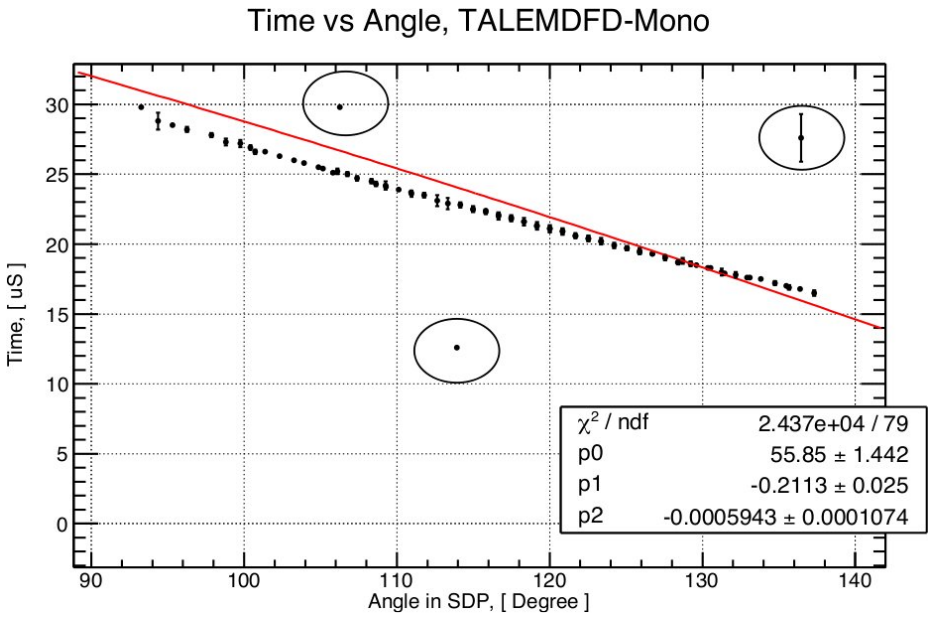

(b) TALE Raw Data Time vs. Angle in Shower Detector Plane. The fit shown is a fit to a simple quadratic equation. The circled tubes are the noise tubes in the event that will be removed in the plane fit process, because they are not on the time vs. angle fit.

Figure 8.1: An Example of a Cosmic Ray Air Shower Observed by the TALE Detector. These figures display the raw tube and timing information used in the plane fitting (STPLN) program. At this level of processing, noise tubes have not yet been removed.

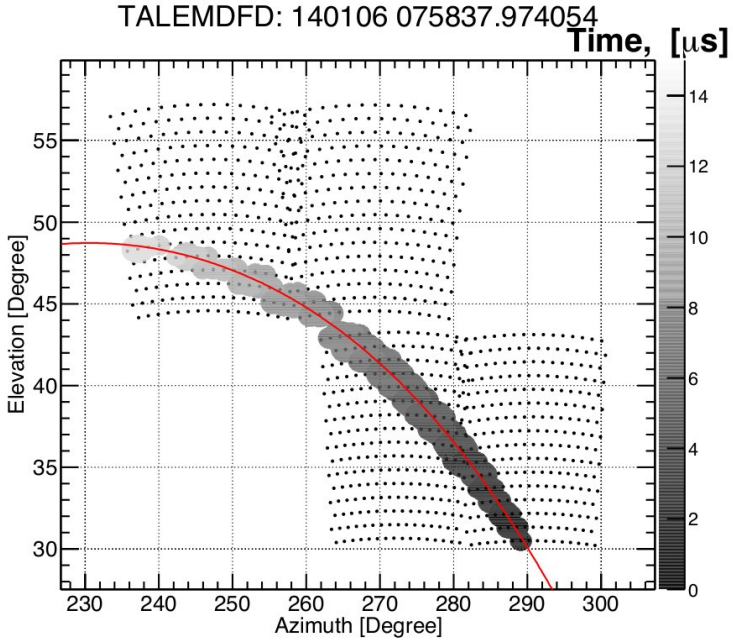

(a) TALE STPLN Data Event Display.

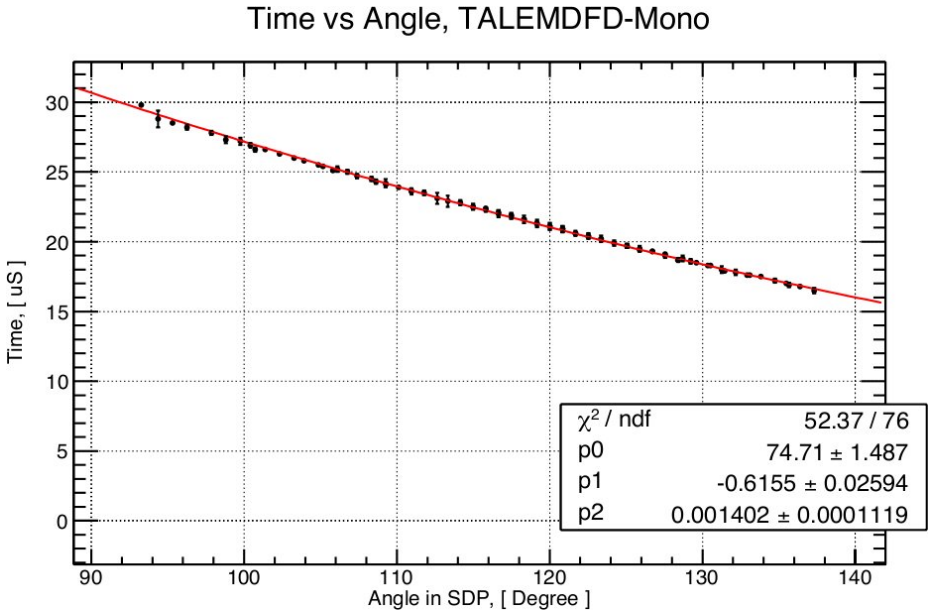

(b) TALE STPLN Data Time vs. Angle in Shower Detector Plane. The fit shown is a fit to a simple quadratic equation.

Figure 8.2: TALE Plane Fit Data Event. The results of processing an event through the plane fit (STPLN) routine. Pictured are both the event display with the noise tubes removed along with the Time vs. Angle plot in the SDP.

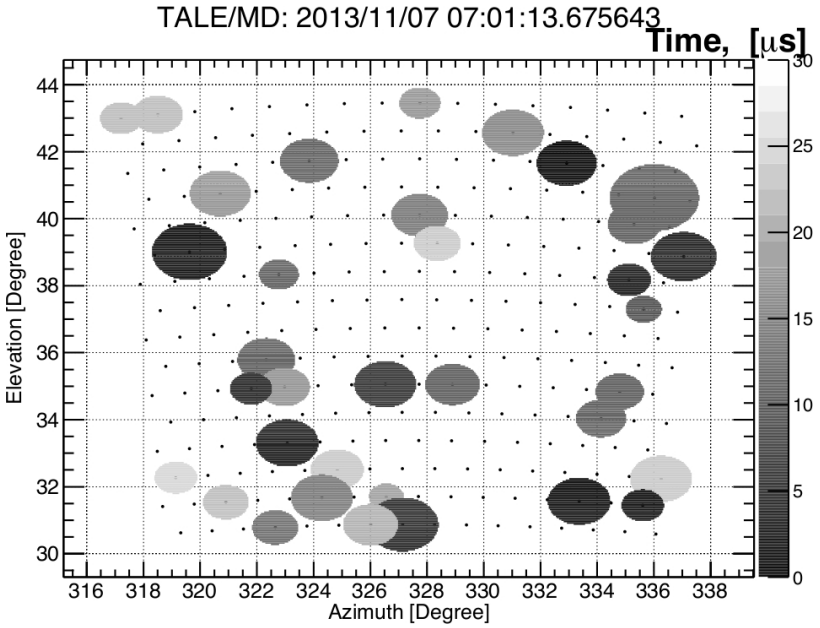

(a) Noise Event Removed by Rayleigh Filter

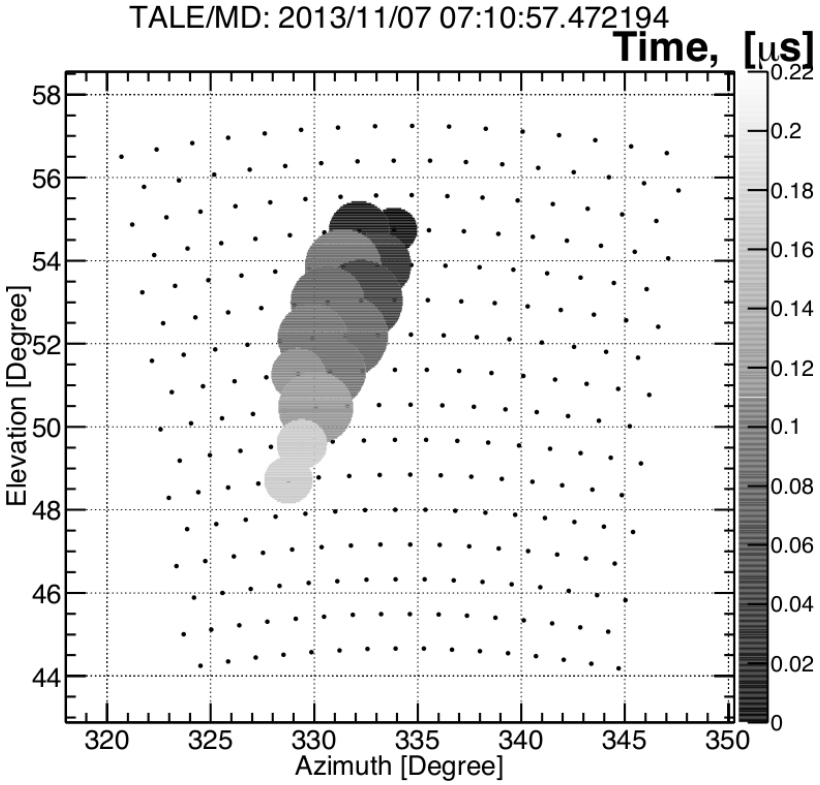

(b) Real Event which Passes the Rayleigh Filter

Figure 8.3: Example Events for STPS2. Two events are shown. The first is a noise event and does not pass the Rayleigh filter. The second is a real event and does pass the Rayleigh filter.

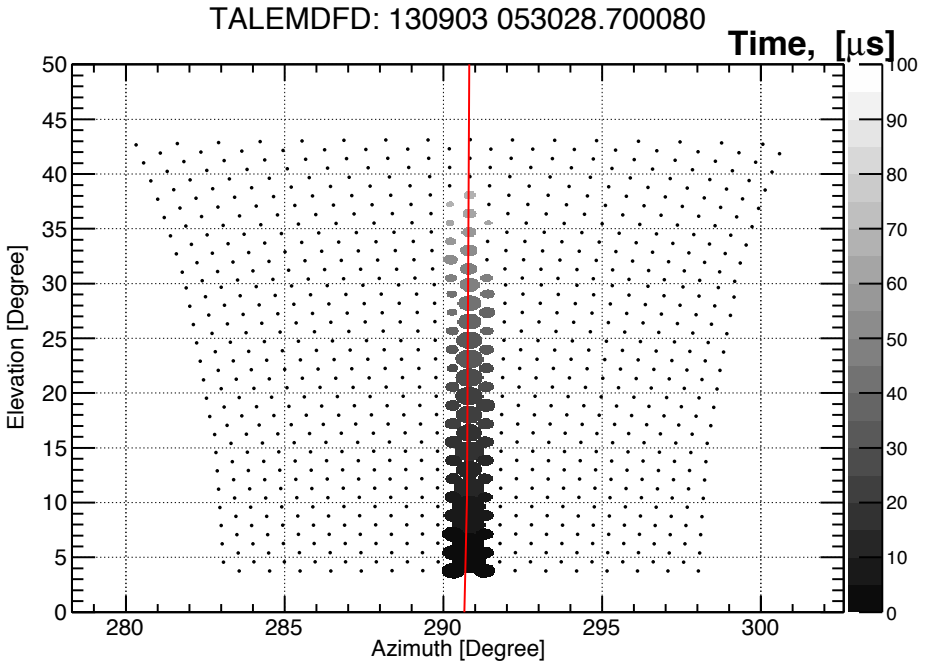

Figure 8.4: CLF Event as Observed by Both the MD and TALE Telescopes. The event includes the tack seen by the MD FD in addition to TALE. Both detectors triggered independently in this data set.

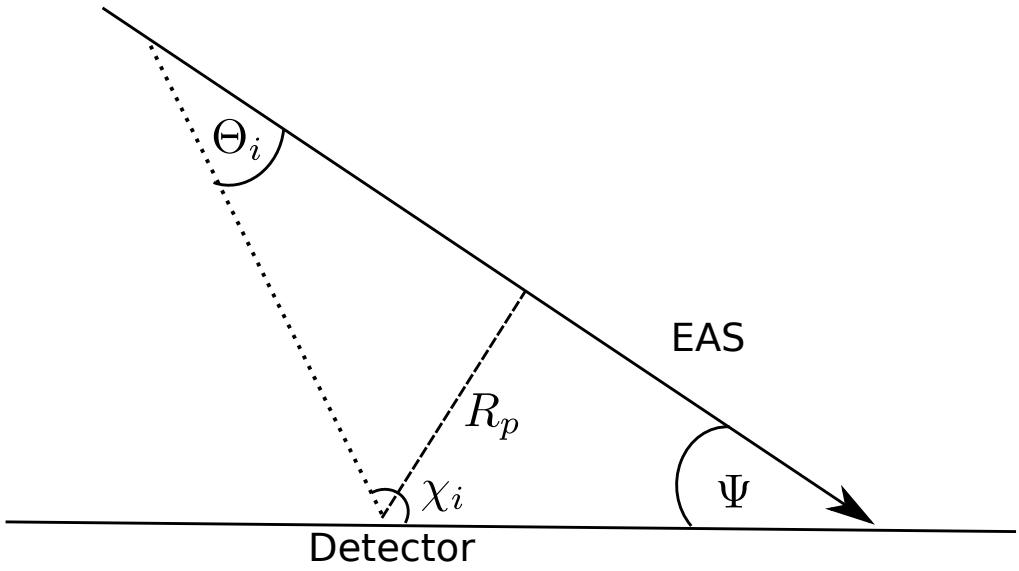

Figure 8.5: Track in SDP Geometry. This figure details the parameters used in the geometry fit. R_p is the distance of closest approach to the Shower Detector Plane (SDP), Ψ is the angle of the air shower in the SDP, and χ is the observation angle to a given track segment.

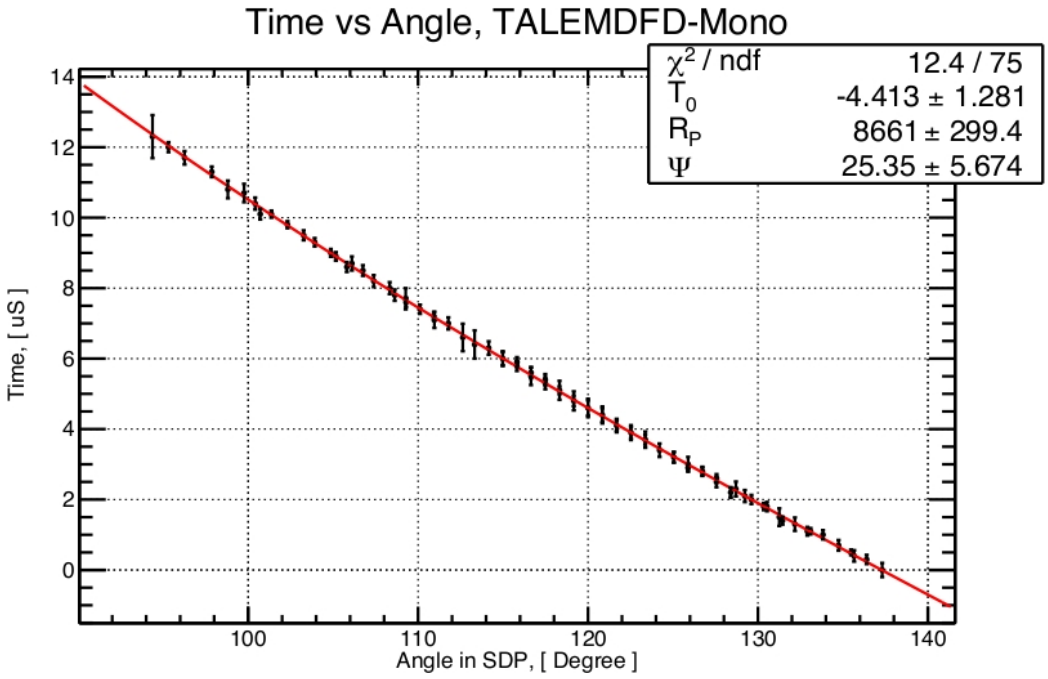

Figure 8.6: STGEO: Time vs. Angle Geometry Fit. The fit parameters yield the geometry of the shower.

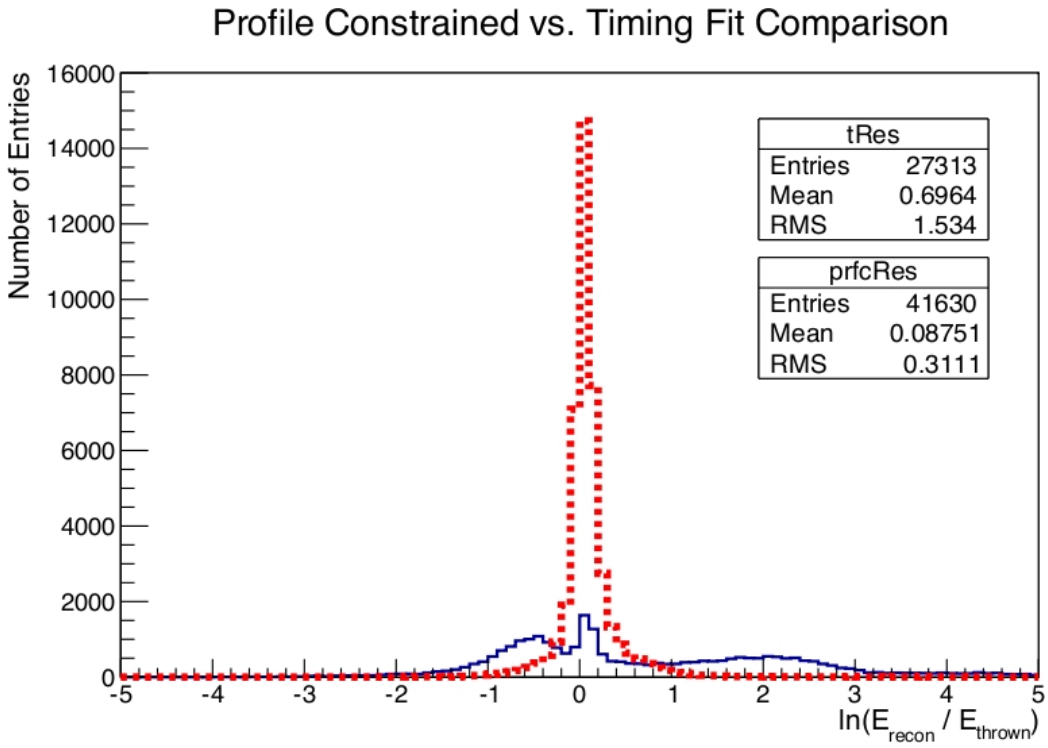

Figure 8.7: PCGF Energy Resolution. This graph compares the energy resolution of reconstructed air showers using the Profile Constrained Geometry Fit (Dashed Lines) and without (Solid Lines). This Monte Carlo Study utilized a QGSJet II-3 proton set of 47000 events that passed geometry reconstruction. Without the PCGF, 40% of events do not reconstruct, and those that do have a 350% uncertainty in the energy. This compares to the 30% energy resolution of the PCGF method. Quality cuts have yet to be applied to either data set.

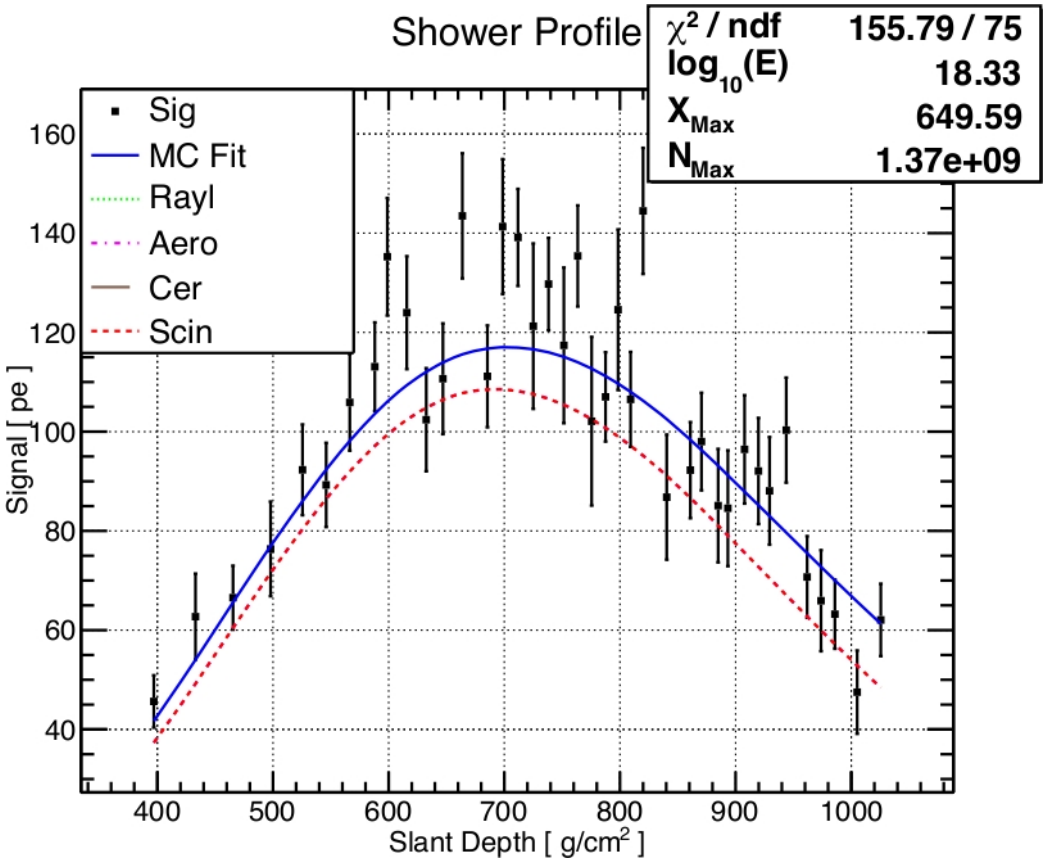

Figure 8.8: PCGF Reconstruction of the Event Display Shown in Figure 8.2a.

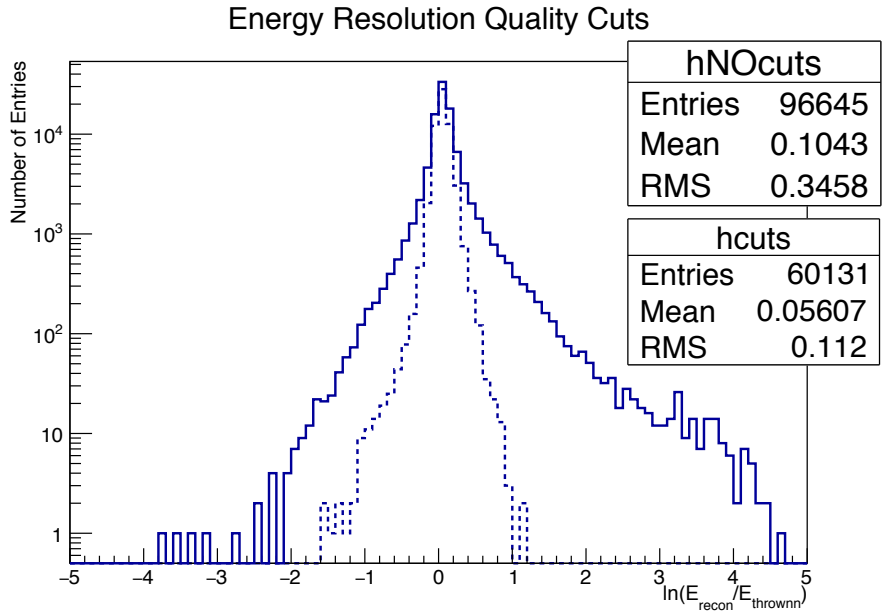

(a) Proton MC

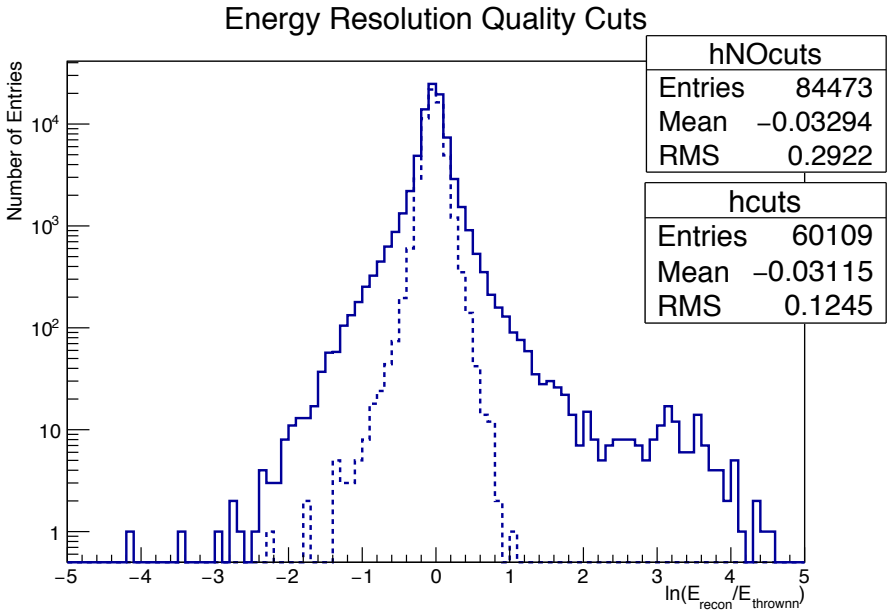

(b) Iron MC

Figure 8.9: Quality Cuts. This histogram shows the effect of applying the static quality cuts of Table 8.5. The solid histogram shows the energy resolution histogram before the cuts are applied, whereas the dashed histogram shows the energy resolution after static quality cuts were applied. The energy resolution of both protons and iron primary types is on the order of 10% after cuts are applied.

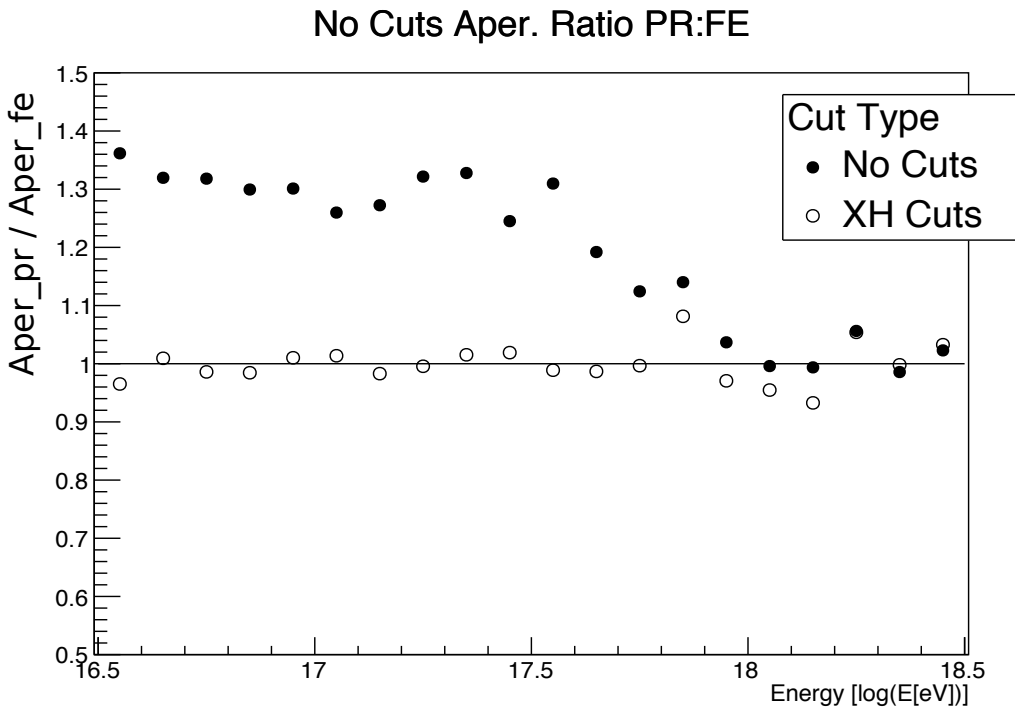

Figure 8.10: Effect of the XH Cut on Aperture. This figure demonstrates the effect of the XH cut on the ratio of the proton aperture to the iron aperture. The solid circles indicate the ratio of the aperture before the implementation of the XH cut, while open circles show the ratio after. Before the cut, the maximal difference in aperture is about 35%, while after the cut, the average difference is on the order of a few percent.

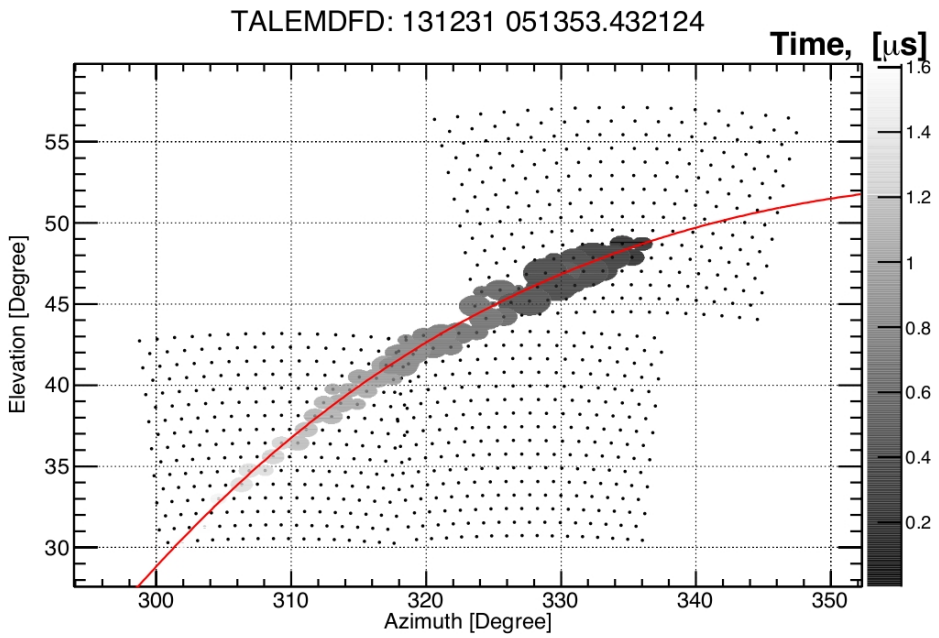

(a) Cherenkov Event Display

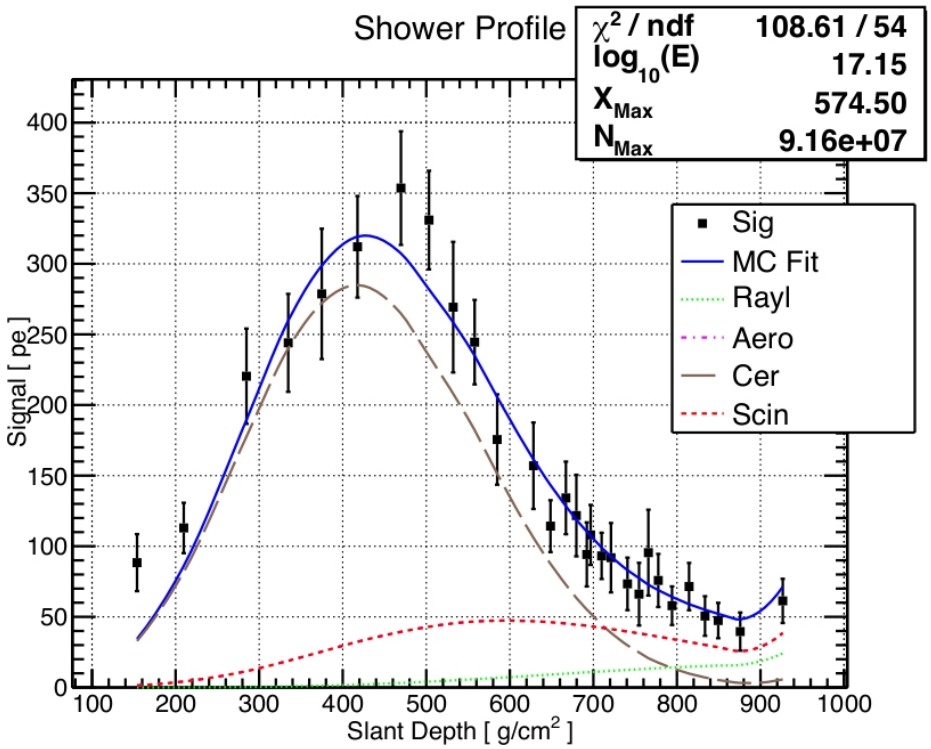

(b) Cherenkov Event Reconstructed Profile

Figure 8.11: TALE Cherenkov Event. This figure shows an event display for a Cherenkov event observed by the TALE detector panel (a). Panel (b) shows the reconstructed profile for the event.

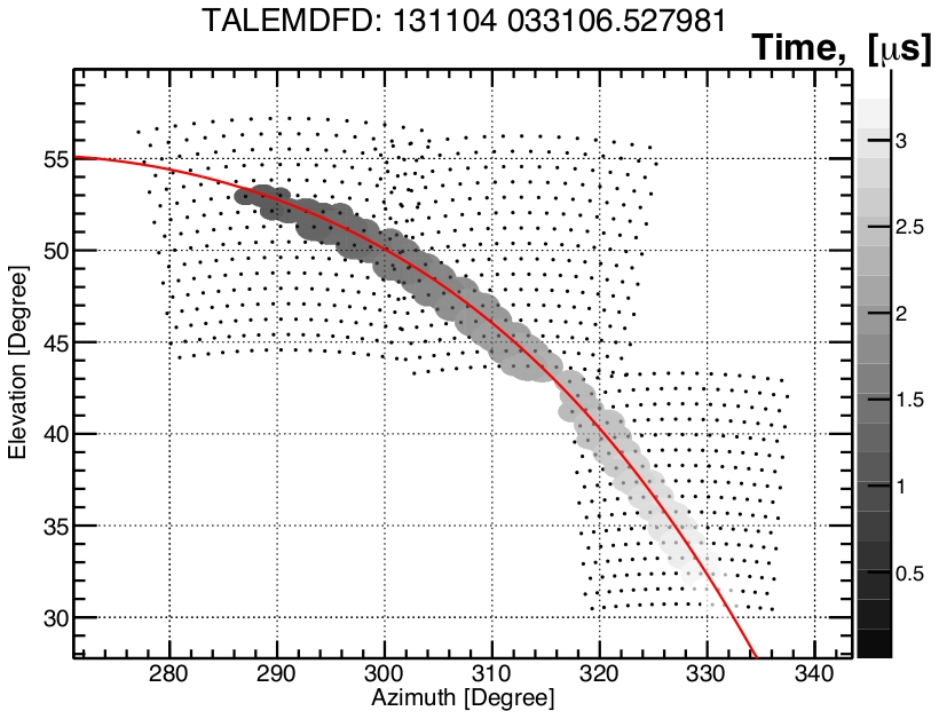

(a) Mixed Event Display

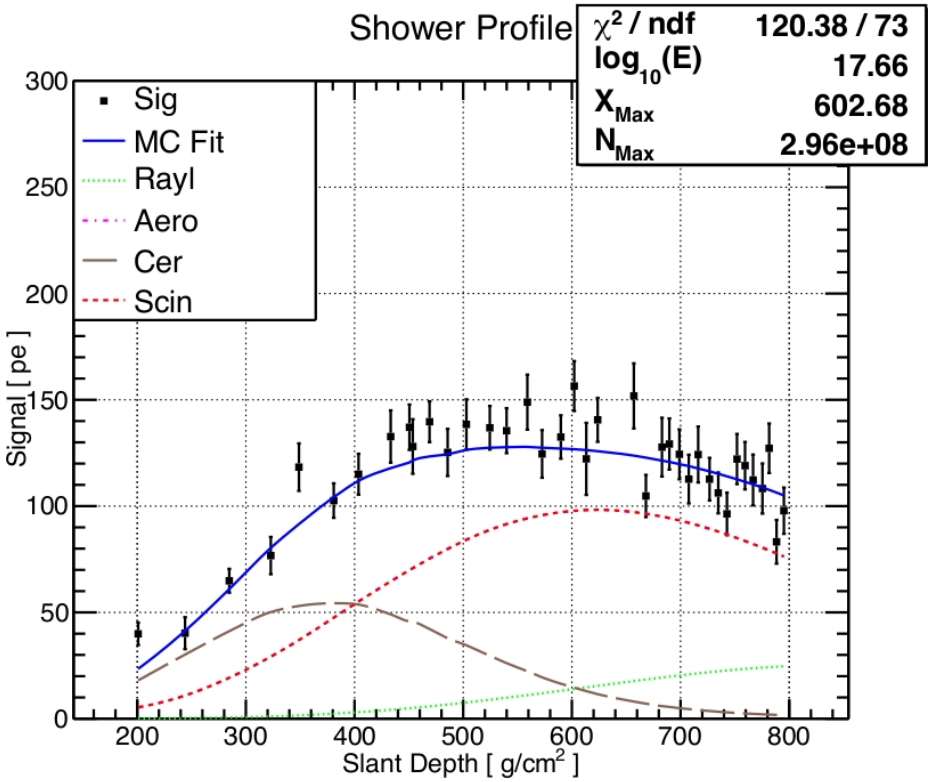

(b) Mixed Event Reconstructed Profile

Figure 8.12: TALE Mixed Event. This figure shows an event display for an event that has contributions to the observed signal from both Cherenkov and scintillation light. Panel (a) shows the event display, while panel (b) shows the reconstructed profile for the event.

CHAPTER 9

TALE SPECTRUM

The principal measurement of this dissertation is the flux of cosmic rays as a function of energy between $10^{16.5}$ and $10^{18.5}$ eV. This chapter reports on the measured flux using the Epoch 1 data set, which was collected between September 2013 and January 2014 and consisted of 246 hours of good weather data.

9.1 Introduction to Flux and Aperture Calculations

Determining the observed flux of comic rays requires knowing the number of observed events in a given energy bin and the exposure of the detector. The cosmic ray flux is calculated using,

$$J(E) = \frac{N(E)}{A\Omega(E) \cdot \Delta t \cdot \Delta E} \tag{9.1}$$

where $J(E)$ is the flux as a function of energy, $N(E)$ is the number of observed events in a given energy bin, $A\Omega(E)$ is the effective aperture as a function of energy, Δt is the on-time of the detector, and ΔE is the width of the energy bin [7].

The effective aperture is the product of the effective area and the solid angle observed by the detector. The solid angle is calculated by determining the area of the surface of the unit sphere subtended by a cone of half width θ as shown in Figure 9.1. The solid angle is calculated using the integral,

$$\Omega_0 = \int_0^\theta 2\pi R \sin\omega \cdot R d\omega, \tag{9.2}$$

where Ω_0 is the solid angle, R is the radius of the sphere (in this case the unit sphere), θ is the maximum opening angle of the cone, and ω is the differential opening angle. Performing the integral and setting the radius of the sphere to unity yields,

$$\Omega_0 = 2\pi(1 - \cos\theta). \tag{9.3}$$

Similarly, the area of the detector is the area of the disk created by the maximum observation radius,

$$A_0 = \int_{RP_{min}}^{RP_{max}} 2\pi R dR = \pi(RP_{max}^2 - RP_{min}^2), \tag{9.4}$$

where RP_{min} and RP_{max} are the minimum and maximum allowed distances of closest approach.

If the TALE detector were equally sensitive to all events, at every energy, in every geometrical orientation, then the aperture would be the product $A_0\Omega_0$. However, the sensitivity of the TALE detector depends on all of these factors and is calculated using Monte Carlo simulations. Events are "thrown" around the detector and the simulated response of the detector is determined. The effective aperture of the detector is then calculated by,

$$A\Omega(E) = A_0\Omega_0 \cdot \frac{N_S(E)}{N_T(E)}, \tag{9.5}$$

where $A\Omega(E)$ is the effective aperture at a given energy, $N_S(E)$ is the number of events that survive reconstruction and cuts in a given energy bin, $N_T(E)$ is the number of thrown events in a given energy bin, and $A_0\Omega_0$ is the aperture into which events were thrown.

The simulations made in the analysis of this dissertation generated air showers in the volume defined by $RP_{min} = 0.5km$, $RP_{max} = 20km$, and $\theta_{max} = 70°$. The number of thrown events is known from Figure 6.2. Applying postreconstruction quality cuts to the simulations and counting the number of remaining events then determine the effective aperture.

9.2 Composition Effects on Reconstruction

The cosmic ray composition impacts the reconstructed energy and effective aperture of events observed by the TALE detector, the effect of which was minimized by the choice of cuts in Section 8.6. The details of the chemical composition effect are detailed in this section. The reconstructed energy is altered by the missing energy correction and the reconstruction bias, whereas the effective aperture is impacted by the differences in the depth of initial interaction and the resulting changes in the shower development.

The reconstructed energy of an air shower depends upon the missing energy correction to the observed calorimetric energy. The missing energy correction accounts for the energy carried away by particles that do not generate significant scintillation light (mouns, neutrinos, etc.). A graph of the ratio of total energy to calorimetric energy calculated using QGSJet II-3 showers is shown in Figure 9.2.

The energy resolution and reconstruction biases are determined by generating a histogram of the natural log of the ratio of the reconstructed to thrown event energies of Monte Carlo simulations. The offset of the mean of the histogram is the reconstruction bias and the width of the distribution is an estimate of the resolution of the reconstruction. An example of the resolution estimate is shown for both protons and iron in the $10^{16.5} - 10^{16.6}$eV energy bin in Figure 9.3.

The cosmic ray composition also alters the effective aperture of the TALE detector. Figure 9.4 shows the effective aperture, calculated using Equation 9.5, for TALE when no postreconstruction cuts are applied to the data and demonstrates how the aperture of proton primaries and iron primaries diverge below 10^{18} eV. However, the choice of cuts detailed in Section 8.6 and Appendix J minimize the effect of the primary type on the effective aperture. The resulting effective aperture after cuts is shown in Figure 9.5. Additionally, Figure 9.6 demonstrates how the applications of the cuts described reduce the ratio of proton to iron aperture from 35% to 5%.

To further reduce any potential effect, I assumed the following composition in calculating the spectrum. For cosmic rays of energy greater than 10^{17}eV, the cosmic ray composition is taken from the measurement of the HiRes-Mia experiment [56]. Alternatively, for energies below 10^{17}eV, the composition is modeled using the H4A predictions from Gaisser *et al* [77] normalized to match the HiRes-MIA result at 10^{17}eV. Figure 9.7 illustrates the assumed composition used in this analysis. Figure 9.8 shows a summary of the reconstruction bias and energy resolution of each energy bin for both proton and iron air showers. The calculated missing energy and bias corrections are applied to the reconstructed calorimetric energy of all data and MC events before an aperture is calculated or data-MC comparisons are made.

9.3 Detector Resolutions

The energy and geometrical resolutions of the TALE detector are determined with Monte Carlo studies. When a simulated event is generated, the thrown parameters of the shower (including energy, RP, zenth angle, azimuthal angle, and angle in the shower detector plane) are stored so that they may be later compared with the reconstructed values. Examples of the energy resolution for all reconstructed Monte Carlo events that pass postreconstruction cuts are shown in Figure 9.9 and demonstrate an energy resolution on the order of 10% after all cuts. The geometrical resolutions are shown in the following figures:

Figure 9.10 Fractional RP Reconstruction Error $ln(RP_{recon}/RP_{thrown})$

Figure 9.11 Error in θ (zenith angle) [degrees]

Figure 9.12 Error in ϕ (azimuthal angle) [degrees]

Figure 9.13 Error in Ψ (Angle in Shower Detector Plane Figure 8.5) [degrees]

The geometrical resolutions show that the majority of the events have the pointing direction reconstructed to within 1° of the thrown direction. This resolution is accomplished due to the angular dependence of the emission of Cherenkov light. However, at energies greater that $10^{17.4}$eV, the majority of the signal observed comes from scintillation light and not Cherenkov. The energy resolution for such events is shown in Figure 9.14, and due to the PCGF method, remains on the order of 10%. Without the constraint of the Cherenkov emission angle to help determine the shower geometry, the uncertainly in Ψ(angle in the shower detector plane) increases from $< 1°$ to 6° as shown in Figure 9.15.

9.4 Data-MC Comparison

Since the aperture of the TALE detector is calculated using a Monte Carlo simulation of the detector, it is important to check that the Monte Carlo gives an accurate description of the detector. Comparing the distributions of reconstructed geometrical parameters of data and Monte Carlo performs this validation.

It is important to note that the geometrical distributions evolve with energy. This means that unless the Monte Carlo is thrown with the same energy spectrum as the data (which is what we are trying to measure in the first place), distributions of data and Monte Carlo should not be expected to match over the full energy range. An example of a data - Monte Carlo comparison for each geometrical parameter is shown according to:

Figure 9.16 RP Data - Monte Carlo Comparison over the full energy range

Figure 9.17 θ (zenith angle) - Monte Carlo Comparison in the $10^{16.75}$eV energy bin

Figure 9.18 ϕ (azimuthal angle) - Monte Carlo Comparison over the full energy range

Figure 9.19 Ψ (Angle in Shower Detector Plane Figure 8.5) - Monte Carlo Comparison in the $10^{16.75}$eV energy bin

Figure 9.20 track length - Monte Carlo Comparison for events with energies greater than $10^{17.5}$eV

This series of figures demonstrates the agreement of the reconstructed geometrical parameters between data and Monte Carlo. Each data-Monte Carlo comparison includes a Kolmogorov-Smirnov (KS) test probability that the data and Monte Carlo are generated

from the same distribution. If the KS test results in a probability of greater than 0.05, then the two distributions are consistent with one another. However, if the KS probability is less than $3 \cdot 10^{-3}$, there is a 3σ certainty that the distributions do not come from the same distribution. As expected, the KS-test values (shown with each comparison) confirm that the distributions match. Appendix I details data-MC comparisons in individual 0.1 log(E) decade bins and demonstrate that the data and MC are in agreement.

9.5 Flux Measurement

The measurement of the cosmic ray flux presented in this dissertation uses the TALE Epoch 1 data set. These data were collected from September 2013 - January 2014 and includes 246 hours of good weather night sky observation. The Monte Carlo was generated to match the detector state during this period. If a telescope shutter was not able to open or a low voltage supply failed, it was simulated in the Monte Carlo to correct the aperture effect.

The cuts used in this analysis are the same as those presented in Section 8.6 and the effective aperture after applying postreconstruction quality cuts can be seen in Figure 9.5. The number of events observed in each energy bin by TALE during the Epoch 1 period that passed postreconstruction cuts is reported in Table 9.1. The cosmic ray flux in a given energy bin is calculated using Equation 9.1 and is presented in Figure 9.21.

Table 9.1: TALE Postreconstruction Event Count. This table documents the number of observed data events in each energy bin, which passed all postreconstruction quality cuts in the Epoch1 period.

Energy log(E[eV])	**Number of Events**
16.55	860
16.65	698
16.75	511
16.85	409
16.95	293
17.05	235
17.15	176
17.25	155
17.35	103
17.45	75
17.55	48
17.65	48
17.75	49
17.85	45
17.95	40
18.05	40
18.15	21
18.25	16
18.35	10
18.45	3

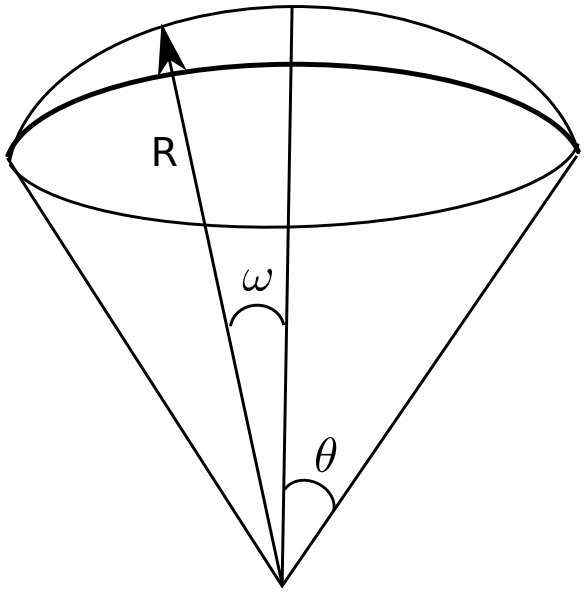

Figure 9.1: Solid Angle Geometry. The solid angle of a detector is the area of the unit sphere subtended by a cone of half width θ.

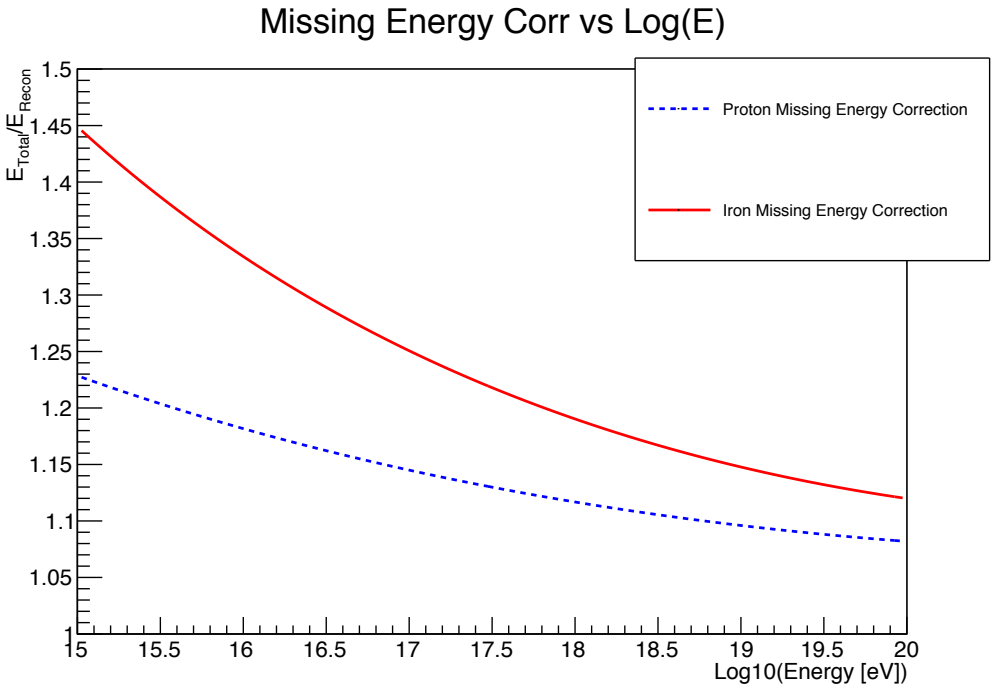

Figure 9.2: TALE Missing Energy Corrections. This figure shows the ratio of thrown to reconstructed calorimetric energy for both protons and iron. This figure shows the missing energy correction curves used in the determination of the TALE flux. The missing energy increases more quickly for lower energy iron showers because produced pions have smaller gamma factors, increasing their chance of decaying into muons and neutrinos rather than interacting strongly with the atmosphere.

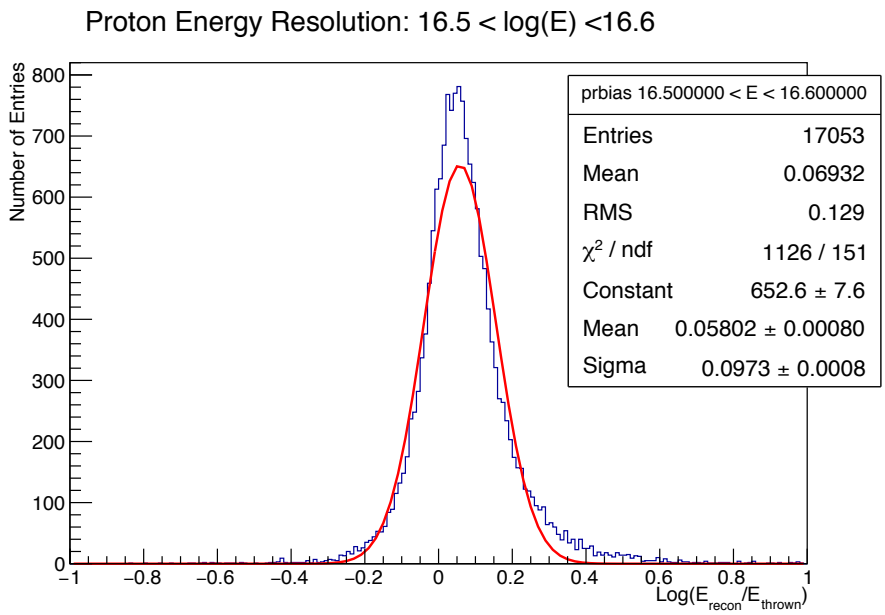

(a) Proton Energy Resolution Histogram

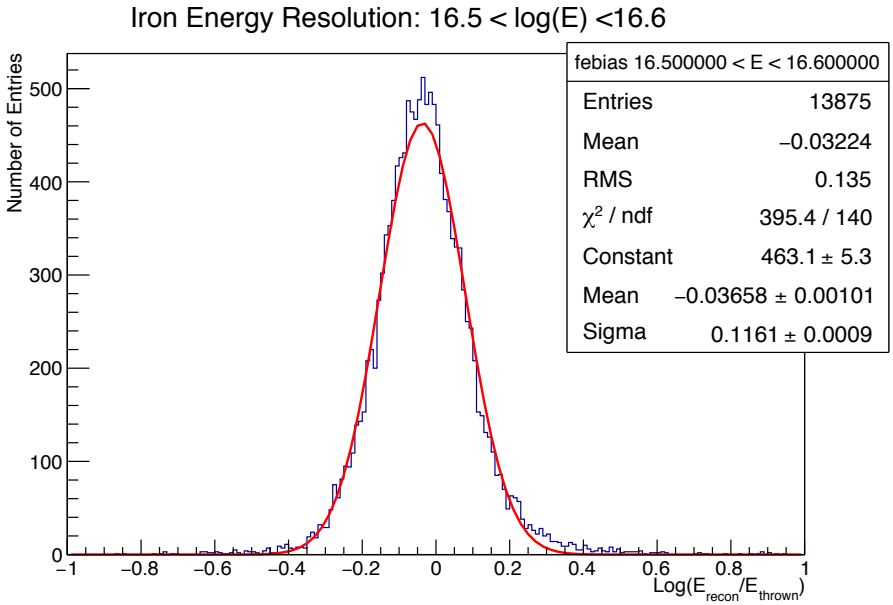

(b) Iron Energy Resolution Histogram

Figure 9.3: Energy Resolution Example. This figure demonstrated the reconstruction bias and energy resolutions for proton (above) and iron (below) in the $10^{16.5} - 10^{16.6}$eV bin. The distributions have similar widths (RMS), but different means.

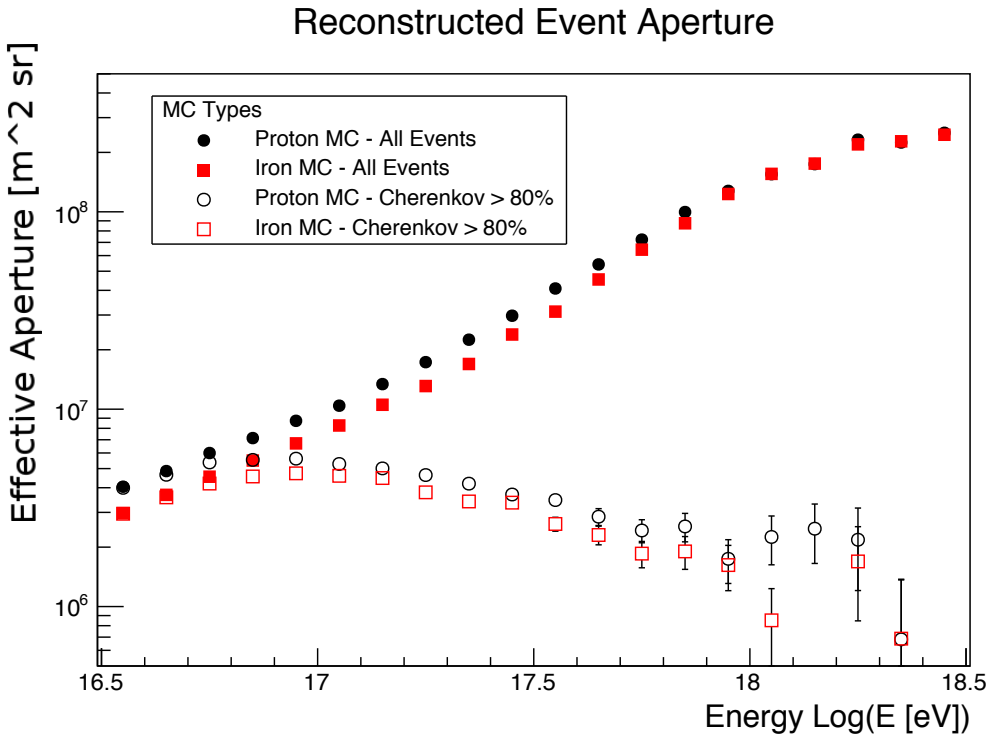

Figure 9.4: The TALE Reconstruction Aperture. The graph shows the calculated reconstructed event aperture of the TALE detector. This aperture does not have any quality cuts applied. Solid points indicate all reconstructed events were included in the calculation while open points indicate the aperture for events where more than 80% of the observed signal came from Cherenkov light. The aperture for proton and iron primaries can be seen to diverge from one another below 10^{18} eV.

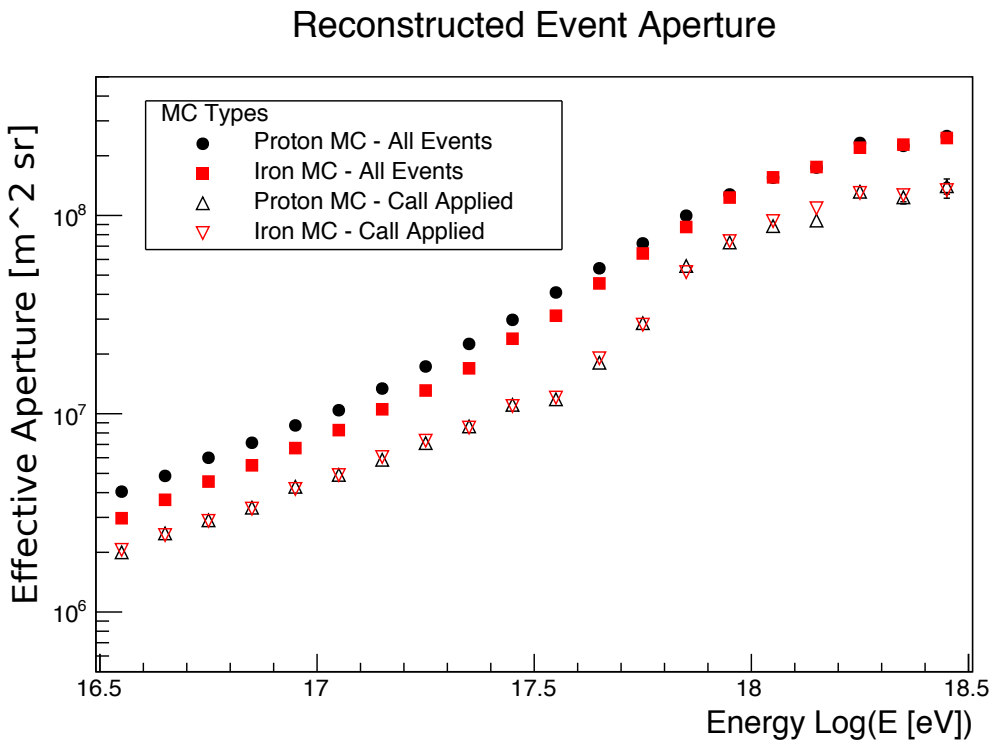

Figure 9.5: TALE Effective Aperture After Cuts. This graph shows the calculated reconstructed event aperture of the TALE detector after all cuts are applied. This aperture has all quality cuts applied. Solid points indicate all reconstructed events were included in the calculation (included for reference), while open points indicates only those events that passed all cuts.

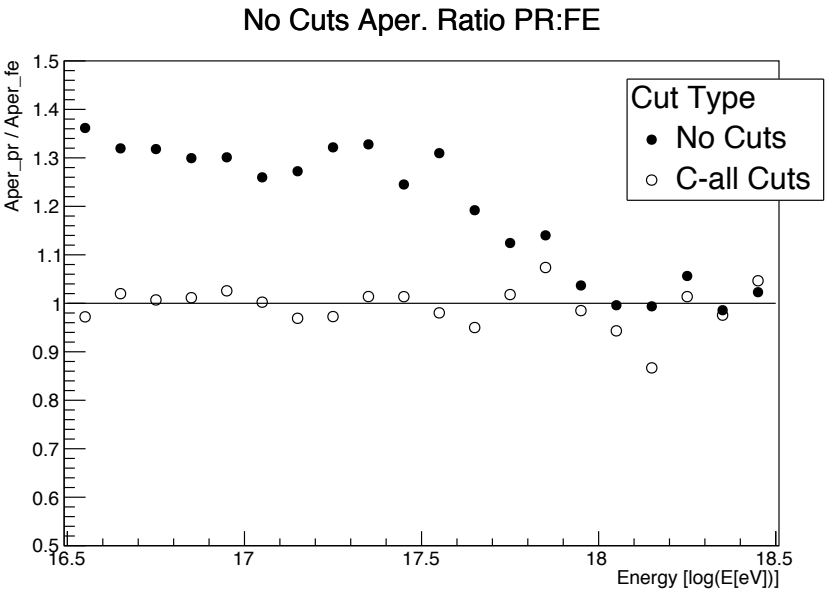

Figure 9.6: TALE Aperture Ratios. This graph shows the ratio of the proton aperture to the iron aperture. The solid points indicate the ratio of the apertures without any cuts being applied, whereas the open points indicate the ratio of the apertures after all cuts are applied. This plot demonstrates how the postreconstruction cuts reduce the uncertainty in the aperture due to composition from 35% to less than 5%.

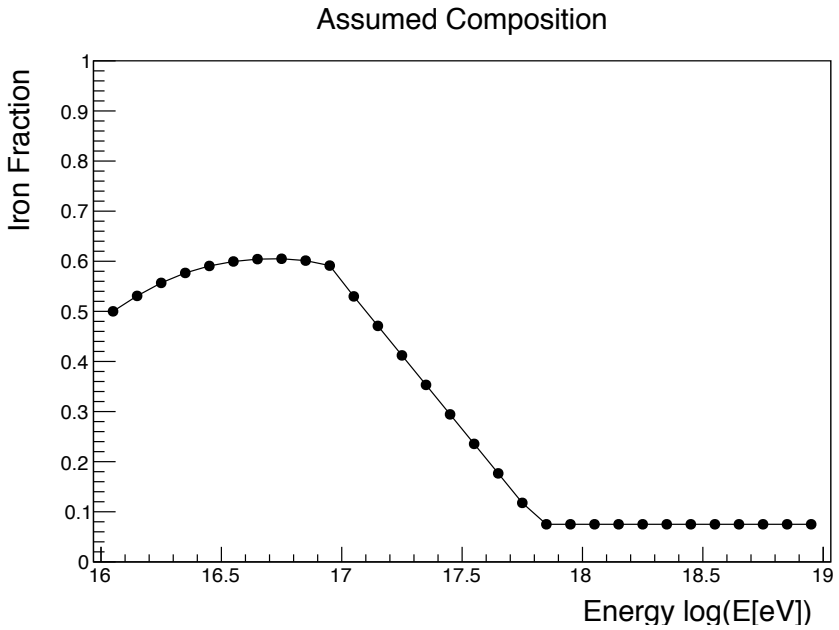

Figure 9.7: Iron Fraction as a Function of Energy. This figure shows the measured or calculated iron fraction as a function of energy. This figure shows the assumed composition used in the calculation of the TALE spectrum. Below 10^{17} eV, the composition is estimated from the Gaisser H4A model. Above 10^{17}eV, the composition is a HiRes-Mia like transition from iron the proton. Above 10^{18}eV, the composition is based on the HiRes stereo composition and is light/protonic.

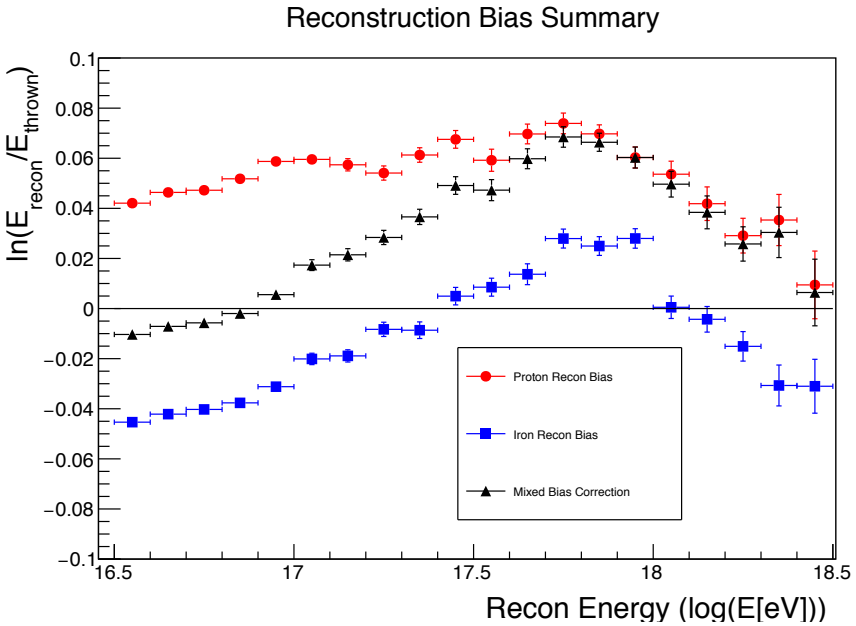

Figure 9.8: TALE Bias Correction Summary. This figure shows the calculated reconstructed bias as a function of energy for the proton and iron MC data sets. Additionally, the weighed reconstruction bias determined by the assumed composition is also shown.

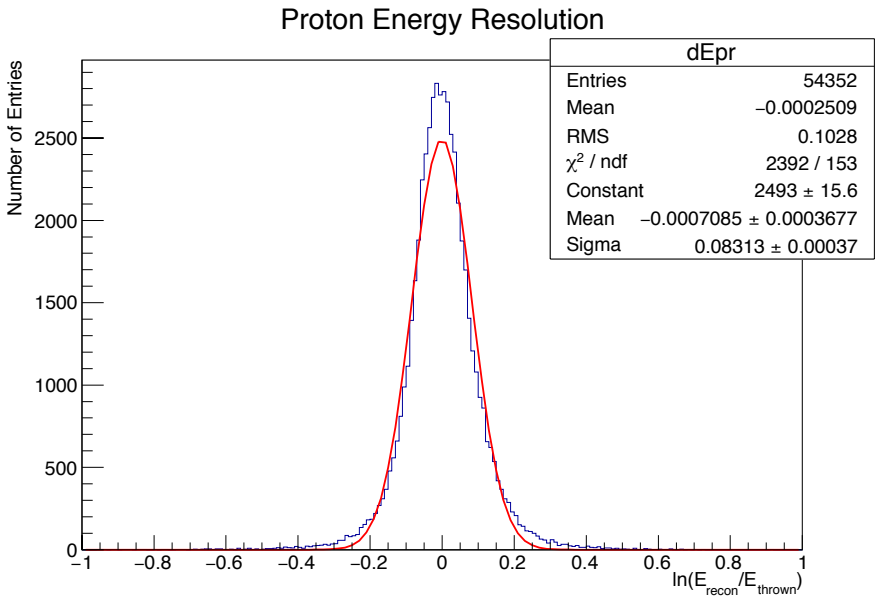

(a) Proton Energy Resolution

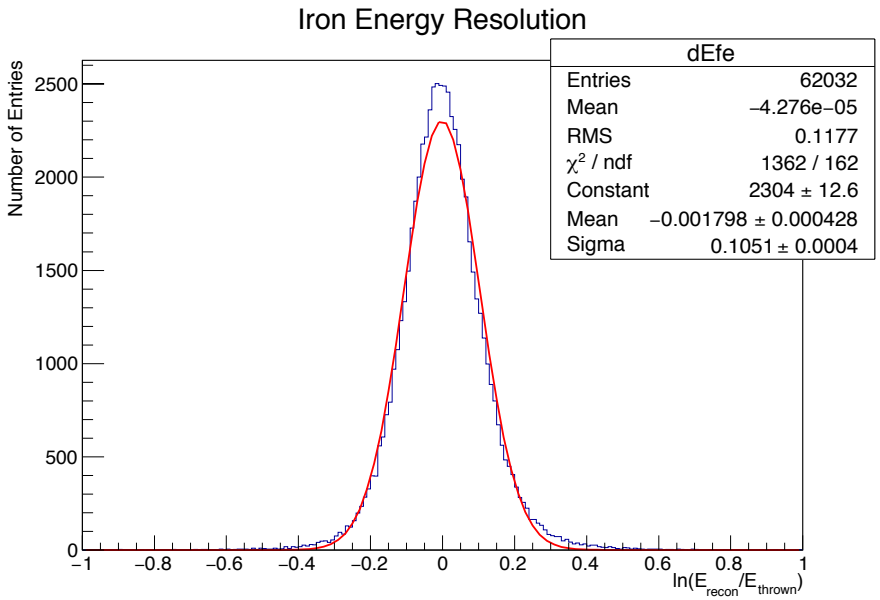

(b) Iron Energy Resolution

Figure 9.9: Reconstructed Energy Resolution. This histogram shows the reconstruction resolution of energy for proton and iron MC for all events that pass the postreconstruction cuts. Both histograms demonstrate the energy resolution is on the order of 10%.

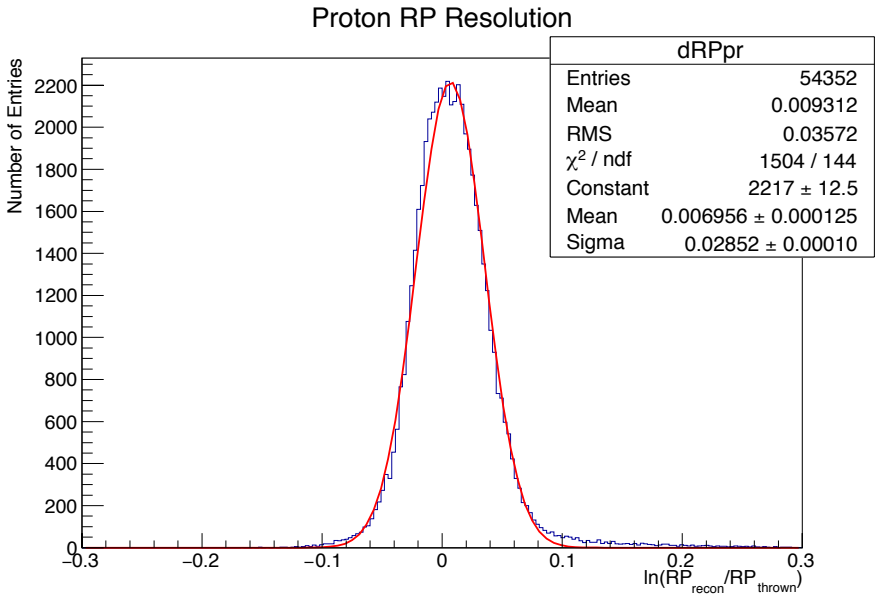

(a) Proton RP Resolution

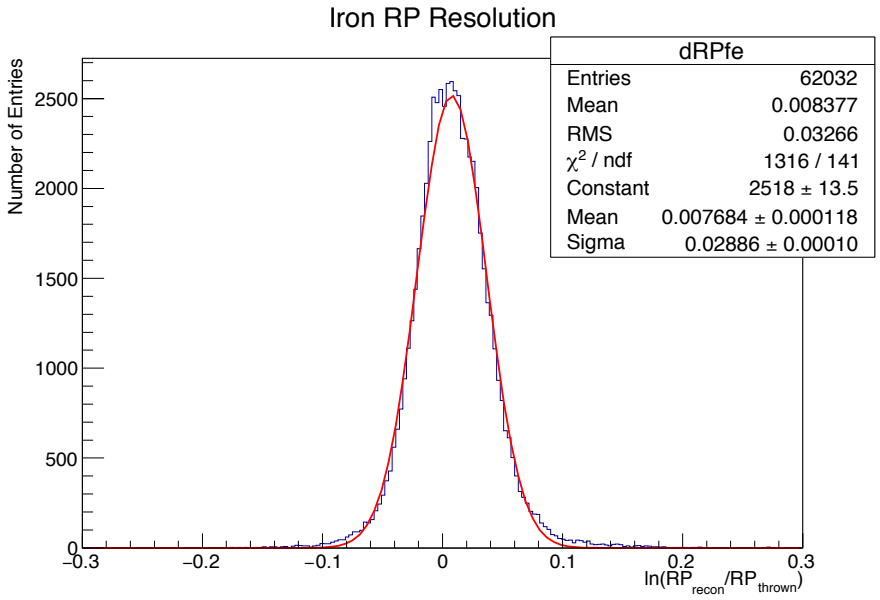

(b) Iron RP Resolution

Figure 9.10: Reconstructed RP Resolution. This histogram shows the RP (distance of closest approach) reconstruction resolution for proton and iron MC. All events that pass postreconstruction cuts are included. A resolution of better than 3% is achieved.

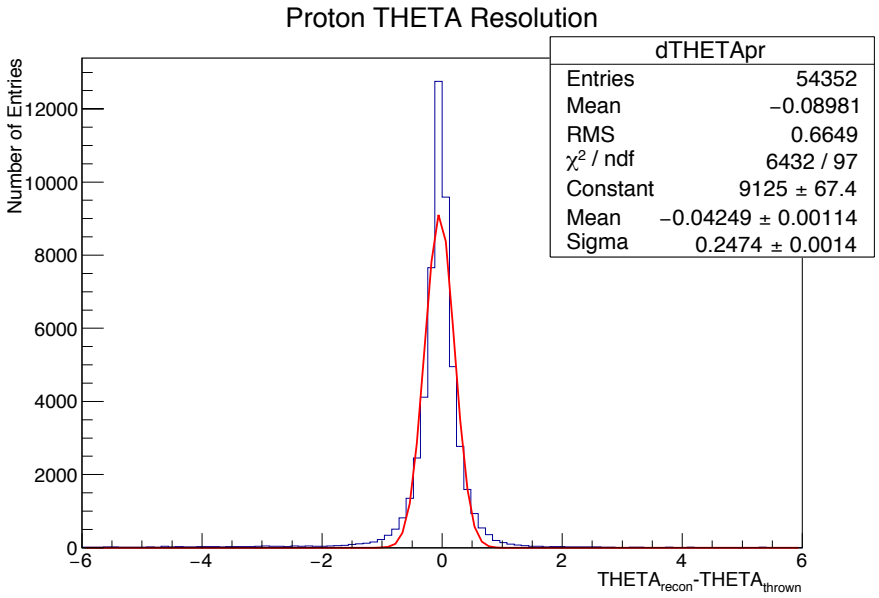

(a) Proton THETA Resolution

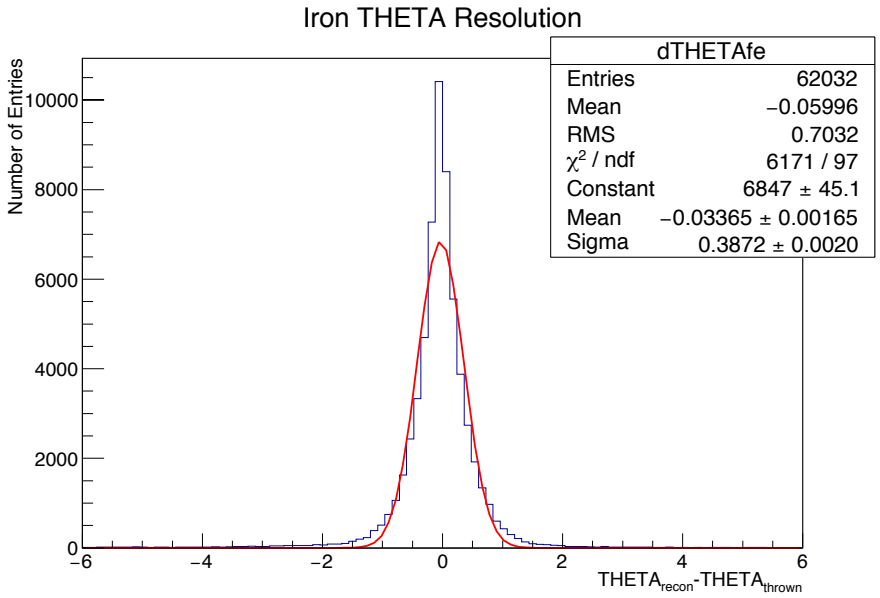

(b) Iron THETA Resolution

Figure 9.11: Reconstructed θ. This histogram shows the θ (zenith angle) resolution for proton and iron MC. All events that pass postreconstruction cuts are included. A resolution of better than 0.5° is achieved.

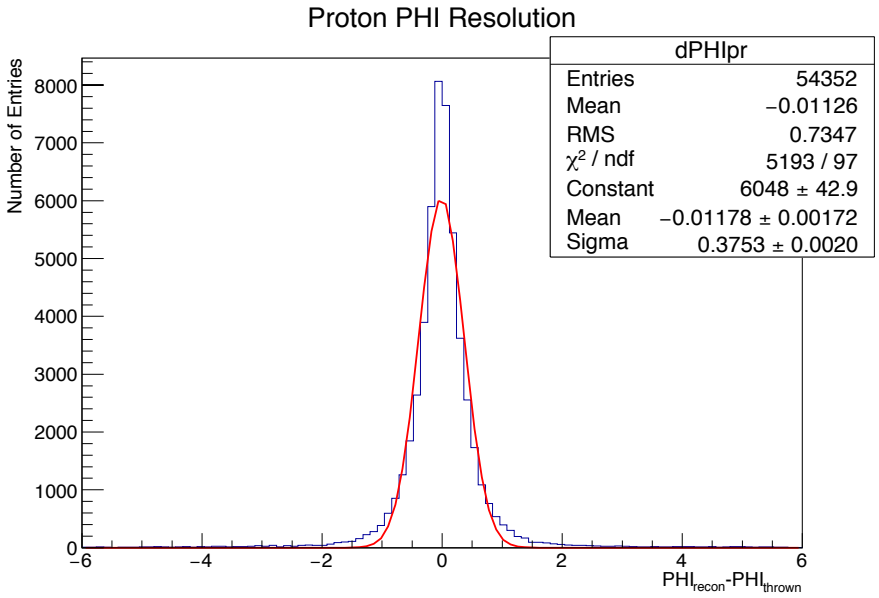

(a) Proton ϕ Resolution

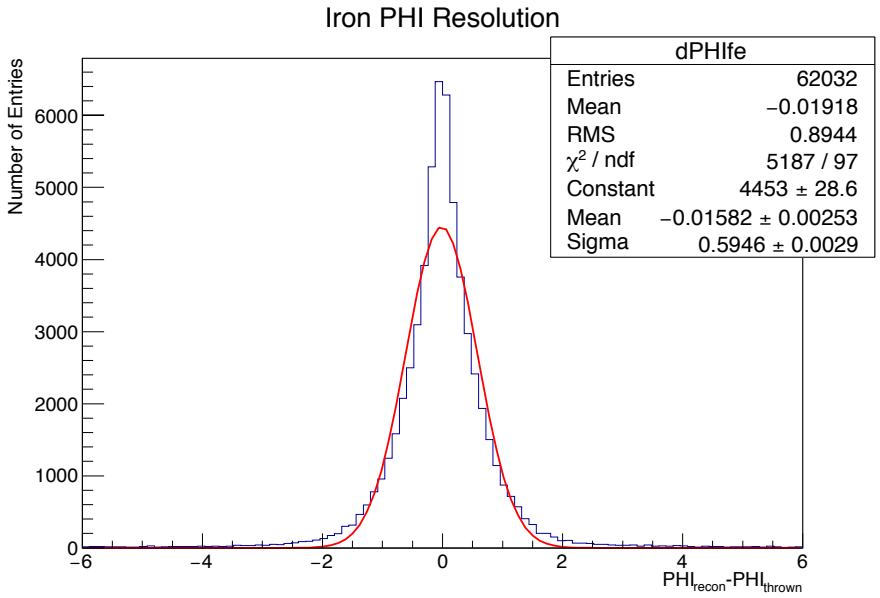

(b) Iron ϕ Resolution

Figure 9.12: Reconstructed ϕ Resolution. This histogram shows the ϕ (azimuthal angle) resolution for proton and iron MC. All events that pass postreconstruction cuts are included. A resolution of better than 0.5° is achieved.

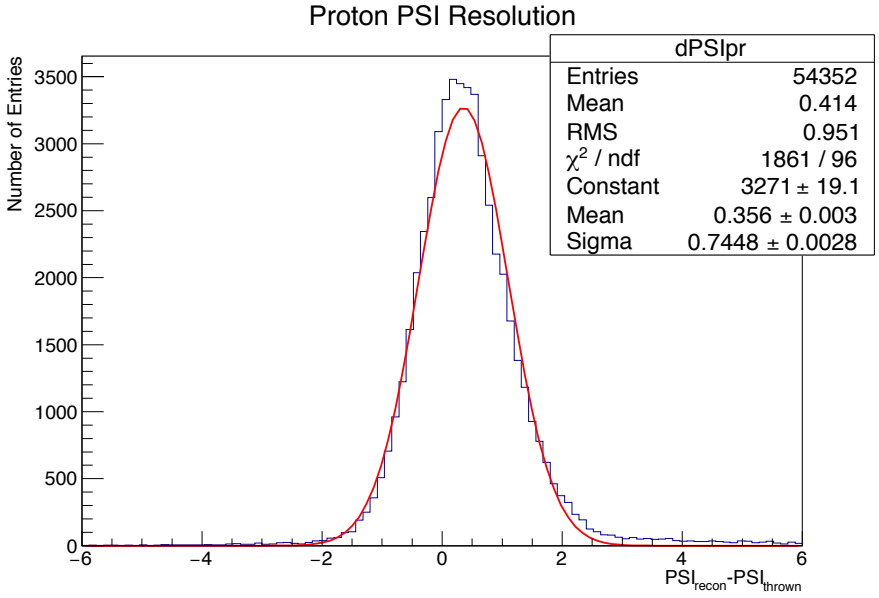

(a) Proton PSI Resolution

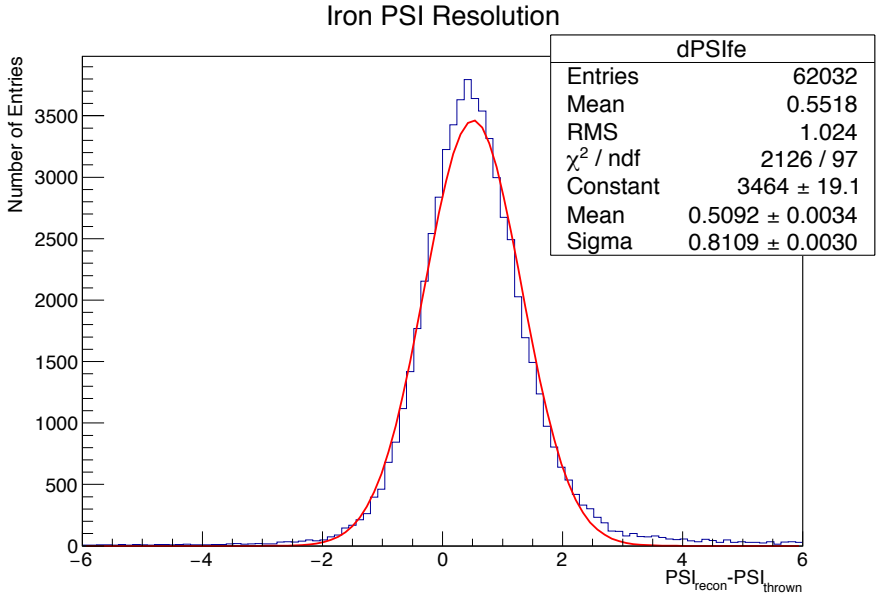

(b) Iron PSI Resolution

Figure 9.13: Reconstructed Ψ Resolution. This histogram shows the Ψ (angle in the shower detector plane Figure 8.5) resolution for proton and iron MC. All events that pass postreconstruction cuts are included. A resolution of better than 1.0° is achieved.

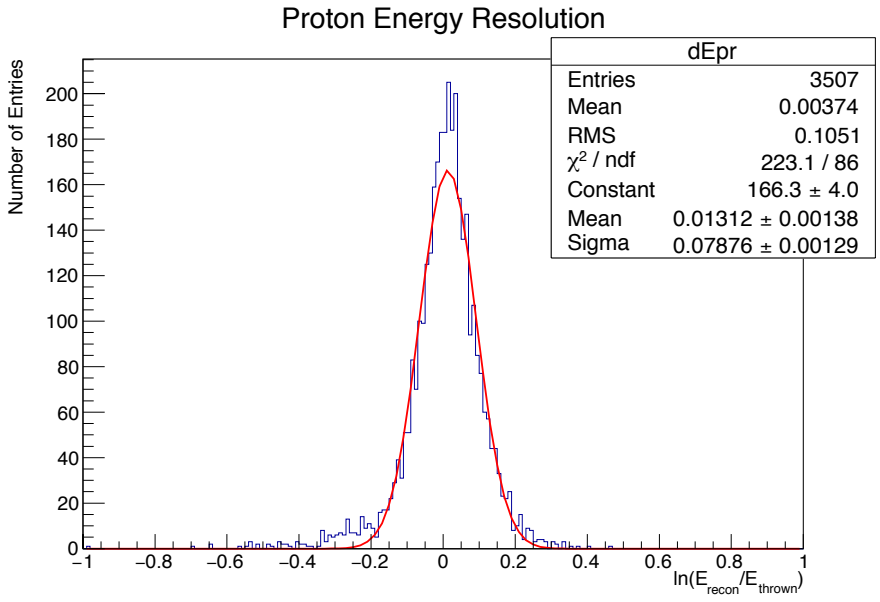

(a) Proton Energy Resolution

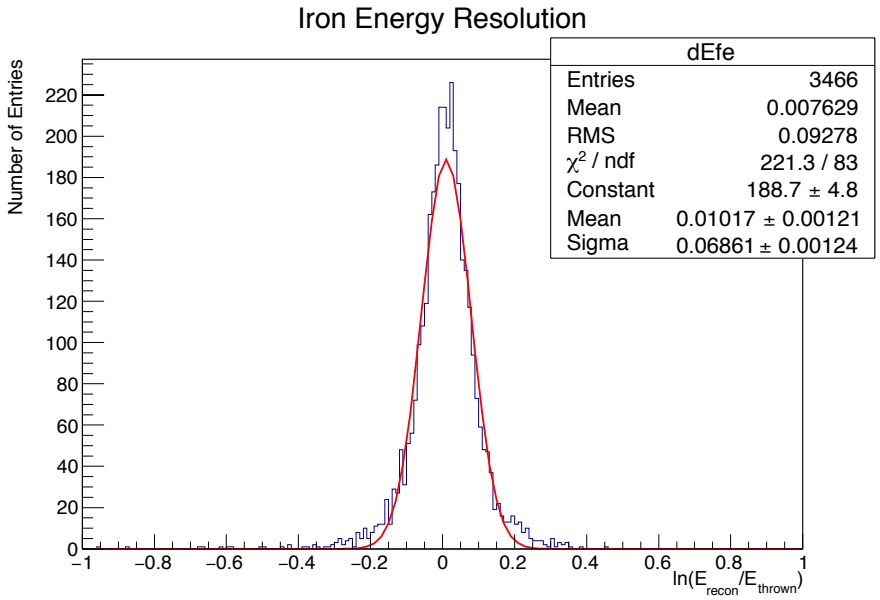

(b) Iron Energy Resolution

Figure 9.14: Scintillation Event Reconstructed Energy Resolution. This histogram shows the energy resolution for proton and iron MC, but only for events that have a fractional contribution of Cherenkov light to their signal of less than 20%. Both histograms demonstrate the energy resolution is on the order of 10% for above $10^{17.4}$eV.

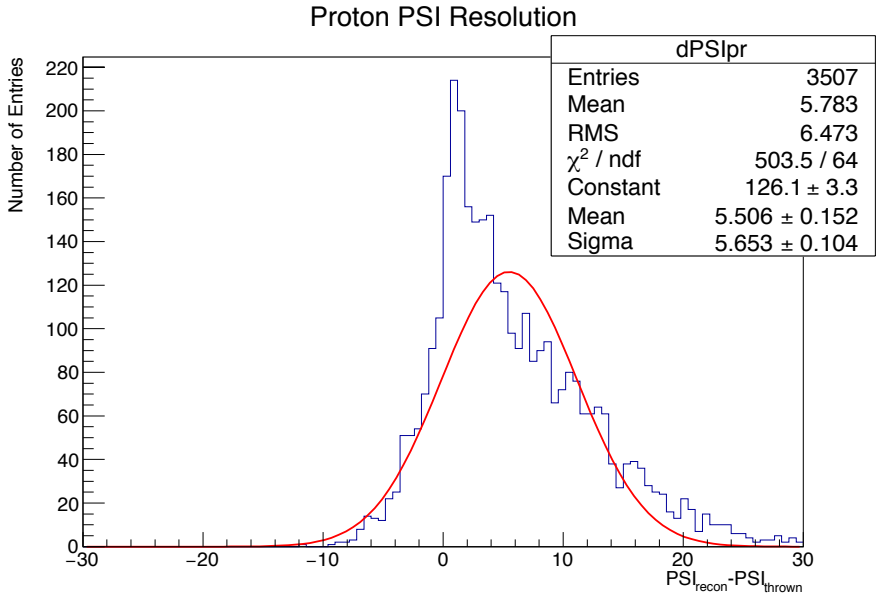

(a) Proton PSI Resolution

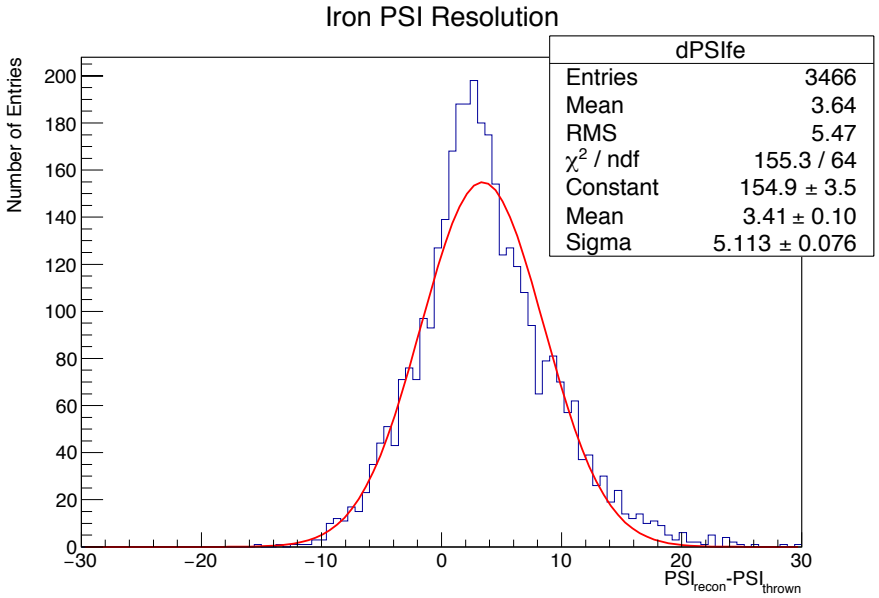

(b) Iron PSI Resolution

Figure 9.15: Reconstructed Scintillation Ψ Resolution. These histograms show the Ψ (angle in shower detector plane Figure 8.5) resolution for proton and iron MC, but only for events that have a fractional contribution of Cherenkov light to their signal of less than 20%. The resolution is reported to be on the order of 6°.

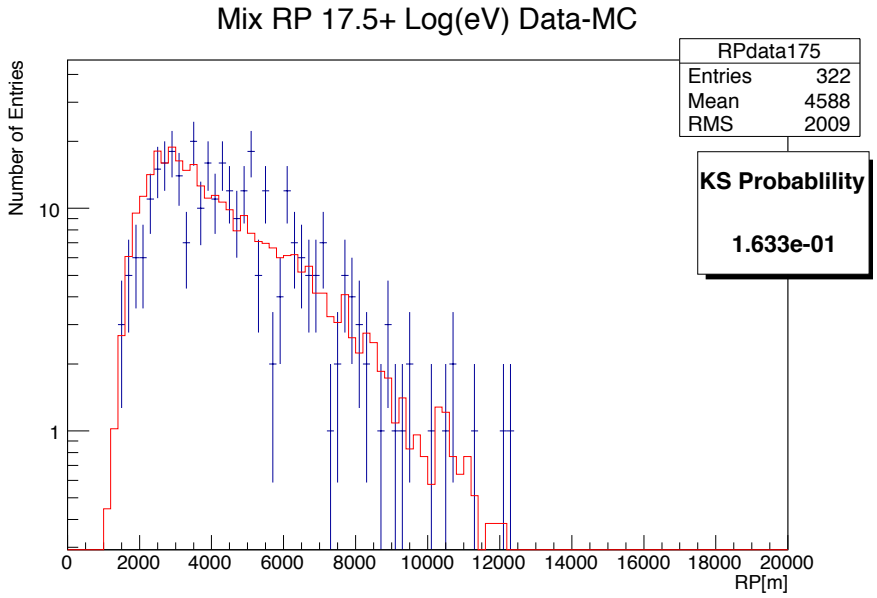

Figure 9.16: Data-MC Comparison of RP. This histogram shows the comparison between the data (points) and Monte Carlo (solid line) for the distance of closest approach (RP).

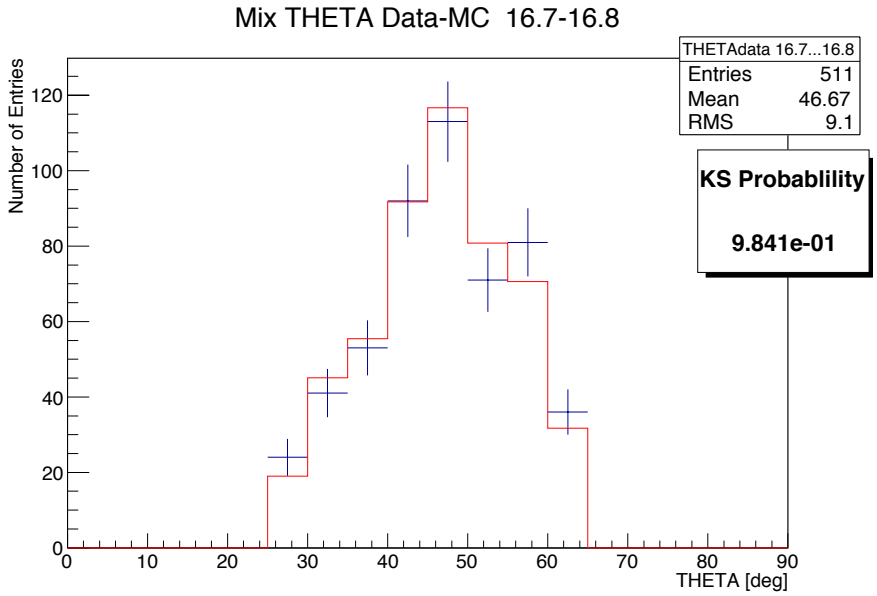

Figure 9.17: Data - MC Comparison of θ . This histogram shows the comparison between the data (points) and Monte Carlo (solid line) for the zenith angle (θ) in the $10^{16.75}$eV energy bin.

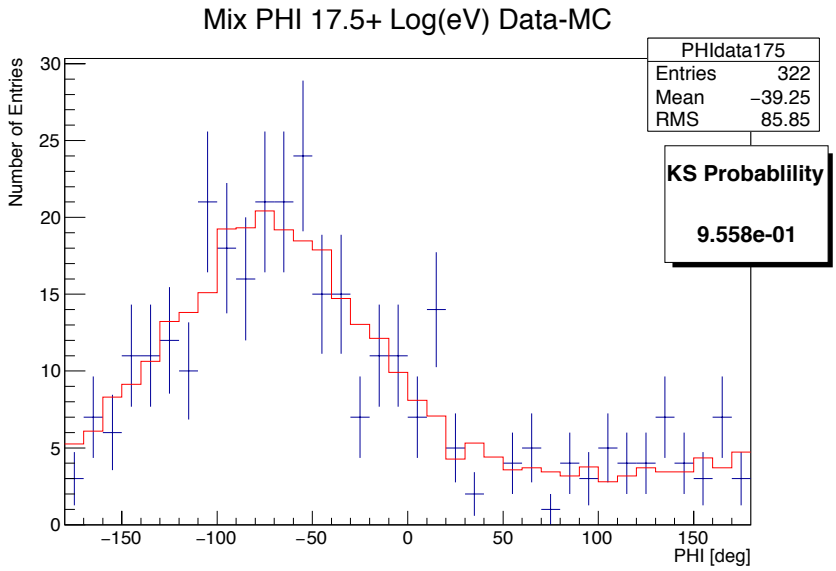

Figure 9.18: ϕ Data - MC Comparison. This histogram shows the comparison between the data (points) and Monte Carlo (solid line) for the azimuthal angle (ϕ) for all events with energies greater than $10^{17.5}$eV.

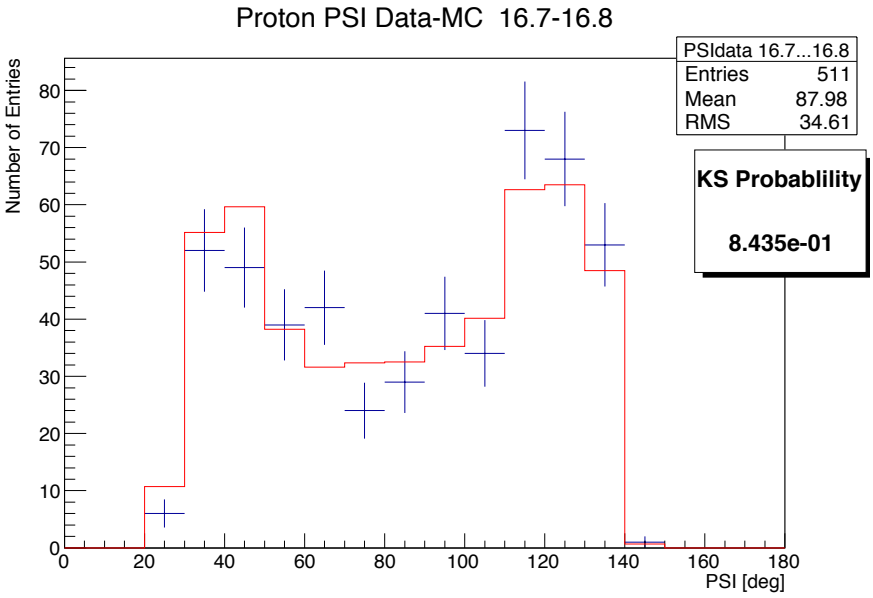

Figure 9.19: Ψ Data - MC Comparison. This histogram shows the comparison between the data (points) and Monte Carlo (solid line) for the angle in the shower detector plane (Ψ Figure 8.5) in the $10^{16.75}$eV energy bin.

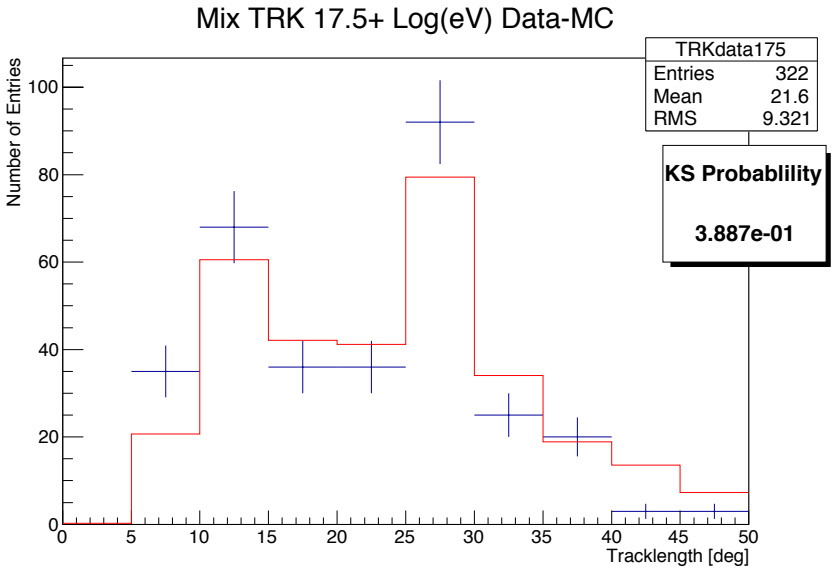

Figure 9.20: Track Length Data - MC Comparison. This histogram shows the comparison between the data (points) and Monte Carlo (solid line) for the track length of showers with energy greater than $10^{17.5} eV$.

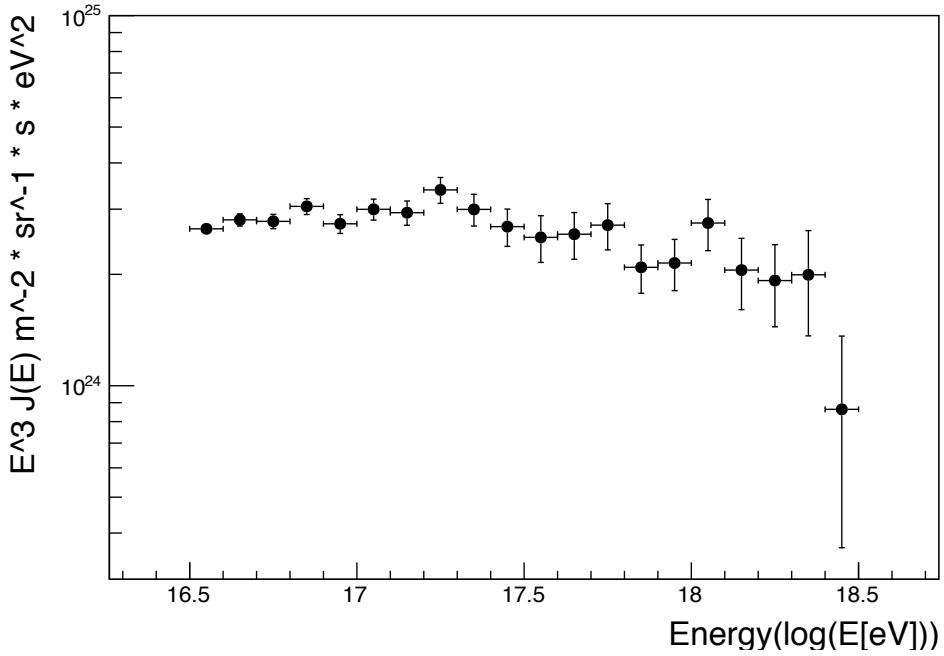

Figure 9.21: TALE Epoch 1 Spectrum. This graph shows the flux of cosmic rays multiplied by the cube of the energy versus the log of the energy of the event. Multiplying by the cube of the energy removes the overall power law of the spectrum and makes it easier to see the finer features in the spectrum.

CHAPTER 10

TALE DISCUSSION

The work of this dissertation is divided into two categories. First is the analysis of the Epoch 1 data recorded between September 2013 and January 2014. Second, this dissertation documents the instrumentation and deployment of the TALE FD detector. The remainder of this chapter discusses the accomplishments made in these two areas and the suggestions for future work.

10.1 TALE FD Spectrum

The goal of the TALE detector is to measure cosmic ray air showers with energies between $10^{16.5}$ and $10^{18.5}$ eV in order to look for evidence of a break in the power law of the spectrum. A break in the spectrum may provide evidence for a transition from a galactic to an extragalactic origin of these cosmic rays. This section details the constraints that can be made on the second knee using the Epoch 1 TALE data.

The spectrum measured by the TALE detector in the Epoch 1 data set is shown in Figure 9.21. The flux of cosmic rays is modeled using a power law of the form,

$$F = CE^{-\gamma}, \tag{10.1}$$

where F is the cosmic ray flux, C is a normalization constant, and γ is the index of the power law. The second knee of the cosmic rays spectrum is expected to be measurable by the TALE detector and would be observed as a distinct change in the index of the measured power law. Figures 10.1a and Figures 10.1b show the best fits to the measured spectrum using one power law and a power law with a single break. The results of the fits are summarized in Table 10.1.

The significance of the break in the spectrum is evaluated with the assistance of Wilk's Theorem [78]. Wilk's theorem is recommended by the Particle Data Group for the comparison of models to binned data [78]. Wilk's theorem states that the deviation,

$$D = -2 \ln \frac{\mathcal{L}(N)}{\mathcal{L}(E)}, \tag{10.2}$$

follows a χ^2 distribution, where D is the deviation, $\mathcal{L}(N)$ is the likelihood that the data matches the null model (N), and $\mathcal{L}(E)$ is the likelihood that the data matches the extended model (E). This theorem holds in cases where the null model is a limited case of the extended model. The deviation D can then be used as a χ^2 value in order to evaluate the significance that the extended model is the correct model. Wick's Theorem continues to state that the number of degrees of freedom of the deviation is given by,

$$d_D = d_E - d_N, \tag{10.3}$$

where d_E is the number of degrees of freedom of the extended model and d_N is the number of degrees of freedom of the null model. In the limiting case where the errors of the measurement are Gaussian,

$$D = \chi^2_N - \chi^2_E, \tag{10.4}$$

where χ^2_N and χ^2_E are the chi-squared deviation for the two models. The significance of the deviation between the two models is,

$$Prob(\chi^2, NDF) = Prob(26.16, 2) = 2.09 \cdot 10^{-6} \cong 4\sigma. \tag{10.5}$$

Due to the significance of the deviation, TALE is able to report evidence for the existence of a break in the cosmic ray spectrum at $10^{17.25}$ eV. The sensitivity of this measurement is limited by statistics and will be improved with the collection and analysis of a larger data set, which already exists.

A second method of testing the significance of the break is to determine the significance that the power law to the right of the break point differs from the power law to the left of the break point. To accomplish this, the spectrum is fit to a single power law to the right of the breakpoint. The resulting power law is then extrapolated to the left of the break point. The uncertainty in the power law fit is used to indicate a standard deviation from the expectation as shown in Figure 10.2. The number of expected events from the best fit and the 1σ deviation of the best fit are calculated using the relationship,

$$N_{evt}(E) = J_{exp}(E) \cdot A\Omega(E) \cdot \Delta t \cdot \Delta E, \tag{10.6}$$

where N_{evt} is the expected number of events at a given energy, $J_{exp}(E)$ is the predicted flux, and $A\Omega(E) \cdot \Delta t \cdot \Delta E$ is the exposure of the detector. The resulting number of events below $10^{17.3}$eV predicted by the best fit extrapolation and the 1σ deviation of the best fit

are 4760 and 4298. The actual number of observed events is 3337. The significance of this is evaluated as,

$$\sigma = \frac{N_{ex0} - N_{observed}}{N_{ex0} - N_{ex1}} = \frac{4760 - 3337}{4760 - 4298} = 3.08, \tag{10.7}$$

where N_{ex0} is the number of observed events predicted by the best fit extrapolation, N_{ex1} is the number events predicted by a 1σ downward uncertainty in the power law fit, and $N_{observed}$ is the number of observed events. The resulting 3σ deviation in the expected number of events seen to the left of $10^{17.3}$eV confirms that there is evidence of a break in the cosmic ray spectrum.

The work presented in this dissertation details the successful instrumentation, calibration, and deployment of the TALE Fluorescence Detector. With the 4-month Epoch 1 data set, TALE is able to report evidence for a break in the power law spectrum near $10^{17.25}$ eV. This is significant because the "second knee" has previously been inferred by combining measurements from many different experiments. The measurement of evidence for break in the spectrum motivates further study of the composition and energy spectrum to determine if cosmic rays in the $10^{16.5} - 10^{18.5} eV$ are consistent with a transition from galactic sources to extragalactic sources. In addition to providing a measurement of the location of the second knee, the analysis of this dissertation is an important check of the operation of the TALE detector and the analysis tool chain.

10.2 The Future of TALE

Despite the substantial technical challenges, the TALE detector was commissioned according to schedule in the fall of 2013 and boasts modern communication, timing, and power networks. In addition to the independent measurement of cosmic ray air showers detailed in this dissertation, the TALE FD has observed air showers in coincidence with the MD FD, the TALE SD array, and presumably the main SD array. An example of an air shower observed by both TALE FD and MD FD is shown in Figure 10.3 and demonstrates the importance of the TALE FD detector in recording the full development of air showers that are close enough to not be contained entirely within the MD field of view. One of the features that is necessary to account for in the MD+TALE 4-ring analysis is the parallax effect resulting from the spatial separation of the MD and TALE buildings. An example which makes the parallax effect evident is a close air showers as shown in Figure 10.4. Without the addition of the TALE detector, MD would not see enough of the shower development to accurately reconstruct the profile of the event. Similarly, air showers have been seen in coincidence with TALE FD, MD FD, and TALE SD array.

The future measurements of the TALE detector will involve using the combined information from the TALE FD, MD FD, and TALE SD in order to better constrain the geometry of the observed air showers and improve the geometrical resolution of the measurements. Most importantly, hybrid observations made with the SD array will allow for a measurement of the average cosmic ray composition and reduce the systematic uncertainty in the measured spectrum.

The success of the TALE detector in being able to observe and reconstruct air showers with high fractions of Cherenkov light has made it a useful tool in evaluating the viability of the proposed Niche array [42]. In February 2015, a prototype NICHE counter was placed in front of the TALE detector in order to observe the pool of Cherenkov light on the ground. A plot of the reconstructed core locations of TALE events seen in coincidence with the NICHE counter is shown in Figure 10.5. A non-imaging Cherenkov array, such as NICHE, would be a valuable tool in confirming the distribution of Cherenkov light produced by air showers. This is an important cross check for TALE since the majority of events below 10^{17} are dominated by Cherenkov light.

In conclusion, the TALE detector has been successfully instrumented and deployed to the field. Evidence has been found for a break in the cosmic ray spectrum at $10^{17.3}$eV. Already, more data have been collected which should turn this into an 8σ observation. The TALE detector will continue to be a valuable tool for measuring cosmic ray air showers with energies in the range of $10^{15.5} - 10^{18.5}$eV. It will enable us to measure the composition and energy spectrum simultaneously and thereby sort out the galactic to extragalactic transition in the cosmic ray sources.

Table 10.1: TALE Power Law Fits.

Number of Break Points	$CHI2/NDF$	**P-Value**	$\gamma Left$	$\gamma Right$	**Break Point**
0	37.4/18	$1.03e-2$	-3.05	n/a	n/a
1	11.24/16	0.78	2.90 ± 0.03	3.23 ± 0.05	17.25

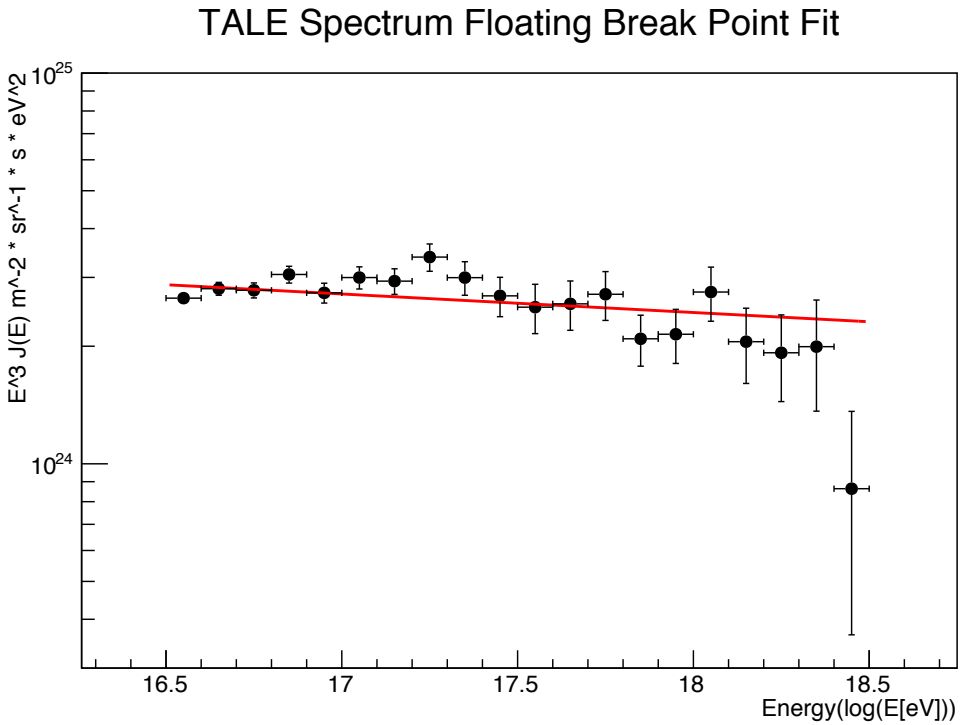

(a) TALE Single Power Law Fit

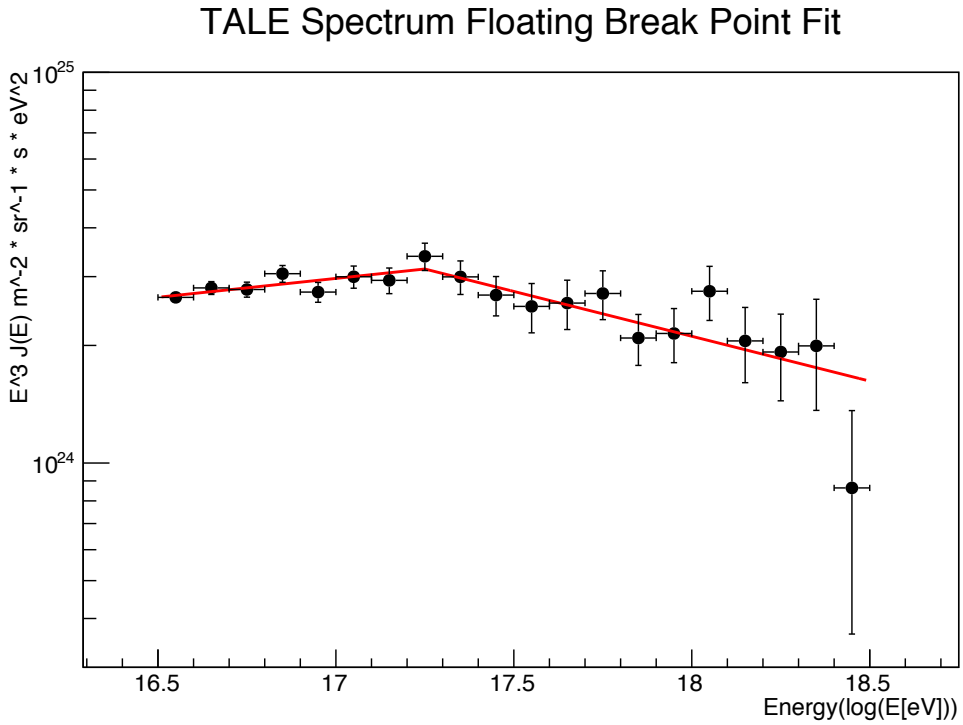

(b) TALE Broken Power Law Fit

Figure 10.1: TALE Spectrum Power Law Fits.

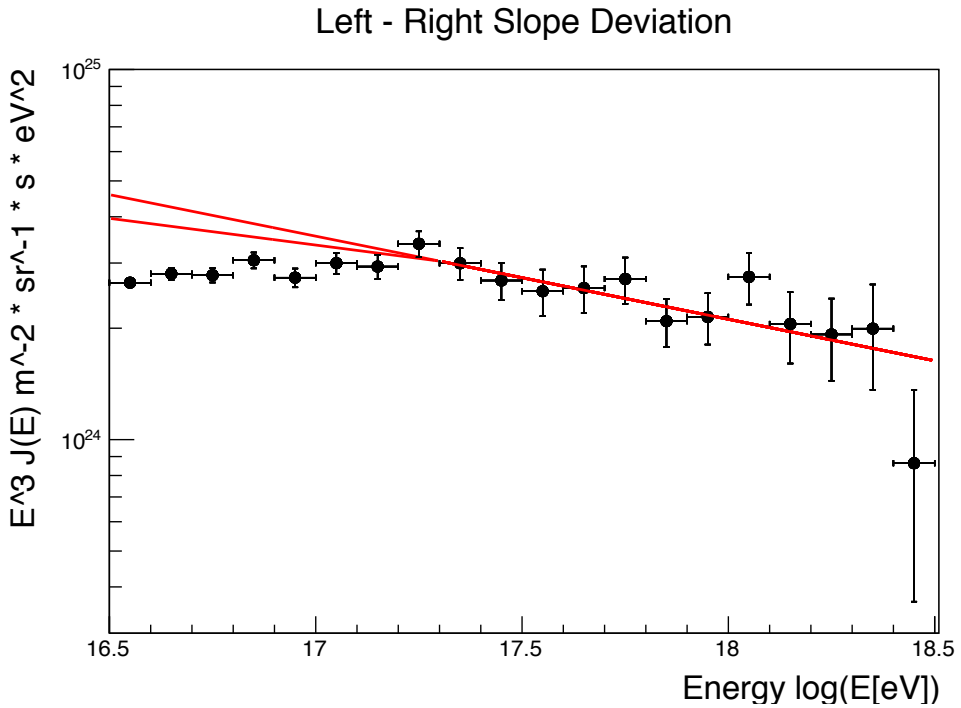

Figure 10.2: Power Law Deviation. This figure demonstrates the deviation of the power law measured to the left side of the break point from the expectation from the power law measured on the right side of the breakpoint. The expected power law (as measured above $10^{17.3}$eV) is extrapolated to the left of the breakpoint. Also drawn is the 1σ downward uncertainty in the power law fit. The data on the left side of the breakpoint are consistent with the 3σ deviation in the slope to the right of the breakpoint.

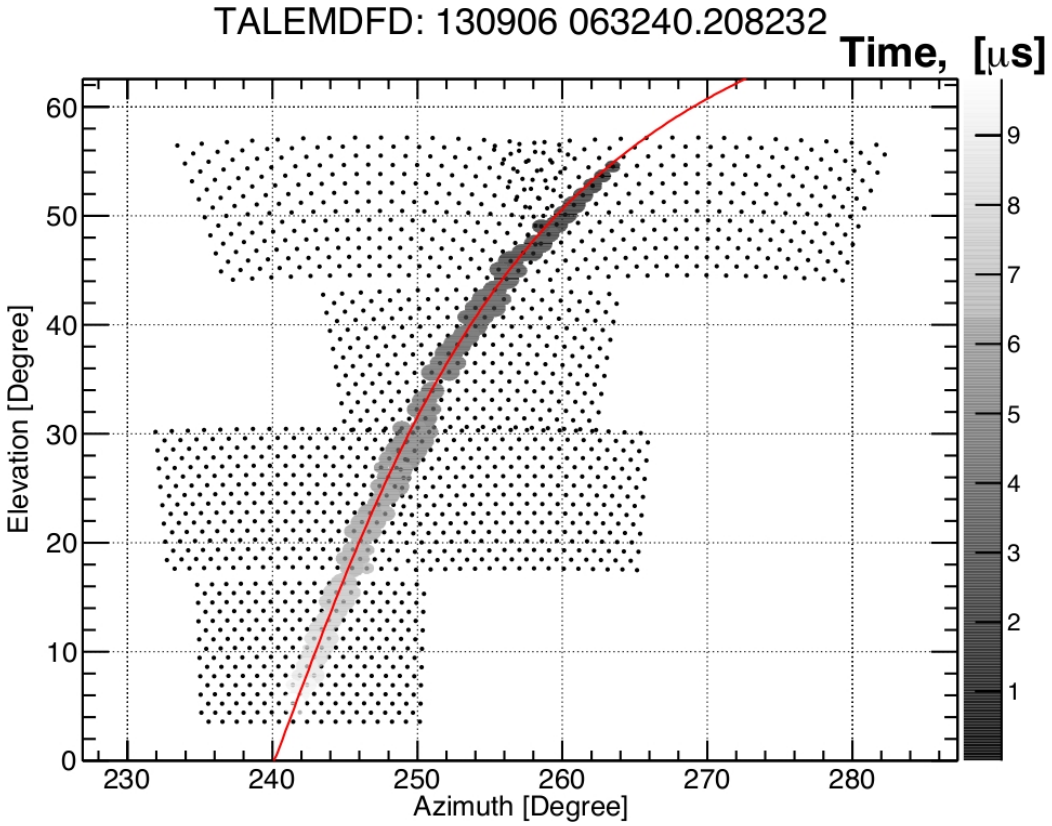

Figure 10.3: TALE-MD Coincident Event. This "four ring" event demonstrates the importance of adding the TALE FD to observe air showers with energies below $10^{18} eV$. Without the TALE detector supplementing the MDFD, the full development of the air shower would not be visible.

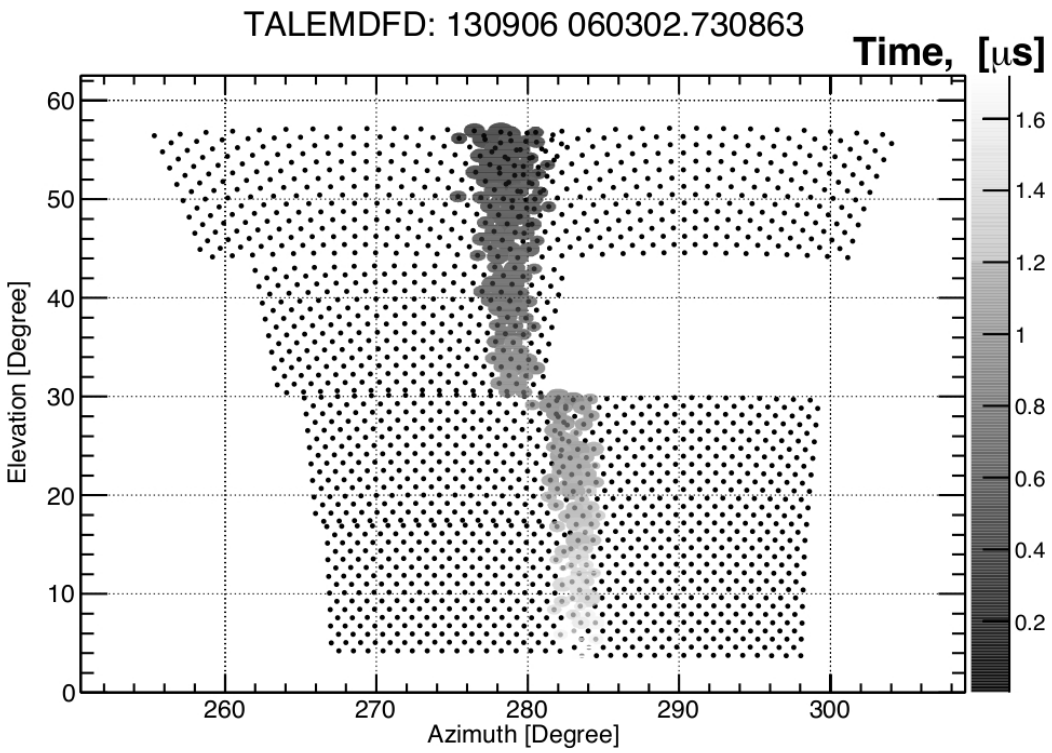

Figure 10.4: TALE-MD Coincident Event with Parallax. This display makes evident the parallax effect seen for events close to the TALE and MD buildings.

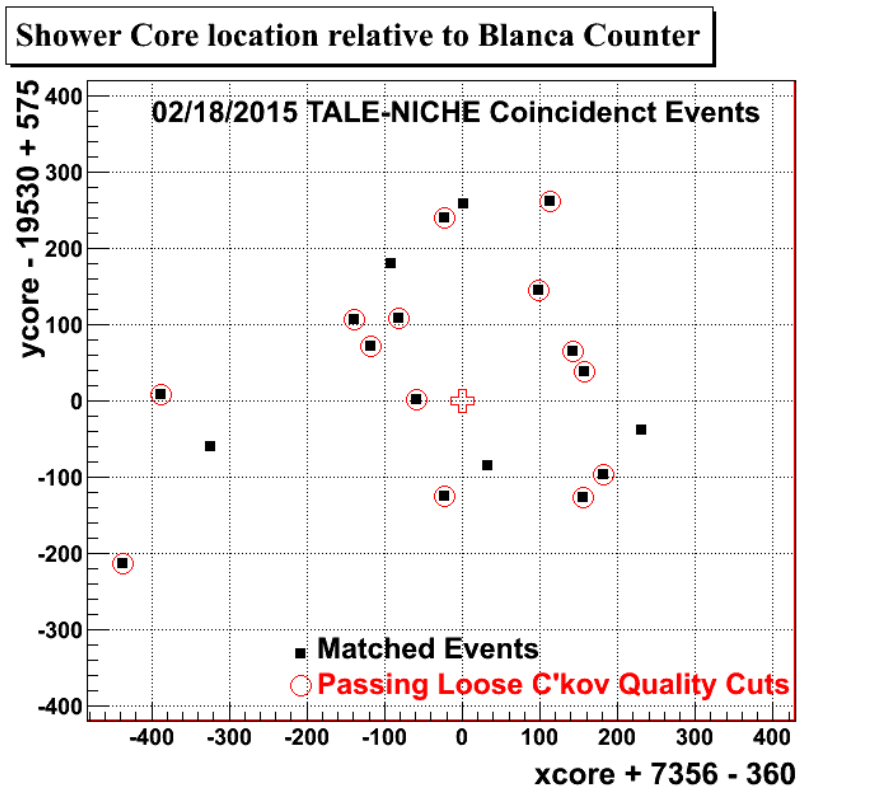

Figure 10.5: TALE - NICHE Prototype Coincident Events. This is a graph of the core location of events seen in coincidence between the TALE and NICHE prototype. The majority of the events are reconstructed with energies in the $10^{15}eV$ decade, which is the high end of the NICHE sensitivity and the low end of the TALE sensitivity. The location of the NICHE counter is indicated by a cross, which is also the origin of the coordinate system. The NICHE counter was 500m directly in front of the TALE detector.

APPENDIX A

SKY OBJECT TRACKING CATALOG

The TALE detector calculates when UV bright objects are in the FOV of a PMT. When such an object is calculated to be within 1.5° of a PMT, the gain of the analog signal from the PMT is set to zero. This ensures that predictable UV sources do not cause excessive trigger rates for the TALE detector.

The catalog of UV bright sources used is show in Table A.1, which also indicates the Right Ascension and Declination of the object. The original catalog used had an incorrect position of Procyon. Using the pointing positions of the tubes and the times for the observed elevated background trigger rate, it was determined that the catalog needed to have the position of Procyon corrected. This is an example of how the careful calibration of the pointing direction of the telescopes was confirmed through astronomical observation. In addition to the UV bright object catalog, the planets Venus, Mars, Jupiter and Saturn are similarly tracked.

Table A.1: UV Bright Night Sky Objects.

Object Name	**RA (Radians)**	**DEC (Radians)**
21 And	0.03658	0.50773
27 Cas	0.2474	1.0597
Algol	0.82103	0.7148
45 Per	1.03782	0.6983
Aldebaran	1.2039	0.28814
Rigel	1.3724	-0.14315
Capella	1.38179	0.8028
Bellatrix	1.41865	0.1108
El Nath	1.42368	0.4993
Psr 0525+21	1.432	0.384
34 Ori	1.44865	-0.00497
Crab Nebula	1.457	0.385
44 Ori	1.46353	-0.10315
Alnilam	1.46695	-0.02098
Alnitak	1.4868	-0.0339
Saiph	1.51735	-0.16877
Betelgeuse	1.54971	0.12928
2 Cma	1.66977	-0.3134
Sirius	1.76779	-0.29175
Adhara	1.82656	-0.50566
Castor	1.98349	0.5566
Procyon	2.0041	0.0912
Pollux	2.0303	0.48915
Regulus	2.6545	0.2089
Spica	3.51328	-0.1948
Alkaid	3.6108	0.8607
Arcturus	3.73348	0.3348
Antares	4.3171	-0.46132
Vega	4.87354	0.6769
Altair	5.1957	0.15478
Cygnus X-3	5.380	0.713
Deneb	5.4167	0.7903
Fomalhaut	6.0111	-0.517
Nunki	4.95346	-0.45896
7 Sco	4.19017	-0.39482
13 Genib	4.3509	-0.18443
Alioth	3.37734	0.97668
Algenib	0.05774	0.265
Menkalinan	1.5687	0.78448
Alhanah	1.7353	0.2862
Atik	1.02158	0.55647
Alphecca	4.07833	0.4663

Table A.1 – continued

Time (s)	Triple chosen	Other feasible triples
Zeta Pup	2.10774	-0.6982
Kappa Sco	4.6341	-0.6812
23 Sco	4.3443	-0.4925
Aludra	1.93772	-0.49398
Graffias	4.2125	-0.34567
6 Sco	4.18043	-0.45577
Pherkad	4.028	1.257
Her X1	4.4358	0.6201
Psr 1937+21	5.137	0.3747
SS433	5.014	0.0855

APPENDIX B

HV STABILITY

To maintain nominal PMT gains within 1.0% it is necessary for the HV be stable to within ± 1.7 V of the intended setting. This relation is easily calculated using the nominal α and β values from PMTs measured in the calibration chapter.

A representative example of the high voltage supply voltage as it is measured during the course of the night is shown in Figure B.1a. The same data are binned in Figure B.1b which demonstrates that this supply is stable over the course of operation with a measured value of $V_{m16} = 1059.4 \pm 0.4$.

These results are reflective of the majority of the HV supplies used in the TALE detector. However, it has been observed that some supplies take a up to two in order to stabilize their output voltage. An example of this HV read back behavior for mirror 17 is seen in Figure B.2a.

The mirror 17 HV supply represents the most dramatic change in the value of any HV supply. The binned HV read back values for mirror 17 are shown in Figure B.2b. The measured value for the supply voltage of cluster 17 is $V_{m17} = 1058.7 \pm 1.1$. Even for the m17 supply, which exhibits the least consistent voltage out of all of the supplies, it is still within the range where the uncertainty in the tube gain due to the fluctuations of the HV supply is below 1%.

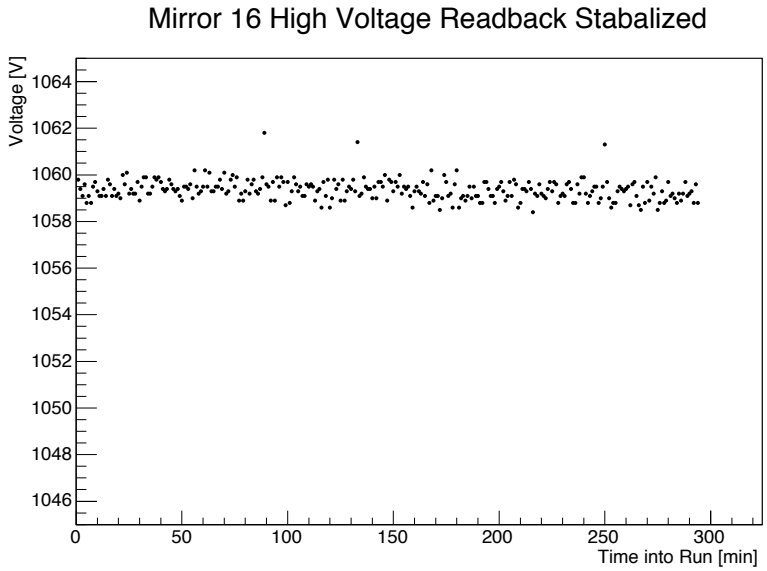

(a) M16 HV Readback Scatter plot

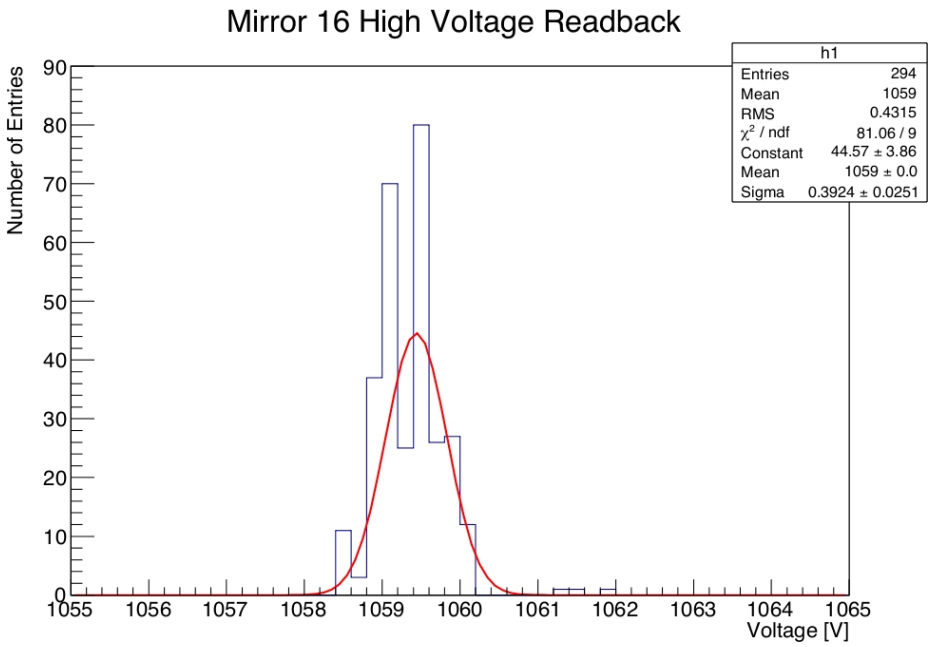

(b) M16 HV Readback Histogram

Figure B.1: M16 HV Readback. The figures show the stability of the HV supplied to M16 over the course of the Feb 17, 2015 operation.

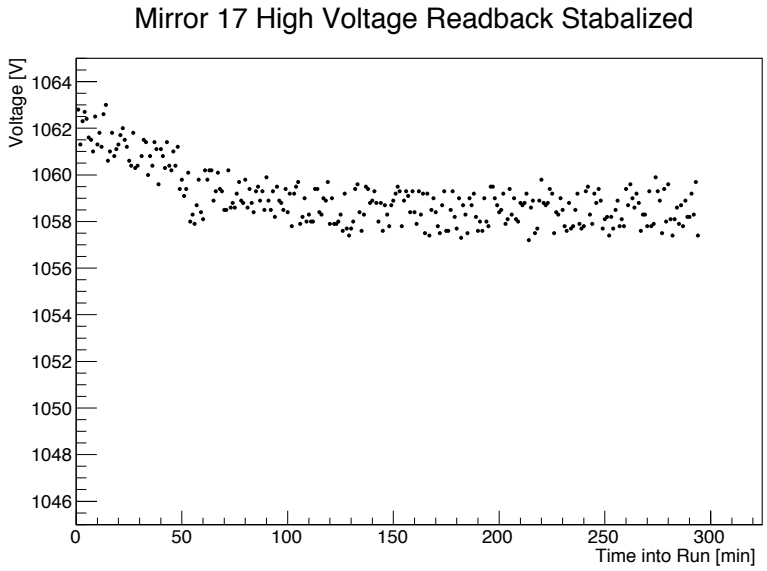

(a) M17 HV Readback Scatterplot

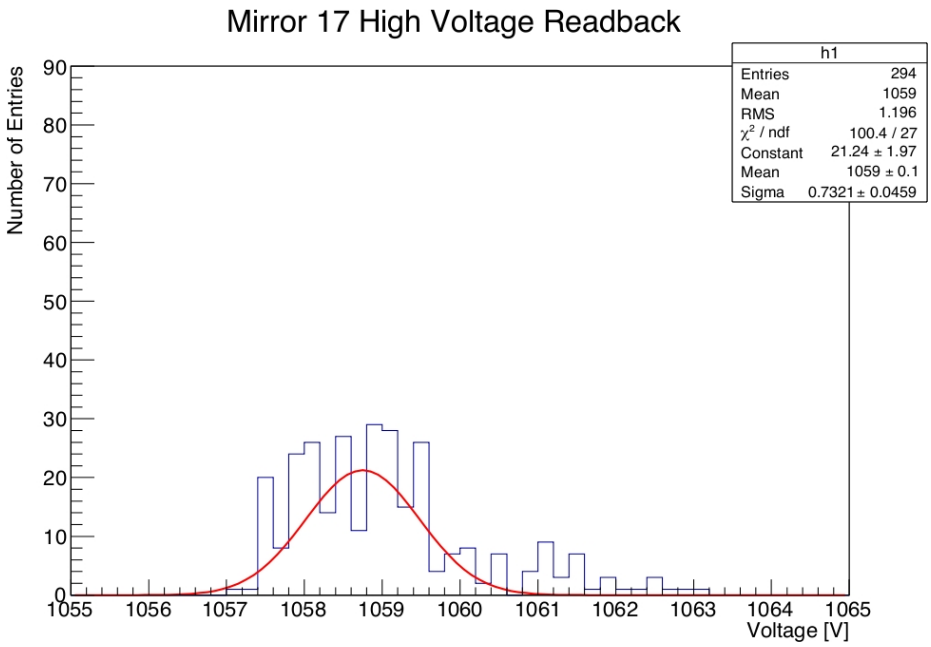

(b) M17 HV Readback Histogram

Figure B.2: M17 HV Readback. The figures show the stability of the HV supplied to M17 over the course of the Feb 17, 2015 operation.

APPENDIX C

DAC GAIN ADJUSTMENT

C.1 Gain Calculation

Solving the circuits diagram for the programmable gain amplifier shown in Figure C.1 yields the following relationships between the input DAC setting and the tube signal gain. First, the gain control voltage V_g is determined by the DAC output voltage, which is controlled with software commands.

$$Vg = (V_{dac} - ((V_{dac} + 5.0)/(R_{d1} + R_{d2})) * R_{d1}); \tag{C.1}$$

This provides a control voltage with a range of -1.25 to 1.82 V which is used to control the National Semiconductor Comlinear CLC522 Op-Amp. This overlaps well with the CLC522 Op-Amp optimum range of -1 to +1. In order to ensure that gains are only set to this optimum range, the set DAC values are limited to the region of $0x14D < DAC < 0xBBB$ (the 0xNNN indicates hexadecimal values).

For this circuit, $R_{d1} = 3k\Omega$, $R_{d2} = 1k\Omega$, and V_{dac} is the DAC output voltage with a range of 0.0 - 4.0 V in 0.001 V steps. This gain control voltage results in an overall gain being applied to the individual PMT channel signals according to,

$$GAIN = 1.85 * (Rf/Rg) * ((Vg + 1.0)/2.0). \tag{C.2}$$

For the pmt channels $R_f = 1.5k\Omega$ and $R_g = 2.0k\Omega$. This yields an overall gain range of 0 to 1.3875. Finally, after tube signals are amplified through the DAC controlled Op-Amp, they are fed through a fixed gain National Semiconductor CLC501 Op-Amp set at a gain of 17. Overall, the input signal has a controllable gain applied to it that varies from 0 to 23.59

C.2 Digitization Noise

Another potential source of noise comes from the CLC522 FADC amplifiers, which have their DC output altered by the input voltage. This means that any noise in the power supply voltage will be propagated to the signal. To control this effect, LV regulators are installed onto the FADC boards. As an important note of documentation, the LV regulators are not included in any of the original circuit diagrams even though they are included on the TALE FADC boards.

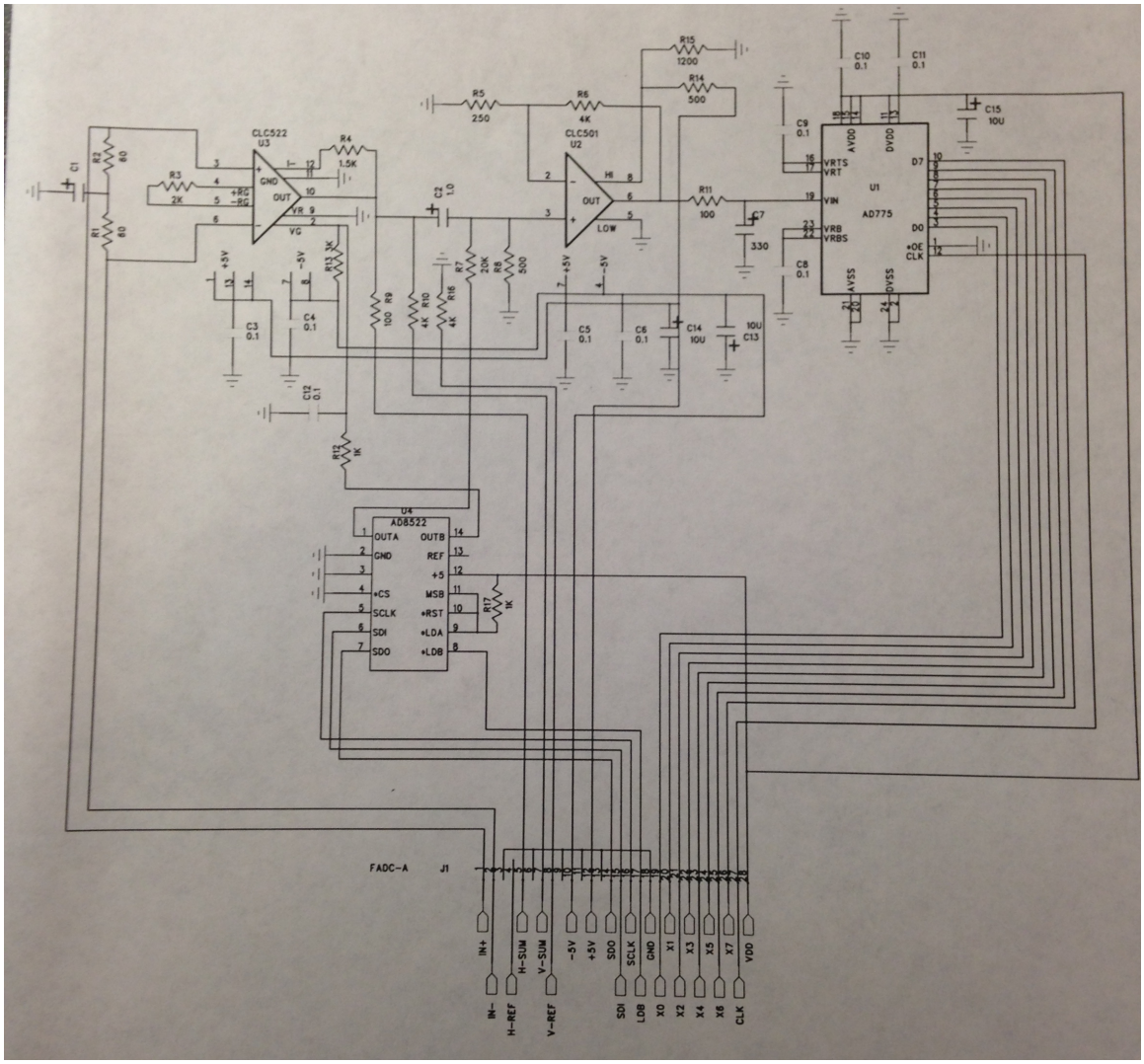

Figure C.1: Hi Gain Circuit Diagram. This is the circuit diagram for the Hi Gain channel. Each PMT channel has an individual channel for readout.

APPENDIX D

DSP OPERATION AND COMMUNICATION

The majority of the communication, control, and trigger software for the rack electronics is run using DSP 56309 [65] on the Trigger Board and the DSP56166 [70] on the FADC boards. The two types of DSPs are mounted on small daughter modules that provide a common interface between the DSPs and the boards regardless of the model of the DSP module used. They are shown in Figure D.1.

The DSP 56309 and DSP 56166 are 24-bit and 16-bit devices, respectively. Both are based on a Harvard architecture, possessing separate program (P-memory) and data (X-memory) spaces. Neither of these devices are equipped with nonvolatile memory aside from small boot-loader programs. This means that every time power is supplied to the DSP, the compiled operational instructions must be loaded into program memory.

The DSP56309 can be operated up to 100MHz using an adjustable internal clock. The TALE detector operates the DSP56309 at 80 MHz. This device employs 24-bit addressing, a barrel shifter, instruction cache, and direct memory access [65]. The DSP56309 has 20480×24 program memory and 7168×24 data memory. An operation diagram of the DSP56309 is shown in Figure D.2. This figure shows how most of the interaction to the DSP56309 occurs by interrupting the DSP. Interrupts come from the Link Module, the Trigger/Timer PLD, and the internal timer. The Link Module interrupts the DSP56039 to request that data be sent up or to request to send a command down to the DSP56309. Commands sent from the Link Module are stored in a command queue to be handled when there are no high priority activities to complete. The Trigger/Timer PLD interrupts the DSP56309 to increment the DSP56309 internal timer counters as the PLD 13-bit timer rolls over. Additionally, this PLD issues interrupts when the Level 0 trigger criteria are met and the DSP56309 needs to issue a STORE and to queue up future scans. When not handling interrupts, the DSP56309 executes queued processes with the following priority: (1) analyze

scan results and set up DMA readout events that pass the Level 2 trigger and (2) handle queued commands from the Link Module.

The DSP56166 has a similar architecture and operates similarly to the DSP56309. However, the DSP56166 has only 2k x16 program memory and 4k x 16 data memory.

The software for the Trigger Board and FADC DSPs are written in assembly language and are compiled using a set of tools documented in Table D.1 that were originally distributed by Motorola for Microsoft DOS and can be executed on Linux-based machines with the help of emulation tools such as Dosbox or Wine [79] [80].

The object code for both DSPs is stored in SREC format and must be parsed by the Link Modules and downloaded to the processor. The Link Modules communicate with the Trigger DSP over the HOST port of the DSP56309 as shown in Figure D.3. The communication lines between the DSP and the Link Module are driven by a series of BTL transceivers on the Trigger Board. The Host port contains a number of registers for communication summarized in Table D.2. The DSP can signal that it needs service from the Link Module by setting the HF2 or HF3 flag bits in the Interrupt Service Register. The different types of requests are listed in Table D.3. The Link Module is capable of servicing the Trigger DSP using the Command Vector Register. The routines that can be executed during an interrupt are summarized in Table D.4.

As an important point of documentation, there are two types of boards on which the DSP56309s have been mounted. One group is labeled dsp56603 3/27/00 and the other is labeled dsp56309 11/12/00. The dsp56603 3/27/00 requires a polled interface during boot and can then be switched to interrupt driven mode after a successful boot. The dsp56309 11/12/00 can be interfaced with using either interrupt or polled interface during boot. This variation was not documented prior to the refurbishment of the HOST-TRIGGER modules.

After a Link Module receives a successful boot messages from a Trigger DSP, the DSP needs to be informed of its telescope number. Setting the telescope numbers for the DSPs is done by modifying a register in the data (X-memory) space of the DSP. Table D.5 summarizes the registers in the Trigger DSP that are modified during detector operation.

Immediately after boot and run configuration, the individual FADC channels are tested to check the response of the gain and pedestal DACs (known as the FADC test). The details of this test are discussed in Appendix H.

After the Trigger DSPs are booted, the program memory of the FADC DSPs is loaded. The program memory of the DSP 56166 is not large enough to contain all of the instruction for both testing the FADC readout and also taking data. Employing a memory overlay after all necessary self-tests on the FADC DSPs are complete circumvents this problem.

A summary of the FADC DSP program memory maps for the two modes is shown in Figure D.4.

The FADC DSPs also need to have a pair of their data (X-memory) registers modified for detector operation. These are summarized in Table D.6. In addition, the registers described in Table D.7 determine the values loaded in the gain and pedestal DACs.

Table D.1: DSP Compilation Tools. This is a list of the Motorola programs necessary in order to compile the assemble code that runs on the Trigger and FADC DSPs.

Program Name
asm56000.exe
asm56100.exe
tiohist.exe
cldinfo.exe
cofdmp.exe
srec.exe
wstubq.exe
cldlod.exe
dos4gw.exe
dsplib.exe
dsplnk.exe
pminfo.exe
strip.exe

Table D.2: HOST/TRIGGER Register Names. This table summarizes the HOST port register names and acronyms.

Register ACRONYM	**Full Name**	**Details**
ISR	Interface Status Register	HOST side register for reading HF2 and HF3 Flags
HCR	HOST control register	DSP side register used to set HF2 and HF3 signal Flags
CVR	Command Vector Register	The register used to signal an interrupt to the DSP
RXH: RXM:RXL	Data Receive Registers	Three 8-bit registers loaded into the 32-bit DSP side HTX register
TXH: TXM:TXL	Data Transmit Registers	Three 8-bit registers loaded from the 32-bit DSP side HRX register

Table D.3: HOST/TRIGGER Service Request. This table details the type of service requested by the Trigger DSP based on the configuration of the HF2 and HF3 ISR bits.

Message Type	**HF3**	**HF2**	**Notes**
Scan Replies	0	0	Scan replies are not sent up
Data	0	1	
Message	1	0	
Trigger	1	1	

Table D.4: Communication Interrupts. This table shows the interrupt routines available for the Link Module to direct the Trigger DSP to using the CVR register on the HOST port.

Subroutine	**Location in Program Memory**	**Interrupt Channel**	**Notes**
ack1	P:0x18	DMA 0	Request Data Packet (RAW data)
ack1	P:0x1A	DMA 1	Request Data Packet (Other FADC packet)
ack2	P:0x1C	DMA2	Request Trigger Board Packet
cmdread	P:0x1E	DMA3	HOST Command (command read)

Table D.5: TRIGGER Configuration. This table details the registers in Trigger DSP X-Memory that must be properly configured for telescope operation.

Memory Address	**Details**
X:0x0000	The Telescope Number (15-24) is stored here
X:0x000A	The Manyhits prescale value is stored here

Table D.6: FADC Configuration. This table details the registers in Trigger DSP X-Memory that must be properly configured for telescope operation.

Memory Address	**Value**	**Details**
X:0x000c	30	Integrated Pulse "HIT" Threshold
X:0x0040	50	Half width of the M2 read window

Table D.7: FADC DAC Configuration. This table details the memory location that must be modified to adjust the DAC setting for the TALE detector.

Memory Address	**Channel**	**Initialized Value**	**Notes**
X:0x0040 - 0x0047	0xF-0x8	0x100	Tubes 15-8 Pedestal DAC values
X:0x0048 - 0x004b	0x13-0x10	0x100	Low Gain HSUM, High Gain HSUM,Low Gain VSUM, HighGain VSUM Pedestal DAC values
X:0x004a - 0x0053	0x7-0x0	0x100	Tubes 7-0 Pedestal DAC values
X:0x0054 - 0x005b	0xF-0x8	0x100	Tubes 15-8 Gain DAC values
X:0x005c - 0x005f	0x13-0x10	0x001, 0x100, 0x001, 0x100	Low Gain HSUM, High Gain HSUM,Low Gain VSUM, HighGain VSUM Gain DAC values
X:0x0060 - 0x0067	0x7-0x0	0x100	Tubes 7-0 Pedestal DAC values

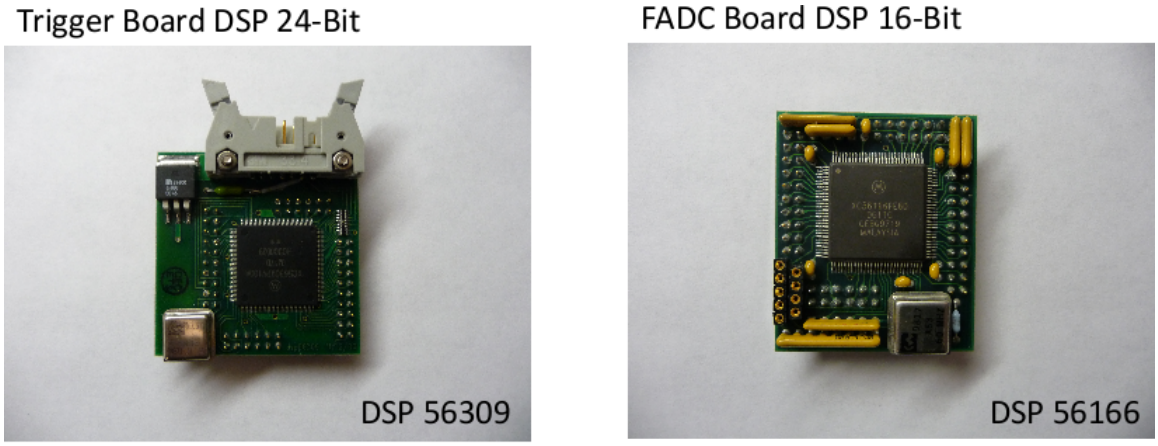

Figure D.1: TALE DSP Picture. This picture shows the DSP 56309 used by the Trigger Boards on the left. The DSP 56166 used by the FADC board is shown on the right.

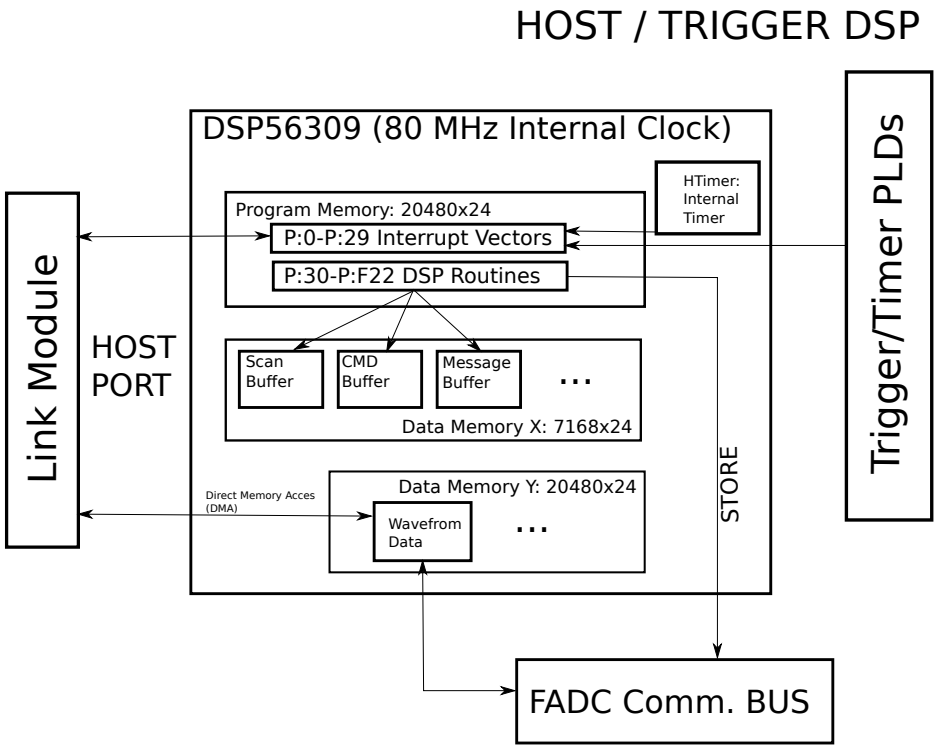

Figure D.2: DSP56309 Operation Overview. This figure shows how most of the interaction to the DSP56309 occurs by interrupting the DSP. Interrupts come from the Link Module, the Trigger/Timer PLD, and the internal timer. When not handling interrupts, the DSP56309 handles queued precesses with the following priority: (1) analyze scan results and set up DMA readout events that pass the Level 2 trigger and (2) handle queued commands from the Link Module.

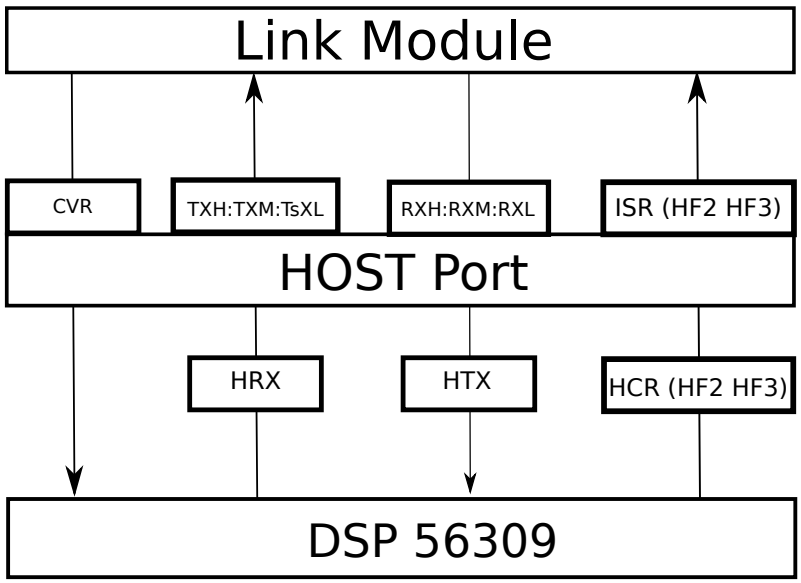

Figure D.3: Link to Trigger DSP Communication. This schematic diagram details how a Link Module communicated to a Trigger Board DSP. The diagram shows the transmit and receive registers available to the host port. In addition, there is a ISR register which allows the DSP to set flags indicating that it needs service from the links module. The CVR register is used to interrupt the DSP and force it to jump to a specific routine in program memory.

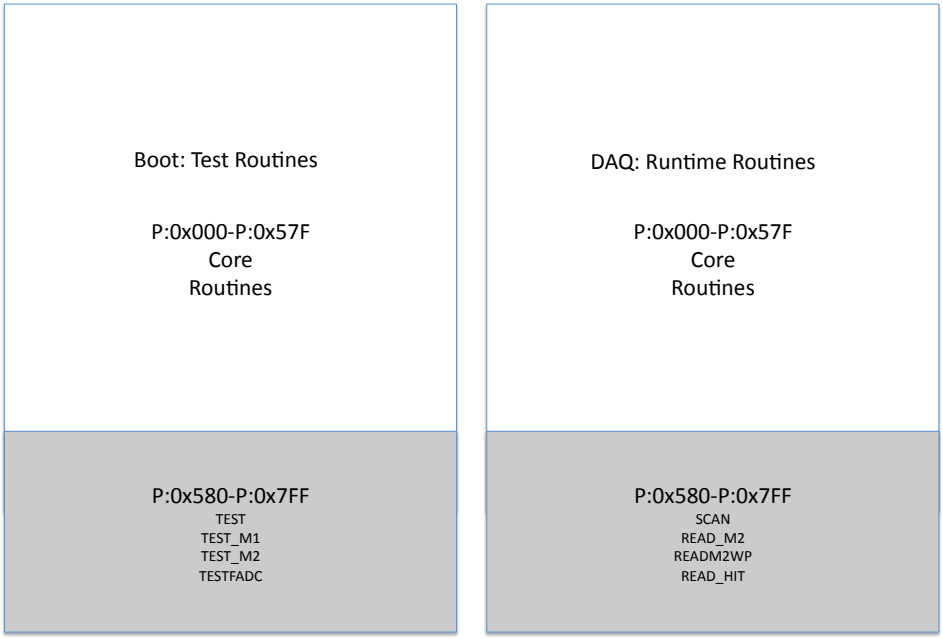

Figure D.4: FADC Program Memory Map. This figure details the region of memory and routines that are involved in the FADC memory overlay.

APPENDIX E

PRE-SCAL CONFIGURATION AND DEADTIME

In order to collect UVLED data, the detector must be set to a calibration mode with a *pre-many* value of zero. This is the default mode of the TALE detector after boot and should not initially need to be modified. The *pre-many* variable was introduced in Table D.5 as one of the important registers to modify during detector operation. A detailed record of the effect the *pre-many* variable has on the detector state is recorded in Table E.1. Importantly, the *pre-many* variable is used to limit the readout of events where more than 200 tubes have recorded pulses for an event. Moreover, the *pre-many* variable alters the manner in which dead time is introduced to the detector.

During normal operation, a TALE Trigger Board keeps a counter (trgscal) that increments up by 3 counts for every triggered event and down by 1 every time the internal htimer interrupts the DSP ($330\mu s$). Should the value of the counter increase above 9, then trigger interrupts are ignored in order to prevent the DSPs from filling up their buffers and crashing. The time it takes the trgscal counter to return to zero and re-enable triggers is called "introduced dead time". The value of the *pre-many* variable determines whether the trgscal counter continues to increment up during the time when triggers are rejected. Should the trgscal register increment while triggers are refused, the amount of introduced dead time is equal to the amount of time it takes the trgscal counter to count down from 10, 11, or 12 on the value of the trgscal counter when incrementation was disabled. However, if the *pre-many* variable is set to a value that causes the trgscal counter to increment during the period of trigger refusal, the detector will avoid re-enabling triggers until the trigger rate returns to an operational level. The effect of properly setting the *pre-many* bit for normal data taking can be seen in Figure E.1 which demonstrated the linear relationship between "dead time" and the number of refused triggers.

Following the UVLED data collection, a check of the memory space of the TALE detector is performed known as the Trigger Test. During this operation, a test pattern is written to

the M2 memory on the FADC boards. Readout for the detector is enabled and the output for each detector is monitored to ensure that the test pattern successfully passed all trigger requirements of the detector and that the correct pattern is read out. Should any region of M2 report a read error, it is flagged as needing to be replaced by the operator. As an essential note, the Trigger Test (performed after the DSP memory overlay) sets bit 7 of the *pre-many* variable described in Table E.1. Failure to change the *pre-many* value of the bit will dramatically influence the stability of the detector. After the UVLED data are taken, *pre-many* is set to a value of 0x40 to ensure stable operation in the event of spurious high trigger rates.

Table E.1: *Pre-many* Effect on Detector Operation. The *pre-many* variable is a way to prescale the number of manyhit events that are read out during periods of high trigger rate or intentional illumination of the PMT camera. However, the value of *pre-many* also influences how the detector introduces deadtime. Should the trigcounter not be incremented after the TRIGGER DSP has set the REFUSE bit, then triggers will quickly be re-enabled and the trigger buffer can be filled up. This leaves the detector highly unstable during data-taking operation when noise from background sources, such as stars, can dramatically change the trigger rate. For data-taking operation, *pre-many* should be set to 0x40.

Premany Values	**CALIB BIT**	**TRG COUNTER INC. on REFUSE**	**Notes**
$<$ 0x3F	1	NO	Calibration Part. Dead time not introduced. All many-hits pre-scaled regardless of event time.
0x40 - 0x7F	0	YES	Regular Data. Many-hits pre-scaled only if they occur during LIDAR firing times.
$>$ 0x80	0	NO	Bit 7 is a control bit. Only to be used for stability testing

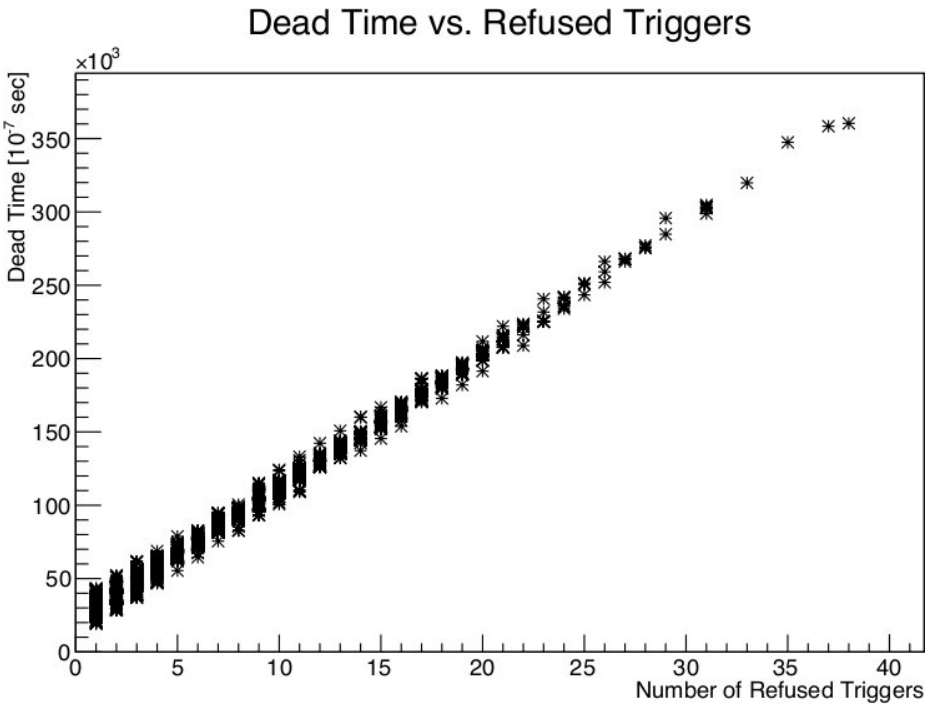

Figure E.1: Dead Time with "trgcal" Counter Enabled. This figure shows a scatter plot of introduced dead time a function of the number of refused triggers. It can clearly be seen that the introduced dead time scales with the trigger rate when the *pre-many* value is set appropriately.

APPENDIX F

UVLED FILTERS AND UNIFORMITY

UVLED flashers are mounted in the center of the each telescope mirror and face the cameras. Each UVLED flasher illuminates its respective camera 500 times. The detector reads out the full waveforms of these flashes. The TALE UVLED flashers were initially instrumented with quartz diffusers during the period of Sept 2013 - Jan 2014. Theses quarts diffusers were found to produce nonuniform illumination of the PMT cameras, as demonstrated in Figure F.1, so they were replaced with teflon diffusers on Jan 20, 2014. The effect of introducing uniform diffusers can be seen in Figure F.2.

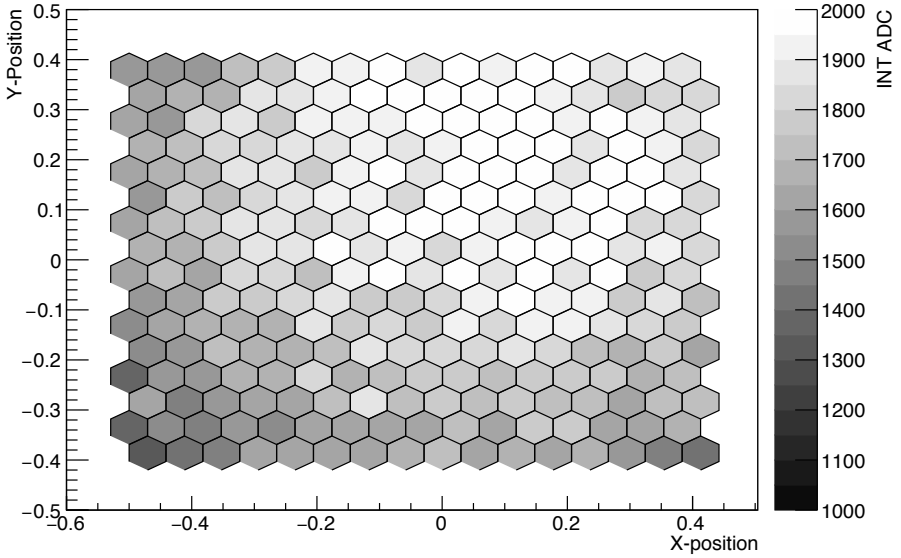

Figure F.1: UVLED Quartz Diffuser. This figure shows the event display of a UVLED event when nonuniform quartz diffusers were installed in the UVLED flashers. The amount of incident light can be clearly seen to vary over the surface of the camera by as much as a factor of two.

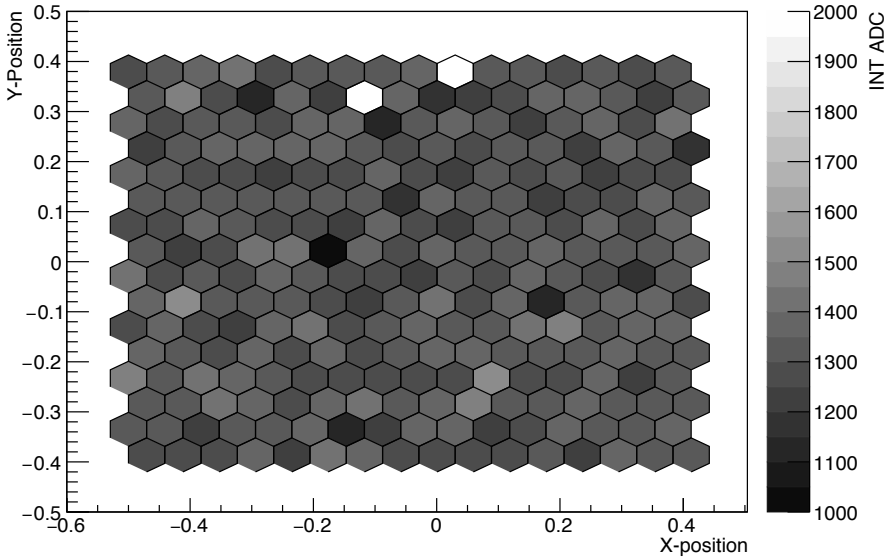

Figure F.2: UVLED Teflon Diffuser. This figure shows the event display of a UVLED event when uniform teflon diffusers were installed in the UVLED flashers. The amount of incident light can be clearly seen to vary only within expectation from photo-statistics. This display of the UVLED also shows two channels that failed to read out. The problem was traced to breaks in the signal cables which were repaired and illustrates one of the other important diagnostic capabilities of the UVLED data.

APPENDIX G

EXCESS NOISE FACTOR SIMULATION

The Excess Noise Factor (ENF) was introduced in Chapter 5 and accounts for the statistical noise generated by the secondary emission process. It is used in determining the number of photoelectrons with Equation 5.3. An estimate of the ENF can be determined through simulation. A simple simulation performed modeled an 8 stage PMT with a QE of 0.262, collection efficiency of 0.9, and a secondary emission distribution modeled as a Poisson with a mean of 3.34. The value of the Poisson mean was determined from the average α and β values for the TALE PMTs. In the simulation, the PMT was illuminated 10,000 times using a light source with the Poisson mean of 60. The resulting distribution of electrons collected at the anode is shown in Figure G.1. Calculating the Excess Noise Factor is done using

$$ENF = (\gamma_{mean} \cdot coll_{eff} \cdot QE) \cdot (RMS^2 / < Sig >^2) \tag{G.1}$$

where γ is the mean number of simulated photons (60), $coll_{eff}$ is the simulated collection efficiency (0.9), QE is the quantum efficiency of the tube (0.262), RMS is the RMS deviation of the simulated signal, and $< Sig >$ is the average simulated signal. In the case of the Figure G.1 simulation, the ENF evaluates to,

$$ENF = (60.0 \cdot 0.9 \cdot 0.262) \cdot ((65135)^2/(203957)^2) = 1.44 \tag{G.2}$$

The simulation resulted in predicting an ENF of 1.44 for secondary emission processes that are perfectly Poisson. However, it is known that the secondary emission process follows a slightly wider distribution than a simple Poisson. A study of the Middle Drum detector, half of which is instrumented with the same phototubes as the TALE detector, shows that the ENF for the TALE PMTs has an average value of 1.55. This value was confirmed by the phototube manufacturer [73].

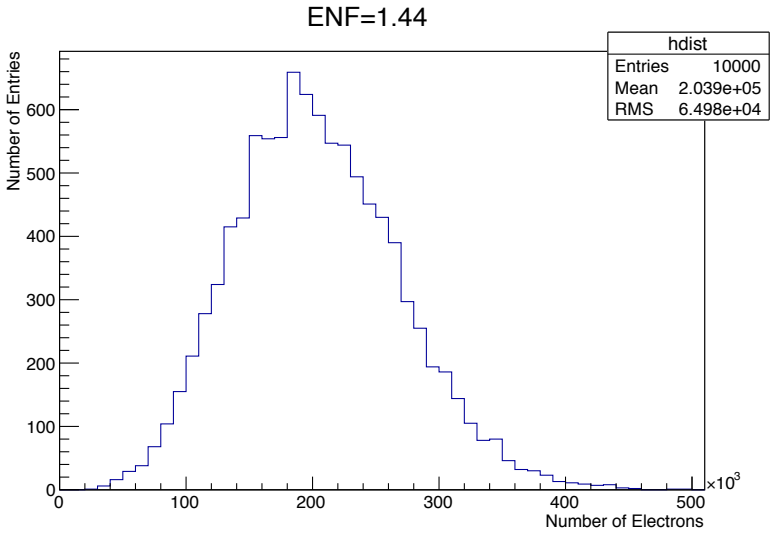

Figure G.1: ENF Simulation. This shows the simulated number of electrons collected at the anode when a PMT is illuminated by a Poisson light source. In this simulation, the secondary emission process created an excess noise factor of 1.44 for the PMT.

APPENDIX H

FADC TESTS

During the FADC test, setting the gain DACs to zero disables the analog input to the FADCs and pedestal and variance measurements are taken on the digitized signals for a series of values for the Pedestal DAC. The results of the signal average and signal RMS for a good channel are shown in Figure H.1a and Figure H.1b, respectively. Any channel that reports as unresponsive or with a signal RMS of greater than 0.8 ADC counts is reported in the operations logs. An example of a channel that is reported for an excessive RMS is shown in Figure H.2. This test also allows the linearity of the pedestal DACs to be checked.

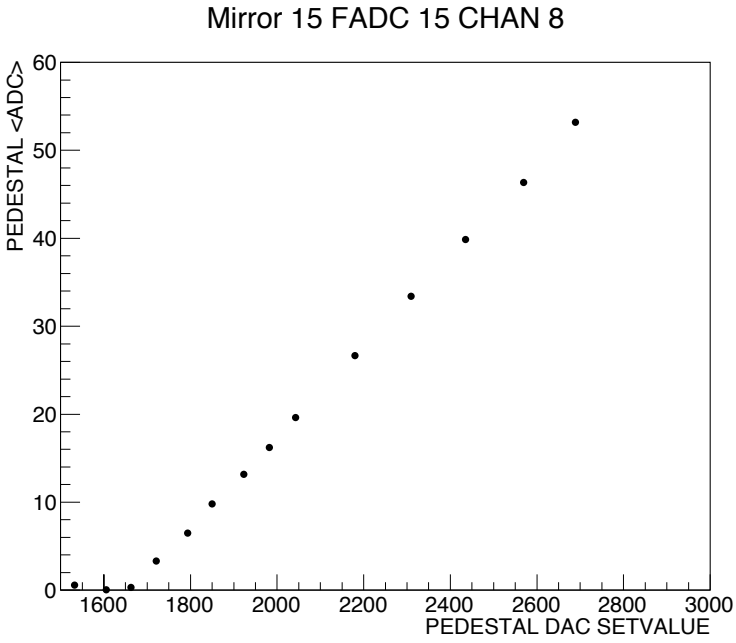

(a) TALE Single Power Law Fit

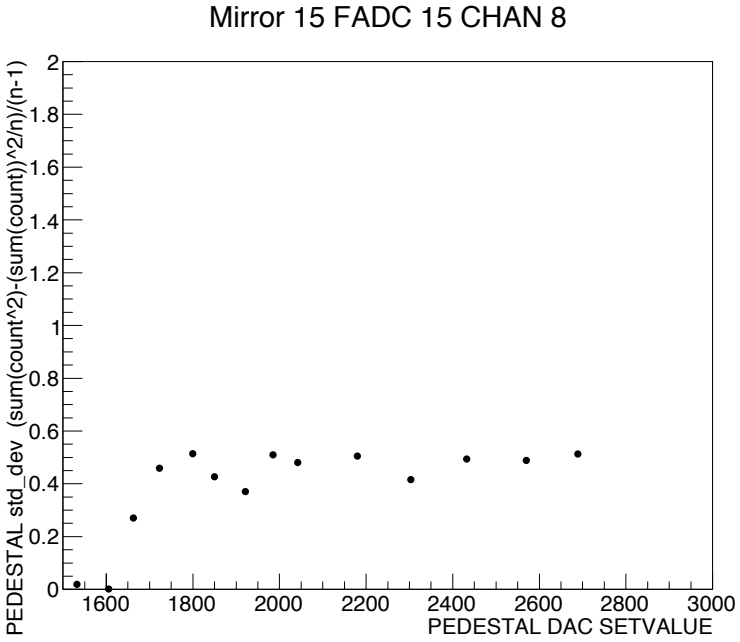

(b) TALE Broken Power Law Fit

Figure H.1: FADC Pedestal Test. Panel A shows the mean output pedestal value for a "good" channel over a series of pedestal DAC settings. Panel B shows the pedestal RMS "good" channel over the same series of pedestal DAC settings.

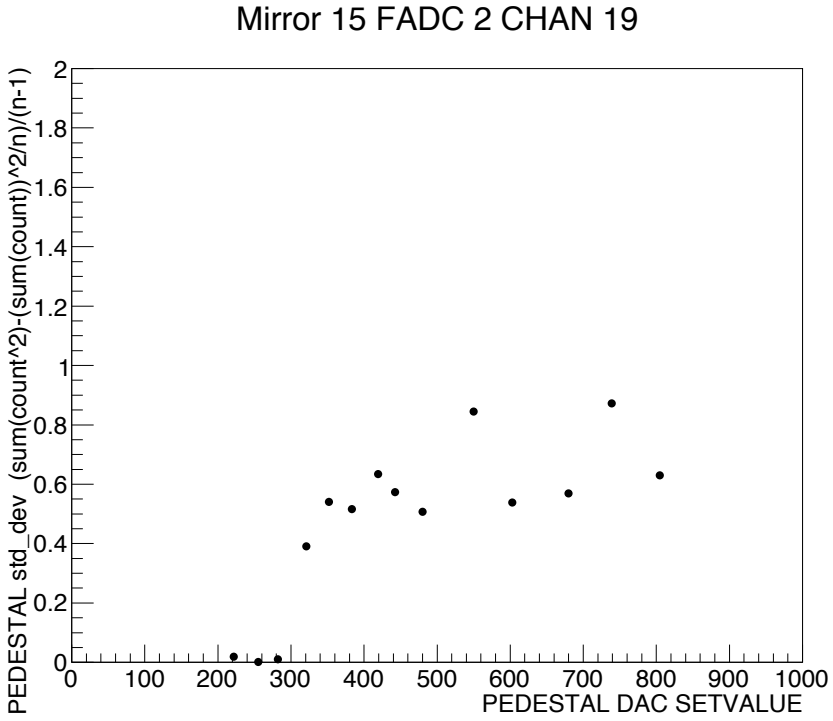

Figure H.2: FADC Test Pedestal RMS Failure. This graph shows the output pedestal RMS value for a "bad" channel for a series of pedestal DAC settings. Since the RMS reported a value above 0.8 ADC counts for two of the DAC settings, it was flagged as "bad".

APPENDIX I

DATA - MC COMPARISIONS

This appendix provides the data Monte Carlo comparisons for the TALE data for each 0.1 $log(E[eV])$ bin in the energy range of $10^{16.5} - 10^{17.5}$ eV. For energies above $10^{17.5}$ eV, the remaining bins are grouped together due to the low statistics of the data. Table I.1 is provided to help the reader lookup the figure number of a given Data-MC comparison at a specific energy.

Table I.1: Table of Energy Dependent Data Monte Carlo Comparisons Figure Numbers. Energy is given by the E ($log(E)eV$) column and the V row list the variables.

E \ V	RP	θ	ϕ	Ψ	track length
16.55	Fig I.1	Fig I.4	Fig I.7	Fig I.10	Fig I.13
16.65	Fig I.1	Fig I.4	Fig I.7	Fig I.10	Fig I.13
16.75	Fig I.1	Fig I.4	Fig I.7	Fig I.10	Fig I.13
16.85	Fig I.1	Fig I.4	Fig I.7	Fig I.10	Fig I.13
16.95	Fig I.2	Fig I.5	Fig I.8	Fig I.11	Fig I.14
17.05	Fig I.2	Fig I.5	Fig I.8	Fig I.11	Fig I.14
17.15	Fig I.2	Fig I.5	Fig I.8	Fig I.11	Fig I.14
17.25	Fig I.2	Fig I.5	Fig I.8	Fig I.11	Fig I.14
17.35	Fig I.3	Fig I.6	Fig I.9	Fig I.12	Fig I.14
17.45	Fig I.3	Fig I.6	Fig I.9	Fig I.12	Fig I.15
17.5+	Fig I.3	Fig I.6	Fig I.9	Fig I.12	Fig I.15

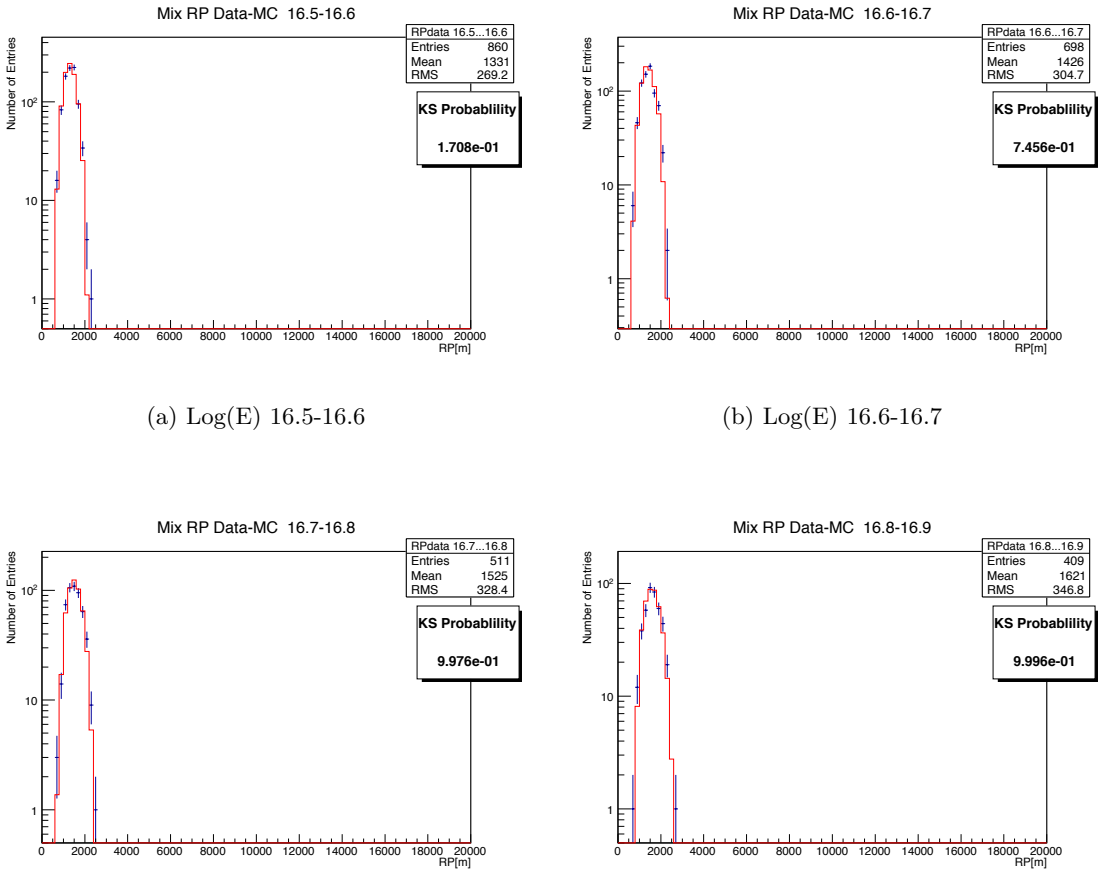

(a) Log(E) 16.5-16.6

(b) Log(E) 16.6-16.7

(c) Log(E) 16.7-16.8

(d) Log(E) 16.6-16.9

Figure I.1: RP Data MC Comparisons by Energy Bin. $16.5 < log(E[eV]) < 16.9$.

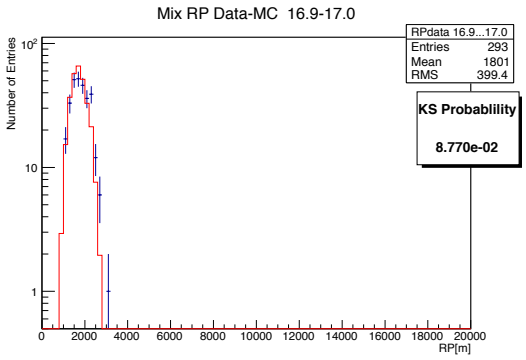

(a) Log(E) 16.9-17.0

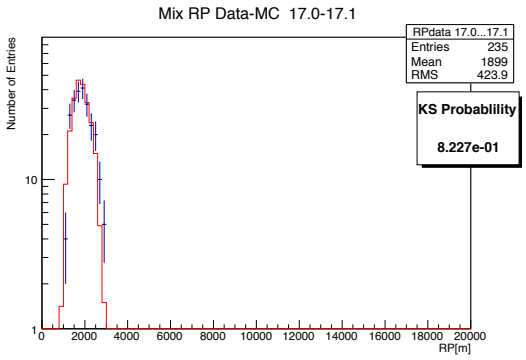

(b) Log(E) 17.0-17.1

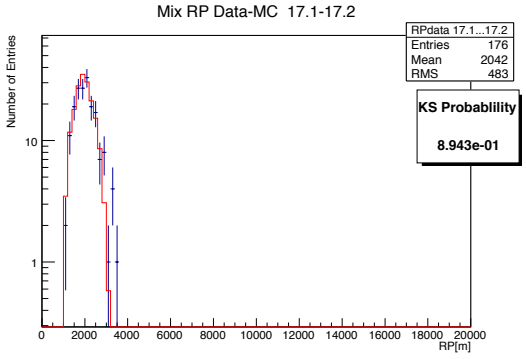

(c) Log(E) 17.1-17.2

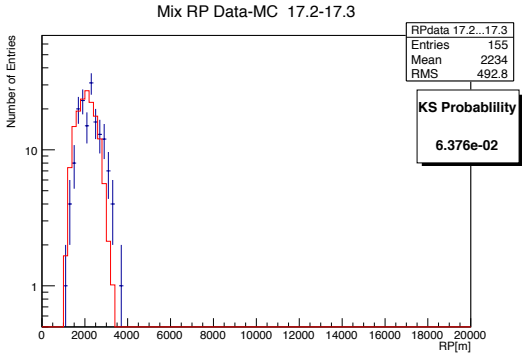

(d) Log(E) 17.2-17.3

Figure I.2: RP Data MC Comparisons by Energy Bin. $16.9 < log(E[eV]) < 17.3$.

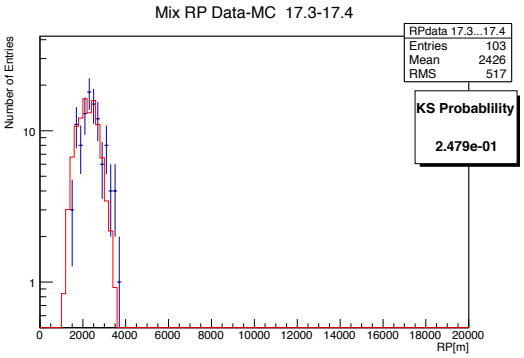

(a) Log(E) 17.3-17.4

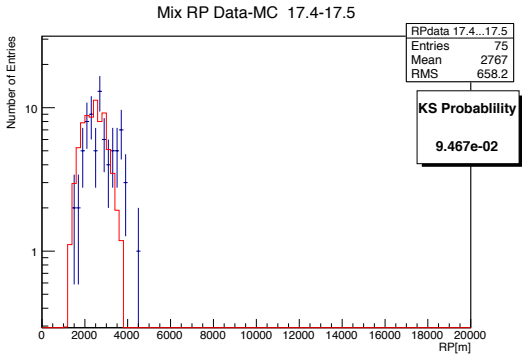

(b) Log(E) 17.4.-17.5

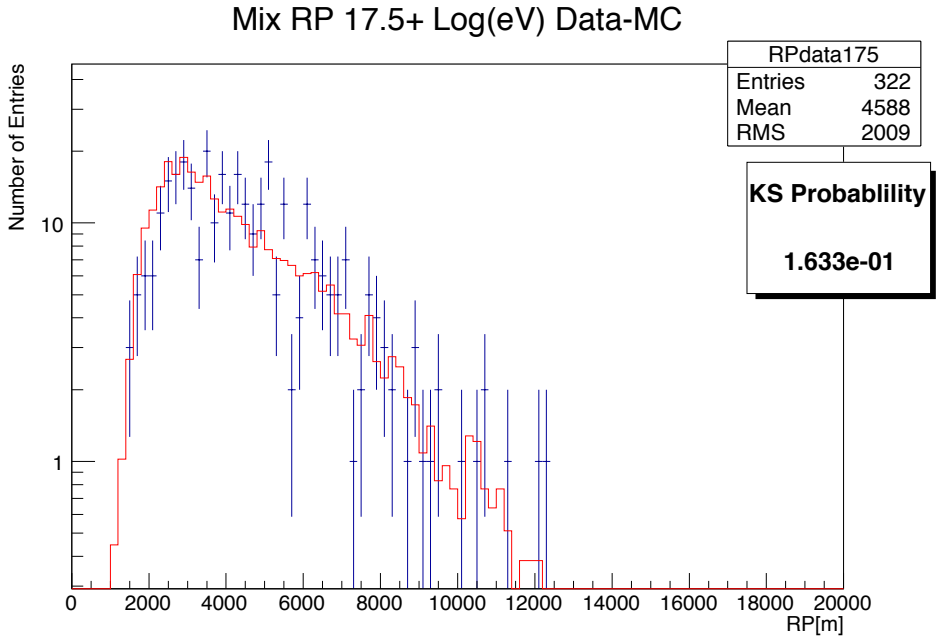

(c) Log(E) 17.5+

Figure I.3: RP Data MC Comparisons by Energy Bin. $17.3 < log(E[eV]) < 18.5$.

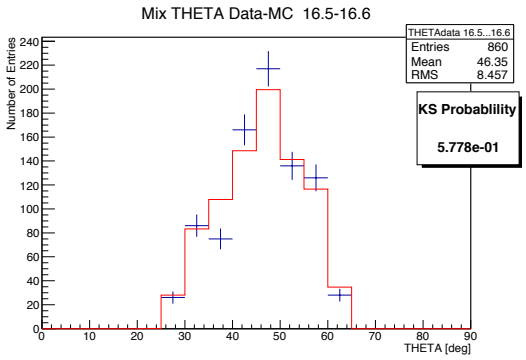

(a) Log(E) 16.5-16.6

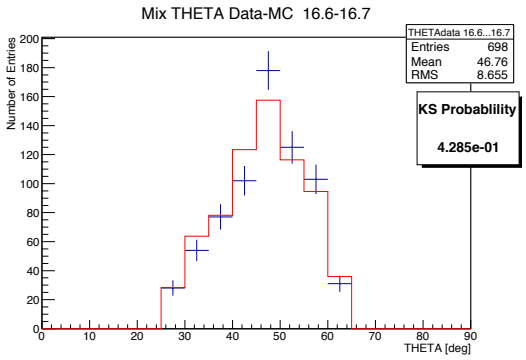

(b) Log(E) 16.6-16.7

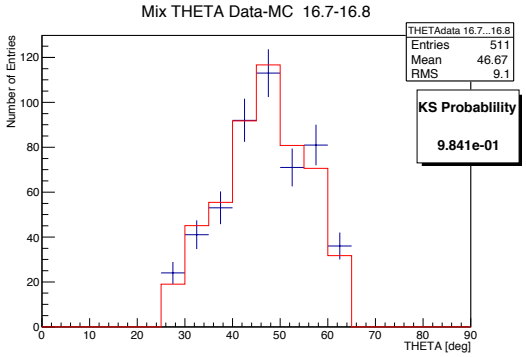

(c) Log(E) 16.7-16.8

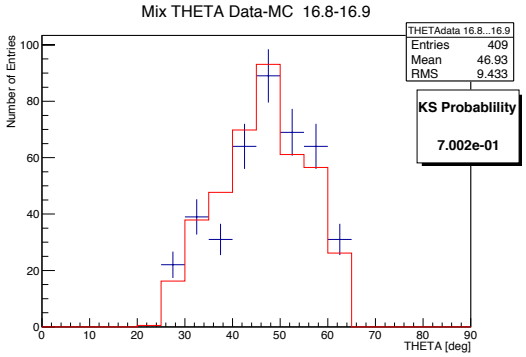

(d) Log(E) 16.6-16.9

Figure I.4: THETA Data MC Comparisons by Energy Bin. $16.5 < log(E[eV]) < 16.9$.

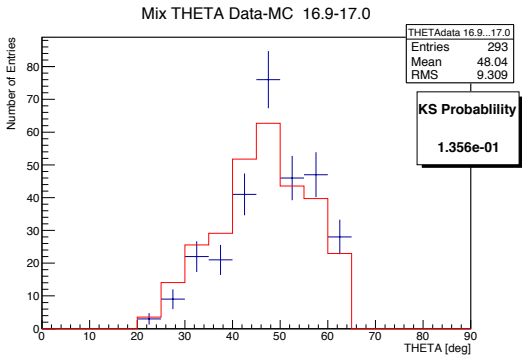

(a) Log(E) 16.9-17.0

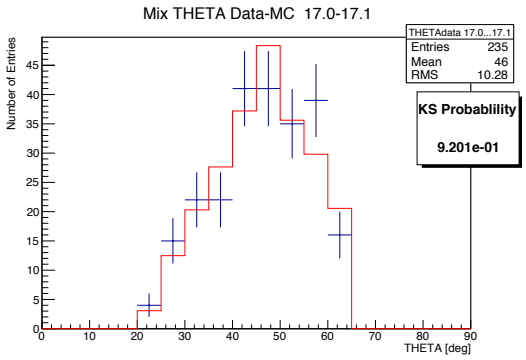

(b) Log(E) 17.0-17.1

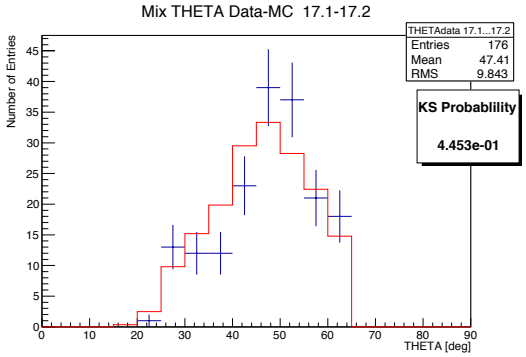

(c) Log(E) 17.1-17.2

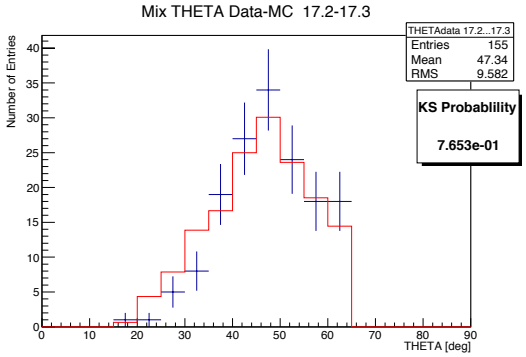

(d) Log(E) 17.2-17.3

Figure I.5: THETA Data MC Comparisons by Energy Bin. $16.9 < log(E[eV]) < 17.3$.

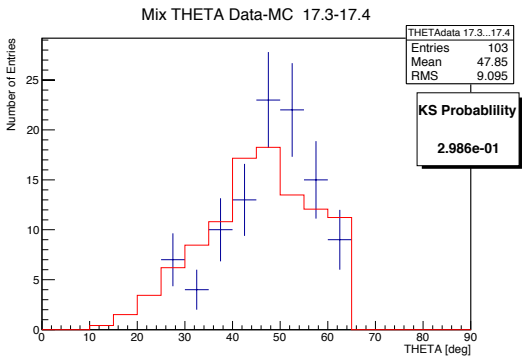

(a) Log(E) 17.3-17.4

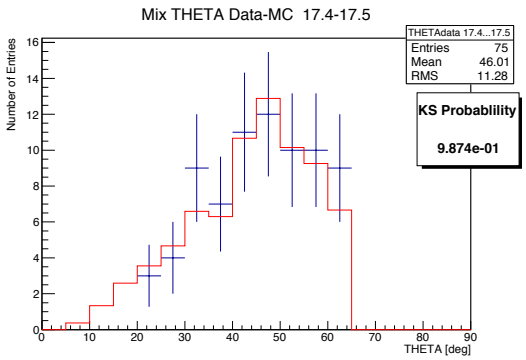

(b) Log(E) 17.4.-17.5

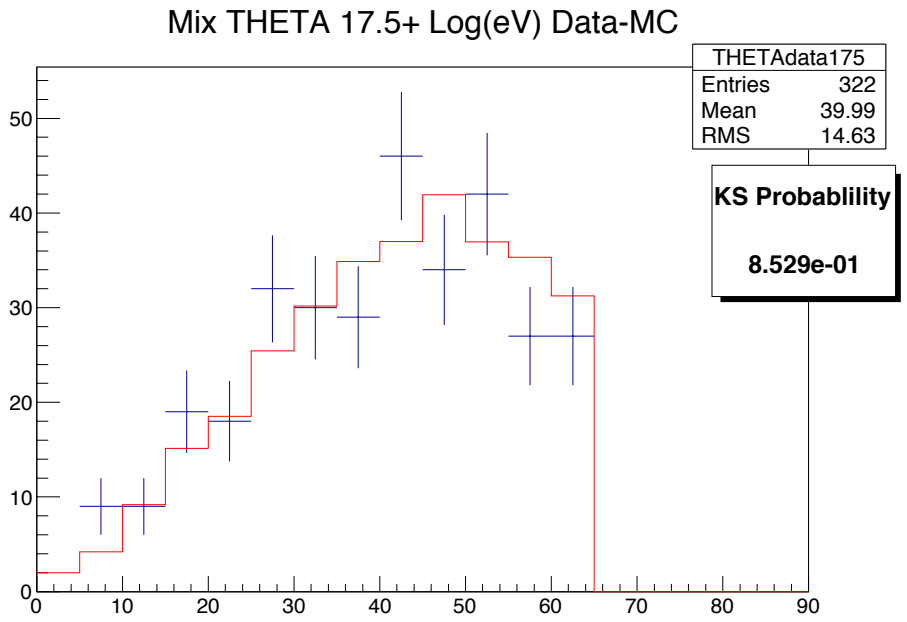

(c) Log(E) 17.5+

Figure I.6: THETA Data MC Comparisons by Energy Bin. $17.3 < log(E[eV]) < 18.5$.

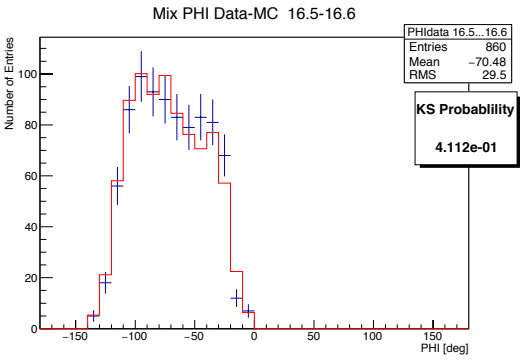

(a) Log(E) 16.5-16.6

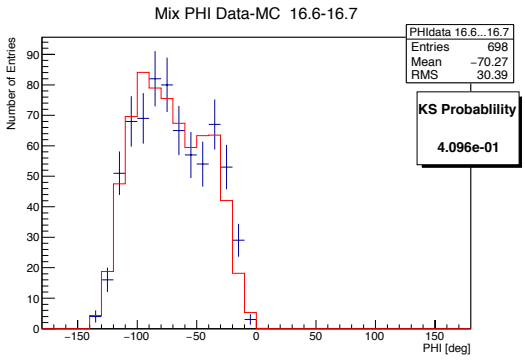

(b) Log(E) 16.6-16.7

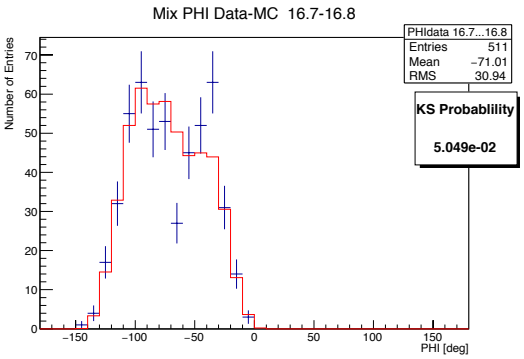

(c) Log(E) 16.7-16.8

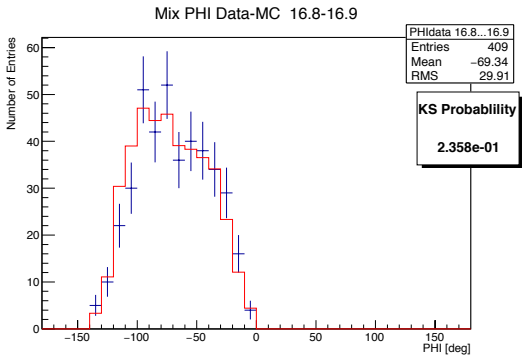

(d) Log(E) 16.6-16.9

Figure I.7: PHI Data MC Comparisons by Energy Bin. $16.5 < log(E[eV]) < 16.9$.

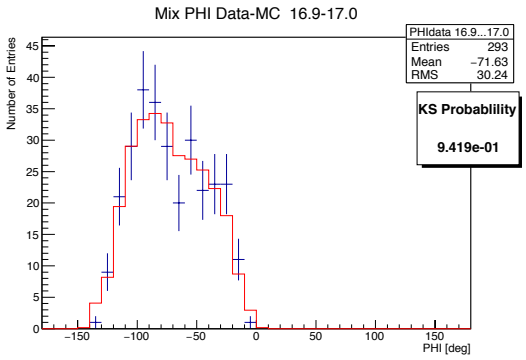

(a) Log(E) 16.9-17.0

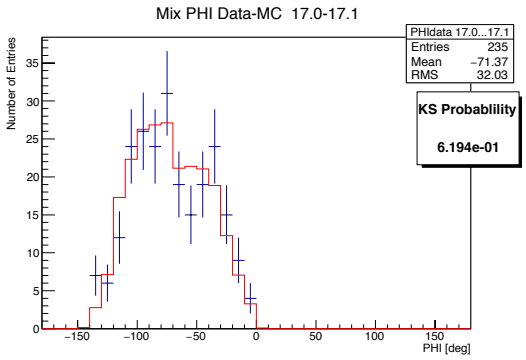

(b) Log(E) 17.0-17.1

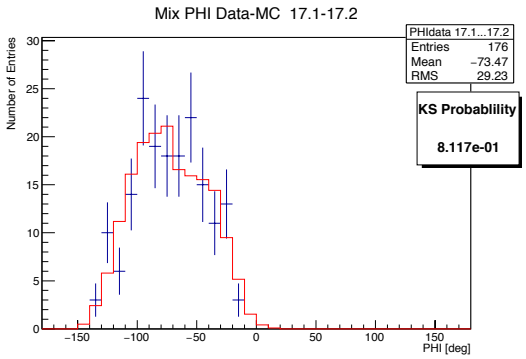

(c) Log(E) 17.1-17.2

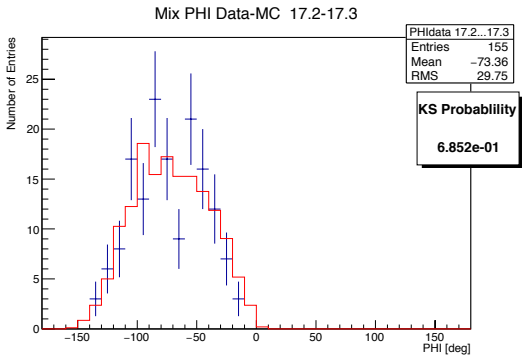

(d) Log(E) 17.2-17.3

Figure I.8: PHI Data MC Comparisons by Energy Bin. $16.9 < log(E[eV]) < 17.3$.

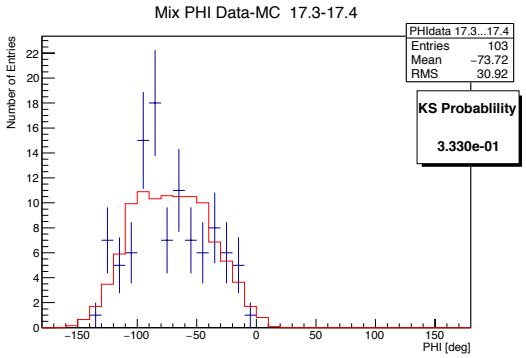

(a) Log(E) 17.3-17.4

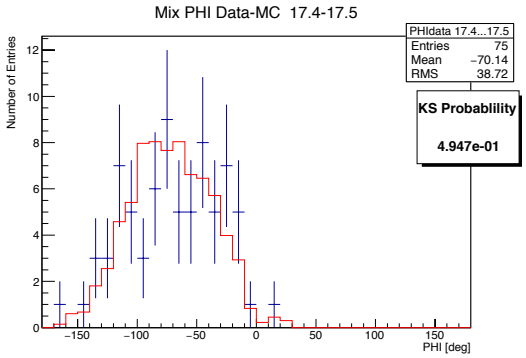

(b) Log(E) 17.4.-17.5

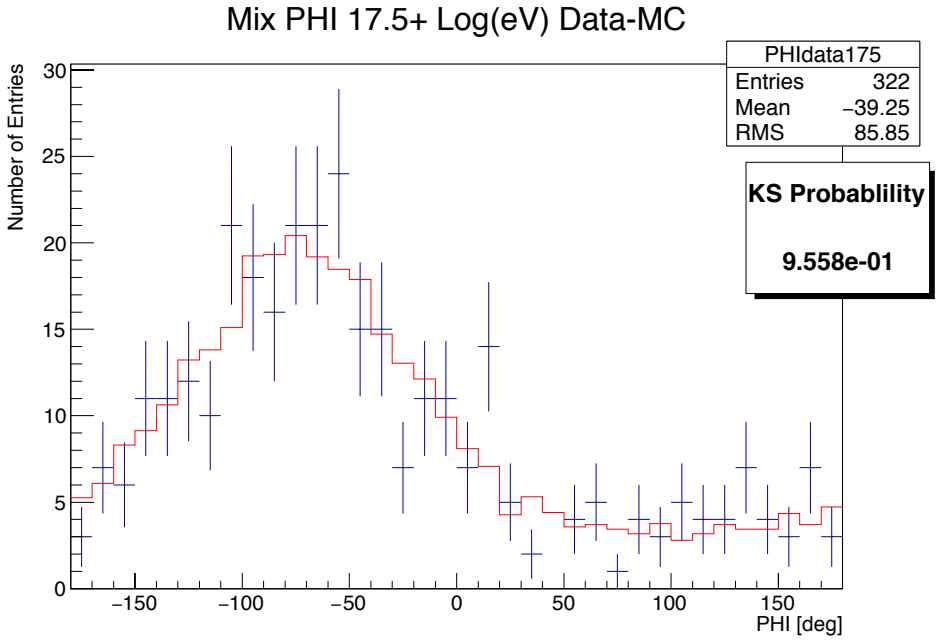

(c) Log(E) 17.5+

Figure I.9: PHI Data MC Comparisons by Energy Bin. $17.3 < log(E[eV]) < 18.5$.

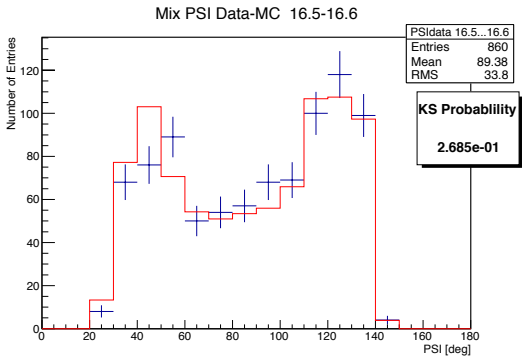

(a) Log(E) 16.5-16.6

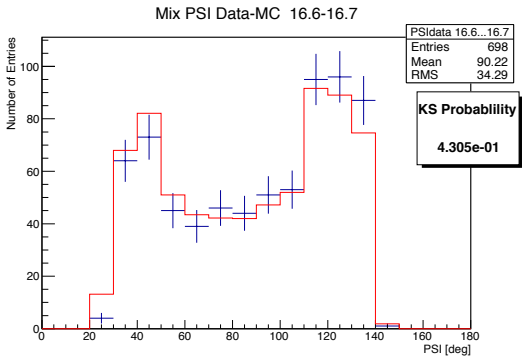

(b) Log(E) 16.6-16.7

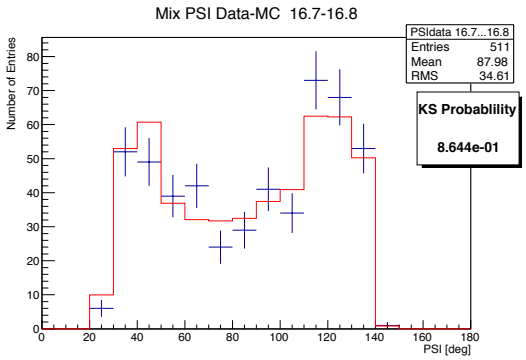

(c) Log(E) 16.7-16.8

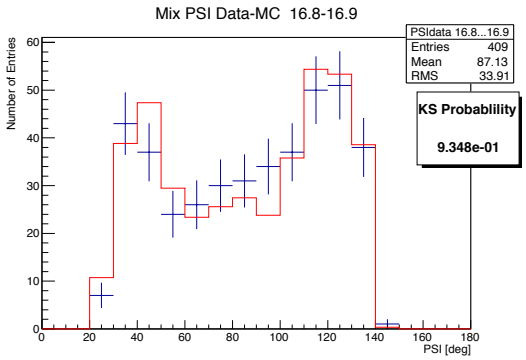

(d) Log(E) 16.6-16.9

Figure I.10: PSI Data MC Comparisons by Energy Bin. $16.5 < log(E[eV]) < 16.9$.

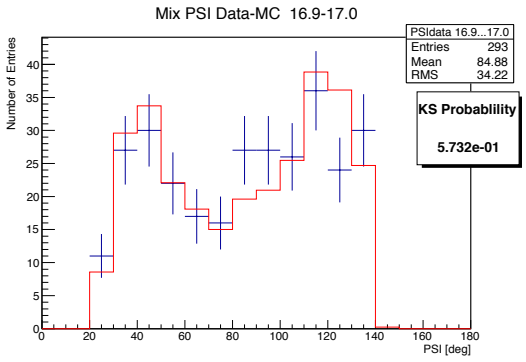

(a) Log(E) 16.9-17.0

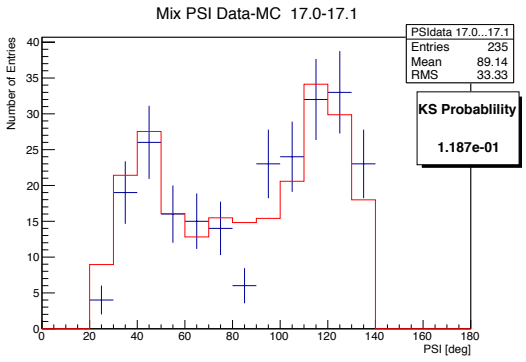

(b) Log(E) 17.0-17.1

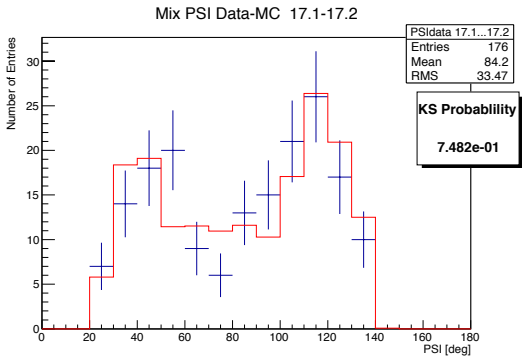

(c) Log(E) 17.1-17.2

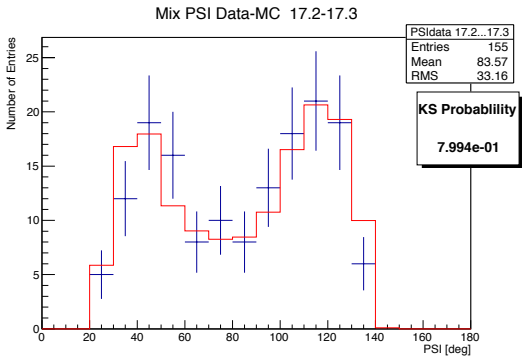

(d) Log(E) 17.2-17.3

Figure I.11: PSI Data MC Comparisons by Energy Bin. $16.9 < log(E[eV]) < 17.3$.

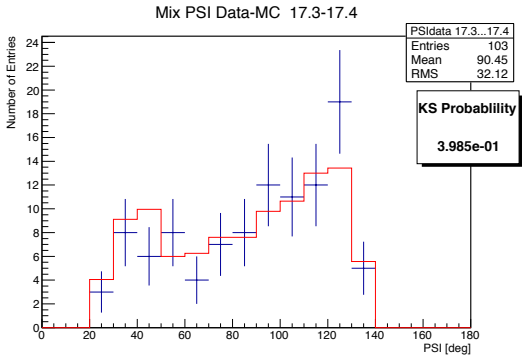

(a) Log(E) 17.3-17.4

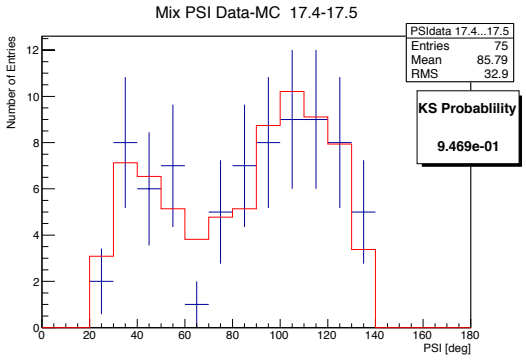

(b) Log(E) 17.4.-17.5

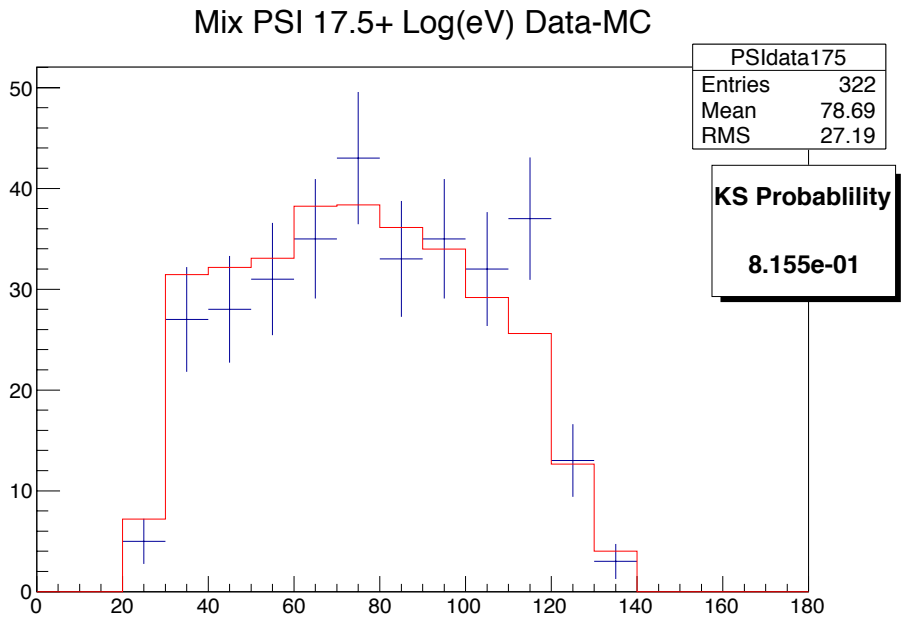

(c) Log(E) 17.5+

Figure I.12: PSI Data MC Comparisons by Energy Bin. $17.3 < log(E[eV]) < 18.5$.

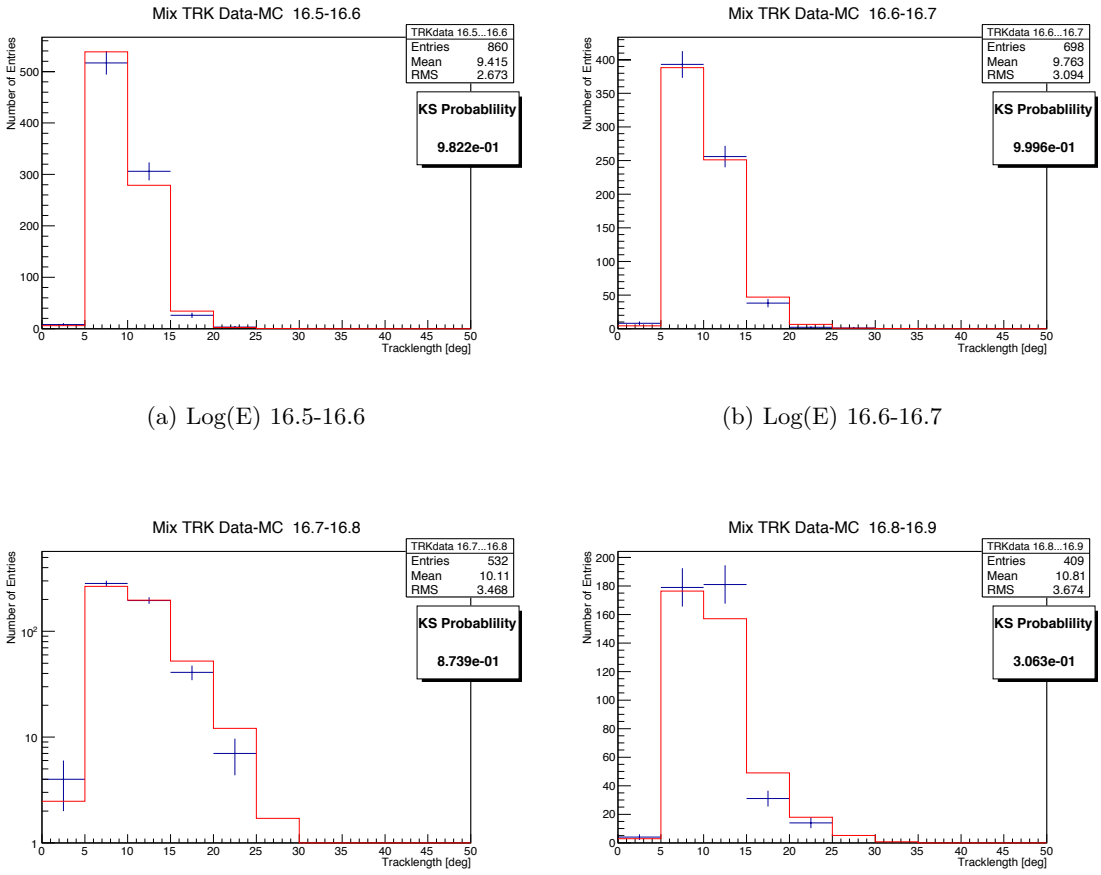

(a) Log(E) 16.5-16.6

(b) Log(E) 16.6-16.7

(c) Log(E) 16.7-16.8

(d) Log(E) 16.6-16.9

Figure I.13: TRK Data MC Comparisons by Energy Bin. $16.5 < log(E[eV]) < 16.9$.

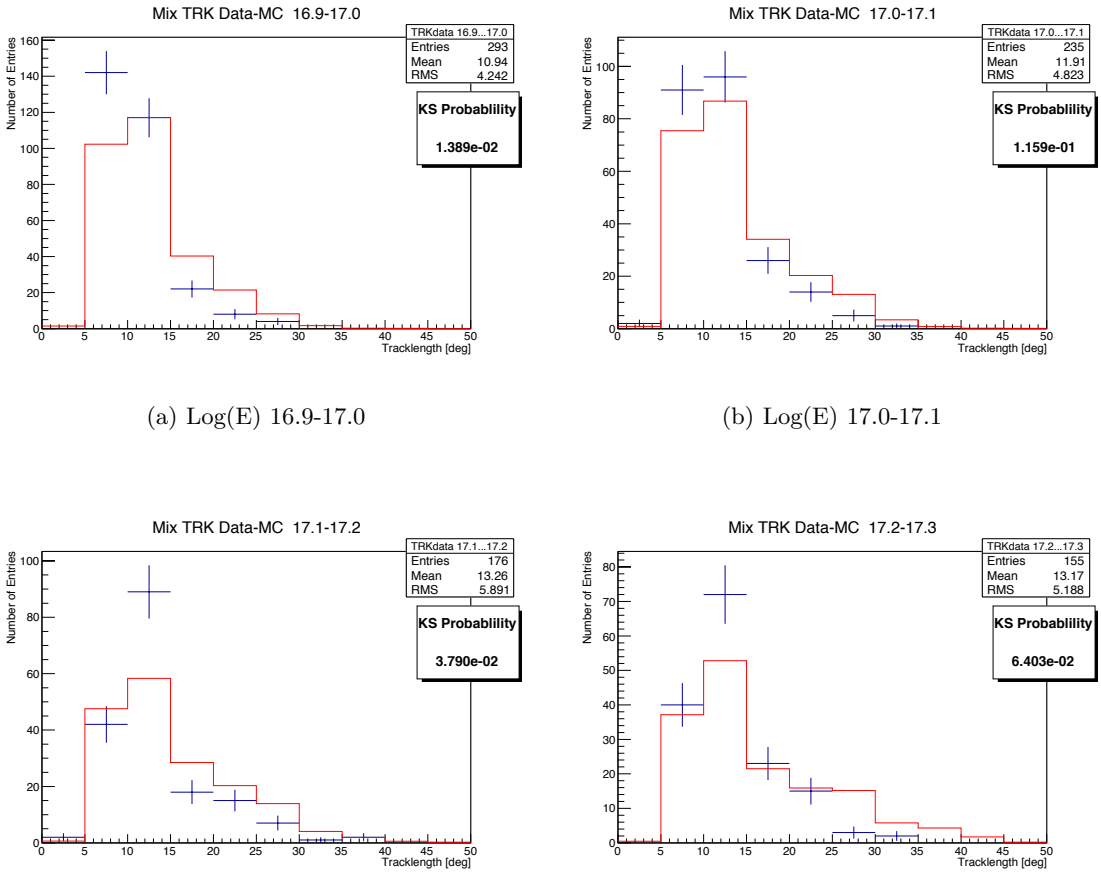

(a) Log(E) 16.9-17.0

(b) Log(E) 17.0-17.1

(c) Log(E) 17.1-17.2

(d) Log(E) 17.2-17.3

Figure I.14: TRK Data MC Comparisons by Energy Bin. $16.9 < log(E[eV]) < 17.3$.

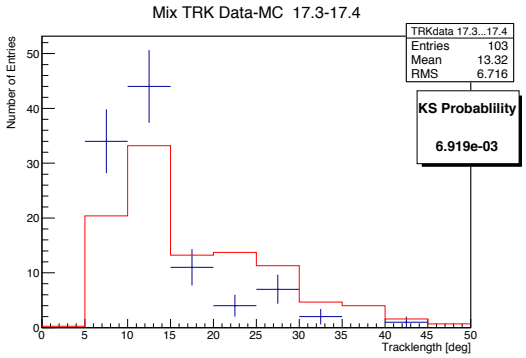

(a) Log(E) 17.3-17.4

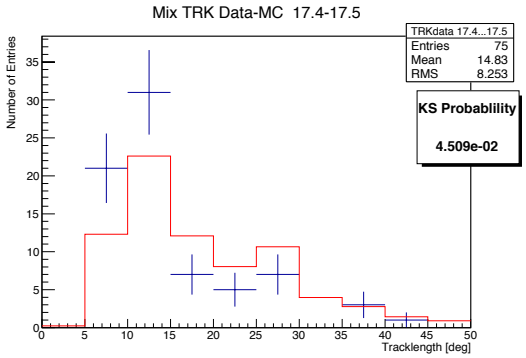

(b) Log(E) 17.4.-17.5

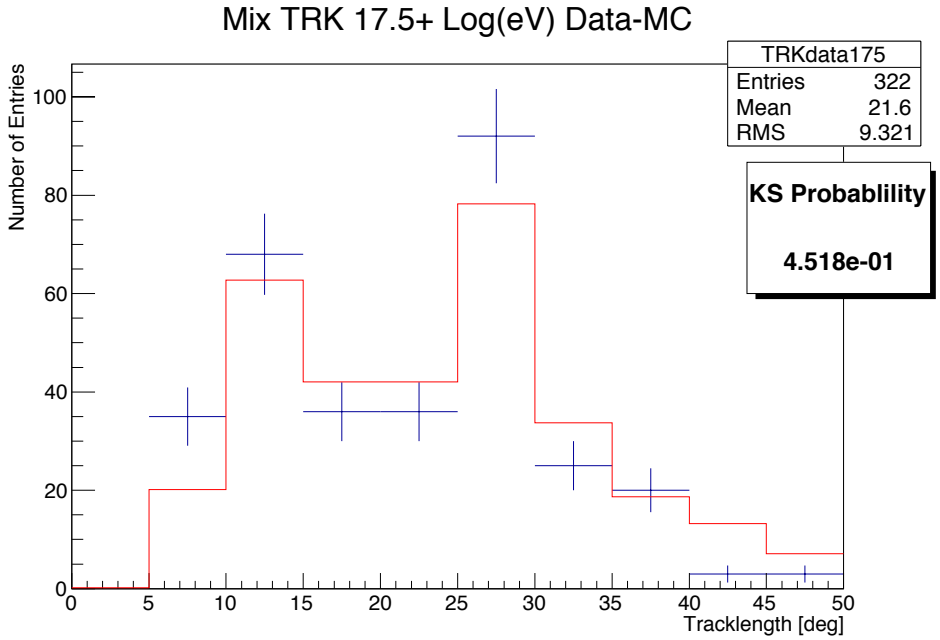

(c) Log(E) 17.5+

Figure I.15: TRK Data MC Comparisons by Energy Bin. $17.3 < log(E[eV]) < 18.5$.

APPENDIX J

ENERGY DEPENDENT CUTS

This section gives details on the determination of the energy dependent cuts reported in Section 8.6. The three parameters that have energy dependent quality cuts are RP_{max} (maximum distance of closest approach), Θ_{min} (minimum zenith angle), and XH (lowest allowed first observed depth of the track). The first two cuts are employed for the purpose of improving the energy resolution.

The RP_{max} cut values were determined by graphing the average energy resolution for protons and iron simulations versus the cut value in each energy bin. An example of this is shown in Figure J.1. The value of the cut is found by determining the point where the energy resolution flattens out and then adds 2km to that value. The method produces a set of cut values summarized in Figure J.2.

The cut values for Θ_{min} are determined by finding the minimum of the energy resolution for each energy bin and then finding the value of the left side of the falling curve that is 5% more than the value of the minimum. This improves the energy resolution without compromising event statistics. An example of the average resolution versus the Θ_{min} cut parameter is shown in Figure J.3. The result of applying this method for all energy bins is shown in Figure J.4.

The final energy dependent cut is the minimum value for the first observed depth of the shower (XH). This cut is implemented in order to make the TALE detector aperture insensitive to the cosmic ray composition. Cosmic rays of lighter composition can penetrate deeper into the atmosphere than heavier cosmic rays (which have larger cross sections). Requiring a minimum first observed depth reduces the number of penetrating protonic cosmic rays that remain in the final analysis. The XH cut is determined by finding the value where the ratio of the proton aperture to the iron aperture (determined from Monte Carlo simulation) is closest to one. An example graph used to determine the XH cut value in an energy bin is shown in Figure J.5.

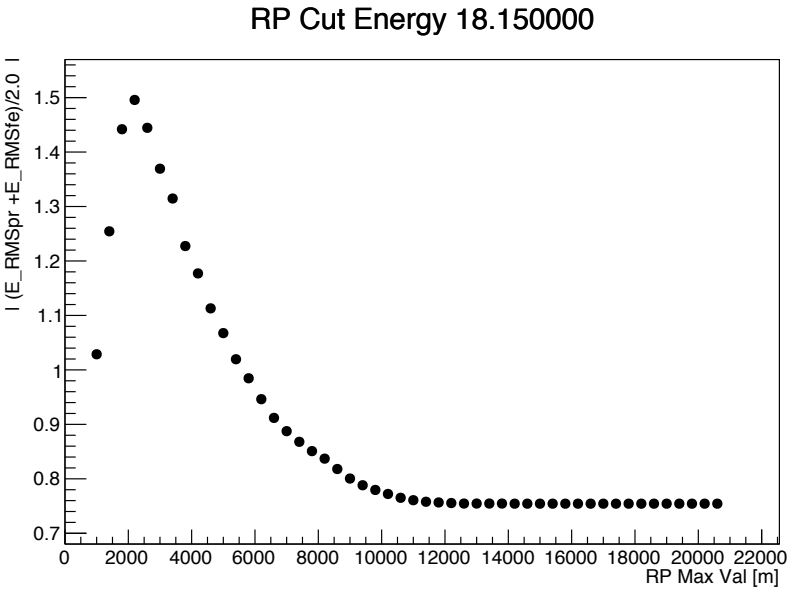

Figure J.1: RP_{max} Energy Dependent Cut Criteria Example. The cut value is determined by locating the point where the resolution flattens and then adds 2km to the value.

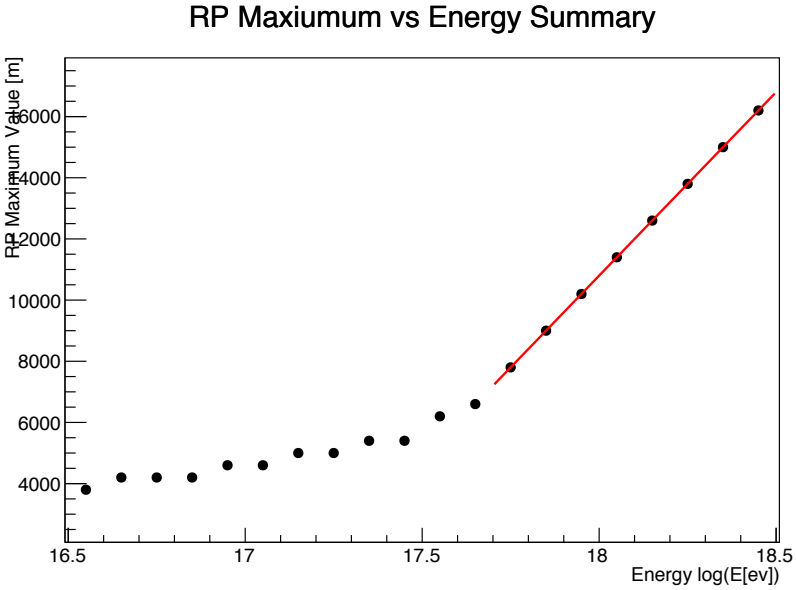

Figure J.2: RP_{max} Energy Dependent Cut Summary. This graph shows the resulting energy dependent cuts for the RP_{max} parameter.

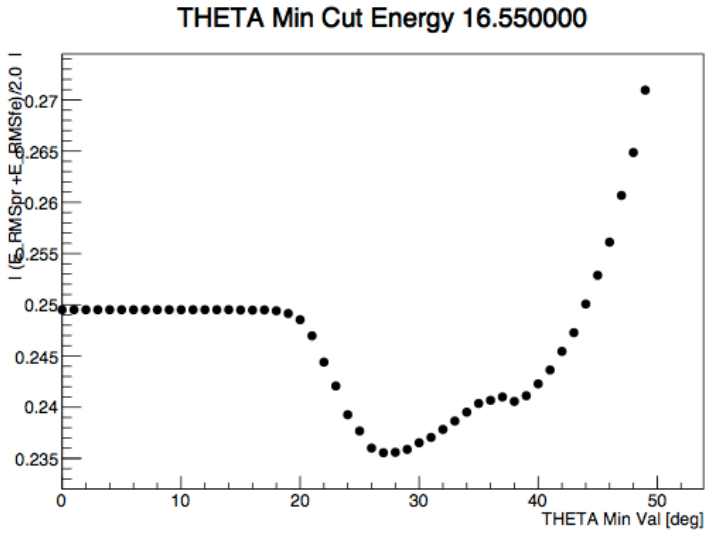

Figure J.3: Θ_{min} Energy Dependent Cut Criteria Example. The cut value is determined by locating the minimum for the resolution and then finding the value of the left side of the falling curve that is 5% more than the value of the minimum.

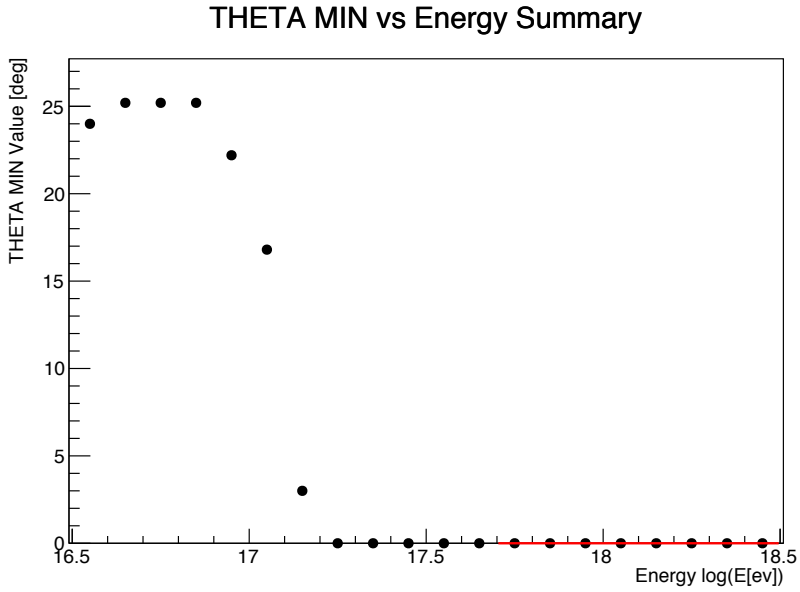

Figure J.4: Θ_{mmin} Energy Dependent Cut Summary. This graph shows the resulting energy dependent cuts for the Θ_{min} parameter. This demonstrates a transition from a cut value of 25° below $10^{17.0}$eV, whereas the cut goes to 0° below $10^{17.2}$eV.

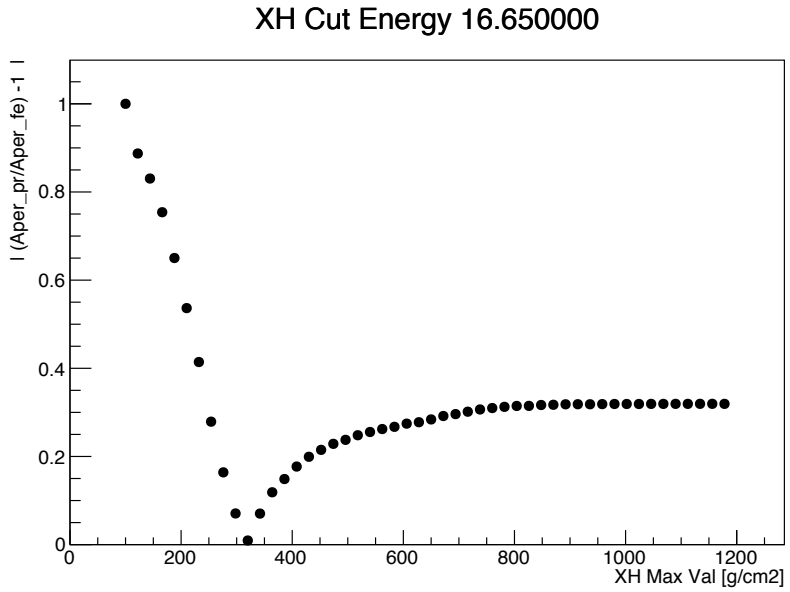

Figure J.5: XH Energy Dependent Cut Criteria Example. The cut value is determined by locating where the ratio of the proton aperture to the iron aperture is closest to 1, which appears as a minimum in this graph.

REFERENCES

[1] Grieder, Peter K.F. *Extensive Air Showers -High Energy Phenomena and Astrophysical Aspects - A Tutorial, Reference Manual and Data Book*, volume 1. Springer, 2nd edition, 2010.

[2] Westfall, G.D. *et al.* Fragmentation of relativistic fe. *Phys. Rev. C, 19,1309*, 1979.

[3] Saito, T. The interaction mean free paths and the fragmentation probabilities of cosmic heavy nuclei at energies above 10 gev/nucleon. *J. Phys. Soc. Jpn., 30,1243-1251*, 1971.

[4] Ave, M. *et al.* Measurement of the pressure dependence of air fluorescence emission induced by electrons. *Astropart. Phys., 28, 41-57*, 2007.

[5] Stopping power and range tables for electrons. `http://physics.nist.gov/PhysRefData/Star/Text/ESTAR.html`. Accessed June 6, 2015. Record from NIST.

[6] Sternheiner, R.H. *et al.* Density effects for the ionization loss of charged particles in various substances. *Atom. Data Nucl. Data Tabl., 30, 261*, 1984.

[7] Rodriguez, D. *The Telescope Array Middle Drum Monocular Energy Spectrum and a Search for Coincident Showers Using High Resolution Fly's Eye HiRes-I Monocular Data*. PhD thesis, University of Utah, 2012.

[8] Cady, R. Telescope array political map. `http://www.telescopearray.org/tawiki/images/0/07/TA110K17Dec2007.pdf`. Accessed June 2, 2015.

[9] Longair, M.S. *High Energy Astrophysics*, volume 2. Cambridge University Press, 3rd edition, 2011.

[10] Bellini, G. and Ludhova, L. *Particle Detectors*. Cambridge University Press, 2nd edition, 2008.

[11] Mathews, J.N. Ta surface detector example photgraph. `http://www.telescopearray.org/internal/gallery/main.php?g2_itemId=31976`. Accessed June 2, 2015.

[12] Kuraray wavelength shifting fiber datasheets. `http://kuraraypsf.jp/pdf/all.pdf`. Accessed June 16, 2015.

[13] Et enterprises 9124sa pmt datasheet. `http://my.et-enterprises.com/pdf/9124B.pdf`. Accessed June 16, 2015.

[14] Abraham, J. *et al.* Trigger and aperture of the surface detector array of the pierre auger observatory' . *Nucl. Instr. Meth., 613, 29-39*, 2009.

[15] Hanlon, W. Cosmic ray spectrum summary. `http://www.physics.utah.edu/~whanlon/spectrum1.png`. Accessed June 2, 2015.

[16] Abu-Zayyad, T. *et al.* The cosmic-ray energy spectrum observed with the surface detector of the telescope array experiment. *Astrophys. J., 48, 16-24*, 2013.

[17] Berezinsky, V., Gazizov, A.Z., and Grigorieva, S.I. Dip in UHECR spectrum as signature of proton interaction with CMB. *Phys. Lett. B, 612, 147-153*, 2005.

[18] Abbasi, R. *et al.* Study of ultra-high energy cosmic ray composition using telescope array's middle drum detector and surface array in hybrid mode. *Astropart. Phys., 64, 49-62*, 2014.

[19] Rossi, B. Misure della distribuzione angolare di intensit della radiazione penetranteallasmara. *La Ricerca Scientifica. Supplement, 1, 579589.*, 1934.

[20] Auger, P and Maze, R. Extension et ouvoir penetrant des grandes geres de rayons cosmiques. *Compt. Rend., 208, 1641-1643*, 1939.

[21] Olive, K.A. *et al.* Review of particle physics. *Chin. Phys.*, C38:090001, 2014.

[22] Alner, G.J. *et al.* A new empirical regularity for multiplicity distributions in place of KNO scaling. *Phys. Lett. B, 160, 199-206*, 1985.

[23] Capdevielle, J.N. and Attallah, R. Parton distribution functions and the uhe cosmic-ray interactions. *Nucl. Part. Phys., 21, 121*, 1995.

[24] Babecki, J. On the dependence of the multiplicity of particles produced in the proton-nucleus interactions at high energies on the mass number of the target. *ICRC, 7, 2253-2257*, 1975.

[25] Adamovich, M.I. *et al.* Produced particle multiplicity dependence on centrality in nucleus nucleus collisions. *Nucl. Part. Phys., 22, 1469-1481*, 1996.

[26] Cerenkov, P.A. Visible radiation produced by electrons moving in a medium with velocities exceeding that of light' . *Phys. Rev., 52, 378*, 1937.

[27] Loftus, A. and Krupenie, P.H. Spectrum of molecular nitrogen. `http://www.nist.gov/data/PDFfiles/jpcrd93.pdf`. Accessed June 2, 2015. Record from NIST.

[28] Keilhauer, B. *et al.* Nitrogen fluorescence in air for observing extensive air showers. *arXiv:1210.1319 [astro-ph.HE]*, 2012.

[29] Kakimoto, F. *et al.* A measurement of the air fluorescence yield. *Nucl. Instr. Meth. Phys. Res., 372, 527-533.*, 1996.

[30] Belz, J.W. *et al.* Measurement of pressure dependent fluorescence yield of air:calibration factor for UHECR detectors. *arXiv:astro-ph/0506741*, 2005.

[31] Nagano, M. *et al.* Photon yields from nitrogen gas and dry air excited by electrons. *Astropart. Phys., 20, 293-309*, 2003.

[32] AbuZayyad, T. *The Energy Spectrum of Ultra High Energy Cosmic Rays.* PhD thesis, University of Utah, 2000.

[33] Hanlon, W. *The Energy Spectrum of Ultra High Energy Cosmic Rays Measured by the High Resolution Flys Eys Observatory in Stereoscopic Mode.* PhD thesis, University of Utah, 2008.

[34] Sokolsky, P. *Introduction to Ultra High Energy Cosmic Ray Physics*. Westview Press, 1st edition, 2004.

[35] Ivanov, D. *Energy Spectrum Measurement by the Telescope Array Surface Detector*. PhD thesis, Rutgers University, 2011.

[36] Fukushima, M. Measurement of ultra-high energy cosmic rays: An experimental summary and prospects. *arXiv:1302.5893 [astro-ph.HE]*, 2013.

[37] Nonaka, T. *et al.* Calibration of the TA surface detectors. *ICRC, 5, 1005-1008*, 2008.

[38] Takeda, M. *et al.* Energy determination in the AKENO giant air shower array experiment. *Astropart. Phys., 19, 447-462*, 2002.

[39] Mason, G.W. *et al.* Observations of extensive air showers by air fluorescence description of experimental techniques. *ICRC, 8, 252-257*, 1977.

[40] Allen, M. *Ultra High Energy Cosmic Ray Energy Spectrum and Composition using Hybrid Analysis with Telescope Array*. PhD thesis, University of Utah, 2012.

[41] Cassidy, M. *et al.* Casa-blanca: A large non-imaging cherenkov detector at casa-mia. *arXiv:astro-ph/9707038*, 1997.

[42] Krizmanic, J. *et al.* The non-imaging cherenkov array (niche): A ta/tale extension to measure the flux and composition of very-high energy cosmic rays. *arXiv:1307.3912 [astro-ph.IM]*, 2013.

[43] Boothby, K. *et al.* A new measurement of cosmic ray composition at the knee. *Astropart. Phys. J., 491, 35-38*, 1997.

[44] Perkins, D. *Particle Astrophysics*. Oxford University Press, 2nd edition, 2009.

[45] Abassi, R. *et al.* First observation of the greisen-zatsepin-kuzmin suppression. *Phys. Rev. Lett., 100, 101101-101105*, 2008.

[46] Capdevielle, J.N. *et al.* Agasa energy spectrum and the GZK cut-off. *Nucl. Phys. B , 196, 231-234*, 2009.

[47] Takeda, M. *et al.* Energy determination in the AKENO giant air shower array experiment. *Astrophys. J,19, 447-462*, 2003.

[48] Abraham, J. *et al.* Observation of the suppression of the flux of cosmic rays above $4x10^{19}$ ev. *Phys. Rev. Lett., 101, 061101*, 2008.

[49] Greisen, K. End to the cosmic-ray spectrum. *Phys. Rev. Lett., 16, 784*, 1966.

[50] Berezinsky, V. and Grigorieva, S.I. A bump in the ultra-high energy cosmic ray spectrum. *Astron. Astrophysics, 199, 1-12*, 1998.

[51] Sokolsky, P. *et al.* Comparison of UHE composition measurements by flys eye, HiRes-prototype/MIA and stereo hires experiments. *ICRC, 7, 381-384*, 2005.

[52] Boncioli, D.. Cosmic ray composition studies with the Pierre Auger observatory. *Nucl. Instr. Meth. Phys. Res., 742, 22-28*, 2014.

[53] Gorbunov, G. *et al.* Evidence for a connection between the gamma-ray and the highest energy cosmic-ray emissions by BL lacertae objects. *Astrophys.J., 577, 93*, 2002.

[54] de Mello, J.R.T. *et al.* Anisotropy studies with the Pierre Auger observatory. *J. Phys., 409, 12108*, 2013.

[55] Abbasi, R. *et al.* Indications of intermediate-scale anisotropy of cosmic rays with energy greater than 57 EeV in the northern sky measured with the surface detector of the telescope array experiment. *Astrophys. J. Lett., 790, 21, 2014*, 2014.

[56] AbuZayyad, T. *et al.* Evidence for changing of cosmic ray composition between 10^{17} and 10^{18} ev from multicomponent measurements. *Phys. Rev. Lett., 84, 4276-4279*, 2000.

[57] AbuZayyad, T. *et al.* Measurement of the cosmic ray energy spectrum and composition from 10^{17} to 10^{18}ev using a hybrid fluorescence technique. *Astrophys.J., 557, 686-699*, 2001.

[58] Boyer, J.H., Knapp, B.C., Mannel, E.J., and Seman, M. FADC-based DAQ for HiRes flys eye. *Nucl. Instrum. Meth., 482, 457-474*, 2002.

[59] Flyckt, S.O. and Marmonier, C.. Photomultiplier tubes principles and applications. `http://www2.pv.infn.it/~debari/doc/Flyckt_Marmonier.pdf`. Accessed June 16, 2015.

[60] FAD. +5 volt, serial input, dual 12-bit dac. `http://www.analog.com/media/en/technical-documentation/data-sheets/AD8522.pdf`. Accessed June 16, 2015.

[61] AD. 8-bit 20 msps, 60 mw sampling a/d converter. `http://www.wvshare.com/datasheet/AD_PDF/AD775.PDF`. Accessed June 16, 2015.

[62] Atmel. Using the atv750, atv750b, and atf750c erasable programmable logic device. `http://www.atmel.com/Images/Atmel-0459-PLD-Using-ATV750-750B-ATF750C-ApplicationNote.pdf`. Accessed June 16, 2015.

[63] IDT. CMOS static ram. `https://www.idt.com/document/dst/7164sl-data-sheet`. Accessed June 16, 2015.

[64] IDT. CMOS static ram 256k. `https://www.idt.com/document/dst/71256sa-datasheet`. Accessed June 16, 2015.

[65] FREESCALE. Dsp56309 users manual. `http://www.freescale.com/files/dsp/doc/ref_manual/DSP56309UM.pdf`. Accessed June 16, 2015.

[66] Atmel. Flex 8000 programmable logic device family. `https://www.altera.com/content/dam/altera-www/global/en_US/pdfs/literature/ds/dsf8k.pdf`. Accessed June 16, 2015.

[67] Atmel. Max 7000 programmable logic device family. `https://www.jameco.com/Jameco/Products/ProdDS/1724529.pdf`. Accessed June 16, 2015.

[68] Smith, R.E.. `http://www.rs485.com/`. Accessed June 16, 2015.

[69] Cameron, J. and Hurd, G. The terminator. Film. 1984.

[70] FREESCALE. Dsp56309 users manual. `http://uploads.cq-dx.ru/pdf/DSP/DSP56166UM0.PDF`. Accessed June 16, 2015.

[71] Weeder technologies. http://www.weedtech.com/. Accessed June 16, 2015.

[72] Matthews, J.N. and Thomas, S. Calibrating the high resolution fly's eye (HiRes) detector. *ICRC, 7, 365*, 2005.

[73] Guerin, D. Xp3062/fl - poisson distribution at the anode. Internal Communication from Photonis to Stan Thomas. 2000.

[74] Heck, D. *et al.* Corsika: A monte carlo code to simulate extensive air showers. https://web.ikp.kit.edu/corsika/physics_description/corsika_phys.pdf. Accessed June 16, 2015.

[75] Jackson, J.D. *Classical Electrodynamics*. John Wiley & Sons ICS., 3rd edition, 1998.

[76] Tale message packet details. http://www.telescopearray.com/tawiki/index.php/TALE_Message_Packets. Accessed June 16, 2015.

[77] Gaisser, T.K. Spectrum of cosmic-ray nucleons, kaon production, and the atmospheric muon charge ratio. *Astropart. Phys., 35, 801-806*, 2012.

[78] Olive, K.A. *et al.* Review of Particle Physics. *Chin. Phys.*, C38:090001, 2014. Accessed June 16, 2015.

[79] Dosbox emulator. http://www.dosbox.com. Accessed June 16, 2015.

[80] Wine emulator. https://www.winehq.org. Accessed June 16, 2015.